HIGH RESOLUTION PHOTOELECTRON SPECTROSCOPY OF SMALL MOLECULES

JON G. GOODE

DOCTOR OF PHILOSOPHY
UNIVERSITY OF EDINBURGH
1995

Declaration

I hereby declare that this thesis has been composed by myself, and except where due acknowledgement is given, the work described in it is my own and was carried out at the University of Edinburgh and the Daresbury Laboratory.

This is not the end. It
is not even the
beginning of the end.
But it is, perhaps, the
end of the beginning.

Sir Winston Churchill,
Mansion House, London,
10 November, 1942

Acknowledgements

There are many people without whom very little of this thesis would have been possible. First and foremost are Professor Robert Donovan and Dr. Kenneth Lawley, without whose support and initial offer of a Ph.D. I would not be writing this now. Very little of the work carried out in Edinburgh over the past three years would have been possible without Robert Maier. Although he is no spectroscopist, as he himself admits, his technical ability has been invaluable to the success of the project. The arrival of Dr. Martin Cockett midway through my research, brought with it a wealth of experience in the field of ZEKE and certainly accelerated the research within the lab for which I am very grateful. The threshold studies which were carried out at the Daresbury Laboratory, again would have been impossible without a number of people. The relaxed attitude of Dr. Andy Hopkirk was very much in contrast to Professor Andrew Yencha but without the dedication and experience of both my time at Daresbury I'm sure would not have been as enjoyable and productive. I must also take this opportunity to thank all the other members of the laser group, especially Dr. Trevor Ridley and Andy Cormack. Last but certainly not least are my family. They have played a very supportive role throughout my days as an undergraduate and a postgraduate for which I am very grateful.

I feel certain people would feel as though I had forgotten something if I did not mention my sailing. I cannot acknowledge all those who have given me reason to escape from the lab, but the many members of Edinburgh University Sailing Club, the 470 squad and also all those I have worked with at the Firbush Point Field Centre deserve a special mention.

I must also take this opportunity to thank SERC, or what is now the EPSRC for funding me over the past three years and the EEC for funding the ZEKE project.

Abstract

The diatomic homonuclear halogens have been investigated using both threshold photoelectron spectroscopy (TPES) and zero kinetic energy pulsed field ionisation (ZEKE-PFI) photoelectron spectroscopy. The threshold photoelectron technique employed synchrotron radiation to obtain a broad overview of the valence ionisation region while ZEKE-PFI photoelectron spectroscopy investigated in detail the ground ionic state of the molecular iodine cation and the iodine-argon van der Waals complex cation.

An extensive TPES study of the chlorine, bromine and iodine cations has been carried out with a new penetrating field electron spectrometer at the Daresbury Laboratory. The spectra recorded for both chlorine and bromine cover the ionisation energy range from the onset of ionisation up to 35 eV whereas that recorded for iodine extends up to 14 eV. The threshold photoelectron spectra typically reveal well resolved vibrational structure on each of the bands corresponding to removal of an electron from the valence molecular orbitals. In addition, vibrational structure is observed in the region between the X $^2\Pi_{g,i}$ and A $^2\Pi_{u,i}$ ionic states of all three halogens which is indicative of the presence of autoionising Rydberg states. The high energy region of both chlorine and bromine contains band structure related to core ionic and satellite ionic state formation.

The *gerade* Rydberg states of jet-cooled iodine have been thoroughly investigated in the region between 53000 and 70000 cm^{-1} using mass resolved (2+1) resonantly enhanced multiphoton ionisation (REMPI) spectroscopy. All the *n*d Rydberg states were found to be heavily perturbed through vibronic coupling with ion-pair states in contrast to most of the *n*s Rydberg states which were found to be unperturbed. The characterisation of these Rydberg states provided the basis for a comprehensive study of the two spin-orbit components of the ground state of the cation using two colour (2+1') ZEKE-PFI photoelectron spectroscopy. The ZEKE-PFI spectrum recorded for the lower spin-orbit state exhibits non Franck-Condon

behaviour in contrast to that recorded for the upper spin-orbit state. This was interpreted in terms of an autoionisation mechanism involving Rydberg states converging on the upper spin-orbit component.

Several new Rydberg states of the iodine-argon van der Waals complex have been investigated using mass resolved (2+1) REMPI spectroscopy in the region between 53000 and 69000 cm^{-1}. The complex spectra exhibit anharmonic vibrational progressions in the $I_2 \cdots Ar$ van der Waals stretching mode in combination with the I_2 stretching progression. The $I_2 \cdots Ar$ stretching frequencies and binding energies were found to increase with the principal quantum number of the Rydberg state which is consistent with a progressive strengthening of the van der Waals bond. This agrees with the expected reduction in effective shielding of the ion core by the Rydberg electron as it is excited into higher principal quantum number orbits. A (2+1') ZEKE-PFI investigation of the van der Waals complex cation revealed a very small binding energy increase in the ion compared to that determined for the n=8 Rydberg state. This small increase indicates that for Rydberg orbitals with $n \geq 8$ the effective shielding of the ionic core by the Rydberg electron is minimal.

Contents

List of Tables

List of Figures

Chapter 1

Introduction

The photoionisation of gas phase species and the subsequent detection of one of the ionisation products is a powerful tool for observing the electronic structure of atomic and molecular ions.

$$M + h\nu \rightarrow M^+ + e^- \qquad 1.1$$

However, the field of ionic state spectroscopy has not seen the same dynamic growth in techniques and ideas as neutral state spectroscopy. Early photoionisation experiments were performed by recording the photoion current as a function of the wavelength (a photoionisation efficiency (PIE) spectrum) which resulted in values for ionisation potentials, but produced little other useful spectral information [1]. The difficulty with PIE spectra is that atomic and molecular photoionisation cross sections remain non-zero after the excitation requirements for a particular transition have been satisfied. A photoionisation spectrum therefore, by its very nature resembles a step function, the excess energy having been converted into the kinetic energy of the photoelectron. In addition autoionisation structure can in some cases hide the step like structure of the direct ionisation process [2]. To overcome these limitations alternative techniques, such as Rydberg series extrapolations [3] were developed to measure ionisation potentials. These have been successful for a few molecules such as nitric oxide [4] and iodine [5], but the presence of perturbations makes the identification and assignment of Rydberg series in many molecules very difficult.

The most generally applicable method for determining ionisation potentials, and in addition the electronic and vibrational structure of a molecular ion, is conventional photoelectron spectroscopy (PES) developed in the 1960's [6,7]. Instead of detecting the ion, it concentrated on measuring the kinetic energy of the photoelectrons emitted from a sample irradiated with a fixed wavelength light source. Although the technique is very successful, its one major limitation is its inability to precisely determine the kinetic energy of the ejected photoelectrons. This restricts the resolution to around 10 meV (80 cm^{-1}) which means that while the electronic structure can for the most part be fully resolved, vibrational structure can only be resolved for the lighter systems and rotational spectroscopy is to all intent and purposes out of the question. An attempt to overcome this difficulty resulted in the development of threshold photoelectron spectroscopy (TPES) [8,9]. Instead of collecting all the products of photoionisation, the threshold technique detected only those photoelectrons with near zero kinetic energy (commonly called threshold photoelectrons) which were produced when the photon energy was resonant with a rovibronic level of the ion. However, the threshold technique requires a highly efficient means of collecting the threshold photoelectrons whilst rejecting all other kinetic electrons which when combined with the low photon bandwidth of VUV continuum sources, has limited the technique's usefulness.

During the development of techniques based on the detection of the products of photoionisation, alternative methods of investigating the electronic structure of molecular ions were evolving. Emission spectroscopy for example, used the fluorescence emitted from excited ionic states to probe the ionic manifold [10]. This approach often resulted in ionic rovibronic structure being resolved but in many cases the high resolution was compromised by a continuum background as a result of emission from higher excited ionic states and neutral states. In addition, the method of generating these excited ions, such as electrical discharges [10,11], electron bombardment [12] and collisions with inert gas atoms in metastable states [13] was so non-specific, that there was often some doubt over the exact position of the expected emission which also made exact assignments very difficult. Some of these limitations

have now been overcome by using laser excitation sources and dispersing the fluorescence from single rovibronic levels in excited ionic states [12,14].

The low resolution inherent in the majority of photoionisation techniques up until the early 1980's meant that the photoionisation process was far from well understood. Even the dynamics of the ejection of an electron in an atom, which is considered to be the simplest species, is not fully understood, even though general rules like conservation of angular momentum and parity are known. The situation in molecules is even more complicated due to additional core effects altering the angular momentum of the ejected electron. To probe the photoionisation process in detail requires the exact quantum state of the ion formed during the photoionisation process to be determined. Unfortunately, this generally requires a rotationally resolved ion spectra which have only been successfully achieved in molecules with large rotational constants, such as H_2 [15]. In 1984, however, a photoionisation technique was developed which was capable of resolving rotational structure in a much larger range of small molecules. Zero kinetic energy photoelectron spectroscopy (ZEKE-PES), developed by Müller-Dethlefs, Schlag and co-workers [16–18] gave, for the first time, a detailed insight into the photoionisation process. The ZEKE technique took advantage of the wavenumber resolution provided by laser excitation sources and employed a time discrimination mechanism to separate zero kinetic energy electrons from those with kinetic energy. However, this mechanism has since been proved to be dominated by a second mechanism. The new mechanism involves the delayed pulsed field ionisation of long lived Rydberg states a few wavenumbers' below rovibronic ionisation thresholds [19] and has led to an amended title for the technique; zero kinetic energy pulsed field ionisation (ZEKE-PFI) photoelectron spectroscopy. The rotational band intensity distributions which have been found in rotationally resolved ZEKE-PFI spectra have revealed much more about the ionisation dynamics and the coupling which can take place between the ejected electron's angular momentum and the rotational angular momentum of the ion core. The wavenumber resolution has also brought about a revolution in other areas of spectroscopic interest,

such as the field of weakly bound van der Waals complex cations with their characteristically low vibrational frequencies [20,21].

1.1 A Comparison of TPES and ZEKE-PFI Photoelectron Spectroscopy

Many of the results presented in this thesis have employed threshold photoelectron spectroscopy (TPES) and zero kinetic energy pulsed field ionisation (ZEKE-PFI) photoelectron spectroscopy. Both of these techniques are based on the photoionisation of an atom or molecule but employ different methods to collect the electrons produced in the photoionisation process. The threshold technique generally employs a continuous extraction field to collect the threshold or very near threshold photoelectrons from just above a rovibronic ionisation limit. The ZEKE-PFI technique, on the other hand, utilises the delayed pulsed field ionisation of long lived high-n Rydberg states (n is the Rydberg principal quantum number) lying just below a rovibronic ionisation threshold. The application of a delay in ZEKE-PFI photoelectron spectroscopy has the advantage that any promptly formed photoelectrons are discriminated against, whereas with TPES there is always the possibility they will be collected and distort the resulting spectrum. Both TPES and ZEKE-PFI photoelectron spectroscopy suffer from the effects of autoionisation when an ionisation threshold is degenerate with an autoionising Rydberg state. In these cases, the measured intensity of an ionic peak does not reflect the direct ionisation cross section.

The other major difference between the two techniques are the excitation schemes employed to promote ionisation. A single-photon VUV excitation scheme is generally employed in the threshold technique, whereas the ZEKE-PFI technique has a number of different excitation schemes, ranging from single-photon VUV excitation to resonantly enhanced multiphoton ionisation (REMPI). The involvement of a resonant intermediate state gives ZEKE-PFI not only molecular selectivity, but also

provides a means to vibrationally or rotationally state select the molecule which is very valuable in assigning the resulting ionic state spectra.

1.1.1 A Review of Threshold Photoelectron Spectroscopy

Threshold photoelectron spectroscopy is characterised more by the number of techniques which have been employed to collect the threshold electrons than by its successes. Threshold photoelectron spectroscopy, like conventional PES, is able to cover wide energy ranges as a result of the broadly tuneable VUV excitation sources employed. This allows a broad picture of the ionic structure to be obtained. In many cases, improved resolution is achieved over that obtained in conventional PES investigations, and in some cases ionic state vibrational levels can be observed through autoionisation processes which have very small Franck-Condon factors for direct ionisation.

The earliest reports of threshold photoelectron investigations were by Villarejo et al. [8] in the late 1960's. Many of these were conducted with the aim of determining improved ionisation potentials of small molecules such as CH_4, and atomic species such as the rare gases, which previously were not known to an acceptable accuracy. Later, improvements in the bandwidth of ionisation light sources and in the collection of threshold electrons made possible a vibrationally resolved study of H_2 [22]. This vibrational resolution was later superseded by Peatman [23] with a rotationally resolved study allowing an accurate set of ionic ground state molecular constants to be determined. Stockbauer [24] continued to study H_2 and D_2 but in a study of N_2 found discrepancies in the length and intensity of the vibrational progressions of the first three electronically excited states when compared with the results of conventional PES studies. These discrepancies in N_2 were explained by a resonant autoionisation mechanism producing threshold photoelectrons which were subsequently detected.

Ionisation light sources up until this point, had generally consisted of VUV continuum sources, such as the Hopfield continuum [25]. However, from the mid 1970's synchrotron radiation became more widely available and groups such as Frey and co-workers employed it in their threshold studies of triatomic molecules such as CO_2 [26] and N_2O [27]. These triatomics along with others have also been studied by Guyon and co-workers [28], using not only threshold photoelectron spectroscopy but also fluorescence techniques. This produced an improved understanding of the fragmentation pathways within these molecules and an explanation for the production of low energy electrons in regions of the ionic spectrum where the Franck-Condon factors are very small. Other studies have included a threshold study on ammonia [29] and one on molecular oxygen [30]. The later study of which displayed significant evidence of resonant autoionisation.

Some interest is now being focused on the comparison between threshold photoelectron results and ZEKE-PFI results. The threshold technique employed by Merkt and co-workers [30] used both angular and time discrimination to selectively detect electrons of low or zero kinetic energy, in a very similar manner to the time discrimination methods used in the ZEKE-PFI technique. Since autoionisation plays a part in ZEKE-PFI spectra [31] as well as in TPE spectra, questions are now being asked as to whether the excited neutral Rydberg states which autoionise to produce the vibrationally excited states of the ion in TPES will survive long enough to be observed in ZEKE-PFI spectra. Initial results indicate that this does seem to be the case [32].

The development of threshold photoelectron spectroscopy has shown amongst other things that the photoionisation of diatomics [33], as well as polyatomic molecules [28], produces threshold energy electrons associated with the formation of highly vibrationally excited ions. This generally occurs in regions of the ionic spectrum where the direct excitation probability, as determined by He(I) PES, is vanishingly small and can therefore reveal substantially more information about ionic states than conventional photoelectron spectroscopy.

1.1.2 A Review of Zero Kinetic Energy Pulsed Field Ionisation (ZEKE-PFI) Photoelectron Spectroscopy

Since the development of ZEKE-PFI photoelectron spectroscopy in the mid 1980's [19], the profile of ionic state spectroscopy has dramatically increased. The number of research papers in the ZEKE-PFI field alone, now exceeds one hundred and fifty. The pioneering experiments of Müller-Dethlefs and co-workers were mostly concerned with developing the technique and improving the resolution [34]. One of the first groups, other than Müller-Dethlefs and co-workers, to employ the ZEKE-PFI technique were White and co-workers who used a single photon VUV ionisation scheme to measure ion rotational state distributions of small molecules, such as O_2 [35] and H_2O [36,37]. A simulation of these intensity distributions using the theoretical expression for rotationally resolved one photon ionisation cross sections derived by Buckingham et al [38] established that the observed rotational branch intensities directly reflected the partial wave distributions of the photoelectron continua. However, many rotationally resolved spectra, such as those recorded for N_2O [39] and HCl [40], have subsequently shown perturbed intensity distributions. These perturbations have been explained by proposing a field induced rotational autoionisation mechanism, involving the coupling of Rydberg states of different ionic core rotational quantum numbers [41,42]. This explanation has also been invoked in resonantly enhanced multiphoton ionisation schemes, such as the two-photon two colour ZEKE-PFI spectrum of NO [43] where anomalous rotational intensity distributions were also observed but could not be explained completely by conventional theory [44]. Rotationally resolved studies of larger molecules such as benzene [45], have also become possible as the technique has developed and laser bandwidths reduced.

The field of weakly bound ionic complexes has also benefited significantly from the improved resolution of ZEKE-PFI. The selectivity of the two colour REMPI excitation scheme combined with the ZEKE-PFI technique has allowed the characteristic low frequency intermolecular vdW vibrational modes of many weakly

bound ionic complexes to be resolved for the first time. The benzene-argon van der Waals complex was the first weakly bound species to be investigated using these techniques and resulted in an accurate ionisation potential being measured [46]. These investigations have since been extended to include many other weakly bound species such as small metal clusters [47]. The investigation of small clusters has also been extended into higher excited ionic states, such as the measurement of the vibrationally resolved spectra of the first three bound states of Xe_2^+ [48]. Other electronically excited ions have also been studied such as NO^+ [49] and N_2O^+ [50].

Hydrogen-bonded clusters are another group of weakly bound complexes for which the ZEKE-PFI technique has been found to be very suitable. With a knowledge of the intermediate neutral state structure, the two-photon two colour ZEKE-PFI technique was employed to study the 1:1 phenol:water complex cation [51,52]. The ZEKE-PFI spectrum exhibited rich intermolecular vibrational spectral information and demonstrated a dramatic lowering (~4500 cm^{-1}) of the ionisation potential compared with the parent phenol molecule. This hydrogen-bonding study has now been expanded to include amongst others, the phenol dimer [53], the phenol-methanol complex [54] and the phenol-ethanol complex [55].

Studies involving a noble gas atom or atoms attached to a parent molecule have included very small complexes such as Ar-NO [56] and large aromatic vdW complexes such as p-Dimethoxybenzene-Ar_n (n=0-2) [57] and Anthracene-Ar_n (n=0-5) [58]. The selectivity of the REMPI excitation process and the high sensitivity of the ZEKE-PFI technique has made possible the assignment of individual vibrational bands in a spectrum to individual geometrical isomers of the complex. The selectivity has also made it possible to obtain information on the relative stabilities of individual aromatic molecular isomers [59,60]. One particular vdW ionic complex which has probably been studied more than any other is aniline-Ar [61]. This complex has recently been employed in an investigation of the dissociation dynamics (on the nanosecond timescale) of the aniline-Ar vdW bond on the S_1 electronic surface, using ZEKE-PFI to probe the ionic products [62]. This investigation was subsequently

improved with the use of picosecond lasers [63]. Lifetime studies have also been carried out by Hillenbrand et al. [64] on the S_1 electronic state of pyrazine.

Most ZEKE-PFI studies reported to date have involved laser excitation schemes with the consequence that such studies have been limited to the ionisation of outer valence shell electrons. So far only a handful of ZEKE studies have ventured beyond ionisation energies of 18 eV. Habenicht et al. [65] have conducted 'low resolution' (100 meV) zero kinetic energy photoelectron-photoion coincidence measurements on Ar and N_2 beyond 250 eV using synchrotron radiation. Double ZEKE coincidence experiments have also been reported [66]. Another area of promise is the use of synchrotron radiation to record ZEKE-PFI spectra [67]. The resolution is nowhere near as good as laser based studies but the broadly tuneable source can provide spectral information over a much wider range of energies thereby providing a survey of regions which can later be probed in detail with the higher resolution of laser sources.

One field of ZEKE research which involves the detection of true ZEKE electrons rather than the pulsed field ionisation of long lived Rydbergs is threshold photodetachment spectroscopy of negative ions [68,69]. This technique probes the electronic and vibrational structure of neutral states [70] and has been employed on a wide variety of small metal clusters, such as Si_2^- [71] and van der Waals complexes such as ICO_2^- [72].

This is just a brief review of some of the fields of study which have been investigated over the past ten years using ZEKE-PFI photoelectron spectroscopy. The initial promise which the technique showed, has been converted into what is now essentially a self contained branch of spectroscopy. The technique, however, is still advancing, evidenced by the rate of development in the ZEKE-PFI field and the related field of mass analysed threshold ionisation (MATI) spectroscopy [73].

1.2 Outline of Research Aims

The research described in this thesis was aimed at combining the relatively low resolution (~10 meV, 80 cm^{-1}) technique of TPES, using synchrotron radiation at the Daresbury Laboratory together with a penetrating field electron spectrometer [74], with the high resolution (~1 cm^{-1}) laser based ZEKE-PFI technique, to study the diatomic homonuclear halogen cations. There were a number of reasons behind this. Firstly, although these molecules have been the subject of many studies, especially in the neutral state, there is still much uncertainty and debate over the spectroscopic character of some of the ionic states of the diatomic homonuclear halogens. Secondly, it was felt that the new design of penetrating field threshold electron spectrometer, which in coincidence studies had been shown to have improved resolution, could make significant improvements on the relatively low resolution valence ionic state spectra recorded using conventional photoelectron techniques. Thirdly, it was also felt that the tendency for autoionising structure to be prevalent in threshold spectra may provide some additional spectroscopic information. Finally, the threshold investigations would provide a good basis for an improved resolution ZEKE-PFI study.

A comprehensive study of a number of the diatomic homonuclear halogens has been successfully achieved with a new penetrating field threshold photoelectron spectrometer and has provided the inspiration for a series of ZEKE-PFI studies. The first of these, which has involved a thorough investigation of the *gerade* Rydberg states of jet-cooled iodine along with a comprehensive study of the two spin-orbit components of the ground state of the cation, has now been completed. The jet-cooling of iodine in an argon carrier gas also provided an ideal opportunity to carry out a comparative study of the related Rydberg excited states of the iodine-argon van der Waals complex and its cation.

The thesis takes the following form. Chapter two continues with a discussion of the theoretical principles behind photoionisation along with some of the

effects which can be observed in ionic state spectra. Chapter three is an experimental chapter providing a brief description of the development of the instrumentation involved with TPES and ZEKE-PFI photoelectron spectroscopy along with a description of ionisation methods and the two spectrometers used in the current work. The subsequent three chapters concentrate on the results obtained and are separated according to the technique employed and the molecule of interest. Chapter four consists of the results obtained for the valence ionic states of the halogens using threshold photoelectron spectroscopy and discusses the differences between these spectra and those obtained using other techniques. Chapters five and six are concerned with molecular iodine and the iodine-argon van der Waals complex, respectively. Both chapters discuss the (2+1) REMPI spectra of the *gerade* Rydberg states of the two molecules before presenting and discussing the (2+1') ZEKE-PFI spectra of the iodine and iodine-argon cations.

1.3 References

[1] K. Watanabe, J. Chem. Phys. **26** (1959) 542

[2] P.M. Dehmer and W.A. Chupka, J. Chem. Phys. **62** (1975) 4525

[3] G. Herzberg, Molecular Spectra and Molecular Structure, Van Nostrand, New York (1950) Vols. 1-3

[4] E. Miescher, Can. J. Phys. **54** (1976) 1769

[5] P. Venkateswarlu, Can. J. Phys. **48** (1970) 1055

[6] J.H.D. Eland, Photoelectron Spectroscopy, Butterworth & Co., England (1974)

[7] J.W. Rabalais, Principles of Ultraviolet Photoelectron Spectroscopy, J. Wiley & Sons, England (1977)

[8] D. Villarejo, R.R. Herm and M.G. Inghram, J. Chem. Phys. **46** (1967) 4995

[9] W.B. Peatman, T.B. Borne and E.W. Schlag, Chem. Phys. Lett. **3** (1969) 492

[10] F.P. Huberman, J. Mol. Spec. **20** (1966) 29

[11] H. Lew, Can. J. Phys. **54** (1976) 2028

[12] T. Harris, J.H.D. Eland and R.P. Tuckett, J. Mol. Spec. **98** (1983) 269

[13] V.E. Bondybey and T.A. Miller, J. Chem. Phys. **70** (1979) 138

[14] V.E. Bondybey and T.A. Miller, J. Chem. Phys. **67** (1977) 1790

[15] J.E. Pollard, D.J. Trevor, J.E. Reutt, Y.T. Lee and D.A. Shirley, J. Chem. Phys. **77** (1982) 34

[16] K. Müller-Dethlefs, M. Sander and E.W. Schlag, Chem. Phys. Lett. **112** (1984) 291

[17] K. Müller-Dethlefs, M. Sander and E.W. Schlag, Z. Naturforsch **39a** (1984) 1089

[18] K. Müller-Dethlefs and E.W. Schlag, Annu. Rev. Phys. Chem. **42** (1991) 109

[19] G. Reiser, W. Habenicht, K. Müller-Dethlefs and E.W. Schlag, Chem. Phys. Lett. **152** (1988) 119

[20] K. Müller-Dethlefs, O. Dopfer and T.G. Wright, Chem. Rev. **94** (1994) 1845

[21] E.J. Bieske and J.P. Maier, Chem. Rev. **93** (1993) 2603

[22] D. Villarejo, J. Chem. Phys. **48** (1968) 4014

[23] W.B. Peatman, J. Chem. Phys. **64** (1976) 4093

[24] R. Stockbauer, J. Chem. Phys. **70** (1979) 2108

[25] J.J. Hopfield, J. Phys. Rev. **35** (1930) 1133

[26] E.W. Schlag, R. Frey, B. Gotchev, W.B. Peatman and H. Pollak, Chem. Phys. **51** (1977) 406

[27] R. Frey, B. Gotchev, W.B. Peatman, H. Pollak and E.W. Schlag, Chem. Phys. Lett. **54** (1978) 411

[28] P.M. Guyon, T. Baer and I. Nenner, J. Chem. Phys. **78** (1983) 3665

[29] R. Locht, K. Hottmann, G. Hagenow, W. Denzer and H. Baumgartel, Chem. Phys. Lett. **190** (1992) 124

[30] F. Merkt, P.M. Guyon and J. Hepburn, Chem. Phys. **173** (1993) 479

[31] F. Merkt and T.P. Softley, J. Chem. Phys. **96** (1992) 4149

[32] W. Kong, D. Rodgers and J.W. Hepburn, Chem. Phys. Lett. **203** (1993) 497

[33] P.M. Guyon, R. Sphor, W.A. Chupka and J. Berkowitz, J. Chem. Phys. **65** (1976) 1650

[34] M. Sander, L.A. Chewter, K. Müller-Dethlefs and E.W. Schlag, Phys. Rev. A **36** (1987) 4543

[35] R.G. Tonkyn, J.W. Winniczek and M.G. White, Chem. Phys, Lett. **164** (1989) 137

[36] R.G. Tonkyn, R. Wiedmann, E.R. Grant and M.G. White, J. Chem. Phys. **95** (1991) 7033

[37] M.-T. Lee, K. Wang, V. McKoy, R.G. Tonkyn, R.T. Wiedmann, E.R. Grant and M.G. White, J. Chem. Phys. **96** (1992) 7848

[38] A.D. Buckingham, B.J. Orr, J.M. Sichel, Philos. Trans. R. Soc. London Ser. **A268** (1970) 147

[39] R.T. Wiedmann, E.R. Grant, R.G. Tonkyn and M.G. White, J. Chem. Phys. **95** (1991) 746

[40] R.G. Tonkyn, R.T. Wiedmann and M.G. White, J. Chem. Phys. **96** (1992) 3696

[41] R.T. Wiedmann, M.G. White, K. Wang and V. McKoy, J. Chem. Phys. **98** (1993) 7673

[42] F. Merkt and T.P. Softley, J. Chem. Phys. **96** (1992) 4149

[43] G. Reiser and K. Müller-Dethlefs, J. Phys. Chem. **96** (1992) 9

[44] H. Rudolph, V. McKoy and S.N. Dixit, J. Chem. Phys. **90** (1989) 2570

[45] R. Lindner, H. Sekiya, B. Beyl and K. Müller-Dethlefs, Angew. Chem. Int. Ed. Engl. **32** (1993) 603

[46] L.A. Chewter, K. Müller-Dethlefs and E.W. Schalg, Chem. Phys. Lett. **135** (1987) 219

[47] J.E. Harrington and J.C. Weisshaar, J. Chem. Phys. **93** (1990) 854

[48] R.G. Tonkyn and M.G. White, J. Chem. Phys. **95** (1991) 5582

[49] W. Kong, D. Rodgers and J.W. Hepburn, J. Chem. Phys. **99** (1993) 8571

[50] W. Kong, D. Rodgers and J.W. Hepburn, Chem. Phys. Lett. **221** (1994) 301

[51] G. Reiser, O. Dopfer, R. Lindner, G. Henri, K. Müller-Dethlefs, E.W. Schlag and S.D. Colson, Chem. Phys. Lett. **181** (1991) 1

[52] O. Dopfer, G. Reiser, R. Lindner and K. Müller-Dethlefs, Ber. Bunsenges. Phys. Chem. **96** (1992) 1259

[53] O. Dopfer, G. Lembach, T.G. Wright and K. Müller-Dethlefs, J. Chem. Phys. **98** (1993) 1933

[54] T.G. Wright, E. Cordes, O. Dopfer and K. Müller-Dethlefs, J. Chem. Soc. Faraday Trans. **89** (1993) 1609

[55] E. Cordes, O. Dopfer, T.G. Wright and K. Müller-Dethlefs, J. Chem. Phys. **97** (1993) 7471

[56] M. Takahashi, J. Chem. Phys. **96** (1992) 2594

[57] M.C.R. Cockett, K. Okuyama and K. Kimura, J. Chem. Phys. **97** (1992) 4679

[58] M.C.R. Cockett and K. Kimura, J. Chem. Phys. **100** (1994) 3429

[59] C. Lakshminarayan, J.M. Smith and J.L. Knee, Chem. Phys. Lett. **182** (1991) 656

[60] M. Takahashi and K. Kimura, J. Chem. Phys. **97** (1992) 2920

[61] M. Takahashi, H. Ozeki and K. Kimura, J. Chem. Phys. **96** (1992) 6399

[62] X. Zhang, J.M. Smith and J.L. Knee, J. Chem. Phys. **97** (1992) 2843

[63] J.M. Smith, X. Zhang and J.L. Knee, J. Chem. Phys. **99** (1993) 2550

[64] S. Hillenbrand, L. Zhu and P.M. Johnson, J. Chem. Phys. **95** (1991) 2237

[65] W. Habenicht, K. Müller-Dethlefs and E.W. Schalg, J. Electron Spectrosc. Relat. Phenom. **52** (1990) 697

[66] B. Krassig and V. Schmidt, J. Phys. B: At. Mol. Opt. Phys. **25** (1992) L327

[67] F. Merkt and P.M. Guyon, J. Chem. Phys. **99** (1993) 3400

[68] R.B. Metz, S.E. Bradforth and D.M. Neumark, Adv. Chem. Phys. **81** (1992) 1

[69] I.M. Walker, T.N. Kitsopoulos and D.M. Neumark, J. Phys. Chem. **94** (1990) 2240

[70] D.M. Neumark, Acc. Chem. Res. **26** (1993) 33

[71] T.N. Kitsopoulos, C.J. Chick, Y. Zhao and D.M. Neumark, J. Chem. Phys. **95** (1991) 1441

[72] Y. Zhao, C.C. Arnold and D.M. Neumark, J. Chem. Soc. Faraday Trans. **89** (1993) 1449

[73] P.M. Johnson, L. Zhu, Int. J. Mass Spec. and Ion. Proc. **131** (1994) 193

[74] R.I. Hall, A. McConkey, K. Ellis, G. Dawber, L. Avaldi, M.A. MacDonald and G.C. King, Meas. Sci. Technol. **3** (1992) 316

Chapter 2

Theoretical principles

2.1 Introduction

Transitions to electronically excited neutral states and ionic states are governed by selection rules which when combined with Franck-Condon factors can dictate which electronic states are accessible from the ground state of the neutral state. The selection rules which are relevant to single photon and multiphoton transitions in diatomic molecules are therefore laid out in this chapter. Photoionisation is also discussed along with autoionisation and its effect on threshold photoelectron spectra. Finally there is a brief review of some of the factors which have been proposed to explain the extended lifetime of the high-n Rydbergs involved in the ZEKE-PFI process.

The interaction of electromagnetic radiation with a gaseous sample is dominated by electric-dipole allowed transitions. At energies below the onset of ionisation, absorption occurs to discrete valence, Rydberg or ion-pair states, whereas at energies above the ionisation limit, photoionisation occurs either directly or via autoionisation [1]. The selection rules for n-photon absorption between states of the neutral molecule are based on changes in the quantum numbers which define the electronic states of the molecule. These rules also apply to photoionisation but tend to be less stringent as the photoelectron can carry away as much angular momentum as is required to satisfy the selection rules.

2.2 Angular momentum coupling in diatomic molecules

In order to explain the selection rules, a description of the various angular momentum coupling schemes in diatomics must be presented [2]. The molecular angular momenta of interest in these coupling schemes consist of the electron spin and electron orbital angular momenta and the angular momentum of nuclear rotation. Nuclear spin angular momentum is neglected. There are five recognised coupling schemes, known as Hund's cases (a) - (e), which describe the majority of situations likely to be encountered [2]. A brief description of those relevant to the diatomic halogens are given below.

2.2.1 Hund's case (a)

This coupling scheme assumes that the nuclear rotation does not interact with the electron spin or the electron orbital angular momentum. Figure 2.1(a) illustrates Hund's case (a) coupling. The orbital angular momenta of all the electrons in the molecule couple to give a resultant **L** and in a similar manner, all the electron spin momenta couple to give a resultant **S**. The spin-orbit coupling between **L** and **S** is weak such that both **L** and **S** are coupled to the z-axis of the molecule-fixed frame, (which corresponds with the line adjoining the two atoms), with projections $\Lambda\hbar$ and $\Sigma\hbar$, respectively. Λ and Σ can be summed to give the vector component $\Omega\hbar$, (indicated on Figure 2.1(a)), where the quantum number Ω is defined by

$$\Omega=|\Lambda+\Sigma| \qquad 2.1$$

When the angular momentum, **R**, due to nuclear rotation is also included, and coupled to the component of the total electronic angular momentum along the internuclear axis, $\Omega\hbar$, the result is the total angular momentum **J**, as shown in Figure 2.1(a). The **R** vector precesses around **J** and therefore the molecule as a whole rotates about **J**

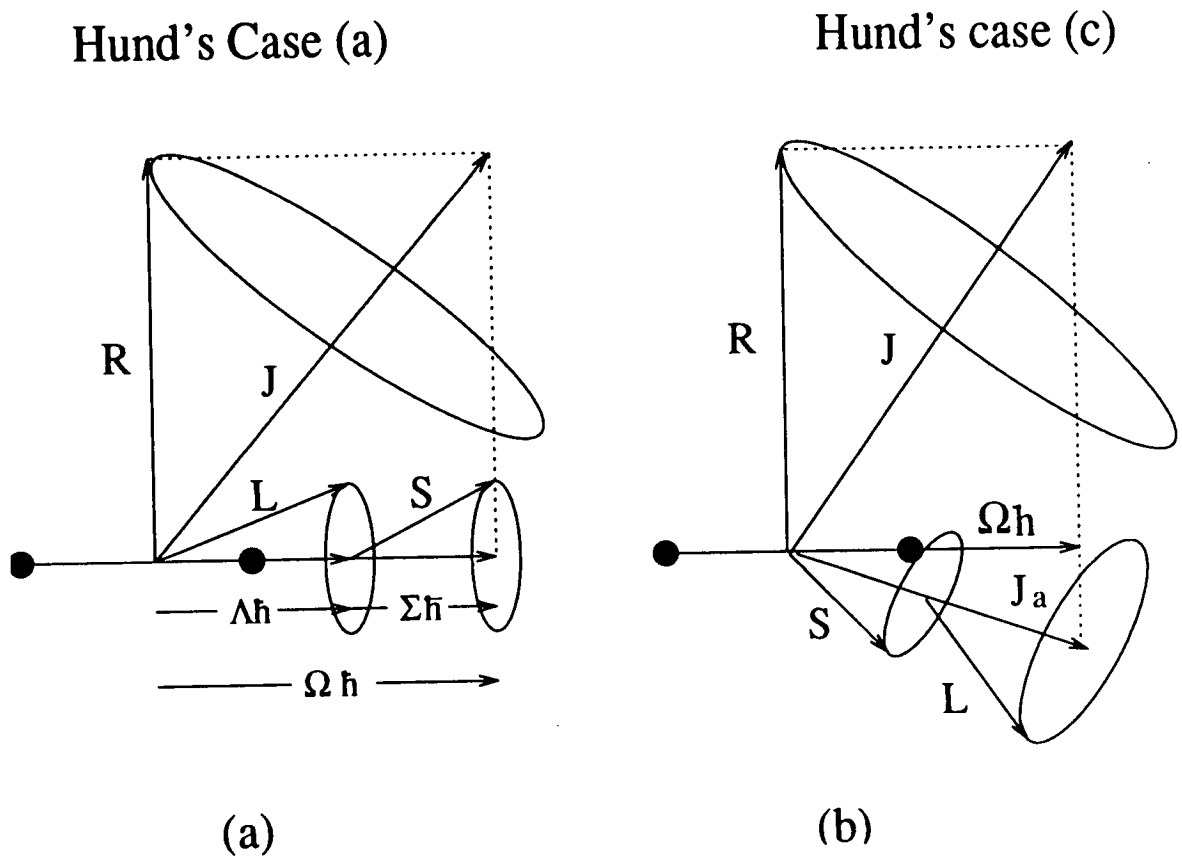

Figure 2.1 A schematic of Hund's case (a) and Hund's case (c) angular momentum coupling schemes in diatomic molecules.

which is regarded as fixed in space. The good quantum numbers in this case are S, Σ, Λ, Ω and J.

2.2.2 Hund's case (c)

For some states of the heavier halogens, the interaction between **L** and **S** may exceed their coupling to the molecular z-axis in which case Hund's case (c) becomes appropriate as illustrated in Figure 2.1(b). In this scheme the spin-orbit coupling is sufficiently large that **L** and **S** are coupled to give the resultant $\mathbf{J_a}$, which has a fixed projection $\Omega\hbar$ on the molecular z-axis. $\Omega\hbar$ and **R** are then coupled to give the resultant **J**, about which the molecule rotates, as in Hund's case (a). The good quantum numbers in this case are S, Ω and J. Hund's case (a) and (c) are in general sufficient to describe the homonuclear diatomic halogens. However, we will also consider Hund's case (d) and (e) which describe high-*n* Rydberg states.

2.2.3 Hund's case (d)

When the ionic core is of Σ symmetry, i.e. $\Lambda^+=0$, the appropriate description of high-*n* Rydberg states is Hund's case (d). In this coupling scheme, the total angular momentum exclusive of spin, $\mathbf{N^+}(=\mathbf{R})$, and the orbital angular momentum of the Rydberg electron, **l**, are coupled to give **N**. Finally, the total spin **S** is added to give **J**.

2.2.4 Hund's case (e)

When the ionic state consists of two spin-orbit components, i.e. $\Lambda^+\neq0$ and $S^+\neq0$, the appropriate description of high-*n* Rydberg states is Hund's case (e). In this coupling scheme, the ionic core is described using Hund's case (c), leading to the core quantum numbers, $\mathbf{J_a}^+$, $\mathbf{J}^+$ and Ω^+. The angular momentum of the Rydberg electron, **j**, is coupled to $\mathbf{J}^+$ to give **J**.

2.3 Electric Dipole Allowed Photoabsorption Selection Rules

We will only consider the selection rules for bound to bound transitions in Hund's case (a) and case (c) notation which are the most common. For Hund's case (a) coupling in diatomic molecules, the quantum numbers Ω, Λ, S, Σ and J are required to specify the single photon electric dipole allowed selection rules, along with two symmetry properties of the electronic wavefunction. These selection rules are given below :

$$\Delta\Lambda = 0, \pm 1 \qquad 2.2$$

$$\Delta S = 0 \qquad 2.3$$

$$\Delta\Sigma = 0 \qquad 2.4$$

$$\Delta J = 0, \pm 1 \qquad 2.5$$

$$\Delta\Omega = 0, \pm 1 \qquad 2.6$$

$$+ \leftrightarrow + \text{ and } - \leftrightarrow - \qquad 2.7$$

$$g \leftrightarrow u. \qquad 2.8$$

For Hund's case (c) coupling all the selection rules given for case (a) apply, except for 2.2, 2.4 and 2.7. Equations 2.2 and 2.4 are not relevant since Λ and Σ are not good quantum numbers and Equation 2.7 becomes

$$0^+ \leftrightarrow 0^+ \text{ and } 0^- \leftrightarrow 0^- \qquad 2.9$$

where the '+' or '–' label now refers to the symmetry or antisymmetry of ψ_e with respect to σ_v when Ω=0. In molecules with a high nuclear charge and which are approximated by case (c) coupling, the ΔS=0 selection rule can also often break down [2].

2.3.1 Photoionisation Selection Rules

The selection rules for photoionisation are far less stringent compared to those described in section 2.3. The formation of an atomic or molecular ion has the advantage over a bound to bound neutral transition in that the electron can carry away whatever angular momentum is required to satisfy the angular momentum selection rules.

$$M + h\nu \rightarrow M^+ + e^- \qquad 2.10$$

If M is an atom then the total change in angular momentum for the process described in Equation 2.10 must obey the electric dipole selection rule $\Delta l = \pm 1$. For example, if the electron is removed from a d orbital of M it can carry away one or three quanta of angular momentum, depending on whether Δl=−1 or +1, respectively. In molecular systems the symmetry of the molecular orbital is generally lower i.e. the MO's are themselves mixtures of AO's, and therefore the ejected electron is described by a more complex mixture of s,p,d,f,... character. One other selection rule which appears as a consequence of the electron removal, is that the spin multiplicity must also change by $\pm$ 1.

$$\Delta S = \pm 1 \qquad 2.11$$

A single photon ionising transition can therefore access all ionic states whose electron configurations differ from the ground state by the removal of a single electron. However, transitions to ionic states which arise from subsequent electron rearrangements or two electron transitions are formally forbidden. Multiphoton transitions on the other hand can in principle access ionic states which have an electron configuration which differs from the ground state by more than a one electron transition.

2.3.2 The Principles of Photoionisation

The simultaneous production of an atomic or molecular ion and a photoelectron from an atomic or molecular species which has interacted with a high energy photon source forms the basic idea behind photoionisation. The technique employed in conventional photoelectron (PE) experiments is to use a fixed photon source to photoionise the atom or molecule and then to measure the kinetic energy imparted to the photoelectron, although variations of this idea have also been tried.

$$M + h\nu \rightarrow M^+ + e^- \text{ (k.e.)} \qquad 2.12$$

Figure 2.2 shows an idealised set of fully occupied atomic orbitals with the electrons bound by characteristic energies I_j, usually referred to as their ionisation energies. When a high energy photon, $h\nu$, interacts with an atom, part of the energy is used to overcome the binding energy of the electron, while the remainder appears as the kinetic energy of the ejected photoelectron, E_k. The kinetic energy imparted to the ion is negligible due to the large disparity in mass between the ion and electron.

$$E_k = h\nu - I_j \qquad 2.13$$

All the information on the final ionic state accessed in the photoionisation process is therefore carried by the photoelectron. In a conventional PE experiment the electrons are detected as a function of their kinetic energies with a signal appearing at energies which correspond to the binding energy of the electron in the atom, i.e. equal to $h\nu$-I_j (see Figure 2.2).

In molecular systems, there are the additional possibilities of vibrational and/or rotational excitation when an electron is ionised from a single molecular orbital. The energies of the photoelectrons can therefore be reduced according to Equation 2.14, such that the spectrum consists of bands containing vibrational and

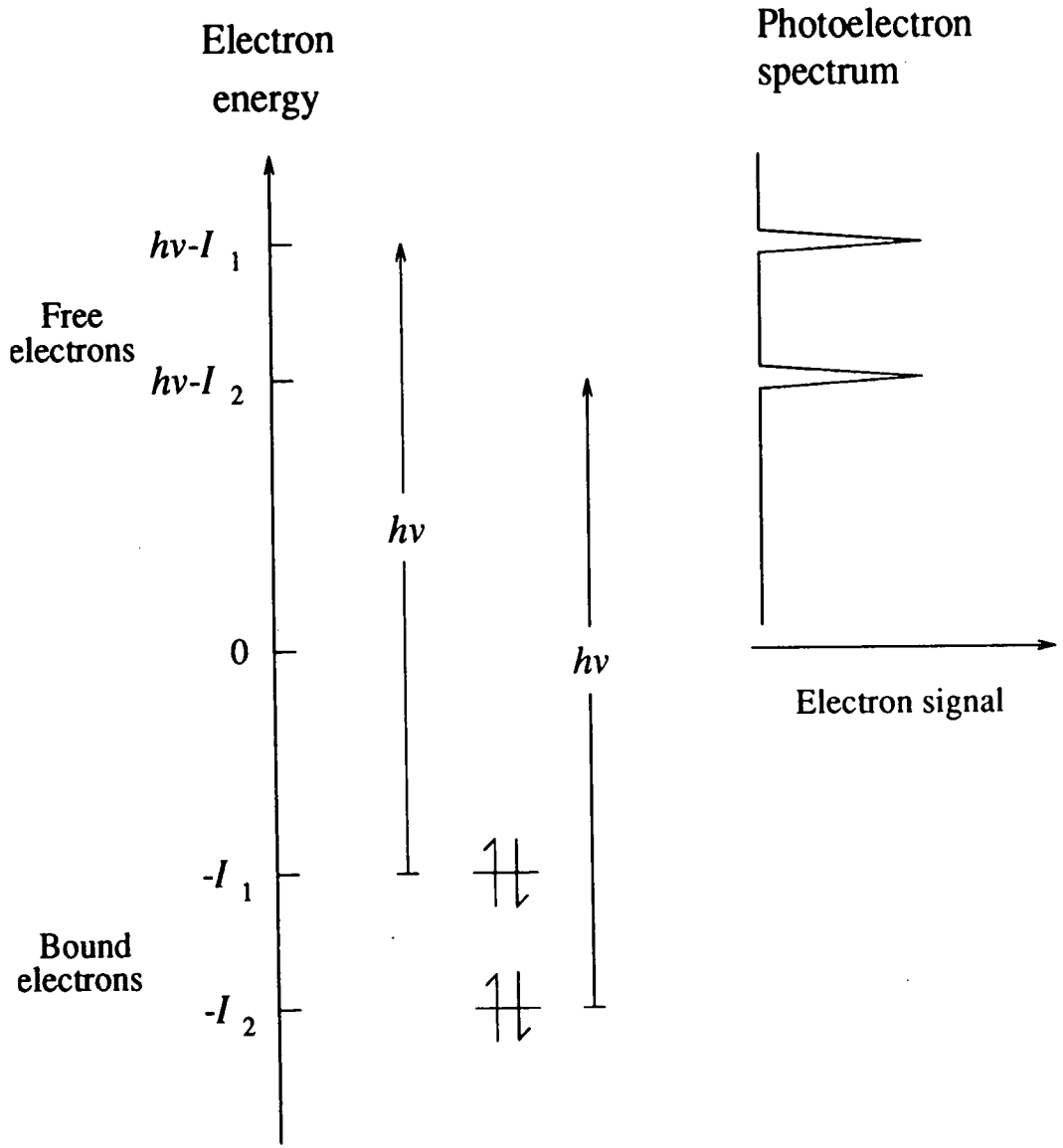

Figure 2.2 A schematic diagram indicating the general principles of conventional photoelectron spectroscopy.

rotational structure. The intensity profile of these photoelectron bands is controlled by Franck-Condon (F-C) factors (see section 2.4).

$$E_k = h\nu - E_j - E^*_{vib} - E^*_{rot} \qquad 2.14$$

The relative intensities of photoelectron bands are controlled by the photoionisation cross section (σ_I) which in the case of conventional photoelectron experiments is a function of the difference between the fixed photon energy and the energy at which the photoelectron band appears. The use of monoenergetic radiation to promote the ionisation process and the precise measurement of E_k permits a direct determination of the ionisation energies I_j. According to an approximation known as Koopmans' theorem [3], each atomic or molecular ionisation energy in a closed shell system, I_j, is equal in magnitude to an atomic or molecular orbital energy. Photoelectron spectroscopy can therefore allow a picture of the relative positions of the atomic or molecular orbitals to be determined. If radiation of a sufficient magnitude to satisfy Equations 2.13 or 2.14 is employed, electrons can be ejected from any occupied energy level in the atom or molecule.

Variations on this theme have also been developed (see chapter 3) which employ tuneable ionising radiation to scan the ionic structure and which rely on the detection of threshold electrons rather than kinetic energy electrons. However, as we will show below, the employment of tuneable ionising radiation is more likely to produce other effects in the ionisation continuum.

2.4 The Franck-Condon Principle

The Franck-Condon principle was developed in the 1920's to explain experimentally observed intensity distributions found in vibronic transitions. The principle is based on the Born-Oppenheimer approximation which assumes that electronic transitions in molecules take place on a much shorter time scale compared to that required for the nuclei to vibrate. In a semi-classical picture, this leads to

vibronic transitions being considered as vertical transitions between two electronic states, with the internuclear distance remaining constant, i.e. the nuclei have very nearly the same position and velocity before and after the transition. To put this on a more quantum mechanical basis, the intensity of a vibronic transition between two electronic states is proportional to the square of the transition moment, $\mathbf{R}_{ev}$,

$$\mathbf{R}_{ev} = \int \psi'_{ev}{}^{*} \mu \psi''_{ev} d\tau_{ev} \qquad 2.15$$

In this case, ψ'_{ev} and ψ''_{ev}, are the vibronic wave functions of the upper and lower electronic states, respectively, μ is the electric dipole moment operator and integration is over electronic and vibrational co-ordinates. Assuming that the Born-Oppenheimer approximation holds, ψ_{ev} can be factorised into electronic and vibrational components $\psi_e\psi_v$. In addition μ can be broken down into a contribution from the electrons and the nuclei. Since the vibrational wave functions are always real and electronic states are, by necessity, orthogonal,

$$\mathbf{R}_{ev} = \mathbf{R}_e \int \psi'_v \psi''_v dr \qquad 2.16$$

where $\mathbf{R}_e$ is the electronic transition moment and can be considered as a constant for all vibronic transitions associated with the electronic transition. The quantity $\int \psi'_v \psi''_v dr$ is called the vibrational overlap integral, and is a measure of the degree to which the initial and final vibrational wave functions overlap. The square of this quantity is known as the Franck-Condon (F-C) factor. Franck-Condon factors allow the relative intensity of vibrational transitions from a vibrational level, v", in one electronic state, such as the molecular ground state, to v' in an upper electronic state, such as the ground ionic state, to be calculated [2]. Some examples of the applicability of the F-C principle are outlined below;

1) An analysis of the intensity profile and the frequency of the vibrational structure in for example a photoelectron band, combined with a knowledge of the neutral

ground state vibrational frequency, can give an indication of the character of the molecular orbital from which the electron has been removed. This in turn can lead to an estimate of the change in equilibrium bond length which occurred upon ionisation.

2) Franck-Condon factors control not only the range of accessible vibrational levels in the upper electronic state, but also to some degree, the accessible electronic states. However, with the advent of double resonance techniques (discussed in the next chapter) and a knowledge of the Franck-Condon factors to intermediate electronic states, these problems can very often be surmounted and vibrational levels of excited electronic states can be accessed which are not within the vertical Franck-Condon window from the neutral ground state.

3) The effects of autoionisation in ionic state spectra can be dramatic (see section 2.5.3). Both steps involved in the autoionisation process are controlled by Franck-Condon factors. These include the initial excitation to vibrational levels of the neutral excited Rydberg state and the autoionisation step leading to, in many cases, the production of highly vibrationally excited ions in regions of the spectrum where the direct Franck-Condon factors are very small. From the resultant final state ionic spectrum and the autoionising F-C profile (see chapter 4), an idea of the relative position of the autoionising excited Rydberg state can be determined.

2.5 Autoionisation

Ionic states can be accessed directly as discussed above and indirectly as we will now show. This indirect process is known as autoionisation and is based on two distinct steps, as shown in Equation 2.17. The initial excitation step involves an electric dipole allowed resonant transition to a discrete rovibronic level of a neutral electronic Rydberg state (M^*) which lies above the ground ionic state of the atom or molecule. The second step then consists of a radiationless transition from the rovibronic level of the neutral Rydberg state to rovibronic levels in the final ionic

state. However, the second step has to follow the selection rule that the symmetry species of the autoionising state and the final state of the ion plus electron must be identical. To balance the energy equation, the excess energy is removed as kinetic energy by the electron. The initial excitation to the rovibronic level in the Rydberg state and the radiationless transition to the final ionic state are both governed by Franck-Condon factors and the product of these govern the final ionic vibrational states accessed.

$$M + h\nu \rightarrow M^* \rightarrow M^+ + e^- \text{ (k.e.)} \qquad 2.17$$

Autoionisation is essentially a decay mechanism for the highly excited neutral Rydberg state and in many cases the features which arise through autoionisation are so intense that they completely hide the structure arising from direct ionisation [4]. However, in certain cases autoionisation from these Rydberg states is in competition with other decay processes such as predissociation or radiative decay which can reduce the effect of autoionisation on an ionic spectrum. The three autoionisation mechanisms, electronic, vibrational and rotational, which can effect ionic spectra are discussed below.

2.5.1 Vibrational/Rotational Autoionisation

Vibrationally and/or rotationally excited Rydberg states converging on an ionic state, can in theory undergo vibrational or rotational autoionisation. In principle this can take place for Rydberg states converging on any ionic core, but in practice it most commonly occurs in Rydberg states converging on the ground ionic state. For autoionisation to take place, the energy of the vibrationally and/or rotationally excited Rydberg state must exceed the ionisation threshold, in which case vibrational and/or rotational energy is transferred to the departing electron leaving the molecular ion in its ground ionic state. Rotational autoionisation is only important for such high values of Rydberg principal quantum number, n, that a few rotational quanta suffice to produce autoionisation, such as found in H_2 [5,6].

A form of rotational autoionisation has also been found in ZEKE-PFI photoelectron spectroscopy in which large differences in the intensity of rotational branches were observed [7,8]. These differences could not be explained using conventional theories, so interactions between individual Rydberg series leading to rotational autoionisation were invoked. The mechanism involves the interaction of high-n Rydberg states (n > 150) with near degenerate low n Rydberg states converging to higher cation rovibronic ionisation limits. The application of the pulsed electric field lowers the ionisation potential and permits the mixed low n Rydberg states to autoionise leading to intensity gains in the rotational branches with negative changes in rotational quantum number [9,10]. The intensity gain, however, depends on the relative rates of predissociation and autoionisation. If the lower n Rydberg states are fully predissociated in the delay time before the application of the extraction pulse, the intensity differences are not observed.

Vibrational autoionisation in diatomic molecules is generally governed by the propensity rule $\Delta v = \pm 1$ [11] or by a weaker Δv=minimum rule [12,13]. These vibrational propensity rules have also been observed in two colour photoionisation studies of polyatomic molecules such as NH_3 [14] and aniline [15]. Vibrational autoionisation has also been invoked by Guyon et al. to explain the observation of low energy electrons in threshold photoelectron measurements on small triatomics such as OCS [16]. The mechanism proposed to account for this involves the coupling of high Rydberg states and a dissociative valence state [17].

2.5.2 Electronic Autoionisation

The autoionisation of electronically excited Rydberg states (i.e. members of Rydberg series converging to electronically excited ionic states) is very common for diatomic and small polyatomic molecules. In this case both electronic and very often vibrational energy of the core are transferred to the departing electron leaving the molecular ion in a lower ionic state.

$$AB + h\nu \rightarrow AB^{*}(v_{Ryd}) \rightarrow AB^{+}(v^{+}) + e^{-}(E_k) \qquad 2.18$$

The fact that electronic autoionisation takes place from an excited Rydberg state can in certain cases lead to dramatically extended vibrational structure in the final ionic state.

Electronic autoionisation is rare in conventional PE experiments, only normally being observed when excitation sources other than the He(I) lamp are employed. This is due to the fact that the 21.22 eV He(I) resonance line is generally above most bound molecular Rydberg states. However, electronic autoionisation has been modelled in diatomics by both Bardsley [18,19] and Smith [20,21], within the framework of the Fano configuration-interaction theory of autoionisation [22,23], and has been successful in explaining the extension of the vibrational progression in the ground state of O_2^+ when Ne(I) radiation was employed [24].

Electronic autoionisation with the production of a threshold electron in polyatomics is further complicated by the increased number of decay channels which are available. Guyon, Baer, Nenner and co-workers have employed threshold photoelectron spectroscopy along with fluorescence measurements to study electronic autoionisation in molecules such as CO_2 [25] and N_2O [26]. Their observations of significant fragmentation within the triatomics and highly vibrationlly excited ions led Guyon et al. [17] to propose a model involving the coupling of dissociative valence states and high Rydberg states along with a vibrational autoionisation mechanism to explain the production of threshold electrons.

2.5.3 Autoionisation in Threshold Photoelectron Spectroscopy

The application of tuneable excitation sources to the study of ionic states, such as those observed in threshold photoelectron spectroscopy (TPES), dramatically increases the probability of observing ionic structure as a result of autoionisation as well as direct ionisation. This is due to the increased likelihood of the exciting radiation becoming resonant with a rovibronic level in a neutral Rydberg state. For the specific example of threshold photoelectron spectroscopy, where the aim is to collect purely threshold photoelectrons generated when the photon energy is equal to the energy difference between the ionic state and the ground state, the formation of threshold electrons as a result of autoionisation can have a dramatic effect on the recorded spectrum. Threshold electrons are generated when the rovibronic level in the excited Rydberg state (ν_{Ryd}) is isoenergetic with a vibrational level of the final ionic state (v^+) and there is a good Franck-Condon overlap.

$$AB + h\nu \rightarrow AB^*(\nu_{Ryd}) \rightarrow AB^+(v^+) + e^- (E_k=0) \qquad 2.19$$

The threshold photoelectron cross section can be written as the sum of the direct ionisation component and terms describing the autoionisation component

$$\sigma(E)_{e=0} = \sigma_X |\langle \chi_{v''} | \chi_{v^+} \rangle|^2 + \sigma_{Ryd} |\langle \chi_{v''} | \chi_{\nu_{Ryd}} \rangle|^2 . \frac{|\langle \chi_{\nu_{Ryd}} | \chi_{v^+_{max}} \rangle|^2}{\sum_{v^+=0}^{v^+_{max}} |\langle \chi_{\nu_{Ryd}} | \chi_{v^+} \rangle|^2} \qquad 2.20$$

where σ_x and σ_{Ryd} are proportional to the transition probablilities for direct ionisation to an ionic state and for excitation of the autoionised Rydberg state. $\chi_{v''}$, χ_{v^+} and $\chi_{\nu_{Ryd}}$ are the vibrational wavefunctions for the neutral ground state, the ionic state and the autoionising Rydberg state, respectively. Equation 2.20 is a general expression which could equally well apply to the cross section for kinetic energy

electrons in He(I) PES. In that case, the probability of autoionisation is generally very low and the spectrum is dominated by the direct photoionisation terms. If on the other hand autoionisation is quite dominant, then depending on the position of the Rydberg state and Franck-Condon factors, the ionic vibrational structure can be enhanced in the region of the ionic spectrum containing the direct ionisation vibrational bands or extended into regions of the ionic spectrum where the direct ionisation Franck-Condon factors are vanishingly small.

Some qualitative examples of autoionisation relevant to the threshold photoelectron spectra presented in chapter 4 are shown in Figures 2.3-2.5 and discussed below. These examples are based on the product of the F-C factors for excitation of the vibrational levels in the Rydberg state and the F-C factors for the autoionising transition into ionic vibrational levels. Although other factors such as the transition intensity to the Rydberg state (which decreases as $1/n^3$ where n is the principle quantum number of the Rydberg states) also play a part in the resulting ion spectrum, they have been ignored in these examples.

Figure 2.3 (a) contains two potentials with similar potential energy curves and R_e values. The lower energy potential has been classified as the ground ionic state whereas the higher energy potential is a neutral Rydberg state converging on an excited ionic state with a similar R_e to the ground state. The Franck-Condon factors for direct ionisation from the neutral ground state (v=0) suggest that only the first five ionic vibrational bands would be observed. However, it is also clear that the F-C overlap between the neutral ground state (v=0) and the low vibrational levels of the neutral Rydberg state ($\sim v_{Ryd}$=0-4) is very good. Unfortunately, the probability of populating high vibrational levels in the ion i.e. v^+=7-12 with the generation of a threshold photoelectron (i.e. autoionisation) is very low as a result of the poor F-C overlap between $\sim v_{Ryd}$=0-4 and v^+=7-12. The predicted vibrational level Franck-Condon intensities in the ion for this case are shown in Figure 2.3 (b). Only the low vibrational levels of the ion, i.e. the direct ionisation components would be expected to be observed.

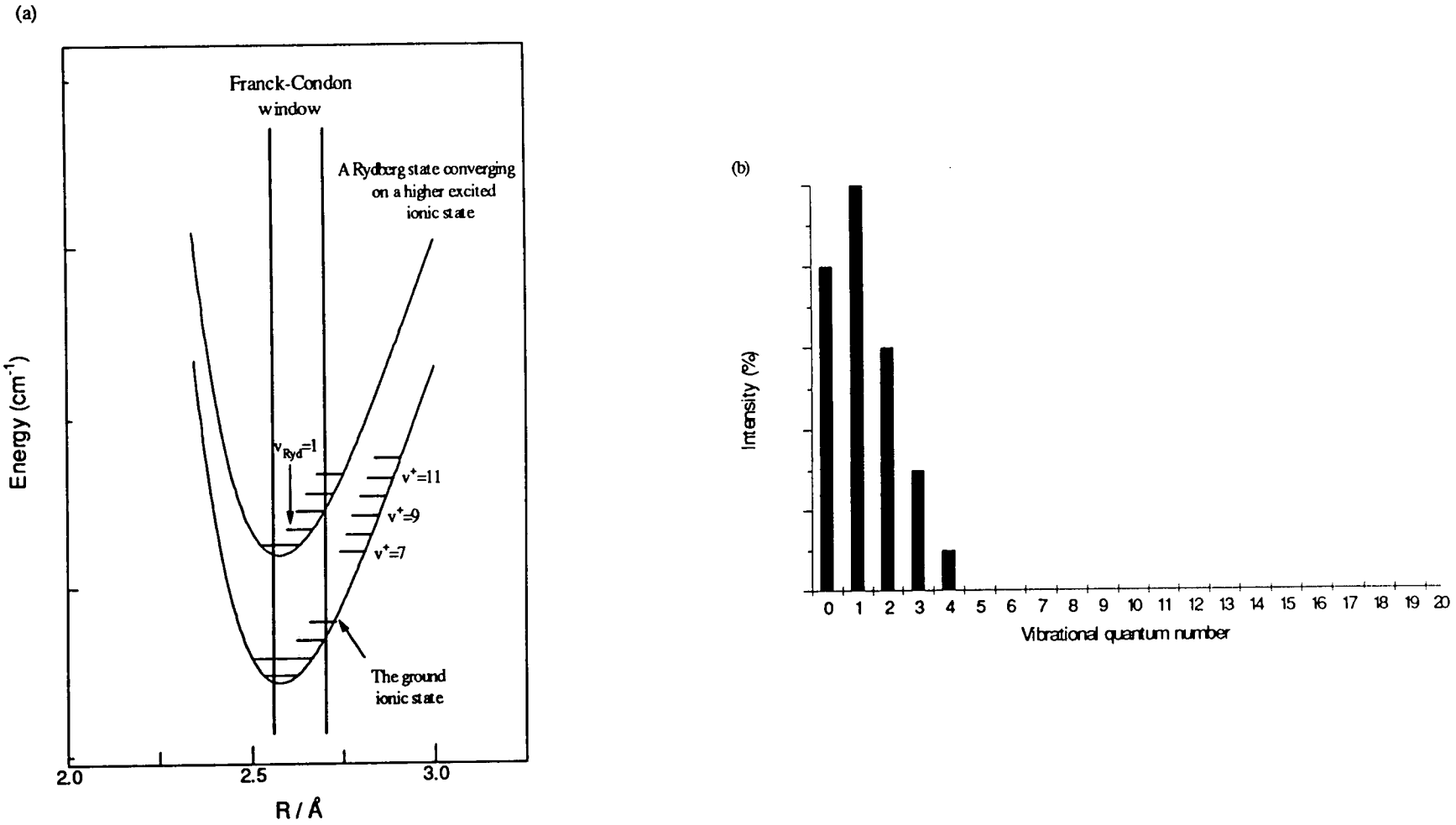

Figure 2.3 (a) A schematic diagram of two potential energy curves in the ionisation continuum in which the lower energy potential curve is the ground ionic state and the higher energy potential is a neutral Rydberg state converging on an excited ionic state with a similar R_e to that of the ground state. (b) The predicted Franck-Condon vibrational intensity pattern in the ground ionic state for the situation depicted in (a) taking into account autoionisation. See the text for details

Figure 2.4 (a) contains two similar potential energy curves with identical R_e values. In contrast to Figure 2.3 (a) the lower potential energy curve (dotted) describes a neutral Rydberg state converging on the ground ionic state (the higher energy potential energy curve). In this case there is very good F-C overlap between individual ionic vibrational levels and Rydberg vibrational levels but only a good F-C overlap between the neutral ground state ($v=0$) and the low vibrational levels of the Rydberg state ($\sim v_{Ryd}=0$-3). Vibrational autoionisation with the production of a threshold electron is therefore likely to enhance only the low vibrational levels of the ion ($v^+=0$-2), resulting in the Franck-Condon intensity pattern in the ground ionic state shown in Figure 2.4 (b).

Figure 2.5 (a) contains two potential energy curves where the lower potential energy curve describes a ground ionic state and the upper potential energy curve describes a neutral Rydberg state converging on an excited ionic state with an R_e which is larger than that of the ground ionic state. In this case the F-C overlap between the neutral ground state ($v=0$) and $v_{Ryd}=2$-11 and between $v_{Ryd}=2$-11 and $\sim v^+=10$-18 is very good resulting in a large chance of populating high vibrational levels of the ground ionic state (i.e. $v^+=10$-18) with the production of a threshold electron via electronic autoionisation. The ground ionic state vibrational Franck-Condon intensity pattern may therefore be expected to be similar to that shown in Figure 2.5 (b) (it should be noted that the intensity of the high vibrational levels in this figure is not to scale). The relative intensity of autoionising vibrational structure is very dependant on the individual molecule investigated along with the positions and vibrational overlap of the Rydberg states (see chapter 4 for examples in the halogens).

These three examples show the effects of autoionisation on threshold photoelectron ionic spectra. In practice there are many Rydberg states in the vicinity of ionic states which can all contribute to the final ionic spectrum. However, the electronic intensity factors along with the restriction that only autoionising transitions

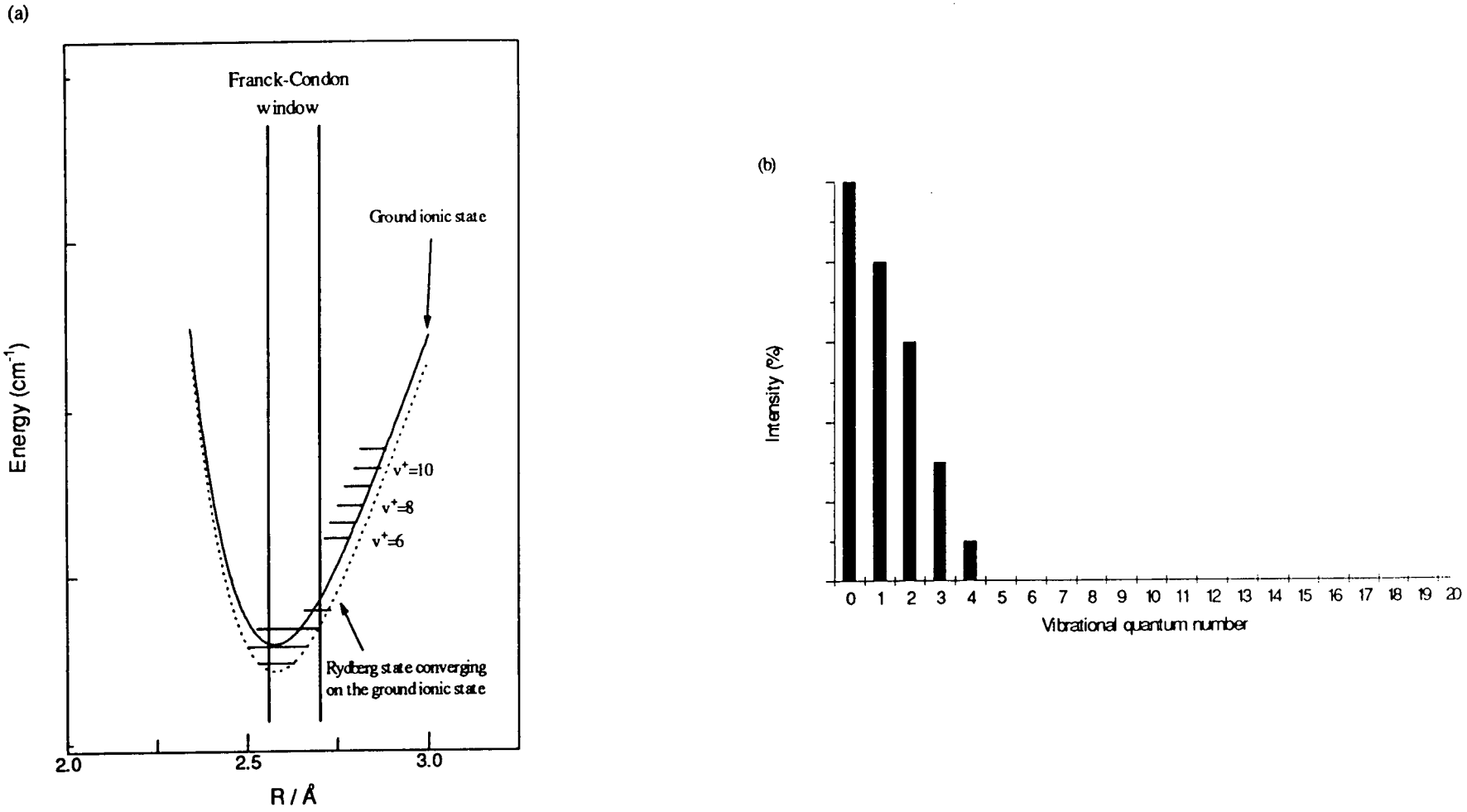

Figure 2.4 (a) A schematic diagram of two similar potential energy curves with identical R_e values. The lower energy potential curve (dotted) is a Rydberg state converging on the ground ionic state (solid). (b) The predicted Franck-Condon vibrational intensity pattern in the ion taking vibrational autoionisation into account. See the text for details

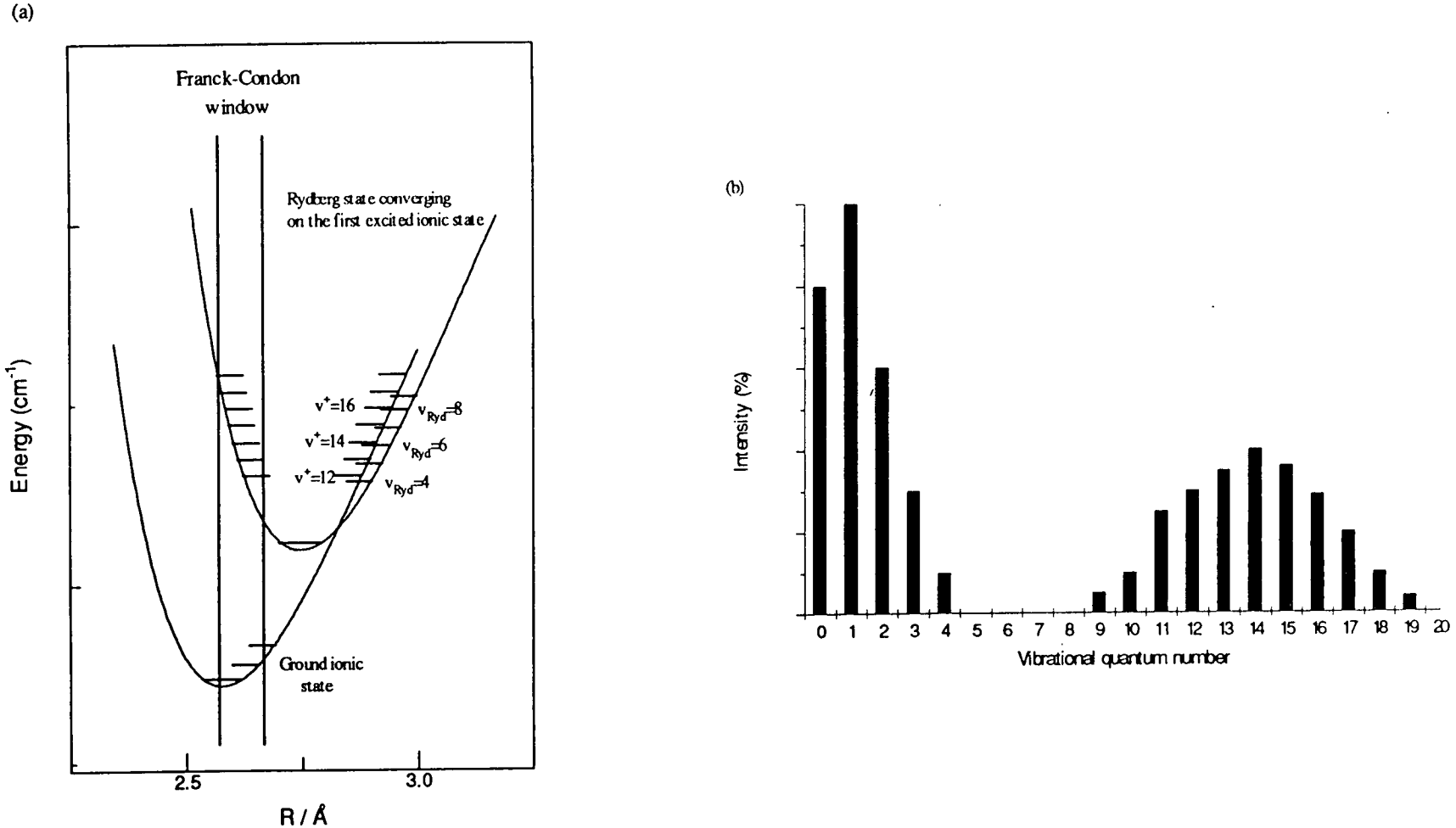

Figure 2.5 (a) A schematic diagram of two potential energy curves in the ionisation continuum in which the lower potential energy curve describes the ground ionic state and the upper potential energy curve describes a neutral Rydberg state converging on a higher excited ionic state. (b) The predicted ground ionic state Franck-Condon vibrational intensity pattern having taken into account electronic autoionisation. See the text for details

which produce a threshold electron will be detected, limit the number of Rydberg states which are actually involved in these processes.

The threshold autoionisation examples given above presume that the Rydberg rovibronic level only autoionises with the production of a threshold electron. In practice, however, there is a competition between this process and autoionisation into lower rovibronic levels of the ionic state with the production of kinetic energy electrons. The suppression of these kinetic electrons is therefore a very important requirement for the success of the threshold technique [27]. Electronic autoionisation can also affect the ZEKE-PFI technique in much the same way as threshold photoelectron spectroscopy, as will be discussed in chapter 5. The only difference in this case is that the autoionising Rydberg states must be long lived to survive the delay prior to the application of the extraction pulse [28].

2.6 Factors Affecting the Lifetime of High-*n* Rydberg States

The pulsed field ionisation mechanism in ZEKE-PFI experiments relies on the universal existence of long-lived high-*n* Rydberg states (where *n* is the Rydberg principal quantum number) lying a few wavenumbers below the ionisation threshold. One question which is now being considered, is why these Rydberg states have these anomalously long lifetimes when theory suggests that these states should have decayed prior to the application of the extraction pulse.

There has been much debate over this question and the possible mechanisms which could extend the lifetime of the high-*n* Rydberg states. The optically accessible high-*n* Rydberg states have low l and m_l character (l and m_l represent the Rydberg electron orbital angular momentum and azimuthal quantum numbers, respectively). It is well known, both theoretically and experimentally, that low l Rydberg states which have large quantum defects, spend more time in the region of the ionic core than high l Rydberg states and therefore have a higher probability of undergoing processes such as predissociation [12], autoionisation [5,29] and radiative

decay. A specific example of a fast decay process is the *n*p Rydberg series in NO which is known to be strongly predissociated [30,31]. An extrapolation carried out by Pratt [32] from a lifetime measurement of the 35p Rydberg state by Fujii and Morita [33] led to a lifetime of between 2 and 4 nanoseconds for the 150p Rydberg state lying 5 cm^{-1} below the ionisation threshold. Even if one ignores these decay processes and scales low n Rydberg lifetimes by the n^3 lifetime scaling factor, it is still not sufficient to explain the long lifetimes observed in the ZEKE-PFI experiments.

The principle behind the lifetime lengthening mechanism is that the initially prepared high-n, low l and low m_l states gain some high l, high m_l character during the delay prior to the application of the pulsed electric field. These high l, high m_l states have vanishingly small quantum defects and therefore have a very low probability of coupling to the ionic core. Several theories have so far been put forward to explain how these high-n Rydberg states could gain high l and high m_l character. The importance of electric field and collisional effects has been proposed [32,34,35,36,37,38,39], along with intramolecular energy redistribution processes [40] and breakdown of the Born-Oppenheimer approximation [41]. In a theoretical paper [34], Chupka discussed the possible effects of both electric fields and collisions on Rydberg state lifetimes. He initially proposed that the presence of stray homogeneous electric fields of the order of 20-50 mV/cm, which are known to exist in many ZEKE spectrometers, would induce l mixing or Stark mixing in the Rydberg states [42], in which the initial high-n, low l Rydberg wavefunction would be spread equally among all states with l values from 0 to n-1, and increase the lifetime of high-n Rydberg states by a factor of $\sim n$. Additionally, l and m_l changing collisions between charged or polar species and the high-n Rydberg states was proposed to increase the lifetime by a second factor of $\sim n$. It is well known that many ions and electrons are produced during the laser pulse which can interact with the spatially large orbits of the high-n Rydberg electrons, and both theory and experiment [43,44] has shown that l changing (and almost certainly m_l changing) cross sections are extremely large for collisions with ions and polar molecules. Such large cross sections can lead to the randomisation of the l and m_l populations, especially since the m_l

degeneracy of $(2l+1)$ favours more stable high l states. Both these mechanisms led Chupka to predict that the lifetimes of high-n, low l, m_l Rydberg states could be extended by a factor somewhere between n and n^2, bringing them in line with experimental observations.

Recently, attempts have been made by a number of different groups to experimentally clarify the situation. Pratt [32] has recorded both ZEKE-PFI and delayed field photoionisation spectra of NO, with and without a small dc field present. With no dc field present, it was found that the ZEKE-PFI signal was independent of delay time (of the order of microseconds) which confirmed that both the processes which stabilise the high-n Rydberg states and those which depopulate the lower lying Rydberg states must be quite rapid. The presence of a small dc electric field, however, not only caused a loss of ZEKE-PFI signal but also blue shifted the onset of the NO pulsed field photoionisation spectra. This indicated that the dc electric field was depopulating the high-n Rydberg states responsible for the ZEKE-PFI signal. Pratt therefore postulated that the dc electric field was mixing low n Rydberg states converging to higher rotational levels of the NO ion with the high-n Rydbergs of interest and as a result of the increased predissociation rates in the lower n Rydberg states, this mixing was proposed to lead to a dramatic reduction in the ZEKE-PFI signal.

Further studies by Merkt et al. on the ZEKE-PFI spectrum of argon employed not only dc electric fields but also pulsed electric fields [36,38]. The application of a dc field ($\leq$ 2 V/cm) led to a similar loss of the ZEKE-PFI signal from the higher spin-orbit component of argon, to that which Pratt had observed. This led him to conclude that electric field induced l mixing (as proposed by Chupka) did not prolong the lifetime of the high-n Rydberg states. Two alternative explanations were put forward to explain this loss. The first was that the dc field induced the decay of these high-n Rydberg states of argon by field induced spin-orbit autoionisation, while the second was that it inhibited the formation of these long lived states altogether. In order to discriminate between the two mechanisms, Merkt replaced the dc field by a

small pulsed electric field applied 50 ns after photoexcitation. This resulted in no loss of ZEKE-PFI signal, from which he concluded that the presence of a dc electric field during ionisation inhibited the formation of the long lived high-n Rydberg states in argon rather than causing their decay.

Attention was then turned to the other theory proposed by Chupka, i.e. collisional effects. Calculations by Merkt and Zare [39] have demonstrated that the large electric fields present in the ionisation volume, as a consequence of the formation of prompt ions, could be sufficient to induce l and m_l changing collisions. It is therefore, now believed that in the absence of a dc field, the presence of these ions in the ionisation volume can lead to a considerable stabilisation of the initially prepared high-n Rydberg state via these large Δl and Δm_l changing collisions, as Chupka had proposed. This has been supported by Zhang et al. [35] who found that very high laser fluences i.e. large numbers of ions and Rydbergs in the ionisation volume, substantially increased the lifetimes of Rydbergs 10-20 cm^{-1} below the ionisation threshold in large aromatic molecules, in contrast to the behaviour observed with low laser fluences. However, it was also observed that these high laser fluences caused the blue edge of the ZEKE-PFI spectra to decay more rapidly than at low laser fluences which was ascribed to long range ion-Rydberg and Rydberg-Rydberg interactions resulting in ionisation of the Rydberg states and loss of the observed signal. The presence of a dc electric field during ionisation, however, would seem to promote rapid field induced l mixing in $\Delta l = \pm 1$ steps, in preference to the large Δl and Δm_l changing collisions. Theoretically therefore, if all the l channels are long lived then stabilisation will eventually take place. However, if a low l channel is very short lived (for e.g. the p channel in NO and the d channel in argon) it can lead to the decay of the Rydberg state prior to it gaining sufficient high l character to be stabilised.

Alternative models have also been proposed to explain the lengthening of high-n Rydberg lifetimes. A study by Levine and co-workers [40,41] on the ZEKE-PFI spectrum of the large aromatic, phenanthrene has generated a theory which has

not been greeted with universal approval. The theory involves two competing mechanisms for the long lived Rydberg states; one of which is intramolecular relaxation and the other, which is excess internal energy assisted ionisation of the Rydberg state, is only possible just below the ionisation threshold. High lying Rydberg states are calculated to decay very quickly into the dissipative quasicontinuum [45] of rovibrational states of large polyatomic molecules, except very close to the ionisation limit. In this region the rate of intramolecular dissipation decreases steeply due to the electron spending most of it's time far away from the core. To compensate for this, the process of internal energy assisted ionisation is rapidly switched on just below the energetic threshold for ionisation. In this process, internal energy is acquired by the electron from the core enabling it to leave. Using this model the experimental Rydberg state lifetimes of phenanthrene have been successfully fitted. However, Zhang et al. [35] also carried out a study of the high Rydberg lifetimes of several molecular systems, including phenanthrene, and measured lifetimes in excess of 25 μs, compared to Bahatt et al.'s [40] experimental value of ~1.1 μs. A collisional effect, (i.e. a large number of ions and Rydbergs in the ionisation volume) was found by Zhang et al. to explain this short lifetime of the high-n Rydberg states observed by Bahatt et al. From Zhang's investigation it was concluded that the lifetime of the highest n Rydberg states was not determined by intramolecular nonradiative relaxation rates but was primarily determined by long range interactions leading to the decay of the Rydberg states. They speculated that in Bahatt et al.'s experiment, very large ion densities had been present in the ionisation volume which had led to their very short measured lifetime. Chupka has also been very critical of Bahatt et al.'s theoretical model in which he found many weaknesses. From their results he has developed an alternative model which explained their results equally well [37].

The picture that is starting to form goes some way towards understanding the extended lifetimes of the high-n Rydbergs. From the experimental work it would seem as though the dominant mechanism is one which involves large Δl and Δm_l changing collisions with charged or polar particles present during the formation of

these high-n Rydberg states. However, a balance must be found between the number of ions required to maximise the stabilisation effects, via Δl and Δm_l changing collisions, and the number of ions required to minimise the collisional ionisation loss mechanism for these high-n Rydberg states.

2.7 References

[1] J. Berkowitz, Photoabsorption, Photoionisation and Photoelectron Spectroscopy, Academic Press, New York (1979)

[2] G. Herzberg, Molecular Spectra and Molecular Structure, Vol. 1-Spectra of Diatomic Molecules, Van Nostrand Reinhold Company (1989)

[3] T.A. Koopmans, Physica **1** (1933) 104

[4] W. Chupka and J. Berkowitz, J. Chem. Phys. **51** (1969) 4244

[5] G. Herzberg and Ch. Jungen, J. Mol. Spec. **41** (1972) 425

[6] S.T. Pratt, J.L. Dehmer and P.M. Dehmer, J. Chem. Phys. **90** (1989) 2201

[7] F. Merkt and T.P. Softley, Int. Rev. Phys. Chem. **12** (1993) 205

[8] R.G. Tonkyn, R.T. Wiedmann and M.G. White, J. Chem. Phys. **96** (1992) 3696

[9] G. Reiser and K. Müller-Dethlefs, J. Phys. Chem. **96** (1992) 9

[10] R.D. Gilbert and M.S. Child, Chem. Phys. Lett. **187** (1991) 153

[11] R.S. Berrry, J. Chem. Phys. **45** (1966) 1228

[12] P.M. Dehmer and W.A. Chupka, J. Chem. Phys. **65** (1976) 2243

[13] P.M. Dehmer and W.A. Chupka, J. Chem. Phys. **66** (1977) 1972

[14] J.H.D. Eland, J. Chem. Phys. France **77** (1980) 613

[15] J.A. Hager, M.A. Smith and S.C. Wallace, J. Chem. Phys. **84** (1986) 6771

[16] J. Delwiche, M-J. Hubin-Franskin, P-M. Guyon and I. Nenner, J. Chem. Phys. **74** (1981) 4219

[17] P-M. Guyon, T. Baer and I. Nenner, J. Chem. Phys. **78** (1983) 3665

[18] J.N. Bardsley, Chem. Phys. Lett. **1** (1967) 229

[19] J.N. Bardsley, Chem. Phys. Lett. **2** (1968) 329

[20] A.L. Smith, Phil. Trans. Roy. Soc. Lond. **A268** (1970) 169

[21] A.L. Smith, J. Quant. Spectrosc. Radiat. Transfer **10** (1970) 1129

[22] U. Fano, Phys. Rev. **124** (1961) 1866

[23] F. Mies, Phys. Rev. **175** (1968) 164

[24] A.J. Blake, J.L. Bahr, J.H. Carver and V. Kumar, Phil. Trans. Roy. Soc. Lond. **A268** (1970) 159

[25] T. Baer and P-M. Guyon, J. Chem. Phys. **85** (1986) 4765

[26] T. Baer, P-M. Guyon, I. Nenner, A. Tabché-Fouhaillé, R. Botter, L.F.A. Ferreira and T.R. Govers, J. Chem. Phys. **70** (1979) 1585

[27] W.B. Peatman, Chem. Phys. Lett. **36** (1975) 495

[28] W. Kong, D. Rodgers and J. Hepburn, Chem. Phys. **203** (1993) 497

[29] R.E. Huffman, Y. Tanaka and J.C. Larrabee, J. Chem. Phys. **39** (1963) 902

[30] J.W.J. Verschuur, J. Kimman, H.B. van Linden van der Heuvell and M.J. van der Weil, Chem. Phys. **103** (1986) 359

[31] E. Miescher and F. Alberti, J. Phys. Chem. Ref. Data **5** (1976) 309, Table I

[32] S.T. Pratt, J. Chem. Phys. **98** (1993) 9241

[33] A. Fujii and N. Morita, J. Chem. Phys. **98** (1993) 4581

[34] W.A. Chupka, J. Chem. Phys. **98** (1993) 4520

[35] X. Zhang, J.M. Smith and J.L. Knee, J. Chem. Phys. **99** (1993) 3133

[36] F. Merkt, J. Chem. Phys. **100** (1994) 2623

[37] W.A. Chupka, J. Chem. Phys. **99** (1993) 5800

[38] F. Merkt, S.R. Mackenzie, R.J. Rednall and T.P. Softley, J. Chem. Phys. **99** (1993) 8430

[39] F. Merkt and R.N. Zare, J. Chem. Phys. **101** (1994) 3495

[40] D. Bahatt, U. Even and R.D. Levine, J. Chem. Phys. **98** (1993) 1744

[41] U. Even, M. Ben-Nun and R.D. Levine, Chem. Phys. Lett. **210** (1993) 416

[42] H.A. Bethe and E.E. Salpeter, Quantum Mechanics of One- and Two- Electron Atoms, Springer-Verlag, Berlin (1957)

[43] K.B. MacAdam, R.G. Rolfes, X. Sun, J. Singh, W.J. Fuqua III and D.B. Smith, Phys. Rev. A **36** (1987) 4254

[44] K.B. MacAdam, D.A. Crosby and R. Rolfes, Phys. Rev. Lett. **44** (1980) 980

[45] J. Jortner and R.D. Levine, Adv. Chem. Phys. **47** (1981) 1

Chapter 3

Experimental Techniques

3.1 Introduction

The experimental details of the various techniques employed to carry out the research described within this thesis are presented in this chapter. A brief review of ionisation light sources and excitation schemes employed in the study of both neutral and ionic states is given in section 3.2. This is followed by a discussion of supersonic molecular beams and a brief outline of conventional VUV photoelectron spectroscopy and electron energy analysers. Section 3.5 continues with threshold photoelectron spectroscopy and gives an account of the development of threshold photoelectron analysers and the experimental details of our penetrating field electron spectrometer. Finally, in section 3.6, the origins of ZEKE-PFI photoelectron spectroscopy are presented along with the experimental details of our spectrometer and a discussion of the field ionisation mechanism.

3.2 Sources of Monochromatic VUV Radiation

The highly excited neutral electronic states and ionised states of small gas phase atomic and molecular species are observed in the vacuum ultraviolet (VUV) region of the electromagnetic spectrum. Fixed wavelength VUV sources, such as gas discharge lamps have been the dominant light source employed in conventional photoelectron investigations of atomic and molecular ions. These discharge sources generate characteristic discrete resonance lines when an electrical discharge is passed

through a low pressure gas, the best known of which is the He(I) line at 58.4 nm (21.22 eV) [1]. The requirement for a single intense monochromatic resonance line in a discharge source is achieved by varying the discharge conditions, such as the gas pressure [2,3]. In this way for example, the He(II) line at 30.4 nm can become dominant [4]. Passing a discharge through the other noble gases produces lower energy (cf. He(I)) resonance lines which lead to a reduction in the electron's kinetic energy and therefore improved electron energy resolution (see section 3.4.1) [5]. However, the noble gas emission lines are doublets (due to spin-orbit splitting) which results in a doubling of all the spectral features [6].

Tuneable VUV sources have also been employed to study atomic and molecular ions. In contrast to fixed wavelength sources, however, they have also been used to investigate neutral atomic and molecular species. Examples of tuneable VUV sources include the argon continuum [7] and the helium Hopfield continuum [8]. These are both generated by converting discrete resonance line gas discharge sources to broad continuum sources by increasing the gas pressure and pulsing the electrical discharge. In recent years there has also been a substantial growth in the number of synchrotron radiation facilities which has resulted in synchrotron radiation becoming the most widely used tuneable VUV source. The production of synchrotron radiation requires electrons to travel at relativistic energies in a circular path which is controlled by a series of "bending magnets". As the electrons pass these magnets the path of the electron is deflected and intense beams of synchrotron radiation are emitted tangentially. The unique properties of this synchrotron radiation make it a very desirable VUV source. These include its broad tunability from the VUV to the X-ray region of the electromagnetic spectrum, its high brightness and high polarisation characteristics. In addition synchrotron radiation is very stable and naturally collimated. The theoretical background to radiation generated by the circular motion of charges goes back to the early 1900's [9] although it was not until the 1940's that the first experimental investigations into the properties of this radiation took place. Synchrotron facilities are now found all over the world including BESSY in Berlin, Germany, the Photon Factory in Tsukuba, Japan, the

Daresbury Synchrotron Radiation Laboratory in the UK and the National Synchrotron Light Source in Brookhaven, USA. Descriptions of some of these sources along with the instrumentation used can be found in Ref. [10]. A general limitation of continuous sources is the requirement for a monochromator to specify the desired wavelength. This inevitably leads to a competition between the required photon flux and the achievable resolution.

Although laser excitation sources have a significantly smaller bandwidth compared to synchrotron and discharge sources, their fundamental spectral output is limited to between approximately 420 and 900 nm depending on the laser system. This can, however, be extended down to ~200 nm with frequency doubling and mixing techniques. The generation of VUV laser light requires a number of other techniques, such as Raman shifting via the anti-stokes lines in H_2. This results in a series of discrete VUV lines shifted toward higher energy [11] but unfortunately the intensity of these lines drops off rapidly with the number of shifts. Intense continuous VUV laser light can be generated by the tripling of visible laser light in non-linear media [12] and four-wave mixing techniques in rare gases [13-15] and metal vapours [16]. Third harmonic generation is generally achieved by focusing visible laser light into a cell or at the output of pulsed or continuous expansion of a noble gas such as xenon or argon [17,18]. However, the poor conversion efficiency of ~ 10^{-6} limits the usefulness of this technique. Four-wave mixing, on the other hand, has the slightly better conversion efficiency of 10^{-4} - 10^{-5}, but requires two laser sources. The first laser is set in resonance with an allowed two-photon transition in the rare gas or metal vapour, while the second laser is scanned. This leads to the emission of a photon with an energy which is either the sum of the three laser photons (sum frequency mixing) or the difference between the two-photon energy and the scanned photon energy (sum-difference frequency mixing). Unfortunately, all these laser based techniques for generating VUV radiation also require a monochromator to select the VUV radiation from the fundamental wavelengths employed to generate it.

3.2.1 Resonance Enhanced Multiphoton Ionisation (REMPI)

Single-photon tuneable VUV sources such as synchrotron radiation and continuum discharge lamps have been used fairly extensively to probe the highly excited neutral states of many atomic and molecular species [19]. The rovibronic structure of these neutral states being recorded via an absorption spectrum [20] or a fluorescence excitation [16] spectrum for example. There are, however, a number of limitations to single-photon VUV excitation schemes. The selection rules for single-photon transitions and in some cases Franck-Condon factors, can severely limit the number of accessible excited states. Furthermore, experimental factors such as the requirement for an evacuated optical path and LiF or MgF_2 optics, can also hinder the application of these VUV sources.

The availability of tuneable laser radiation from the infrared to the ultraviolet, has made it possible to explore the electronic structure of molecules using the unique selection rules arising in nonresonant multiphoton transitions. Initially these transitions were detected by direct absorption and fluorescence excitation [21] techniques. However, in the mid 1970's, an ionisation detection technique, multiphoton ionisation (MPI), was developed in which the bound state transitions of the molecule appeared as resonances in the ion yield spectrum [22]. The intense, tuneable monochromatic laser radiation is utilised to promote multiphoton transitions, involving the absorption of one or more photons, to a resonant intermediate state followed by the absorption of further photons to the ionisation continuum, in an (n + m) ionisation scheme. In this notation, n, is the number of photons of fixed energy required to access the intermediate state and m is the number of photons of the same energy required to bring about ionisation from the intermediate state. An important factor in resonant ionisation processes is the lifetime of the real intermediate state. A long lifetime means that the absorption of a second photon during the same laser pulse has a relatively high probability, unless predissociation is important [23]. The most efficient resonance enhanced multiphoton ionisation (REMPI) scheme is (1 + 1) resonant ionisation (shown in Figure 3.1(a)), in which the photons are absorbed

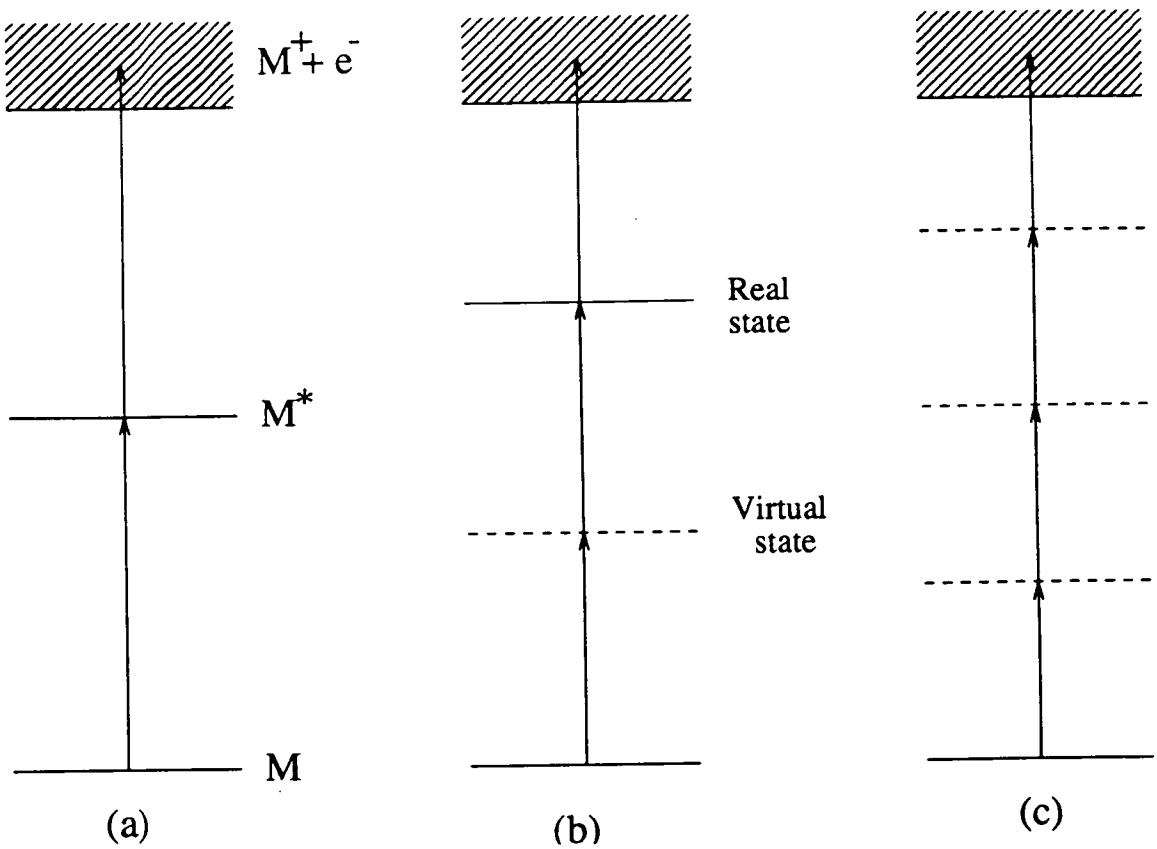

Figure 3.1

Three examples of multiphoton ionisation schemes ; (a) a (1+1) resonant ionisation scheme, (b) a (2+1) resonant ionisation scheme and (c) a non-resonant ionisation scheme.

sequentially i.e. incoherently. The simplest of REMPI experiments therefore consists of a tuneable UV laser beam focused into a low pressure gas. The ions created by the laser pulse are collected, the current amplified and the resultant signal recorded as a function of wavelength. Whenever the laser photon energy is resonant with a bound-bound transition from the ground state of the molecule, a significant increase in the ion signal is recorded thereby revealing the electronic, vibrational and rotational structure of the molecule. A reduction in ionisation efficiency and therefore signal can, however, be observed if non-radiative processes (e.g. predissociation) deplete the population of the intermediate state. However, the population of the intermediate state with focused laser beams and nanosecond lasers is usually sufficiently rapid that some ionisation can generally be detected in all but the most extreme cases.

An alternative approach to resonance enhanced multiphoton ionisation is to use the non-linear properties of the molecules themselves to bring about simultaneous n photon ($n \geq 2$) absorption to reach the real state (see Figure 3.1(b)). In this process a virtual intermediate state of the molecule is involved, which by its nature has a very short lifetime ($\sim 10^{-15}$ s). Thus, if a second photon is incident on the molecule within this timescale, both photons are absorbed simultaneously i.e. coherently. Clearly, excitation only occurs when the resonance condition $2h\nu = \Delta E$ (where ΔE is the energy difference between the ground state and the real intermediate state) is met. Higher order processes involving 3 or more photons have been observed but the cross-sections for such processes fall rapidly with n. Typical values for coherent two and three photon cross sections are $\sim 10^{-51}$ $cm^4 s$ and $\sim 10^{-82}$ $cm^6 s^2$, respectively [24]. High laser intensities, such as those obtained with a focused laser beam, are therefore essential to promote n-photon resonant transitions. However, these high laser intensities can broaden spectral peaks and also produce extensive fragmentation due to the absorption of further photons by the ion.

The absorption of two or more photons without the involvement of a real intermediate state, as shown in Figure 3.1(c), can also promote ionisation. However, such non-resonant ionisation has a significantly lower probability than processes

involving real intermediate states and therefore a tightly focused laser beam is essential to achieve ionisation. Although non-resonant ionisation can be employed as an ionisation scheme it produces no spectral information on neutral excited states.

The addition of a second laser into the resonant ionisation scheme introduces the possibility of accessing a much wider range of excited states through double resonance excitation schemes. Applications of optical-optical double resonance excitation to the study of excited electronic states have been numerous and have included investigations of the ion-pair states of the halogens and interhalogens [25] which are particularly difficult to access with one colour REMPI spectroscopy. A schematic diagram of two possible excitation schemes is shown in Figure 3.2(a). A pump laser (ω_1) is tuned to a rovibronic level of an intermediate state, commonly a valence state and the probe laser (ω_2) is scanned through a higher electronic state. If the intensity of the fixed frequency pump laser is kept low such that the absorption of further pump photons from the intermediate state is minimised, then the absorption of tuneable probe laser photons is maximised and a spectrum of the higher electronic state can be recorded. Two colour excitation (n + m') schemes (where the prime indicates that the probe laser is a different frequency to the pump laser) have a number of advantages over the single colour REMPI scheme. Firstly, selecting a single rotational or vibrational level in the lower electronic state can dramatically simplify the spectrum of the higher excited state. For example, hot bands can be eliminated through the selective excitation of vibrational bands in the intermediate state. Secondly, by selecting a vibrational level in the intermediate electronic state which is shifted from the Franck-Condon maximum, vibrational levels in the upper electronic state can be accessed which would otherwise be weak or inaccessible in a vertical transition from the ground state.

The investigation of ionic electronic structure can be thought of as an extension of conventional neutral state REMPI to one in which the final resonant state is in the ionisation continuum. In the work presented here, the ionic structure is recorded by collecting zero kinetic energy electrons which reveal a rovibronic

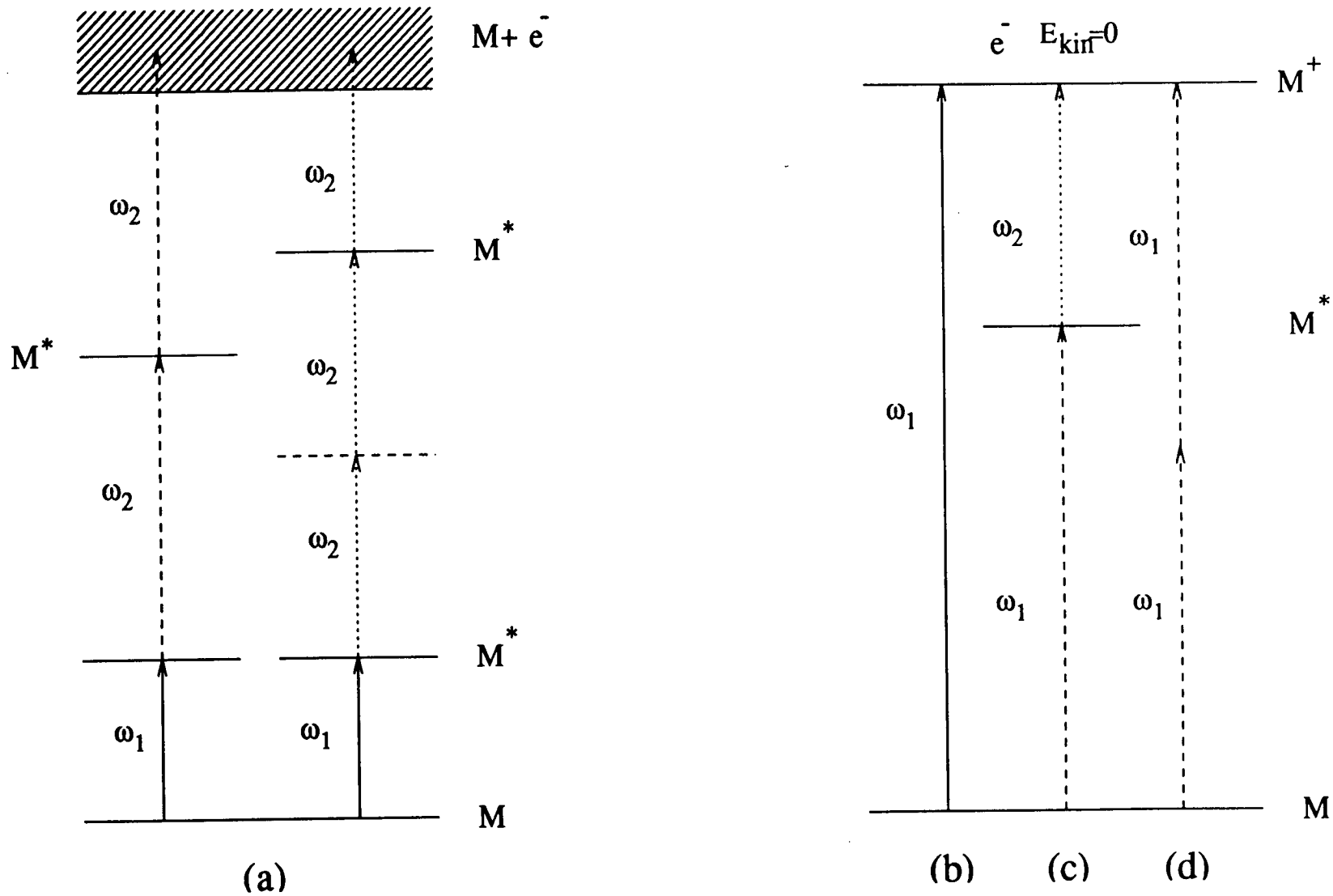

Figure 3.2 Examples of excitation schemes employed in the study of; (a) intermediate neutral excited states via two colour REMPI spectroscopy and (b)-(d) ionic states, via TPES and ZEKE-PFI photoelectron spectroscopy.

resonance in the ionisation continuum. Threshold photoelectron investigations generally employ single photon resonant ionisation schemes using synchrotron VUV radiation (see Figure 3.2(b)) [26]. ZEKE-PFI photoelectron investigations, on the other hand, have employed a number of excitation schemes. These have included 1) single photon VUV laser ionisation schemes (Figure 3.2(b)) [27,28] 2) multiphoton (n+m') schemes (Figure 3.2(c)) [29-31] and 3) non-resonant multiphoton ionisation schemes (Figure 3.2(d)) [32,33]. The majority of ZEKE-PFI investigations, however, have involved a resonant intermediate state. The selection of known intermediate vibrations and rotations can assist in the identification of their counterparts in the ZEKE-PFI spectrum which is particularly useful in large molecules, such as aromatics, which have a large number of vibrational modes. Ionisation via an intermediate state can also allow minor species in molecular beams, such as van der Waals complexes, to be selectively ionised.

3.2.2 Time-of-Flight Mass Spectrometry

Initial REMPI experiments recorded neutral state rovibronic spectra by measuring the total ion current in a static cell [34]. Unfortunately, this method often leads to many unassigned spectral peaks due to the fact that the parent molecular ion is very often not the only species produced in the ionisation volume. Fragments of the parent molecular species were also often ionised and detected. The problem of identifying which atomic or molecular species was responsible for each spectral feature was resolved by mass analysing all the ions formed in the ionisation volume. This was achieved using the basic principle that ions of different mass, having been given a fixed initial acceleration take different times to travel a fixed distance. By selecting a particular time gate the REMPI spectrum of an individual atom, molecule or molecular fragment can be recorded. One difficulty with time-of-flight mass detection, which is particularly relevant to weakly bound complexes, is to identify whether a spectrum recorded for a particular mass did not in fact arise from a higher species which had fragmented either in the neutral or ionic state.

3.3 Molecular Beams

Room temperature spectra can be very complex as a result of the large number of transitions which can occur from the many rotationally and vibrationally populated levels of the ground state. In order to reduce the number of populated ground state levels, supersonic expansion techniques were developed which cooled the translational, vibrational and rotational degree's of freedom of the molecular samples. A supersonic expansion is achieved by expanding a high pressure sample, either neat or in a carrier gas such as helium or argon, through a small orifice or nozzle into a low pressure region. The cooling achieved in this expansion arises from an approximately isentropic free expansion of the gas through the nozzle during which the random thermal motion is converted into directed mass flow with the result that the translational temperature decreases, while the velocity associated with directed flow increases. In the postnozzle region of the expansion the cold translational bath acts as a refrigerant for the other degree's of freedom via two-body collisions. These collisions generally cool the rotational degrees of freedom more efficiently than the vibrational degrees of freedom. As the expansion proceeds, the density of the gas drops and eventually becomes too low to provide the collisions necessary to connect the internal degrees of freedom with the translational bath, leaving the system in a highly nonequilibrium state. One consequence of the fact that condensation is a much slower process (a three body collision) than rotational or vibrational relaxation is that extensive internal cooling can be achieved before condensation takes place. Supersonic expansions are generally referred to under two titles depending upon whether the flow is collimated by an aperture downstream of the nozzle in which case it is a supersonic molecular beam or not, in which case it is a supersonic free jet.

Supersonic expansions provide the means of preparing an isolated gas phase sample with low internal temperatures and are generally classified by their resultant translational, vibrational and rotational temperatures. The degree of cooling depends on the number of collisions during the expansion which in turn is proportional to the product of the beam density (i.e. reservoir backing pressure) and

nozzle diameter. However, the practical limit to the performance of a supersonic expansion is the requirement for adequate pumping capacity to handle the gas flow through the nozzle. Two techniques have been developed to partially overcome this limitation. The first was due to Campargue [35,36], who developed a method of continuously expanding gases into a relatively high pressure (0.1 – 1 Torr) expansion chamber compared with conventional chamber pressures of 10^{-3} – 10^{-4} Torr. This approach involved the creation of a free jet shock front, where the internal free jet core is protected by a high pressure jet boundary and can undergo cooling collisions. The second approach involved pulsed nozzle sources [37]. In this case the gas flows for only a small fraction of the duty cycle which, if the expansion chamber is sufficiently large, allows the experiment to be performed before any warm background gas is produced. In spectroscopic experiments the limited duty cycle of pulsed nozzles can be a disadvantage but the requirement for pulsed lasers in many cases fixes the duty cycle. Pulsed nozzle sources also have the distinct advantage that significantly higher backing pressures can be employed with a concurrent increase in jet density.

Supersonic molecular beams and free jets have been incorporated into a wide variety of spectroscopic applications. The spectral simplification which results from the small number of populated rotational and vibrational levels can often allow the analysis of spectra (especially rotational structure) which would otherwise be hopelessly complicated in room temperature studies [38]. The 'cold' environment of supersonic expansions also allows the preparation and study of weakly bound or reactive species, such as van der Waals complexes, which are difficult or impossible to generate in any other way.

3.4 Conventional Photoelectron Spectroscopy

Conventional VUV photoelectron spectroscopy (PES) has long been one of the principal techniques for studying atomic and molecular ions. Its origins can be traced back to the independent efforts of the research groups of A.N. Terenin [39] in

Leningrad and D.W. Turner [40] at Imperial College, London to develop the He(I) resonance ionisation source for an electron spectrometer. K. Siegbahn [41,42] developed a similar technique but concentrated on the study of solids using X-rays.

Conventional PES is based on the measurement of the kinetic energy imparted to a photoelectron when an atomic or molecular species is ionised with a fixed energy light source. A conventional photoelectron spectrometer consists of (1) a source of ionising radiation, (2) a means of analysing the kinetic energies of the ejected electrons, (3) an electron detecting and recording system, and (4) a vacuum chamber housing for the spectrometer. In a typical experiment the VUV monochromatic radiation is directed such that it crosses the sample vapour flowing through the chamber. The ejected electrons are then separated according to their kinetic energies and recorded, the resulting spectrum being converted by means of suitable calibrants into electron signal vs. ionisation energy E_I. Photoelectron kinetic energy analysers, however, are unable to precisely measure the kinetic energy of the photoelectron which almost invariably leads to a resolution limit of some 10 meV (80 cm^{-1}). This has, with the exception of H_2^+ [43], D_2^+ [44] and high rotational states of NO^+ [45], precluded the use of PES as a general technique for the investigation of the electronic structure of molecular ions with rotational resolution. On the other hand, vibrational structure is, in many cases, resolvable for small, rigid molecules with vibrational frequencies greater than ~ 100 cm^{-1} [46].

Conventional single photon PES is limited not only by its resolution but also by the fact that it is not a molecule selective technique. This limitation, however, was overcome with the introduction of resonance enhanced multiphoton ionisation photoelectron spectroscopy (REMPI-PES). Combining this with simpler time-of-flight electron energy analysers and pulsed supersonic molecular beams has not only improved the electron energy resolution (~ 5 meV in a study of benzene [47]) but has also allowed vibrational progressions in the photoelectron spectrum to be assigned by tuning the laser to selected intermediate vibrational states [48,49].

3.4.1 Electron Kinetic Energy Analysers

An integral component of a conventional photoelectron spectrometer is the electron kinetic energy analyser. The function of the analyser is to separate the photoelectrons according to their kinetic energies. This ideally requires an analyser with a high collection efficiency and a high resolution. Unfortunately, these are conflicting requirements and a large array of devices have therefore been explored to optimise efficiency and resolution. Electron kinetic energy analysers can be broadly classified into two categories depending upon whether or not the electrons are spatially separated. Analysers which are nondispersive include time-of-flight analysers [49-52] and the relatively simple retarding field analyser [40,53]. However, these have generally been superseded by the improved resolving capabilities of spatially dispersive or deflection analysers such as the parallel plate analyser [54] and the 127° cylindrical analyser [55,56]. These deflection analysers rely on the fact that an electron trajectory in an electrostatic or magnetic field is a function of its kinetic energy. Electrons with different kinetic energies follow different paths and can be focused onto the detector by varying the voltage on the analyser plates.

The resolution of a PE spectrometer is defined as the smallest energy difference between two groups of kinetic electrons which results in separate photoelectron bands in the spectrum. The resolving power $\frac{E_k}{\Delta E}$ of for example, the 127° cylindrical deflection analyser [57], is given by

$$\frac{\Delta E}{E_k} = \frac{W}{2R} \qquad 3.1$$

where R is the radius of the electron trajectory, W is the total slit width of the analyser (entrance plus exit), E_k is the electron kinetic energy and ΔE is the resolution. A typical analyser has a resolving power of around 1000, so an electron with 5 eV kinetic energy has a ΔE_{theor} of 5 meV. If the kinetic energy of the photoelectron, E_k, is reduced by employing a lower energy radiation source then a significant improvement

in resolution can theoretically be achieved. Unfortunately, the drop in the transmission function of the analyser for electrons of low kinetic energy tends to limit this improvement. Recently the popularity of time-of-flight (TOF) analysers has increased, partly because of their simplicity and partly because laser ionisation sources have become more common. These analysers operate on the same principle as TOF mass analysers discussed earlier. In this case the electrons flight time from the ionisation region to the detector is dependant on its initial kinetic energy. The resolution of a TOF analyser is in general improved with a longer flight tube but this also increases the risk of the electrons being scattered and lost. The minimisation of stray magnetic and electric fields along with space-charge effects is very important in both deflection analysers and time-of-flight analysers to achieve good resolution. In addition the source of the ionising radiation and the sample temperature can also affect the experimental resolution.

3.5 Threshold Photoelectron Spectroscopy

Threshold photoelectron spectroscopy (TPES) [58,59] was developed in the late 1960's as an alternative approach to the study of the electronic structure of atomic and molecular ions. As its name implies, it involves the detection of very low energy, or threshold photoelectrons, produced when the energy difference between an ionic and a neutral state is exactly matched by the exciting photon energy. In contrast to conventional PES, the technique requires a tuneable VUV light source and a method of selectively collecting threshold photoelectrons. This ability to tune the excitation source over the valence ionisation region, however, can also lead to the production of a large number of kinetic energy photoelectrons. These kinetic energy electrons are produced both from autoionisation (see chapter 2) and direct photoionisation and must be discriminated against for the technique to be successful. The threshold technique has a number of advantages over conventional PES. Firstly, the energy scale is established absolutely by the photon energy and therefore does not require any calibration gases. Secondly, autoionisation can also produce threshold

electrons in addition to kinetic energy electrons in regions of the spectrum not directly accessible with direct ionisation.

Theoretically the relative intensities of ionic bands observed in TPES can be compared directly since the partial photoionisation cross section, $\sigma_I[h\nu\text{-}E_I]$ (where E_I is the band ionisation energy) is constant over all the ionic bands. This is in contrast to conventional PES where the partial photoionisation cross section is dependent on the energy difference between the ionising radiation and the ionic state. In practice, however, the presence of autoionisation in some molecules can distort direct photoionisation band intensities.

3.5.1 The Development of Threshold Photoelectron Analysers

The reduction in the transmission function of conventional electron analysers, such as deflection analysers, with low kinetic energy electrons, has led to the development of several new detection techniques for threshold electrons. Villarejo and co-workers [58,60] employed a technique whereby all the electrons produced in the ionisation region were accelerated to a fixed energy (~6 eV) and directed towards a cylindrical energy analyser. Threshold electrons were then collected by choosing the analyser pass energy to equal the acceleration energy. However, this method suffered from low transmission and poor resolution (~ 100 meV), due to the detection of some electrons with kinetic energy. Later methods, such as the one developed by Spohr et al. [59], used an angular discrimination method to select only threshold electrons. The sample was ionised in a uniform electrostatic field between a pair of parallel electrodes, the positive electrode of which contained parallel tubular channels which allowed only electrons with velocities parallel to the channels to pass. The uniformity of the electron extraction field led to only electrons with near-zero kinetic energy or with an initial trajectory parallel to the channels being detected. Kinetic electrons with a component of velocity perpendicular to the accelerating field direction were discriminated against. Guyon et al. [61] employed this spectrometer to record the threshold photoelectron spectrum of HF, DF, and F_2

with an experimental resolution of ~12 meV (FWHM) as measured on the $Kr^+ {}^2P_{3/2}$ peak.

These early threshold electron analysers yielded spectra which were complicated by features which corresponded to the detection of electrons with some measure of kinetic energy. The problem stemmed from the existence of a straight line trajectory from the photoionisation region to the detector which led to transmission functions with tails which never went to zero. Typically, a few percent of electrons with as much as 0.05-0.10 eV energy were transmitted. Several techniques were subsequently developed to suppress these non-zero kinetic energy electrons. These arranged either for the detector and the source of the photoelectrons not to be in direct line-of-sight or employed a time-of-flight method to discriminate against the kinetic energy electrons. The approach used by Peatman et al. [62] was to apply a particular set of electrostatic fields in the ionisation chamber to extract only the threshold electrons. With this experimental set-up a threshold spectrum of H_2 was recorded with an experimental resolution of 8 meV (FWHM) as measured on the $Ar^+ {}^2P_{3/2}$ peak [63,64]. An alternative approach by Stockbauer [65] accelerated all the electrons into a drift tube and a 127° cylindrical plate analyser at the end of the drift tube was then tuned to pass electrons which only had the energy provided by the accelerating potential. Although this reduced the kinetic energy electron problem, the spectral resolution was only ~28 meV (FWHM) on the $Kr^+ {}^2P_{1/2}$ peak. An alternative strategy adopted both by Baer et al. [66] and Merkt et al. [26] was to combine angular discrimination with time-of-flight electron discrimination using a pulsed synchrotron excitation source and gating electronics.

A rather different approach to the detection of near-zero kinetic energy electrons is to use scavenger molecules such as SF_6 and $CFCl_3$. These molecules have a high cross section for electron attachment at near-zero energy [67,68] and when combined with a mass spectrometer tuned to the appropriate anion mass peak (SF_6^- for example) can serve as a threshold electron detector. This technique has been employed on studies of argon and nitrogen [69].

A novel method of detecting threshold photoelectrons was developed by Cvejanovic and Read in electron impact studies [70]. They incorporated a small penetrating electrostatic field which produced a saddle point in the potential distribution within the collision region. This had the effect of collecting the threshold electrons over a very large solid angle (~4πsr) and directing them towards a 90° cylindrical deflection analyser. The technique was found to be very efficient for the collection of electrons between 0 and 3 meV whilst also discriminating against those of higher energy. This basic idea has been further developed by King et al. [71] to include a 127° cylindrical deflection analyser and an electrostatic lens system to match the penetrating field stage to the cylindrical deflection analyser. A resolution of 17 meV (FWHM) was achieved on the $Ar^+ {}^2P_{3/2}$ peak, but was limited by the photon resolution [71]. This design was subsequently improved by Hall et al. [72] with the addition of a more complex electrostatic twin-lens system, yielding a resolution of ~6 meV.

3.5.2 The Threshold Photoelectron Spectrometer Based at the Daresbury Synchrotron Radiation Laboratory

A collaboration between The University of Edinburgh Chemistry Department, The Daresbury Synchrotron Radiation Laboratory and The University of Manchester Physics Department, has led to the design and construction of a threshold photoelectron spectrometer for use with synchrotron radiation. The design is based on the penetrating electrostatic field method of collecting threshold electrons, developed by Cvejanovic and Read [70] and improved by King et al. [71]. A schematic diagram of the overall experimental set-up is shown in Figure 3.3. The spectrometer containing the electron optics is housed within a cylindrical stainless steel vacuum chamber, mounted on a 3500 ls^{-1} ADP cryopump which can be isolated using a gate valve. Two layers of mu-metal within the chamber shield the spectrometer from external magnetic and electric fields. Beamline 3.2 of the Daresbury Laboratory Synchrotron Radiation Source (see section 3.5.4) provides the

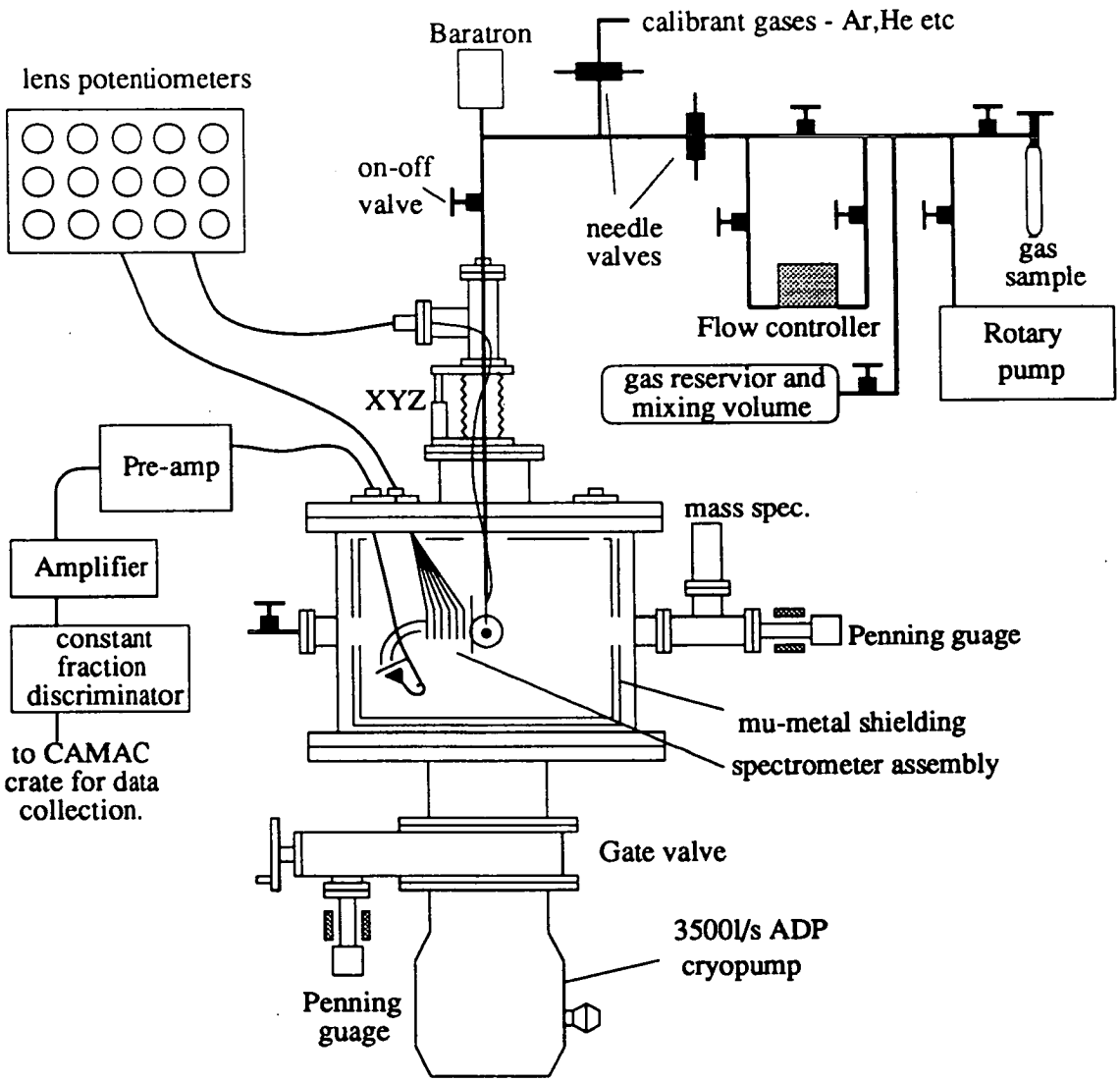

Figure 3.3

A schematic diagram of the overall experimental set-up of the threshold photoelectron spectrometer based at the Daresbury laboratory.

VUV radiation which is wavelength dispersed by a 5 m monochromator (0.3 Å (FWHM) nominal band pass based on beamline literature). The radiation enters the spectrometer through a 2 mm inner diameter glass capillary which forms the differential pumping interface between the spectrometer and the monochromator. The spectrometer is connected to the post monochromator mirror box by a flexible evacuated bellows assembly surrounding the capillary.

A schematic diagram of the electron spectrometer is shown in Figure 3.4. The spectrometer can be separated into two sections; the first contains the interaction region, while the second contains the collection optics which direct the threshold electrons to the detector. The interaction region contains the sample gas beam, photon beam and penetrating field, all of which are directed perpendicularly. The electrically isolated platinum needle (0.8 mm internal diameter) acts as the gas nozzle, producing an effusive beam at 90 degrees to the photon beam and directed into the cryopump. The position of the needle can be externally adjusted with an X-Y-Z translator to allow the effusive beam position to be optimised with respect to the photon beam. This adjustment is also required to minimise the spurious generation of electrons from the metal surface of the nozzle. A potential can be applied to the needle, when necessary, to eliminate local patch fields and fields due to contact potentials. The glass capillary which directs the VUV radiation into the spectrometer and is coated in graphite to reduce charge build up, stops approximately 40 mm short of the interaction region. The intensity of the VUV radiation is measured by recording the current produced by a copper grid placed in the path of the photon beam. The gas sample, which generally consists of a mixture of argon and the molecule of interest, is held in a large mixing volume. The mixture is delivered into the vacuum chamber at a pressure of typically ~200-300 Torr via a needle valve which controls the flow rate and chamber pressure. Typical chamber pressures are therefore of the order of ~ 10^{-5} Torr as measured on an ion gauge. To counteract the radiative cooling effect of the cryopump on the gas needle, the chamber is heated to approximately 100 °C. This maintains the needle at approximately 30 °C as measured on a temperature probe situated approximately 3 cm from the needle opening. The

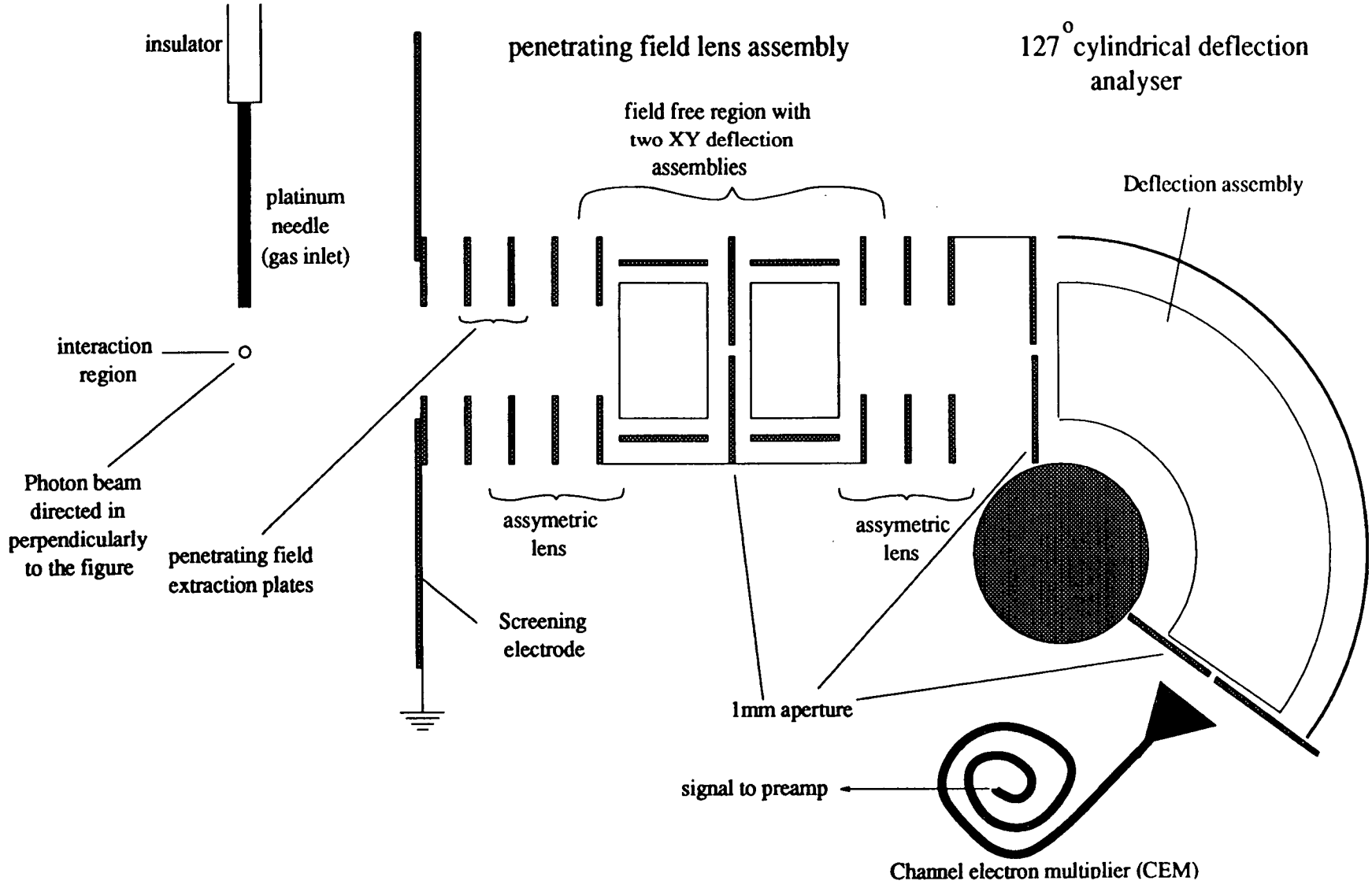

Figure 3.4 A schematic diagram of the interaction region and threshold electron collection optics within the threshold photoelectron spectrometer.

beam temperature is estimated to be of the order of 235 K based on hot-band structure found in the TPE spectrum of the $X\ ^2\Pi_{g,3/2}$ state of bromine.

The electrostatic lens system, 127° cylindrical deflection analyser and electron detector are shown in Figure 3.4. A potential well is formed in the interaction region from the penetration of the field produced by the extraction electrode through a grounded screening electrode. Figure 3.5 shows near threshold (2 meV) electron trajectories calculated by SIMION along with the equipotential contours which demonstrate the effect of the penetrating field. The field gradient in the interaction is calculated to be approximately 150 meV/cm. The field extracts the low-energy photoelectrons over a very large solid angle (~4πsr) and focuses them onto a crossover point at the entrance to the spectrometer which then acts as a point source for the lens system. A typical voltage on the extraction electrode is ~ 40 V. The electrostatic lens system contains two, triple-aperture asymmetric lenses with a spacing to bore ratio (A:D) of 0.5 where D equals 5 mm. The first lens images the crossover point from the extraction stage onto the intermediate 1 mm aperture, while the second lens images the intermediate aperture onto the 1 mm entrance aperture of the cylindrical deflection analyser (CDA). The advantage of this twin lens system is that the transmitted electron trajectories are well defined thereby leading to the strong suppression of unwanted energetic electrons. The 127° CDA acts as a high energy electron filter, removing any fast electrons which have initial trajectories along the axis of the lens system and would otherwise lead to the production of a high energy tail on the electron signal. The CDA is generally operated with a pass energy in the region of 2 eV and the transmitted electrons detected using a channel electron multiplier (Mullard X919/BL01). The electron signal is amplified before being fed into a constant fraction discriminator to reduce background noise. The signal is then fed into a CAMAC crate on the beamline. A personal computer on the beamline is used to provide control over the experimental timing and monochromator and also to store the incident photon energy, flux and detected electron counts.

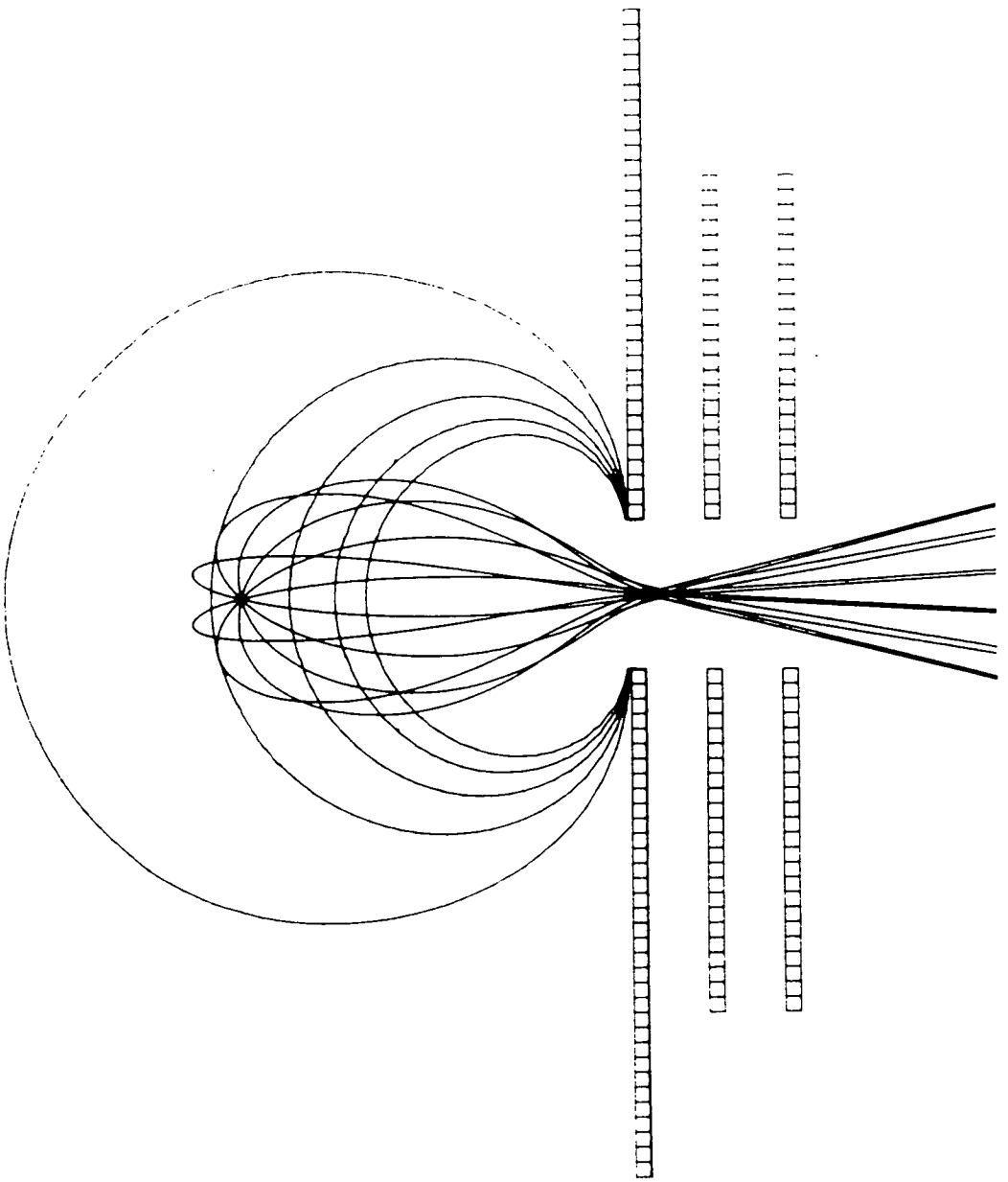

Figure 3.5

Schematic diagram demonstrating the effect of the penetrating field within the interaction region. Near threshold (2 meV) electron trajectories calculated by SIMION along with the equipotential contours are shown. Both the extraction electrodes were at 5 V.

3.5.3 Performance of the Threshold Photoelectron Spectrometer

The performance of the threshold photoelectron spectrometer was tested using argon whose threshold photoelectron spectrum is simple and has well known photoionisation cross sections. The removal of a p electron from the filled outer $3p^6$ orbital of the argon atom forms two spin-orbit ionic states, the $^2P_{3/2}$ and $^2P_{1/2}$ states. Converging on both ionic thresholds are a number of Rydberg series including a strong s series and a weaker d series. Various members of the *n*s Rydberg series converging on the $^2P_{1/2}$ ionic threshold (specifically $n \geq 11$) are found above the $^2P_{3/2}$ ionic threshold and can autoionise into the lower lying $^2P_{3/2}$ ionic state. This leads to the emission of electrons with kinetic energies equal to the difference in energy between the Rydberg level and the $^2P_{3/2}$ ionisation threshold (i.e. 3, 38, 62, 81 meV for the 11s, 12s, 13s and 14s Rydberg states) [73]. The TPE spectrum shown in Figure 3.6 was recorded with the threshold spectrometer tuned to collect these low kinetic energy electrons and clearly shows the presence of these autoionising Rydberg states. The ability of the spectrometer to suppress these low kinetic energy electrons is therefore a good test of its performance. The threshold spectrum shown in Figure 3.7 demonstrates the high performance of the penetrating field electron spectrometer. Threshold electrons are produced as the photon energy is scanned over the $^2P_{3/2}$ and $^2P_{1/2}$ states of Ar^+ at 15.759 eV and 15.937 eV [73] respectively. A very weak peak at 15.797 eV is also present in Figure 3.7 which corresponds to the 12s autoionising Rydberg state. Almost no evidence of any higher energy electrons is found. The 11s autoionising state, which lies just 3 meV above the $^2P_{3/2}$ ionic state, cannot be resolved from the direct ionisation peak by the spectrometer. Consequently, the observed $^2P_{3/2}$ ionic state peak intensity is composed of contributions from both the 11s Rydberg state and the direct photoionisation peak which explains why the ratio of the heights of the two peaks is ~ 9:1 and not the expected statistical weight ratio of 2:1. On average, count rates of around 300,000 counts/s were observed on the $^2P_{3/2}$ peak and a resolution of ~ 11 meV (FWHM) was measured on the Ar^+ $^2P_{3/2}$ peak.

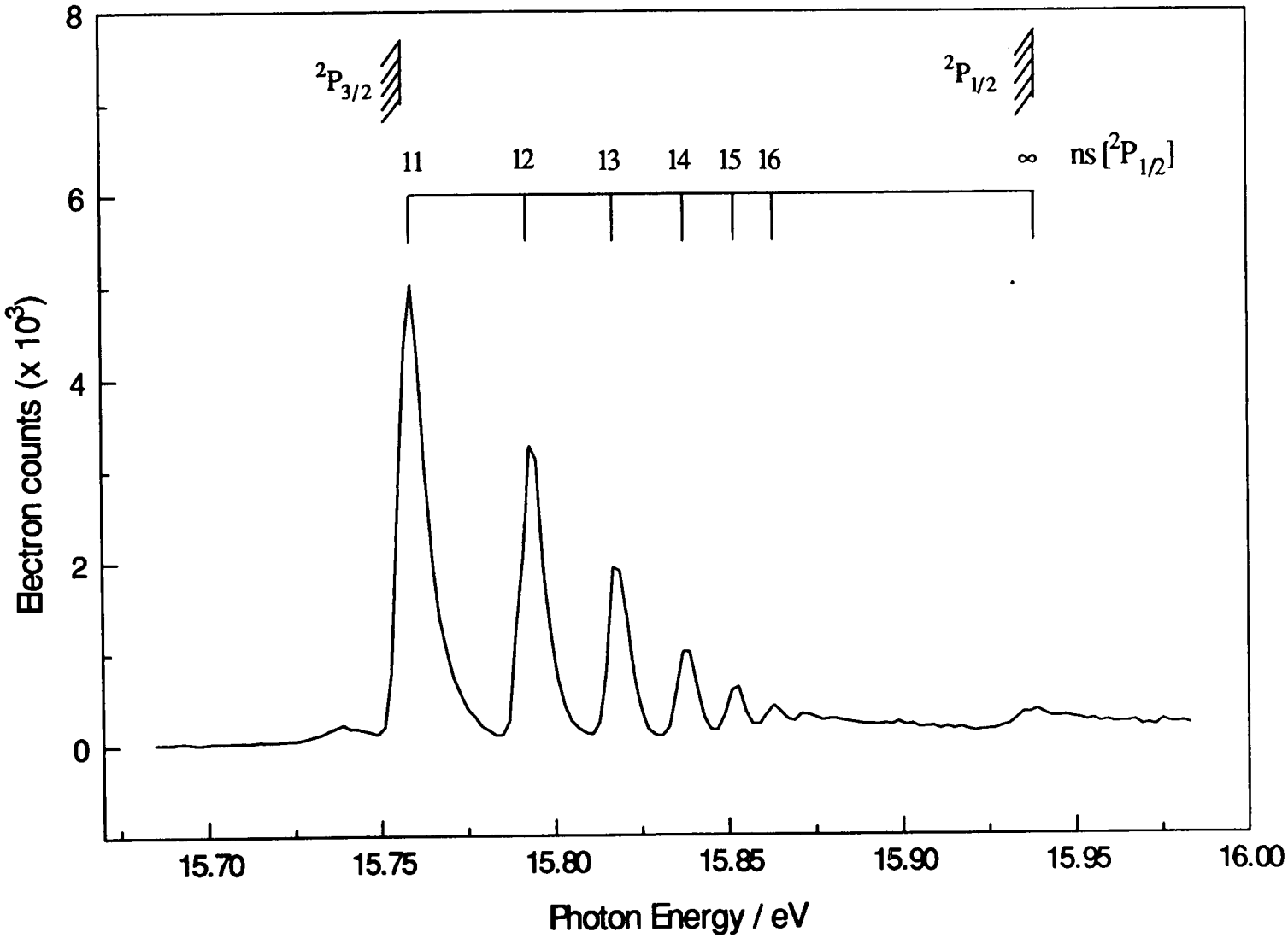

Figure 3.6 A threshold photoelectron spectrum of argon with the spectrometer tuned off threshold. The extra structure between the two ionic thresholds (shown) results from the autoionisation of neutral Rydberg states converging on the higher spin-orbit state with the subsequent production of kinetic energy electrons.

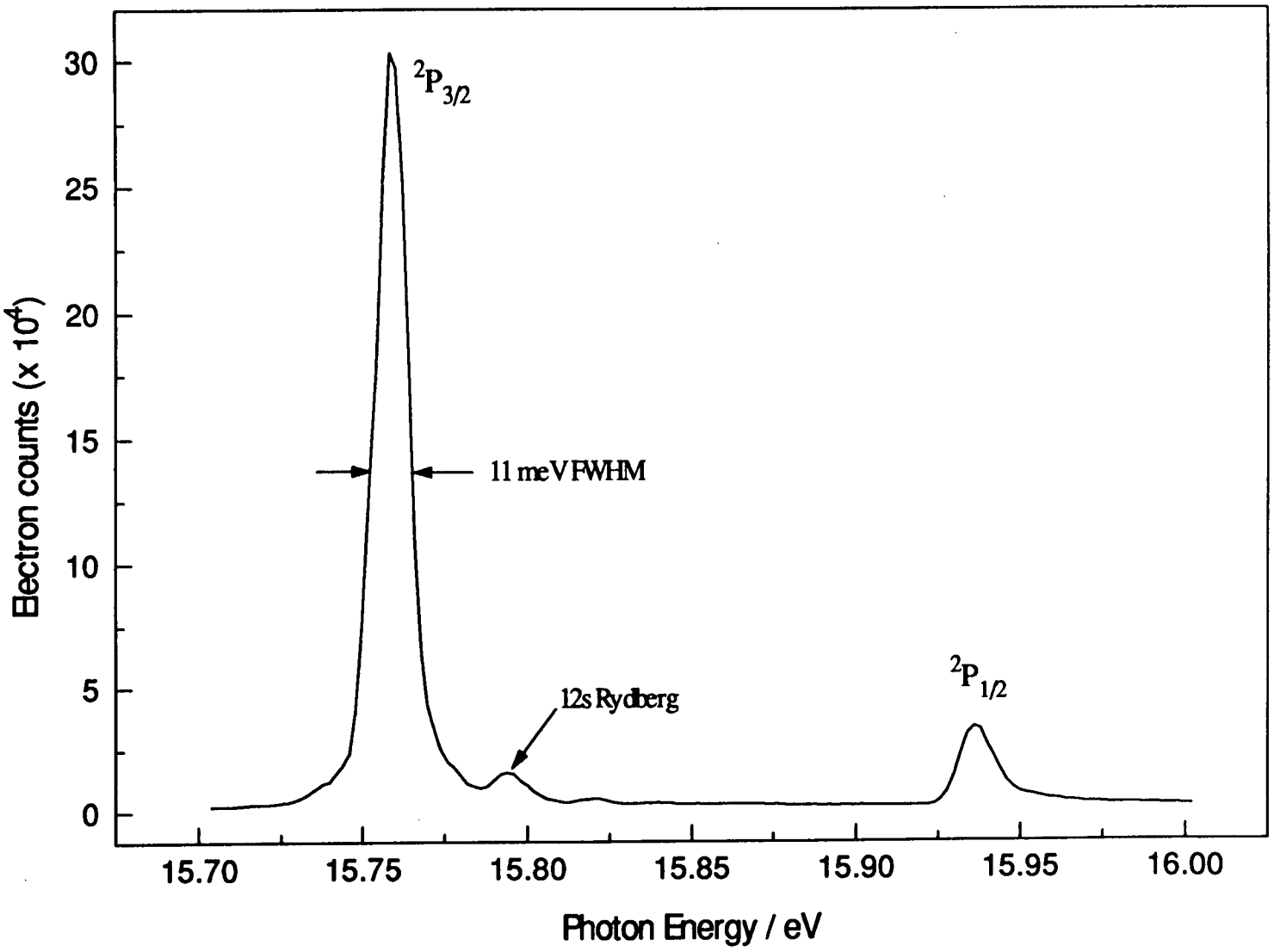

Figure 3.7 A threshold photoelectron spectrum of argon with the spectrometer tuned to collect threshold electrons. Only a weak autoionising peak at 15.779 eV is observed, demonstrating the efficiency of the spectrometer.

Optimisation of the spectrometer on the argon threshold peak is a fairly complex task. Nineteen individual potentials are required to operate the spectrometer and optimisation is therefore achieved by tuning the monochromator to the $Ar^+ {}^2P_{3/2}$ peak at 15.579 eV and continuously adjusting the potentials while monitoring the electron count rate. The spectrometer is successively tuned to lower photon energies until the peak intensity drops. This ensures that optimisation is occurring on the threshold electrons and not the 3 meV electrons. After each optimisation a scan is recorded to check the resolution.

The electron energy resolution of the threshold photoelectron spectrometer is ultimately limited by the photon bandwidth achieved from the 5m monochromator. All the TPE spectra were recorded with a photon bandwidth of ~0.3Å, which on the argon $^2P_{3/2}$ peak at 15.579 eV results in a photon bandwidth of ~6 meV. The photon flux is a function of both the decay of the synchrotron current and the wavelength and as such all spectra are corrected to take account of these factors. All the threshold photoelectron spectra were energy calibrated by recording the threshold photoelectron spectrum of the lowest ionisation threshold in helium, neon, argon, krypton and xenon [73].

3.5.4 The Daresbury Synchrotron Radiation Source

The VUV radiation employed in the threshold photoelectron study of the halogens was supplied by the Synchrotron Radiation Source (SRS) located at the Daresbury Laboratory. The Daresbury Laboratory SRS was the world's first high energy electron accelerator dedicated to the production and utilisation of synchrotron radiation. It is a 2 GeV electron storage ring which consists of dipole magnets to bend the electron orbit, quadrupole magnets to focus the electrons, and a radio frequency accelerating system to replace the energy the electrons emit as synchrotron radiation. In order to prevent the electrons being scattered out of orbit they circulate within an ultra-high vacuum system. A schematic diagram of the ring and accelerators is shown in Figure 3.8. The storage ring, booster synchrotron and injection system

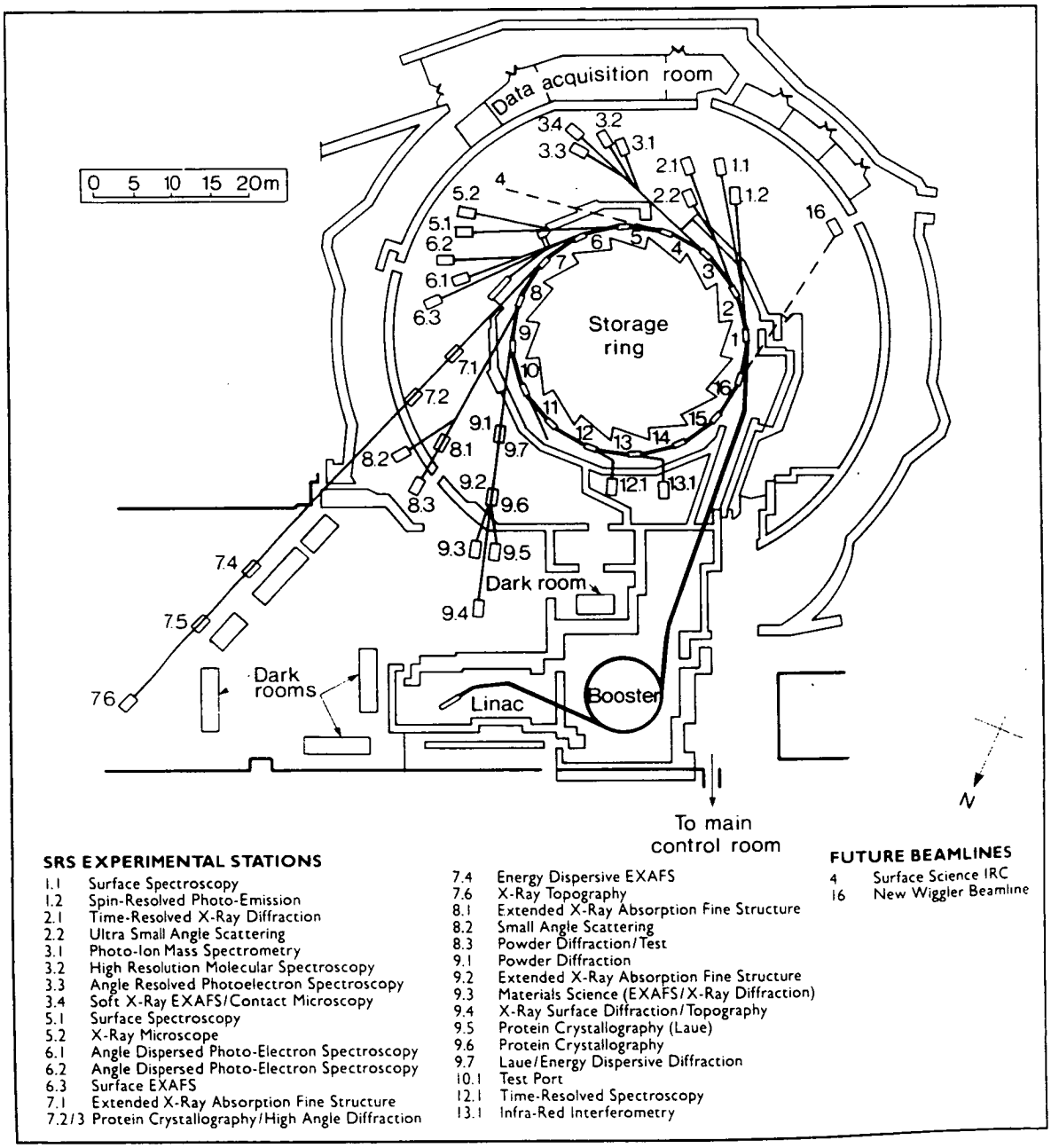

Figure 3.8

Schematic diagram of the Daresbury synchrotron radiation laboratory, including booster synchrotron and beamlines. Beamline 3.2 is shown in red.

are all controlled by a computer system. The electrons for the ring are provided by an injection system comprising a linear accelerator and a booster synchrotron. The linear accelerator consists of a hot cathode which emits electrons. These are subsequently accelerated to 12 MeV in two stages before entering the booster synchrotron where they are accelerated up to 600 MeV. The storage ring accumulates electrons from the injection system, accelerates them to a peak energy of 2 GeV, and then keeps them orbiting for approximately 12 hours. The circulating electron beam is not strictly continuous. It consists of 160 discrete bunches of electrons, but since the orbital period of any electron bunch is 320 ns, for most experiments it is considered quasi-continuous. The synchrotron radiation is directed down sixteen beamlines on the storage ring to the experimental stations. The beamlines are numbered by reference to the particular magnet from which they originate and are subsequently split further to supply more experimental stations. Each beamline includes a shutter to block off the radiation when not required, and a mirror to focus the light into the station.

Beamline 3 at the Daresbury Laboratory Synchrotron Radiation Source is designed to produce radiation in the VUV and soft x-ray region. Station 3.2 is set up to carry out high resolution molecular spectroscopy and is equipped with a high resolution 5 m monochromator to achieve a narrow bandpass in the region between 9 and 35 eV. Radiation emerging from the "bending magnet" on the ring is split and focused, using two pre-monochromator mirrors, onto the entrance slit of the monochromator. The normal incidence monochromator has a 5 m radius of curvature, is vertically dispersing with a ruling density of 1200 lines/mm. This gives it a resolving power of approximately 20,000. However, in practice the experimental resolution of the monochromator is defined by the widths of the entrance and exit slits which is usually set to compromise between photon flux and photon resolution [74]. A post-monochromator mirror is attached to the exit port of the monochromator to control the beam of radiation entering the experimental apparatus. It also forms a stage of differential pumping between the experimental apparatus and the monochromator. This allows the experimental apparatus to be operated at the high pressures required for gas phase experiments whilst ensuring low pressures in the

mirror chamber and monochromator. Scanning of the monochromator is controlled by the station computer. The monochromator and its performance have been described previously by Holland et al. [75].

3.6 Zero Kinetic Energy (ZEKE) Photoelectron Spectroscopy

In 1984 Müller-Dethlefs and co-workers developed zero kinetic energy photoelectron spectroscopy (ZEKE-PES), a laser based technique [76] with a resolution almost two orders of magnitude better than conventional PES [77]. The technique is based on the collection of zero kinetic energy photoelectrons, similar to that employed in threshold photoelectron spectroscopy [58], but uses the high resolution capabilities of laser sources and a novel method of discriminating against kinetic energy electrons to obtain wavenumber resolution.

The underlying mechanism behind zero kinetic energy photoelectron spectroscopy is that a photoelectron of exactly zero kinetic energy (ZEKE) is produced when there is an exact correspondence between a photon of energy $h\nu$ and the energy separation between an ionic state and a molecular state. If, however, the energy match is not exact, i.e. the photon energy exceeds the energy separation, then the ejected (non-ZEKE) photoelectron acquires a kinetic energy. By virtue of the fact that ionisation is carried out in a field-free environment, the ZEKE electrons remain where they were formed whereas the non-ZEKE electrons, which have a kinetic energy and are formed simultaneously with the ZEKE electrons, move away. After a suitable time delay, a draw out field is applied and both the ZEKE and non-ZEKE electrons are accelerated into a field free drift tube. This transforms the spatial separation of the electrons into a time-of-flight separation and allows selective detection of the ZEKE electrons. If the delay is extended beyond a certain limit all the non-ZEKE electrons will have left the ionisation region, leaving only the ZEKE electrons to be detected when the drawout field is applied.

In an early ZEKE experiment on NO a discrepancy of 2.7 cm^{-1} was found between the ionisation energy of NO obtained from Rydberg extrapolations and that measured from the ZEKE spectrum [77]. The magnitude of the discrepancy was very small when compared with the margins of error which usually accompanied ionisation energies determined in PES, but indicated that something was wrong either in the theory behind ZEKE or in the experiment. The original mechanism involving the generation of ZEKE electrons [76] had always assumed that the lifetime of high lying Rydberg states a few wavenumbers below the ionisation threshold in molecular systems was much shorter than the field free delay time (of the order of microseconds), and therefore that the Rydberg state population would have decayed completely prior to the application of the draw-out field. However, evidence was provided by Reiser et al. [78] that there were indeed Rydberg states with long lifetimes (up to 10's of microseconds), a few cm^{-1} below the ionisation threshold. It turned out that these Rydberg states, which have very high principal quantum numbers (n>~150) and converge to rovibronic states of the ion, were in fact providing the major source of the observed electron signal, rather than the true ZEKE electrons. A correction therefore had to be applied to the measured ionisation energy to account for the energetic shift imposed by the pulsed field ionisation of the high-n Rydberg states. This correction was given by the classical equation $\Delta E(cm^{-1}) = 6\sqrt{F(V/cm)}$ (where F is the applied field in V/cm) describing field ionisation [79] and allowed the true (field free) ionisation energy to be determined. The new mechanism has now been incorporated into the title of the technique; zero kinetic energy pulsed field ionisation (ZEKE-PFI) photoelectron spectroscopy. To date, these long lived Rydberg states have been found in all atoms and molecules which have been investigated using this technique [80]. The detection of true ZEKE electrons is now only being employed in photodetachment studies of anions which do not have Rydberg states [81-84].

The essential simplicity of the technique has meant that most ZEKE-PFI spectrometers are very similar in design to REMPI-TOF spectrometers. The only real difference which arises as a result of the analysis of electrons rather than ions is the

employment of mu-metal shielding around the flight tube to minimise stray electric and magnetic fields which could disturb the path of the electrons. However, certain groups have dispensed with this shielding altogether and with short flight tubes have still managed to record ZEKE-PFI spectra [85]. ZEKE-PFI spectrometers generally contain pulsed supersonic molecular beams and only differ in the length of the electron flight tube and the ionisation scheme. A variation on this theme has recently appeared which incorporates a magnetic bottle electron spectrometer to direct the electrons down the flight tube [86]. This spectrometer contains a 1 T permanent magnetic field which contrasts dramatically with the minimal stray magnetic fields found in most ZEKE-PFI spectrometers. However, it has been shown to give results identical to those obtained on conventional ZEKE-PFI spectrometers.

3.6.1 Mass Analysed Threshold Ion (MATI) Spectroscopy

A general disadvantage of the detection of electrons rather than ions is the absence of mass information. Mass information can be useful in systems such as clusters where an unambiguous identification of the ionised species is required or in systems which fragment [87]. In 1991, Zhu and Johnson [88] developed a technique known as mass analysed threshold ion (MATI) spectroscopy which allowed a mass resolved ion spectrum to be recorded. It was based on the same principles as ZEKE-PFI (i.e. the delayed pulsed field ionisation of high Rydberg states) but detected the ions produced rather than the electrons. The problem in this case is to separate the high-n Rydberg excited molecules from the prompt photoions produced in the laser pulse. This is significantly more difficult than separating kinetic electrons from PFI electrons, because the promptly formed ions cannot escape from the ionisation region during the delay prior to the application of the extraction pulse. The solution to this problem was to apply a small electric field directly after the laser excitation pulse to spatially separate the high-n neutral Rydberg excited molecules from the promptly formed photoions. In the experiments of Zhu and Johnson a series of four grids with individual potentials were employed. These served to 1) separate the prompt ions from the high-n neutral Rydberg excited molecules, 2) field ionise the spatially

separated long lived Rydberg excited molecules and 3) accelerate all the ions into an in line time-of-flight mass spectrometer. Selective detection of the pulsed field ionised high-n Rydberg molecules could then take place by gating on a specific ion signal in the time-of-flight spectrum. As in ZEKE-PFI experiments the individual fields employed to separate the prompt photoions and Rydbergs had to be taken into account when correcting for field ionisation shifts. The observed resolution achieved by Zhu and Johnson in a study of pyrazine was between 5 and 10 cm^{-1}. However, since then Dietrich et al. [89] have improved the resolution such that it is now comparable to that achieved when detecting electrons. Alternative methods of separating the prompt photoions from the long lived Rydberg excited molecules have also been developed, including the employment of magnetic fields by Nemeth et al. [90] and a method based on energy selection in the reflecting electrostatic field of a linear reflectron mass spectrometer [91].

The MATI technique is therefore the first technique which allows the unambiguous assignment of the ionic spectrum of an individual molecule or atom. It also has the advantage that in a single colour ionisation scheme it is capable of recording simultaneously an ionic spectrum of not only the parent molecule but also its complexes.

3.6.2 The Field Ionisation Mechanism

Both the ZEKE-PFI and MATI techniques rely on the field ionisation of long lived Rydberg states which as we have seen necessitates a correction to be made to the measured ionisation energy to take account of the applied field. Initially, the shift $\Delta E(cm^{-1}) = 6\sqrt{F(V/cm)}$ was applied universally to obtain the field free ionisation energy. However, interest has recently been focused on whether this adiabatic classical description of field ionisation is correct in the high-n (n>~150) region or whether a diabatic mechanism would be more appropriate.

The ionisation of Rydberg excited atoms by means of an externally applied electric field has for a long time attracted considerable theoretical and experimental interest [92]. Field ionisation in atoms is now fairly well understood and has become an invaluable experimental technique for the detection and study of atomic Rydberg states up to approximately n=100 [93-95]. However, the field ionisation of Rydberg states in molecules is far more complex and has only recently been considered [96,97]. In principle, there are two mechanisms through which Rydberg states can field ionise; an adiabatic and a diabatic mechanism [92]. However, the electric field dependence of each mechanism is different and it is therefore important to define the mechanism applicable to individual molecules to allow an accurate extrapolation of the ionisation threshold to the field free limit.

The classical way of considering field ionisation is the simple "saddle point" model. In the absence of an external field, the long-range potential for a Rydberg electron is Coulombic. This is shown schematically in Figure 3.9 and can be expressed as

$$V(z) = \frac{e}{4\pi\varepsilon_o z} \qquad 3.2$$

where z describes the distance of the Rydberg electron from the core. The introduction of a uniform external electric field, F, in the direction z, adds an additional term to the long-range potential such that the new potential, shown schematically in Figure 3.9, is expressed by

$$V_F(z) = \frac{e}{4\pi\varepsilon_o z} + Fz \qquad 3.3$$

V_F has a maximum on the applied field axis at $z = \sqrt{\frac{e}{4\pi\varepsilon_o F}}$ which is actually a saddle point and occurs at an energy

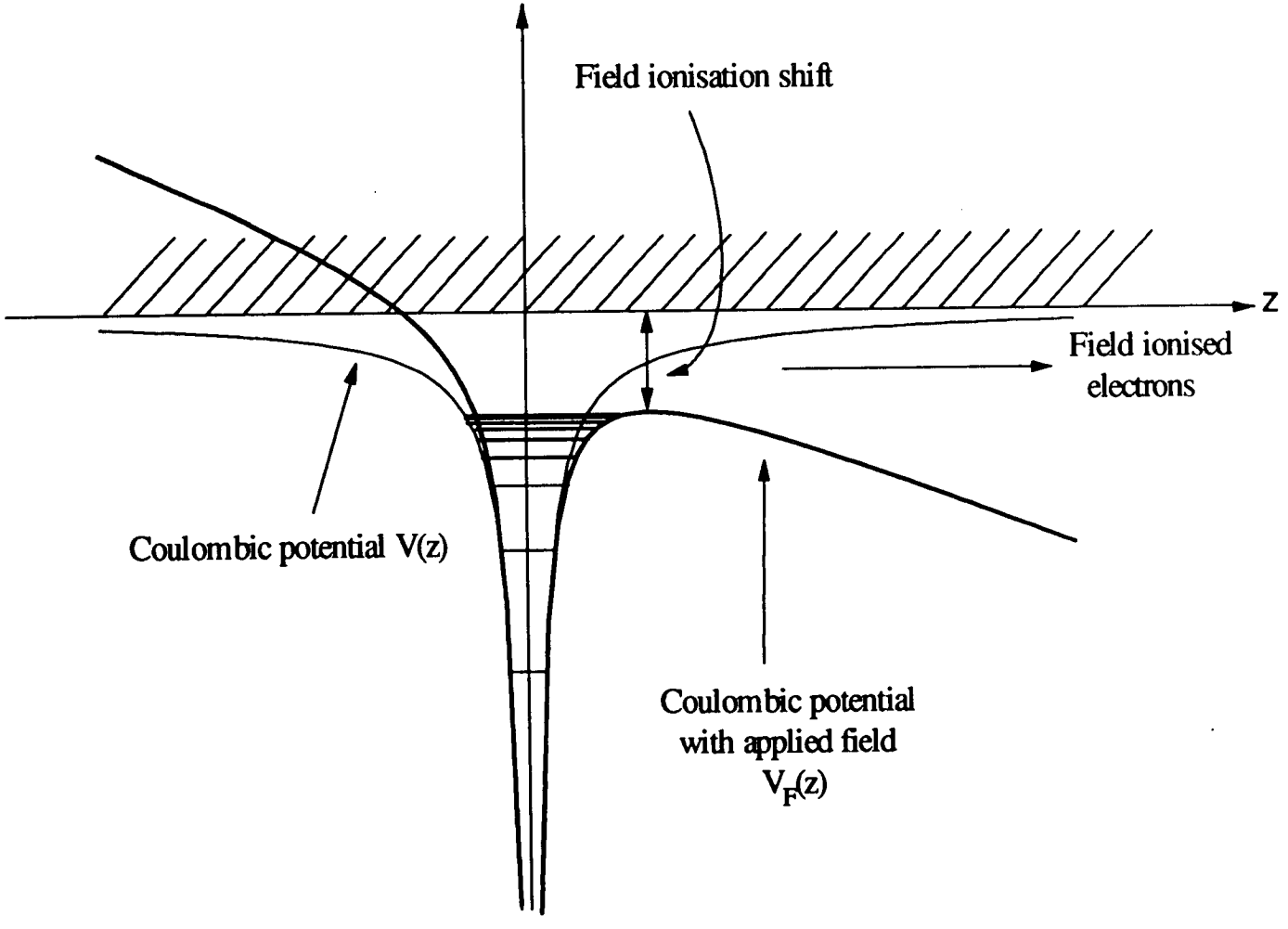

Figure 3.9 A schematic diagram of the pulsed field ionisation process in which high principle quantum number Rydberg states are field ionised by an applied potential. The shift in the ionisation energy is shown.

$$E_{sp} = 2\sqrt{\frac{e^3 F}{4\pi\varepsilon_o}} \qquad 3.4$$

below the asymptotic field free ionisation threshold. Classically ionisation of a Rydberg electron in a specific orbital will only occur if the applied field is large enough to lower the saddle point below the electrons binding energy resulting in a sharp ionisation threshold that is shifted from the field free value by the amount

$$\Delta E(cm^{-1}) = -6\sqrt{F(V/cm)} \qquad 3.5$$

The result of the classical model is equivalent to the shift expected from the adiabatic field ionisation mechanism and has been verified in a number of studies involving different atoms and molecules [79,98,99].

In practice when an atom or molecule is subjected to an electric field, every Rydberg state, n, is split into $\sim n^2$ Stark states, which are individually defined by their quantum numbers [92]. As the applied field is increased, the separation between individual Stark states increases as shown in Figure 3.10. When individual Rydberg states are energetically well separated as is the case for low n Rydberg states, the Stark manifolds associated with each Rydberg state do not overlap unless very large electric fields are applied. In this diabatic description of field ionisation the initial Rydberg state can evolve along a number of paths to the classical field ionisation limit. Two critical electric fields, E_L and E_U, (as shown in Fig. 3.10) are required to take account of the lowest and highest energy members of the Stark manifold [100] and the corrections required to account for the shifts in the ionisation threshold have been calculated to be in the range $4.6\sqrt{F(V/cm)}$ to $3.1\sqrt{F(V/cm)}$. In principle, this means that the diabatic process does not have a sharp threshold. Chupka [100], however, noted that the critical fields for the different members of a given Stark manifold are clustered together resulting in a field dependence of

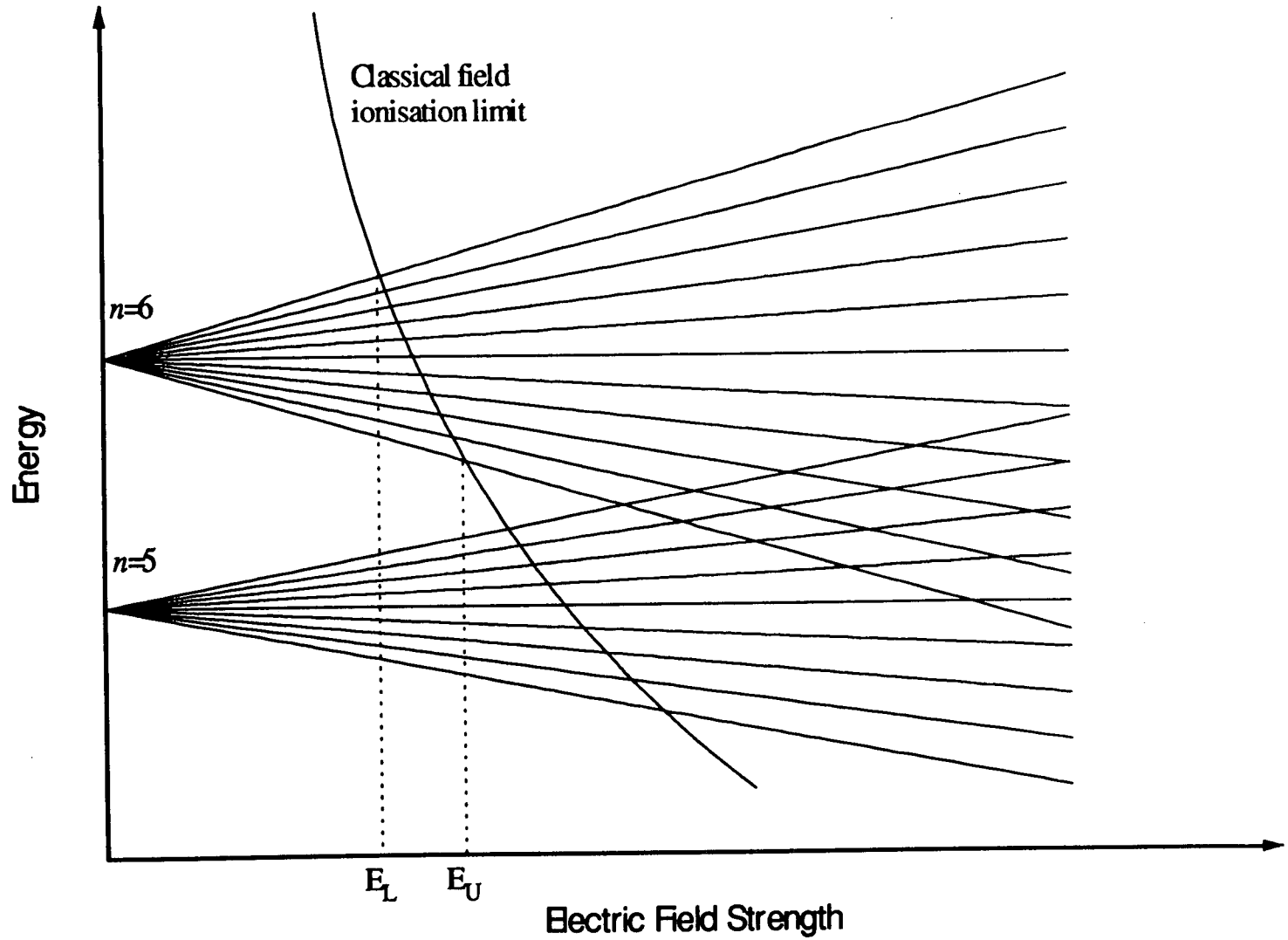

Figure 3.10 The Stark states of the n=5 and n=6 Rydberg states of a hypothetical molecule, indicating the increased Stark splitting with increasing field. The classical field ionisation limit is indicated along with the two field strengths (E_L and E_U) required to take account of the two extreme field ionisation paths in the n=6 Stark manifold.

$$\Delta E\ (cm^{-1}) \approx -4\sqrt{F(V/cm)} \qquad 3.6$$

If, on the other hand, Rydberg Stark manifolds overlap, as is found in the region of high-n Rydberg states populated in ZEKE-PFI, then there is the possibility that individual Stark states from the different manifolds can form avoided crossings. The magnitude of these avoided crossings then controls the field ionisation mechanism. The magnitude is dependant on the quantum defect of the Rydberg level (the higher the quantum defect the larger the avoided crossing) and the rise time of the extraction pulse. In general a slowly rising extraction pulse will cause the initially prepared Rydberg state to traverse the avoided crossings adiabatically before field ionisation occurs. This is consistent with the simple classical formulation of $\Delta E(cm^{-1}) = -6\sqrt{F(V/cm)}$. In contrast a fast rise time and/or a very small or zero avoided crossing results in a diabatic passage and a field ionisation shift of $\Delta E\ (cm^{-1}) \approx -4\sqrt{F(V/cm)}$. These two possible mechanisms are shown schematically in Figure 3.11.

It is impossible to predict which field ionisation mechanism will apply to individual molecules and it is therefore essential that a plot of the observed peak position vs. $\sqrt{F(V/cm)}$ is made to allow the relevant shift to be determined. A diabatic ionisation mechanism will be characterised by a significantly smaller slope than an adiabatic ionisation mechanism. Ideally a series of ZEKE-PFI spectra should be recorded under identical experimental conditions for a range of extraction fields. However, identical experimental conditions are very difficult to achieve and only recently has a solution to this problem been found by Lindner et al. [101]. They employed an extraction pulse with a multi-step "staircase slope", in which the measured ZEKE-PFI signals correlate with the different field strengths in each step thereby allowing the field ionisation shift to be determined in a single scan.

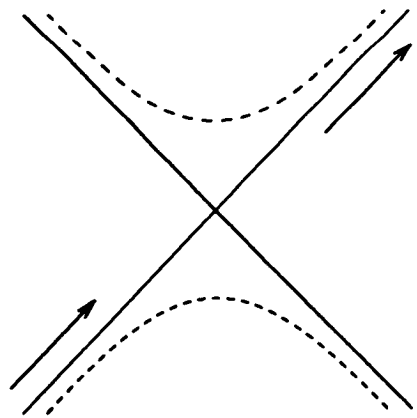

A fast rising extraction pulse and/or
a very small or zero avoided crossing
results in diabatic field ionisation

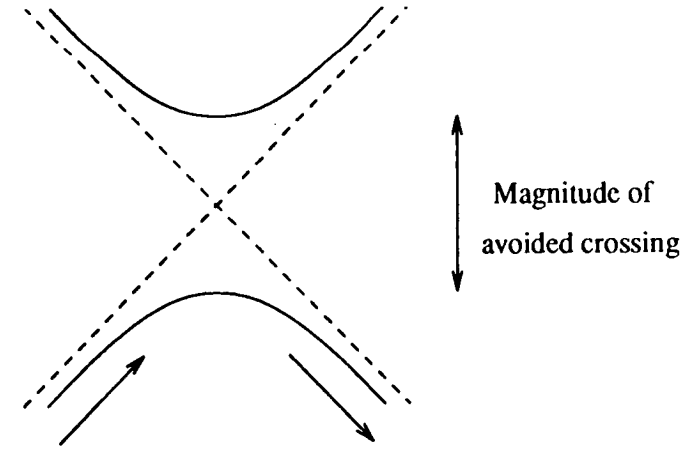

A slowly rising extraction pulse
forces the Stark state to follow the avoided crossing
and results in adiabatic field ionisation

Figure 3.11 A schematic diagram of the two possible paths Stark states can take when they reach an avoided crossing. Which of these paths is taken depends on the rise time of the extraction pulse and the magnitude of the avoided crossing and dictates the field ionisation mechanism.

3.6.3 The Determination of the Field Ionisation Shift Applicable to I_2

In order to determine the field free adiabatic ionisation energy of molecular iodine, the field ionisation shift has to be calculated. The excitation scheme, which is discussed in more detail in chapter 5, involves a two-photon transition into v=1 of the $[^2\Pi_{3/2}]_c$ 7s; 2_g Rydberg state and then one further photon into v^+=1 of the X $^2\Pi_{3/2,g}$ state of the ion. To evaluate the field ionisation shift, ZEKE-PFI spectra of the v^+=1 band were recorded with extraction potentials ranging from ~7 V/cm to ~1 V/cm with a delay of 580 ns. All the ZEKE-PFI spectra of the v^+=1 band are shown in Figure 3.12. As expected, the spectra show different peak positions and intensities depending on the extraction potential employed. The spectrum of the v^+=1 band of the X $^2\Pi_{g,3/2}$ state of I_2^+ recorded with the largest pulse amplitude (~7 V/cm) shows a broad peak centred to the red of the field free ionisation threshold (indicated by the dotted vertical line). As the magnitude of the potential is reduced, the width of the v^+=1 band is reduced and its position shifts towards the field free ionisation limit. These changes in the peak are understood when it is realised that the magnitude of the extraction potential controls the depth of Rydberg states below the field free ionisation limit, from which electrons are detected. The larger the potential, the greater the depth of Rydberg states field ionised and the wider and more intense the ZEKE-PFI band. The vibrational band peak positions measured in Figure 3.12 were plotted against $\sqrt{F(V/cm)}$, as shown in Figure 3.13. A linear fit of this data resulted in a slope of -1.6 ± 0.3 which is significantly lower than either the diabatic value of ~4, or the adiabatic value of ~6. The quoted error in the peak positions for I_2 in chapter 5 are ± 2 cm^{-1}. However, in this case the pump laser was fixed throughout all the scans and the same region of the ionic spectrum was recorded as the potential was varied. It is therefore felt that an error of this magnitude is inappropriate in this situation. It should however be noted that there are errors present, in for example the exact measurement of the extraction potentials, although it is very difficult to quantify them.

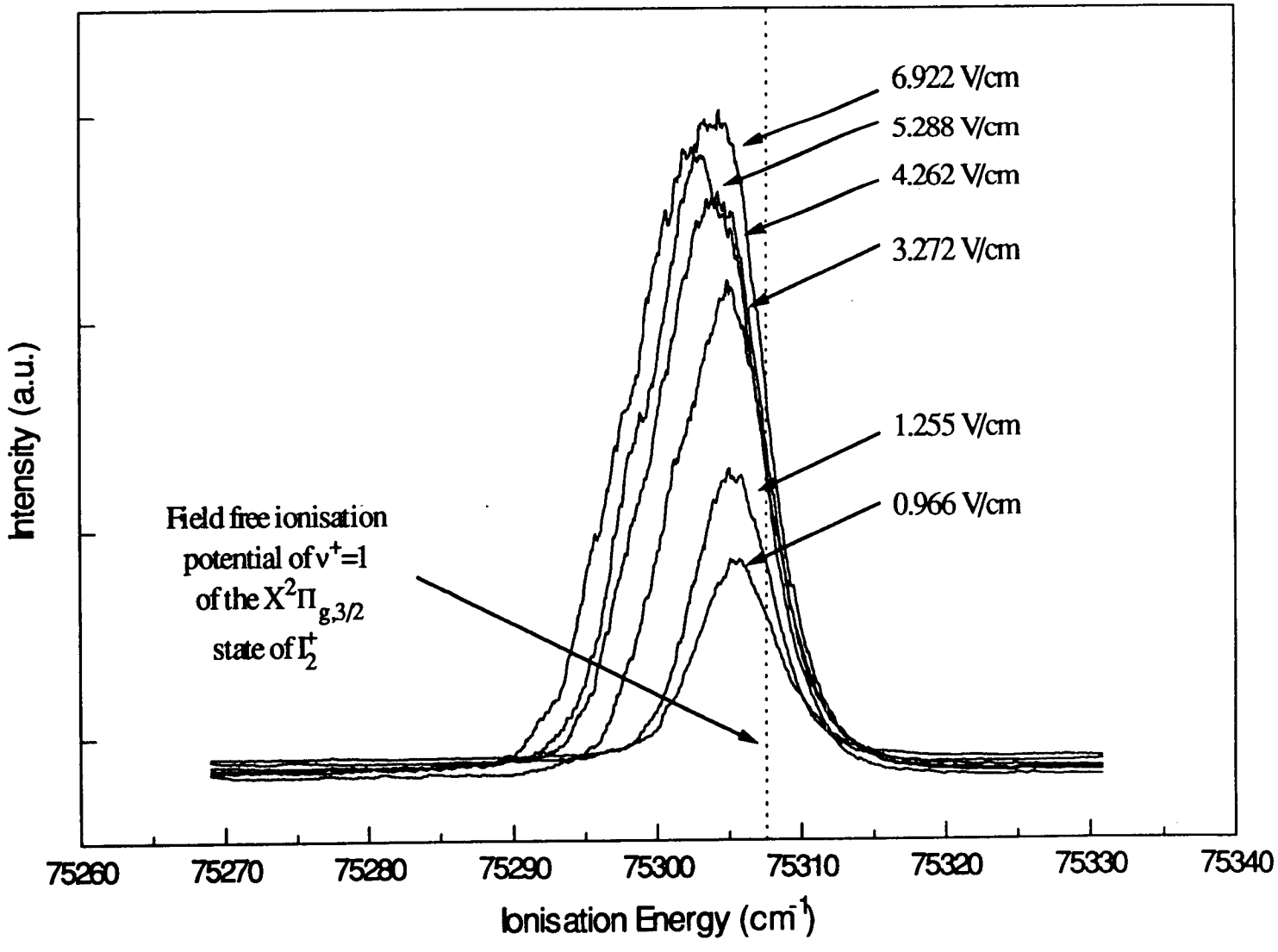

Figure 3.12 ZEKE-PFI spectra of $v^+=1$ of the $X\ ^2\Pi_{g,3/2}$ state of I_2^+ recorded with different extraction potentials. These spectra were all recorded *via* $v=1$ of the $[^2\Pi_{3/2}]_c$ 7s; 2_g Rydberg state.

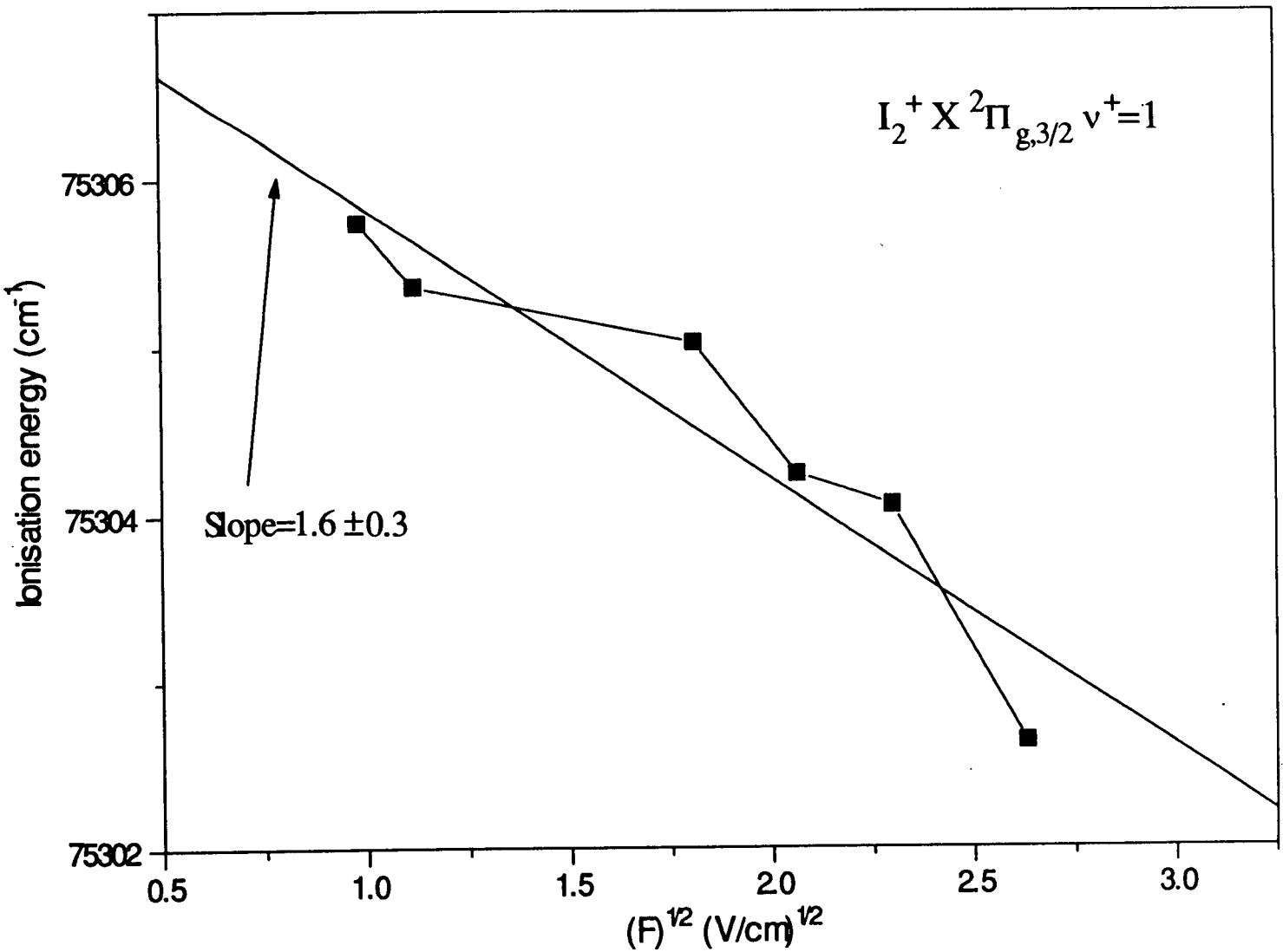

Figure 3.13 A plot of the peak position of the $v^+=1$ of the $X\ ^2\Pi_{g,3/2}$ state of I_2^+ vs. the square root of the applied extraction potential.

The exact reason for this large difference between the expected value and the experimentally determined value is unknown. However, a number of possible ideas can be suggested. The first of these is related to the fact that our calculation of the field ionisation shift was based on transitions to $v^+=1$ of the $X\ ^2\Pi_{g,3/2}$ ionic state rather than the more usual ionic state band origin measurements. The reason for this was the low Franck-Condon transition intensity of the $v=0$ band in the intermediate $[^2\Pi_{3/2}]_c$ 7s; 2_g Rydberg state which would have made small extraction field measurements, significantly more difficult. It seems doubtful that the field ionisation mechanism taking place within Rydberg states converging to higher vibronic thresholds is any different to that for the band origin. If, however, different mechanisms did apply to individual rovibronic thresholds then it would not be possible to apply a blanket field ionisation shift to a ZEKE-PFI spectrum. Autoionisation, which is shown in chapter 5 to perturb the experimental vibrational band intensities in the $X\ ^2\Pi_{g,3/2}$ ionic state, is another possibility. Unfortunately, autoionisation only affects the intensity of ionic rovibronic bands in ZEKE-PFI spectra (discussed in chapter 2) and not the band positions, so it would seem unlikely that this is the cause. A final point concerns the fact that many of the experimentally measured $\sim 4\sqrt{F(V/cm)}$ or $\sim 6\sqrt{F(V/cm)}$ field ionisation shifts have been determined in investigations of atomic species or rotationally resolved molecular species. This contrasts dramatically with the rather broad, vibrationally resolved bands which are observed for molecular iodine and for which, the identification of the peak maximum is much more difficult.

A simple explanation for this discrepancy is therefore not forthcoming. However, the question has to be put forward as to whether it is appropriate to extrapolate the field ionisation shifts found for atoms and small molecules, to a heavy diatomic and still expect a value of $\sim 4\sqrt{F(V/cm)}$ or $\sim 6\sqrt{F(V/cm)}$? Until a better understanding of the lifetime lengthening and field ionisation mechanisms in these high-*n* Rydberg states is found, the only way of determining a specific molecular field ionisation shift, is experimentally.

3.6.4 Factors Affecting the Resolution Achievable in ZEKE-PFI Photoelectron Spectroscopy

In principle, the resolution achievable in ZEKE-PFI experiments is ultimately laser limited. However, in practice there are two other main factors which determine the resolution of a ZEKE-PFI spectrum:-

1) According to equations 3.5 and 3.6, the magnitude of the pulsed electric field(s) determines the field ionisation range (i.e. the energy range below the field-free ionisation threshold) over which electrons are released. In general the smaller the applied pulsed potential, the narrower the band (δn) of high-n Rydberg states which are pulse field ionised and the better the resolution [102]. However, most spectrometers are limited to a minimum value of electric field because of the dramatic reduction in signal intensity found when reducing the extraction pulse below a certain limit. One solution to this problem is to use two pulsed potentials of different magnitudes and at different delays. The first pulse removes prompt electrons and field ionises the Rydberg states down to a depth defined by equation 3.5 or 3.6. A second delayed pulse then field ionises those Rydbergs which are left to a depth dependent on the pulse magnitude. In this way a slice of the Rydberg manifold can be sampled, thereby improving the resolution. In some cases, where large extraction potentials have been employed (10's of V/cm), the resolution is very often much better than expected [103,32]. This has been ascribed to the fact that Rydberg states below a certain limit decay before the application of the pulsed field (as discussed in Chapter 2). The minimum resolution in this case depends on the Rydberg state lifetimes within the Rydberg manifold. Those which have not decayed prior to the application of the extraction potential will determine the resolution.

2) Slowly rising or staircase style extraction fields ionise the higher lying Rydberg states before the lower lying states. By gating the electron signal it is possible to discriminate between electrons released at different times and hence achieve a

resolution that is higher than that predicted by equations 3.5 and 3.6 and in the end comparable with the laser bandwidth [101].

3.6.5 The ZEKE-PFI Spectrometer

The spectrometer used in the present work was designed and built in Edinburgh to record both mass resolved ion spectra and ZEKE-PFI electron spectra. A schematic diagram of the spectrometer is shown in Figure 3.14. The spectrometer consists of two differentially pumped vacuum chambers, the smaller of which (the expansion chamber) houses the pulsed nozzle (300 μm) assembly (General Valve Corporation). The nozzle produces a pulsed supersonic jet (of duration 300μs and repetition rate 10 Hz) which is skimmed (Beam Dynamics, diam. 0.49 mm) downstream before entering the main ionisation chamber. The alignment of the nozzle and skimmer is achieved by varying the nozzle position with an X-Y translator and monitoring the molecular beam on an in-line VG SX200 quadrupole mass spectrometer as shown in Figure 3.14. The expansion chamber is pumped by a 700 ls^{-1} Edwards 160-700 diffusion pump fitted with a liquid nitrogen trap and backed by an Edwards ED200 rotary pump. The gas inlet system to the nozzle contains a sample holder and a sample bypass line. The sample along with the gas inlet lines could be heated to approximately 100 °C although the nozzle remained at room temperature. The sample is generally seeded in an argon carrier gas at pressures ranging from 300 Torr up to 6 atmospheres. A typical operating pressure of 600 Torr led to a pressure of approximately 8 x 10^{-5} Torr in the expansion chamber.

The main ionisation chamber contains the ion/electron collection optics, a 40 cm time-of-flight mass spectrometer (as measured from the point of ionisation) and a dual micro-channel plate (Galileo) detector with matched anode. The chamber is pumped by a Balzers TPU 510S 500 ls^{-1} turbomolecular pump backed by Maruyama CP-80 rotary pump and has a typical background pressure of 1-2 x 10^{-7} Torr. With the nozzle operating the main chamber pressure can rise to 2 x 10^{-6} Torr. The time-of-flight tube incorporating the ion/electron optics and detector are enclosed in a

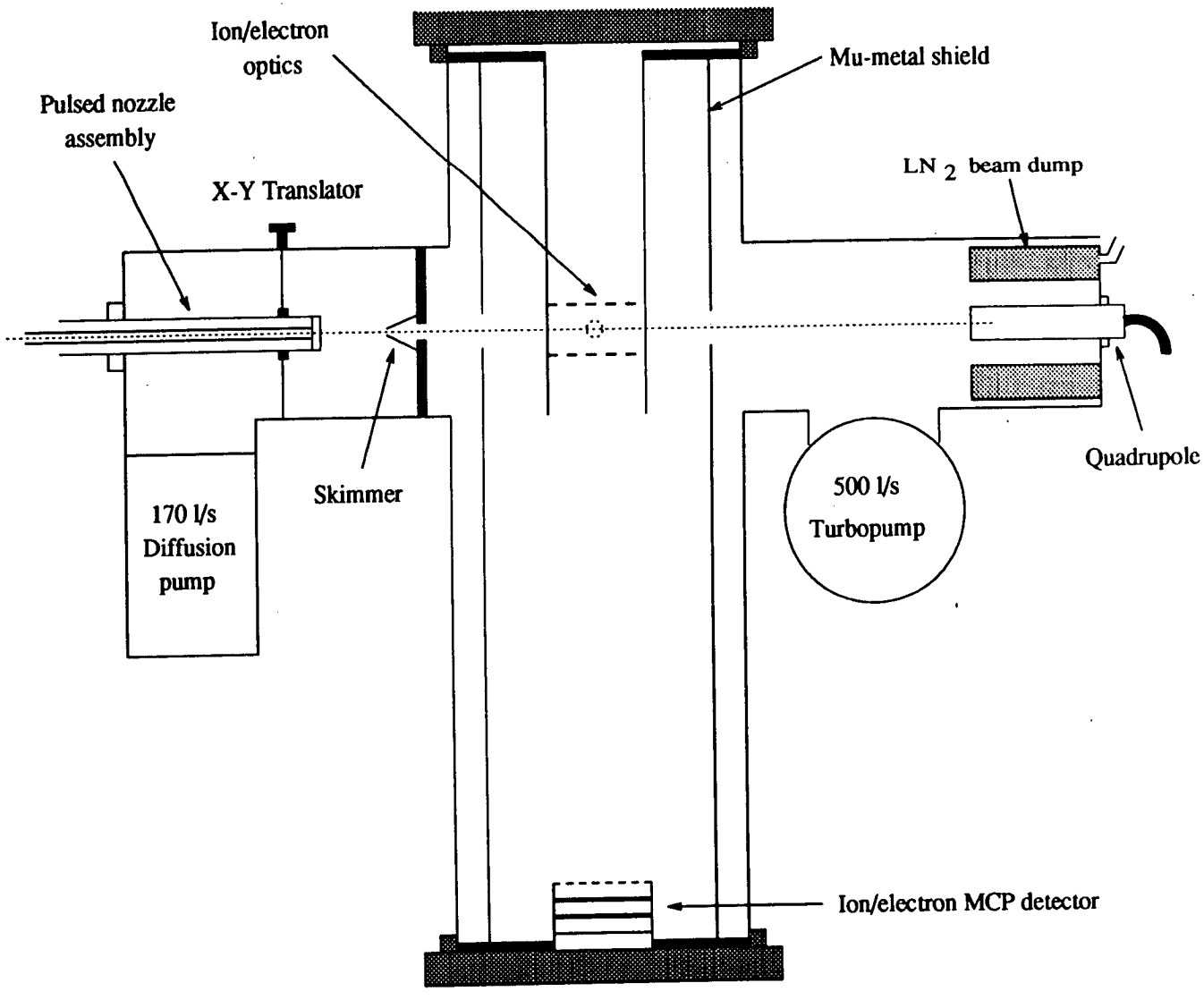

Figure 3.14 A schematic diagram of the spectrometer employed to record ZEKE-PFI electron spectra and mass resolved ion spectra.

single layer of 2 mm thick mu-metal magnetic shielding as shown in Figure 3.14. The ion/electron collection optics consist of two copper mesh grids mounted 3 cm apart such that the molecular beam and laser beams intersect perpendicularly midway between the grids. The ions and electrons are both extracted perpendicularly down the flight tube to the detector. The potential biasing of the grids and detector depends on the photoionisation product being detected. In the case of ions, 1.9 kV is applied to the upper grid to extract the ions and a potential of approximately 400 V is applied to the lower grid to improve the ion signal at the detector. The time-of-flight mass spectrum is monitored on a Lecroy 9310 oscilloscope and processed unamplified by a Stanford Research Systems SRS250 boxcar integrator. The resulting spectrum is recorded on an IBM XT microcomputer and a chart recorder. With molecular iodine, flight times of around 18μs were normally observed for the parent ion, I_2^+. For ZEKE-PFI electron detection, the grids are grounded during the laser excitation and after a time delay ranging from 500 ns to 4 μs (extendible up to 10 μs) a negative repeller potential is applied to the top grid, and a positive extraction potential is applied to the bottom grid. In general the extraction potential applied to the lower grid was up to ~2.5 V whereas the repeller potential applied to the top grid varied between ~2 V and 20 V. The repeller potential is supplied by a home built, variable output, pulsed voltage unit which ranges from 0.6 - 21 V with the delay controlled by an EG&G digital delay generator. The delay and magnitude (30 mV to 10V) of the extraction pulse are controlled by a Farnell pulse generator. The two pulsed potentials field ionise the long-lived Rydberg states and accelerate the electrons onto the microchannel plate detector. The electrons produced by PFI are readily distinguished from photoelectrons arising from direct ionisation as the arrival of the former depends on the pulse delay and voltage. The electron time-of-flight signals are monitored on the Lecroy 9310 oscilloscope and processed unamplified by a Stanford Research Systems SRS250 boxcar integrator. The resulting spectra are recorded on an IBM XT microcomputer and a chart recorder. An example of an electron time-of-flight spectrum is shown in Figure 3.15. The ringing in the spectrum is an experimental artifact which has since been improved by using a matched anode in the detector. The laser Q-switch trigger controls all the experimental timing except for

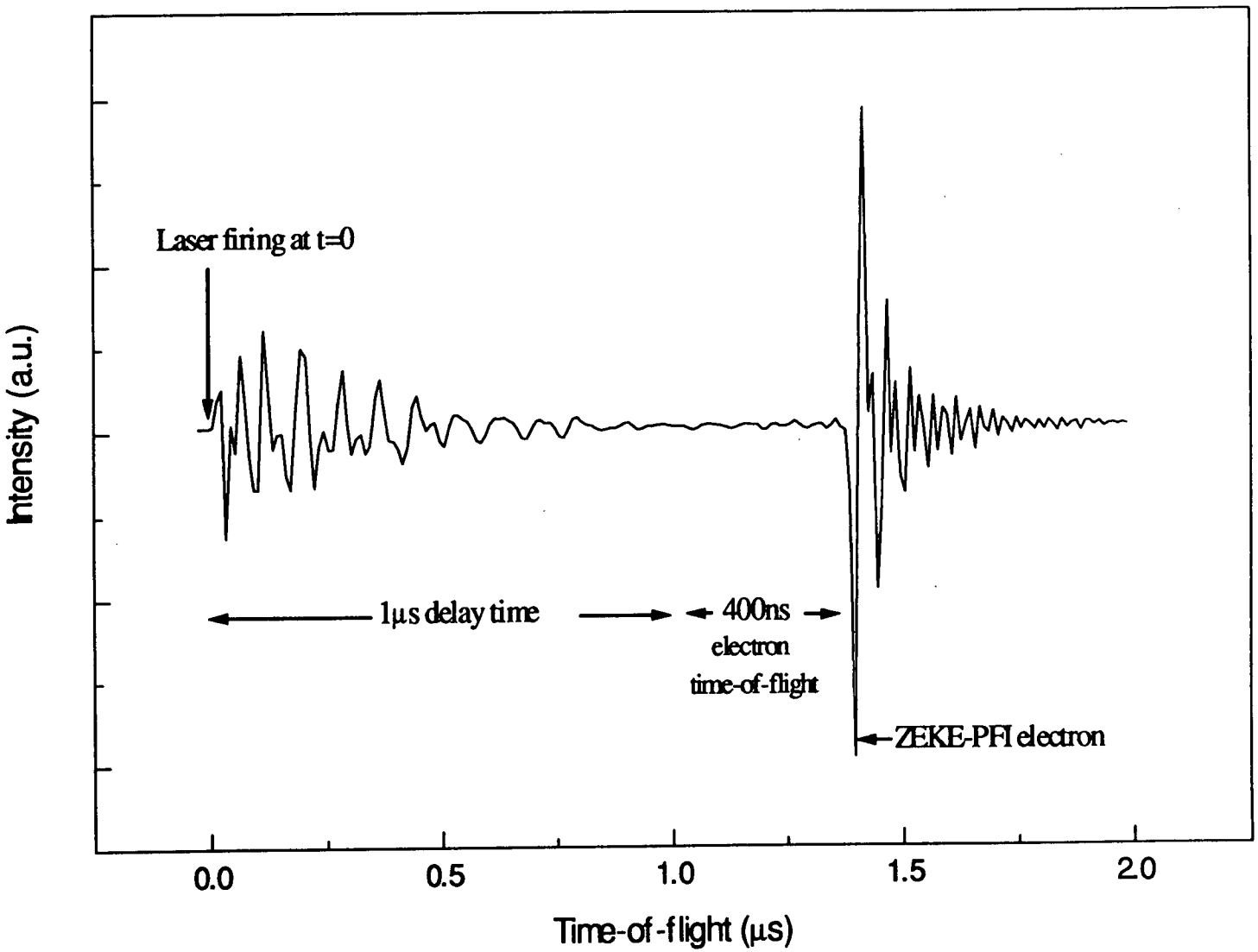

Figure 3.15 An example of an electron time-of-flight spectrum for iodine recorded with a 1 μs delay.

the General Valve nozzle which is triggered from the laser oscillator trigger. A home built delay circuit is employed within the General Valve control unit to adjust the overlap between the gas pulse and laser pulses. An experimental timing diagram is shown in Figure 3.16.

The laser system consists of a Q-switched Nd:YAG laser (Quanta Ray DCR2A, pulse duration ~10 ns) operating at 10 Hz which pumps two tuneable dye lasers (A Quanta Ray PDL-2 and a PDL-3A). The PDL-2 dye laser has a resolution of ~0.5 cm^{-1} whereas the PDL-3A dye laser has a resolution of ~0.1 cm^{-1}. A schematic diagram of the laser set-up is shown in Figure 3.17. The Nd:YAG laser produces 1064 μm radiation which can be both frequency doubled to 532 nm and tripled to 355 nm in a frequency mixing module to pump the two dye lasers [104]. A wide range of Exciton and Lambda Physik dyes were employed to produce radiation from ~420-900 nm [105]. Ultraviolet radiation (215-420 nm) is produced in doubling and mixing crystals, which were mounted in a wavelength extender module (Quanta Ray) [106]. Scanning the dye lasers is controlled by a home built stepper motor triggered by the IBM XT computer. In the case of the (2+1') ZEKE-PFI experiments, both laser beams were directed into the spectrometer from opposite sides and focused to intersect the molecular beam with adjustable 7.6 cm focal length lenses. The probe laser pulse was delayed with respect to the pump by increasing its path length prior to entering the spectrometer. None of the spectra recorded were corrected to take account of variations in laser intensity. Calibration of wavelengths above 355 nm was obtained from a neon optogalvanic spectrum and below 355 nm from the I_2 B→X fluorescence excitation spectrum, using the dye fundamental. Circular polarisation of the frequency doubled output was achieved by passage through a Steeg & Reuter Soleil Babinet polariser.

An early one-colour two-photon non-resonant ZEKE-PFI spectrum of NO, recorded using the PDL-2 dye laser, is shown in Figure 3.18 to demonstrate the rotational resolution of the ZEKE-PFI technique. The rotational assignment is based on Refs. [32] and [107].

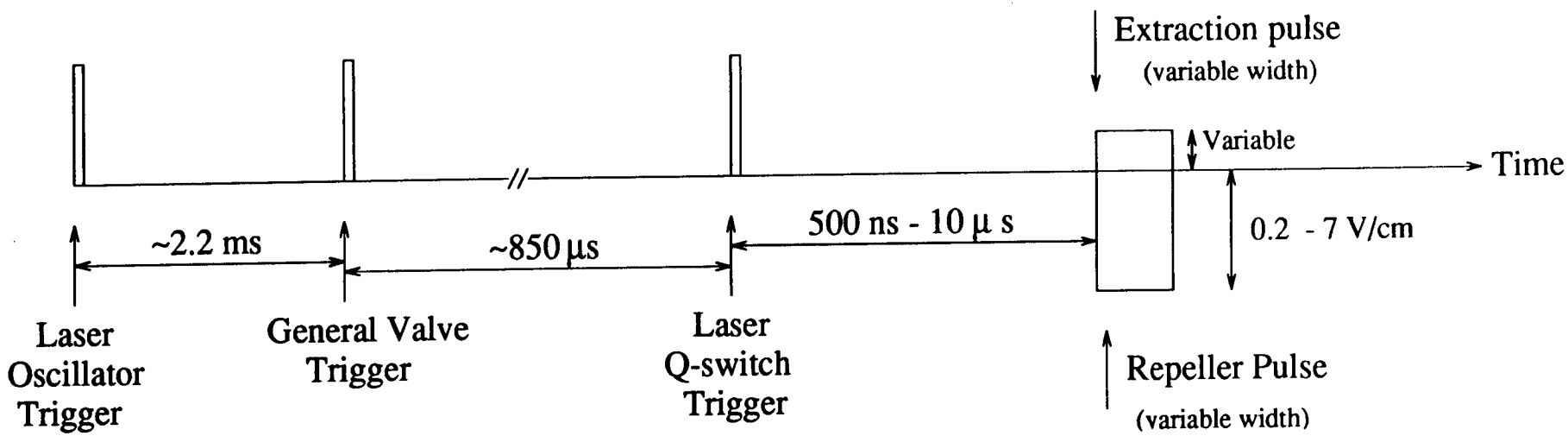

Figure 3.16 The general timing sequence employed in the ZEKE-PFI investigations of molecular iodine and iodine-argon.

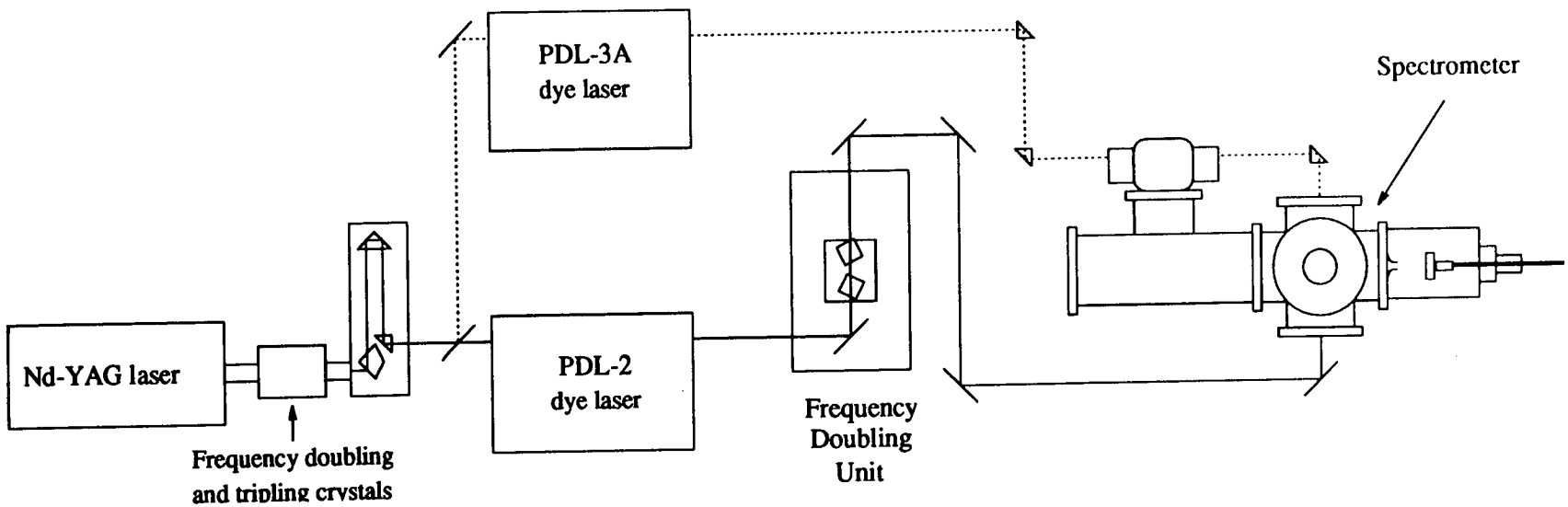

Figure 3.17 A schematic diagram of the Nd:YAG pumped dye laser set-up employed with the spectrometer. The two colour ZEKE-PFI investigations required the use of the second dye laser indicated by the dotted line.

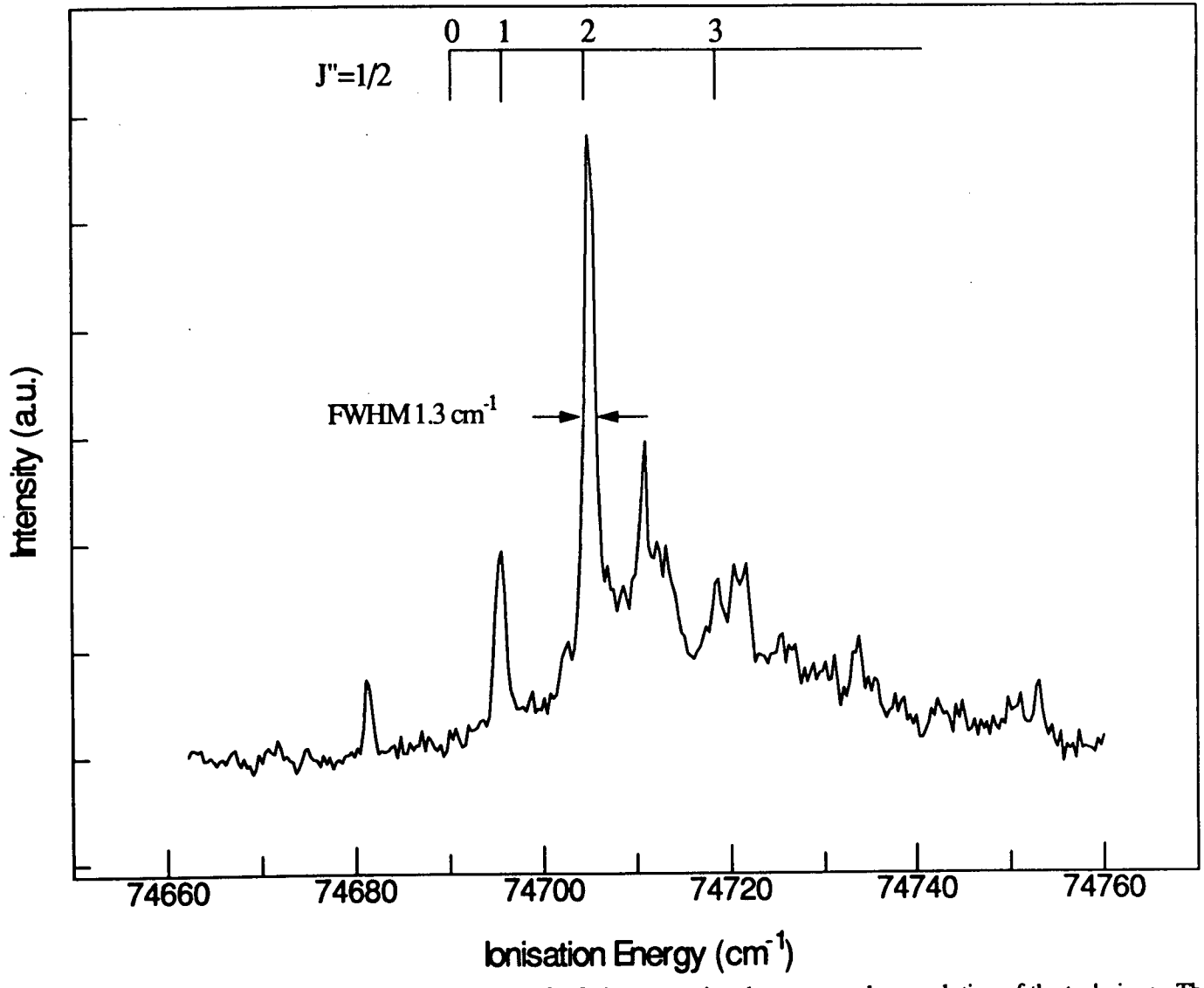

Figure 3.18 A one colour nonresonant ZEKE-PFI spectrum of NO demonstrating the wavenumber resolution of the technique. The rotational bands with quantum number J^+ are drawn as a function of J".

3.7 References

[1] D.W. Turner and M.I. Al-Joboury, J. Chem. Phys. **37** (1963) 3007

[2] J.W. Rabalais, Principles of Ultraviolet Photoelectron Spectroscopy, Wiley, New York (1977)

[3] J.A.R. Samson, Techniques of Vacuum Ultraviolet Photoelectron Spectroscopy, Wiley, New York (1967)

[4] A.W. Potts, H.J. Lempka, D.G. Streets and W.C. Price, Phil. Trans. Roy. Soc. London A **268** (1970) 59

[5] H. van Lonkhuyzen and C.A. de Lange, Chem. Phys. **89** (1984) 313

[6] J.H.D. Eland, Photoelectron Spectroscopy, Butterworth & Co., England (1974)

[7] Y. Tanaka, J. Opt. Soc. Am. **45** (1955) 710

[8] J.J. Hopfield, J. Phys. Rev. **35** (1930) 1133

[9] K.R. Lea, Phys. Rep. (Section C of Physics Letters) **43** (1978) 337

[10] Synchrotron Radiation Research, edited by H. Winick and S. Doniach, Plenum Press, New York (1980)

[11] V. Wilke and W. Schmidt, Appl. Phys. **18** (1979) 177

[12] J.C. Miller, R.N. Compton and C.D. Cooper, Laser Techniques for Extreme Ultraviolet Spectroscopy, edited by T.R. McIlrath and R.R. Freeman, New York: Am. Inst. Phys. (1982)

[13] J. Hager and S.C. Wallace, Chem. Phys. Lett. **90** (1982) 472

[14] R. Hilbig and R. Wallenstein, IEEE J. Quant. Electron. **QE-19** (1983) 1759

[15] H.H. Fielding, T.P. Softley and F. Merkt, Chem. Phys. **155** (1991) 257

[16] R.H. Lipson and A.R. Hoy, J. Chem. Phys. **90** (1989) 6821

[17] E.E. Marinero, C.T. Rettner, R.N. Zare and A.H. Kung, Chem. Phys. Lett. **95** (1983) 486

[18] R.G. Tonkyn and M.G. White, Rev. Sci. Instrum. **60** (1989) 1245

[19] K.P. Huber and G. Herzberg, Molecular Spectra and Molecular Structure, Vol. 4, Van Nostrand Reinhold, New York (1979)

[20] P. Venkateswarlu, Can. J. Phys. **48** (1970) 1055

[21] R.G. Bray, R.M. Hochstrasser and J.E. Wessel, Chem. Phys. Lett. **27** (1974) 167

[22] P.M. Johnson, M.R. Berman and D. Zakheim, J. Chem. Phys. **62** (1975) 2500

[23] R.J. Donovan, R.V. Flood, K.P. lawley, A.J. Yencha and T. Ridley, Chem. Phys. **164** (1992) 439

[24] S.H. Lin, Y. Fujimara, H.J. Neusser and E.W. Schalg, Multiphoton Spectroscopy of Molecules, Academic (1984)

[25] P.J. Wilson, T. Ridley, K.P. Lawley and R.J. Donovan, Chem. Phys. **182** (1994) 325

[26] F. Merkt, P.M. Guyon and J. Hepburn, Chem. Phys. **173** (1993) 479

[27] W. Kong, D. Rodgers, J. Hepburn, K. Wang and V. McKoy, J. Chem. Phys. **99** (1993) 3159

[28] R.T. Wiedmann, M.G. White, K. Wang and V. McKoy, J. Chem. Phys. **98** (1993) 7673

[29] K. Müller-Dethlefs, M. Sander and E.W. Schlag, Chem. Phys. Lett. **112** (1984) 291

[30] M.C.R. Cockett, M. Takahashi, K. Okuyama and K. Kimura, Chem. Phys. Lett. **187** (1991) 250

[31] X. Zhang, J.M. Smith and J.L. Knee, J. Chem. Phys. **97** (1992) 2843

[32] A. Strobel, I. Fischer, J. Staecker, G. Niedner-Schatteburg, K. Müller-Dethlefs and V.E. Bondybey, J. Chem. Phys. **97** (1992) 2332

[33] G. Reiser, W. Habenicht and K. Müller-Dethlefs, J. Chem. Phys. **98** (1993) 8462

[34] P.M. Johnson, J. Chem. Phys. **62** (1975) 4562

[35] R. Campargue, Rev. Sci. Instrum. **35** (1964) 111

[36] R. Campargue, J. Chem. Phys. **52** (1970) 1795

[37] M.G. Liverman, S.M. Beck, D.L. Monto and R.E. Smalley, J. Chem. Phys. **70** (1979) 192

[38] R.E. Smalley, L. Wharton and D.H. Levy, J. Chem. Phys. **63** (1975) 4977

[39] F.I. Vilesov, B.L. Kurbatov and A.N. Terenin, Sov. Phys. Dokl. **6** (1961) 490

[40] M.I. Al-Joboury and D.W. Turner, J. Chem. Soc. (1963) 5141

[41] K. Siegbahn and K. Edvardson, Nucl. Phys. **1** (1956) 137

[42] C. Nordling, E. Sokolowski and K. Siegbahn, Phys. Rev. **105** (1957) 1676

[43] J.E. Pollard, D.J. Trevor, J.E. Reutt, Y.T. Lee and D.A. Shirley, J. Chem. Phys. **77** (1982) 34

[44] W. Peatman, F.-P. Wolf and R. Unwin, Chem. Phys. Lett. **95** (1983) 453

[45] W.G. Wilson, K.S. Viswanathan, E. Sekreta and J.P. Reilly, J. Phys. Chem. **88** (1984) 672

[46] K. Kimura, S. Katsumata, Y. Achiba, T. Yamazaki and S. Iwata, Handbook of He(I) Photoelectron Spectra of Fundamental Organic Molecules, Halsted Press, New York (1981)

[47] S.R. Long, J.T. Meek and J.P. Reilly, J. Chem. Phys. **79** (1983) 3206

[48] S.L. Anderson, D.M. Rider and R.N. Zare, Chem. Phys. Lett. **93** (1982) 11

[49] J.T. Meek, E. Sekreta, W. Wilson, K.S. Viswanathan and J.P. Reilly, J. Chem. Phys. **82** (1985) 1741

[50] B. Tsai, T. Baer and M.L. Horovitz, Rev. Sci. Instrum. **45** (1974) 494

[51] G.C. Baldwin and S.I. Friedman, Rev. Sci. Instrum. **38** (1967) 519

[52] D.G. Wilden, P.J. Hicks and J. Comer, J. Phys. B **9** (1976) 1959

[53] K. von Puttkamer, Z. Naturforsch. **25a** (1970) 1062

[54] T.S. Green and G.A. Proca, Rev. Sci. Instrum. **41** (1970) 1409

[55] A.L. Hughes and V. Rojansky, Phys. Rev. **34** (1929) 284

[56] M. Arnow and D.R. Jones, Rev. Sci. Instrum. **43** (1972) 72

[57] P. Marmet and L. Kerwin, Can. J. Phys. **38** (1960) 787

[58] D. Villarejo, R.R. Herm and M.G. Inghram, J. Chem. Phys. **46** (1967) 4995

[59] R. Spohr, P.M. Guyon, W.A. Chupka and J. Berkowitz, Rev. Sci. Instrum. **42** (1971) 1872

[60] D. Villarejo, R. Stockbauer and M.G. Inghram, J. Chem. Phys. **48** (1968) 3342

[61] P.M. Guyon, R. Spohr, W.A. Chupka and J. Berkowitz, J. Chem. Phys. **65** (1976) 1650

[62] W.B. Peatman, G.B. Kasting and D.J. Wilson, J. Electron Spectrosc. Relat. Phenom. **7** (1975) 233

[63] W.B. Peatman, Chem. Phys. Lett. **36** (1975) 495

[64] W.B. Peatman, J. Chem. Phys. **64** (1976) 4093

[65] R. Stockbauer, J. Chem. Phys. **70** (1979) 2108

[66] T. Baer, P-M. Guyon, I. Nenner, A Tabché-Fouhaillé, R. Botter, L.F.A. Ferreira and T.R. Govers, J. Chem. Phys. **70** (1979) 1585

[67] W.M. Hickman and R.E. Fox, J. Chem. Phys. **25** (1956) 642

[68] R.N. Compton, L. G. Christophorou, G.S. Hurst and P.W. Reinhardt, J. Chem. Phys. **45** (1966) 4634

[69] A. Chutjian and J.M. Ajello, J. Chem. Phys. **66** (1977) 4544

[70] S. Cvejanovic and F.H. Read, J. Phys. B: Atom. Molec. Phys. **7** (1974) 1180

[71] G.C. King, M. Zubek, P.M. Rutter and F.H. Read, J. Phys. E: Sci. Instrum. **20** (1987) 440

[72] R.I. Hall, A. McConkey, K. Ellis, G. Dawber, L. Avaldi, M.A. MacDonald and G.C. King, Meas. Sci. Technol. **3** (1992) 316

[73] C.E. Moore, Atomic Energy Levels, Volumes 1-3, Natl. Bur. Std. Circ. 467, US Govt. Printing Office, Washington (1949)

[74] D. Holland, Station 3.2 Experimenters Handbook, EPSRC Daresbury Laboratory, Warrington, Cheshire, U.K.

[75] D.M.P. Holland, J.B. West, A.A. MacDowell, I.H. Munro and A.G. Beckett, Nucl. Instrum. Methods, **B44** 233 (1989)

[76] K. Müller-Dethlefs, M. Sander and E.W. Schlag, Z. Naturforsch **39a** (1984) 1089

[77] M. Sander, L.A. Chewter, K. Müller-Dethlefs and E.W. Schlag, Phys. Rev. A **36** (1987) 4543

[78] G. Reiser, W. Habenicht, K. Müller-Dethlefs and E.W. Schlag, Chem. Phys. Lett. **152** (1988) 119

[79] M.A. Duncan, T.G. Dietz and R.E. Smalley, J. Chem. Phys. **75** (1981) 2118

[80] K. Müller-Dethlefs and E.W. Schlag, Annu. Rev. Phys. Chem. **42** (1991) 109

[81] T.N. Kitsopoulos, I.M. Walker, J.G. Loeser and D.M. Neumark, Chem. Phys. Lett. **159** (1989) 300

[82] T.N. Kitsopoulos, C.J. Chick, Y. Zhao and D.M. Neumark, J. Chem. Phys. **95** (1991) 5479

[83] C.C. Arnold and D.M. Neumark, J. Chem. Phys. **99** (1993) 3353

[84] G.F. Gantefor, D.M. Cox and A. Kaldor, J. Chem. Phys. **93** (1990) 8395

[85] K. Takazawa, M. Fujii, T. Ebata and M. Ito, Chem. Phys. Lett. **189** (1992) 592

[86] E. de Beer, W.J. Buma and C.A. de Lange, J. Chem. Phys. **99** (1993) 3252

[87] H. Krause and H.J. Neusser, J. Chem. Phys. **97** (1992) 5923

[88] L. Zhu and P.M. Johnson, J. Chem. Phys. **94** (1991) 5769

[89] H-J. Dietrich, R. Lindner and K. Müller-Dethlefs, J. Chem. Phys. **101** (1994) 3399

[90] G.I. Nemeth, H.L. Selzle and E.W. Schlag, Chem. Phys. Lett. **215** (1993) 151

[91] H. Krausse and H.J. Neusser, J. Chem. Phys. **97** (1992) 5923

[92] D. Kleppner, M.G. Littman and M.L. Zimmerman, Rydberg States of Atoms and Molecules, edited by R.F. Stebbings and F.B. Dunning, (Cambridge University Press, New York) (1983)

[93] T.F. Gallagher, L.M. Humphrey, W.E. Cooke, R.M. Hill and S.A. Edelstein, Phys. Rev. A **16** (1977) 1098

[94] W.E. Cooke and T.F. Gallagher, Phys. Rev. A **17** (1978) 1226

[95] J.R. Rubbmark, M.M. Kash, M.G. Littman and D. Kleppner, Phys. Rev. A **23** (1981) 3107

[96] W.L. Glab and J.P. Hessler, Phys. Rev. Lett. **62** (1989) 1472

[97] G.R. Janik, O.C. Mullins, C.R. Mahon and T.F. Gallagher, Phys. Rev. A **35** (1987) 2345

[98] S.T. Pratt, J.L. Dehmer and P.M. Dehmer, J. Chem. Phys. **90** (1989) 2201

[99] E.D. Poliakoff, J.L. Dehmer, A.C. Parr and G.E. Leroi, Chem. Phys. Lett. **111** (1984) 128

[100] W.A. Chupka, J. Chem. Phys. **98** (1993) 4520

[101] R. Lindner, H-J. Dietrich and K. Müller-Dethlefs, Chem. Phys. Lett. **228** (1994) 417

[102] F. Merkt and T.P. Softley, Phys. Rev. A **46** (1992) 302

[103] C. Lakshminarayan, J.M. Smith and J.L. Knee, Chem. Phys. Lett. **182** (1991) 656

[104] Instruction manual for the Quanta-Ray DCR-2A Pulsed Nd:YAG laser

[105] Users manual for the Quanta-Ray pulsed dye laser system

[106] Users manual for the Quanta-Ray wavelength extender system

[107] G. Reiser and K. Müller-Dethlefs, J. Phys. Chem. **96** (1992) 9

Chapter 4

Threshold Photoelectron Spectroscopy of Cl_2, Br_2 and I_2

4.1 Introduction

The spectroscopic properties of the diatomic homonuclear halogens, fluorine, chlorine, bromine and iodine, have been extensively studied over the past 50 years [1]. Much of the spectroscopic interest in these molecules has arisen as a result of their use in rare-gas halide lasers and through their potential value as laser systems in their own right [2,3].

The ground state molecular orbital configuration of the diatomic homonuclear halogens consists of the ten valence electrons (five from each halogen *n*p atomic orbital), distributed amongst the four highest valence molecular orbitals in the form $(\sigma_g)^2(\pi_u)^4(\pi_g^*)^4(\sigma_u^*)^0$. In this description the superscripts represent the molecular orbital (MO) occupation numbers which are often given in the notation [2440] and the symbol within the brackets represents the molecular orbital. The neutral ground state of the halogens is therefore classified as a $^1\Sigma_g^+$ state. The removal of an electron from each of the filled valence molecular orbitals in turn leads to three positive ionic states. The ground ionic X $^2\Pi_g$ state is the result of removing an electron from the highest occupied molecular orbital of the $^1\Sigma_g^+$ ground state, namely the π_g MO, whereas the higher energy A $^2\Pi_u$ and B $^2\Sigma_g^+$ ionic states arise from the removal of an electron from the π_u and σ_g MO's, respectively. A schematic diagram of the relative positions of the

ionic potential energy curves of the halogens is shown in Figure 4.1. The removal of an electron from a fully occupied degenerate molecular orbital (a π_g or π_u MO in the case of the homonuclear halogens) leaves the corresponding molecular ion in an orbitally degenerate doublet state. However, this degeneracy is lifted as a result of the coupling of the spin and orbital angular momenta of the molecule. In the case of the halogens, this angular momentum coupling is representative of Hund's case (a) coupling as described in Chapter 2. Both the X [2430] and A [2340] ionic states of the halogens have a total orbital angular momentum (Λ) of 1 and a total spin angular momentum (Σ) of $\pm$ ½ which can couple to give two $^2\Pi$ states; the $^2\Pi_{3/2}$ and the $^2\Pi_{1/2}$ states. The ground X state is therefore split into a $^2\Pi_{g,3/2}$ and a $^2\Pi_{g,1/2}$ state whereas the first excited A state is split into a $^2\Pi_{u,3/2}$ and a $^2\Pi_{u,1/2}$ state.

The magnitude of this coupling and therefore the energetic splitting between the two states (spin-orbit splitting) is controlled by the spin-orbit interaction parameter, ς. The magnitude of this interaction parameter is dependent on the molecular orbital in which the unpaired electron is found and the atomic orbitals which constitute the molecular orbital. In the case of the atomic halogens the interaction parameter is approximately given by

$$\zeta = 2\beta^2\left\langle \frac{Z_x^{EFF}}{r_x^3} \right\rangle \qquad 4.1$$

where β is the Bohr magneton, and Z^{EFF} is the screened nuclear charge [4,5]. This expression is just equal to 2/3 of the atomic spin-orbit splitting for the same effective nuclear charge and mean radius [6]. In fact the molecular spin-orbit splitting is approximately equal to the atomic interaction parameter which increases from fluorine to iodine [7] as shown in Table 4.1. The energies of individual molecular spin-orbit states are therefore given by

$$E = E_0 + \varsigma\Lambda\Sigma \qquad 4.2$$

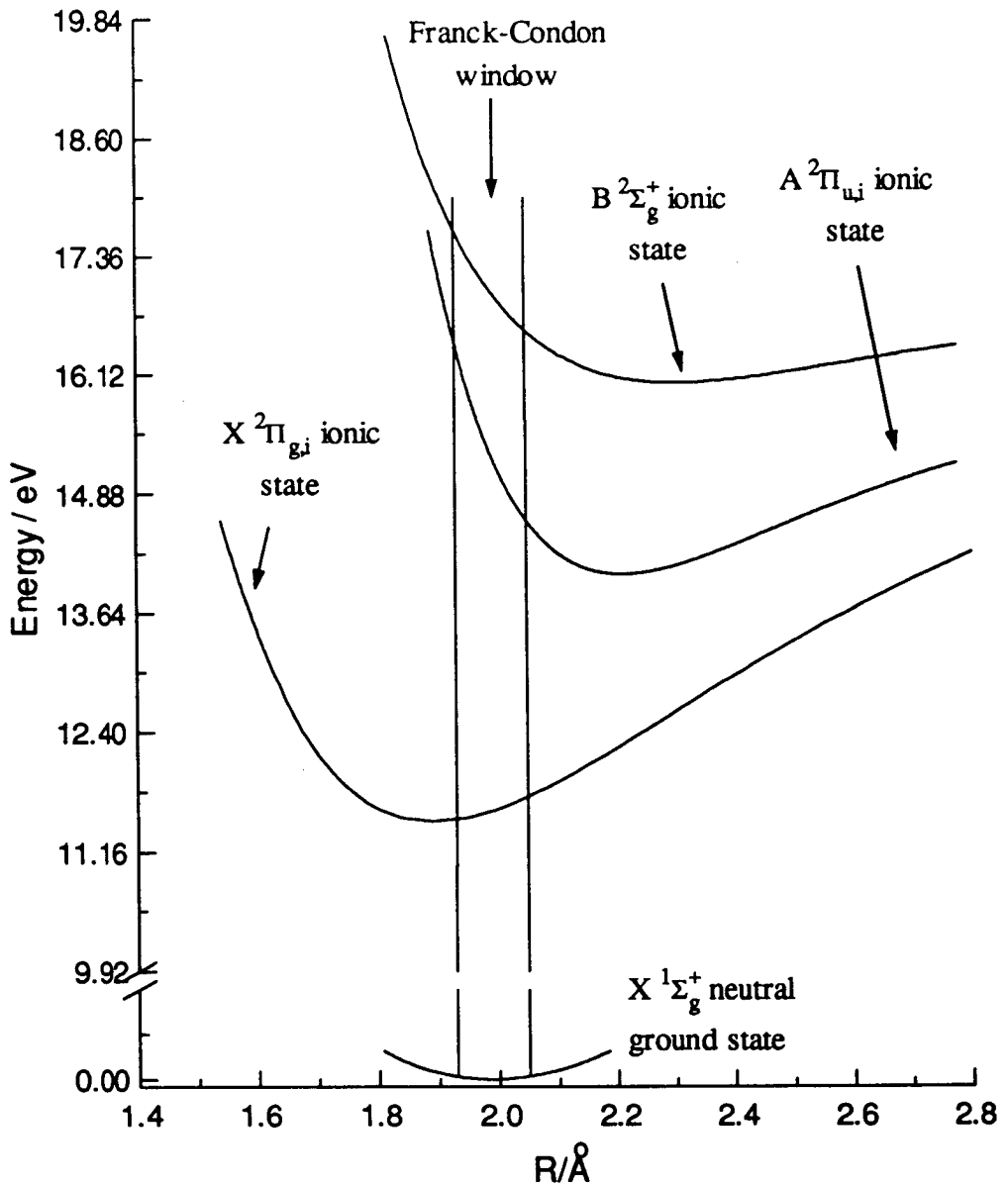

Figure 4.1

A schematic diagram of the relative positions of the ionic potential energy curves of the halogens. The positions of the potentials are based on chlorine in this case.

where E_0 is the energy of the degenerate state in the absence of spin-orbit coupling, Λ is the total orbital angular momentum of the degenerate state and Σ is the total spin angular momentum of the degenerate state.

Table 4.1 Atomic halogen interaction parameters, ς, and spin-orbit splittings

Atomic orbital	Halogen atom	Atomic interaction parameter ς, / cm^{-1}	Atomic spin-orbit splitting ($^2P_{1/2}$ - $^2P_{3/2}$) / cm^{-1} [8]
2p	Fluorine	269	404
3p	Chlorine	587	881
4p	Bromine	2457	3685
5p	Iodine	5068	7603

4.2 Spectroscopic Investigations of the Electronic Structure of the Homonuclear Diatomic Halogen Cations

The electronic structure of the homonuclear diatomic halogen cations has been extensively investigated using a wide variety of techniques. However, there is still a great deal of uncertainty in the precise spectroscopic character of many of these ionic states. From a spectroscopic perspective, the small vibrational frequencies and unfavourable band origin Franck-Condon factors in the excited ionic states of the halogens, especially the heavier halogens have made spectral assignments very difficult. The perturbed nature of some halogen electronic states has also complicated matters. From an experimental viewpoint, the reactive and corrosive nature of these species also makes their study particularly challenging. Conventional photoelectron spectroscopy [9] and optical emission spectroscopy [7] have been the two main techniques employed to investigate the diatomic halogen cations. However, the poor resolution of conventional photoelectron investigations allied with the density of information produced in optical emission studies has made the spectroscopic characterisation of the electronic states of the ion particularly difficult.

The early characterisation of the electronic structure of the diatomic homonuclear halogen cations employed electron [10] and photon impact [11,12] techniques to measure ionisation potentials. A conventional photoelectron study by Frost et al. [13] managed to improve the accuracy of these ionisation potentials using a He(I) source and a retarding field energy analyser. However, the incorporation of a spherical electrostatic monochromator improved the resolution significantly (~30 meV) [14] and enabled vibrational structure and spin-orbit splittings to be resolved in the ground X $^2\Pi_{g,i}$ ionic states of all the halogens along with approximate values for the spin-orbit splittings in the A $^2\Pi_{u,i}$ ionic states of Br_2 and I_2. A weakly resolved vibrational progression in the A $^2\Pi_{u,i}$ ionic state of chlorine was also observed in a separate study by Potts and Price [15]. The early experiments on I_2, with it's low vibrational frequencies, were unsuccessful in resolving any vibrational structure in the X $^2\Pi_{g,i}$ ionic state due to the assumed presence of hot band structure [15]. To reduce the hot band contributions, a variable temperature study was undertaken by Higginson et al. [16] in which the adiabatic ionisation potentials of the two spin-orbit components of the X $^2\Pi_{g,i}$ ionic state were established. A high resolution photoelectron study of the first four diatomic halogens by van Lonkhuyzen and de Lange [17] some 14 years later, improved the resolution and resulted in resolved vibrational structure and spin-orbit splittings in each of the X $^2\Pi_{g,i}$ and A $^2\Pi_{u,i}$ ionic states of F_2, Cl_2 and Br_2 along with vibrational structure in the $^2\Sigma_g^+$ ionic state of F_2 and Cl_2.

Optical emission spectroscopy is another technique which has been applied to investigate the halogen cations F_2 [18], Cl_2 [19,20] and Br_2 [21]. Unfortunately, although much of the emission could be attributed to the A $^2\Pi_{u,i} \rightarrow$ X $^2\Pi_{g,i}$ ionic transition and useful information about the rotational structure was obtained, the high rotational temperatures meant that detailed vibrational data was unreliable. However, Tuckett and co-workers have overcome the early problems of the blending of rotational and vibrational structure in emission spectra by observing the fluorescence emitted from rotationally cooled ions in a crossed molecular beam / electron beam

experiment. This has enabled them to extend known experimental data on the $X\ ^2\Pi_{g,i}$ and $A\ ^2\Pi_{u,i}$ ionic states of F_2 [22], Cl_2 [23], Br_2 [24] and I_2 [25]. Theoretical work on the cationic states of F_2 [26], Cl_2 [23,27], Br_2 [28,29] and I_2 [30] has also kept pace with the experimental findings and in many cases has aided the interpretation of spectroscopic results.

The results obtained in a threshold photoelectron investigation of the valence ionic states of the three diatomic halogens, Cl_2, Br_2 and I_2, employing a penetrating field electron spectrometer at the Daresbury synchrotron radiation source are presented in the following sections. The spectra recorded for both chlorine and bromine cover the ionisation energy range from the onset of ionisation up to 35 eV whereas that recorded for iodine extends up to 14 eV. The only diatomic halogen to have been studied using threshold photoelectron spectroscopy previously is F_2, and in that study only the $X\ ^2\Pi_{g,i}$ ionic state was investigated [31].

4.3 The Threshold Photoelectron (TPE) Spectrum of Cl_2

The complete valence ionisation threshold photoelectron (TPE) spectrum of Cl_2 (11-17 eV) is shown in Figure 4.2. The spectrum contains vibrational bands, as identified in the figure, which are typical of those observed in conventional He(I) photoelectron studies [14,15,17,32], together with the Ar^+ doublet lines. The three main ionic bands contain resolved vibrational structure and are associated with the ground $X\ ^2\Pi_{g,i}$ ionic state, and the first two excited, $A\ ^2\Pi_{u,i}$ and $B\ ^2\Sigma_g^+$ ionic states. In addition, there is a significant amount of vibrational structure between the main X and A vibrational bands and to a lesser extent between the A and B vibrational bands, which has not been previously observed in any conventional photoelectron investigation. This extra structure can be attributed to autoionisation processes producing vibrationally excited ions in regions where the Franck-Condon overlap

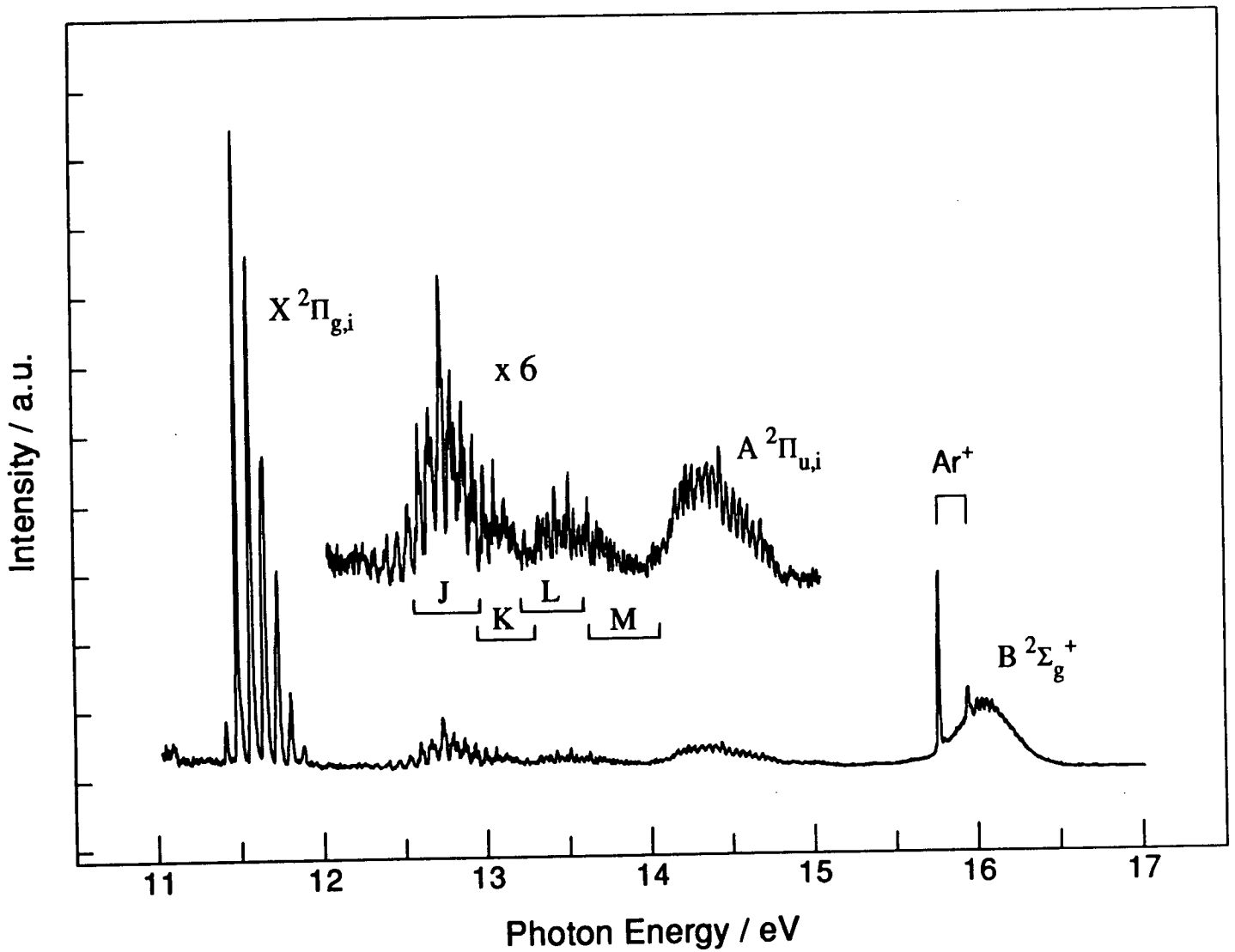

Figure 4.2 The threshold photoelectron spectrum of the valence ionisation region of Cl_2 showing the X $^2\Pi_{g,i}$, A $^2\Pi_{u,i}$ and B $^2\Sigma_g^+$ bands of Cl_2^+. The vibrational structure between the X and the A bands is due to autoionisation processes. The bracketed regions J, K, L and M are discussed in the text.

between the neutral ground state and ionic states is very poor. All of the features observed in the valence ionisation region are described in detail below.

4.3.1 The TPE Spectrum of Cl_2 between 11.4 and 12.0 eV

The TPE spectrum of the low vibrational bands of the X $^2\Pi_{g,i}$ ionic state of Cl_2 is shown in Figure 4.3. The resolution as measured on the (0,0) band of the X $^2\Pi_{g,3/2}$ state is 11 meV. Clear evidence of two vibrational progressions associated with the two spin-orbit components of the X $^2\Pi_{g,i}$ ionic state is observed. This is particularly noticeable between the (2,0) band of X $^2\Pi_{g,3/2}$ spin-orbit component and the (1,0) band of the X $^2\Pi_{g,1/2}$ spin-orbit component. The similarity between the vibrational frequency and the spin-orbit splitting of the X $^2\Pi_{g,i}$ ionic state, coupled with poor resolution (> 25 meV) has up until now, always led to the observation of a single vibrational progression [17]. The measured adiabatic ionisation potential of the X $^2\Pi_{g,3/2}$ ionic state is 11.481 ± 0.003 eV, whereas overlapping vibrational bands necessitate the adiabatic ionisation potential of the X $^2\Pi_{g,1/2}$ ionic state to be calculated from a third order Dunham fit of the X $^2\Pi_{g,1/2}$ vibrational bands (see below). This leads to a value of 11.576 ± 0.003 eV for the adiabatic ionisation potential of the X $^2\Pi_{g,1/2}$ ionic state and gives a spin-orbit splitting in the X $^2\Pi_{g,i}$ ionic state of 95 ± 6 meV (766 ± 48 cm^{-1}). The value of 766 cm^{-1} is over 100 cm^{-1} larger than the measured vibrational frequencies of the two spin-orbit components (see Table 4.8). This agrees in principle with the findings of van Lonkhuyzen and de Lange [17] who required a spin-orbit splitting of 725 cm^{-1} to model their He(I) photoelectron spectrum of the X $^2\Pi_{g,i}$ ionic state when their measured vibrational frequency was ~645 cm^{-1}. The assignment shown in Figure 4.3 is based on fitting a third order Dunham expression to the individually resolved vibrational bands of each spin-orbit component in the energy range shown in Figure 4.3 and in the region between the X and A vibrational bands (see sections 4.3.2 and 4.3.3). The vibrational constants derived from the fits are given in Table 4.8. The experimental and

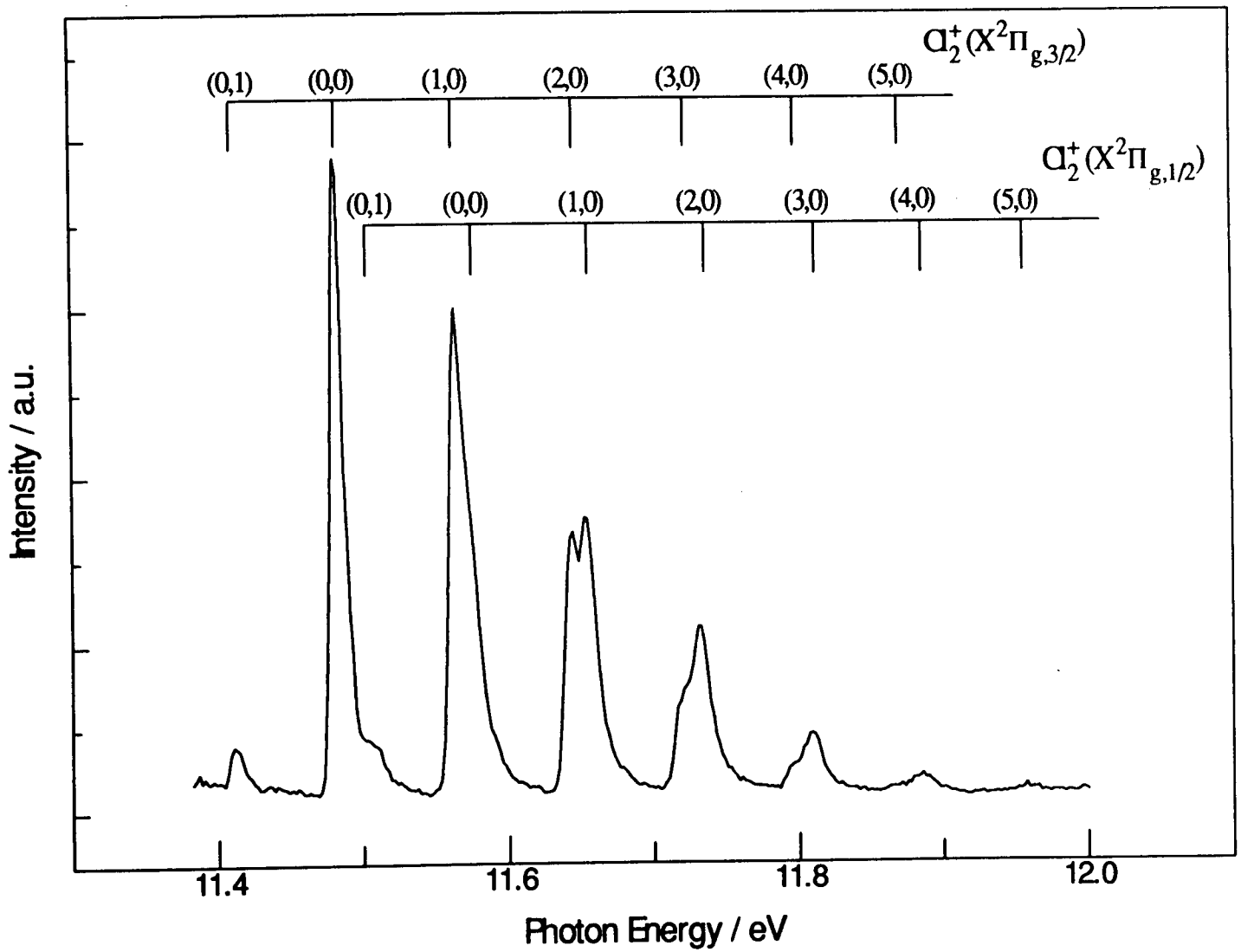

Figure 4.3 A high resolution (~11 meV at 11.5 eV) threshold photoelectron spectrum of Cl_2 covering the low vibrational bands of the two spin-orbit components of the $X\ ^2\Pi_{g,i}$ ionic state.

calculated transition energies are shown in Table 4.3. The predicted vibrational band positions agree very well with the experimental spectral features shown in Figure 4.3.

The relative vibrational intensities of the first six vibrational bands shown in Figure 4.3 are given in Table 4.2. These can be compared with those found in the He(I) photoelectron spectrum [17] and those calculated from Franck-Condon factors for the transition between Cl_2^+ ($X\ ^2\Pi_{g,i}$) $\leftarrow$ Cl_2 ($X\ ^1\Sigma_g^+$) which are also given in Table 4.2. From the relative intensity distribution, it would seem as though autoionisation plays some role in populating the lower vibrational levels of the $X\ ^2\Pi_{g,i}$ ionic state in the TPE spectrum. Although the appearance of the overall band is significantly different in the threshold spectrum compared with the conventional PE spectrum [17] and would seem to suggest a larger role, this can be accounted for in the difference in resolution achieved in the two studies.

4.3.2 The TPE Spectrum of Cl_2 between 12.25 and 13.25 eV

The TPE spectrum of Cl_2 in the 12.25 - 13.25 eV range is shown in Figure 4.4. It consists of a series of triplet peaks which have been assigned to partially resolved vibrational bands of the two spin-orbit components of the $X\ ^2\Pi_{g,i}$ ionic state of the $^{35,35}Cl_2$ isotopomer of chlorine along with the weaker $^{35,37}Cl_2$ isotopomer. The vibrational band assignments were made by fitting the observed peak positions for the two spin-orbit components of the $^{35,35}Cl_2$ isotopomer to third order Dunham expressions (see Table 4.8) and then introducing the reduced mass dependence into the Dunham expression to generate the $^{35,37}Cl_2$ isotopomer peak positions. The observed and calculated peak positions for the $^{35,37}Cl_2$ isotopomer are shown in Table 4.4 with the observed and calculated peak positions for the $^{35,35}Cl_2$ isotopomer shown in Table 4.3. The observation of $X\ ^2\Pi_{g,i}$ vibrational bands in this region of the spectrum, where Franck-Condon factors are of the order of 10^{-10} or less, implies that autoionisation processes must be involved. The origin of this vibrational structure and the neutral excited Rydberg states involved will be discussed in section 4.3.5. Although the overall profile of the vibrational structure in this figure is approximately

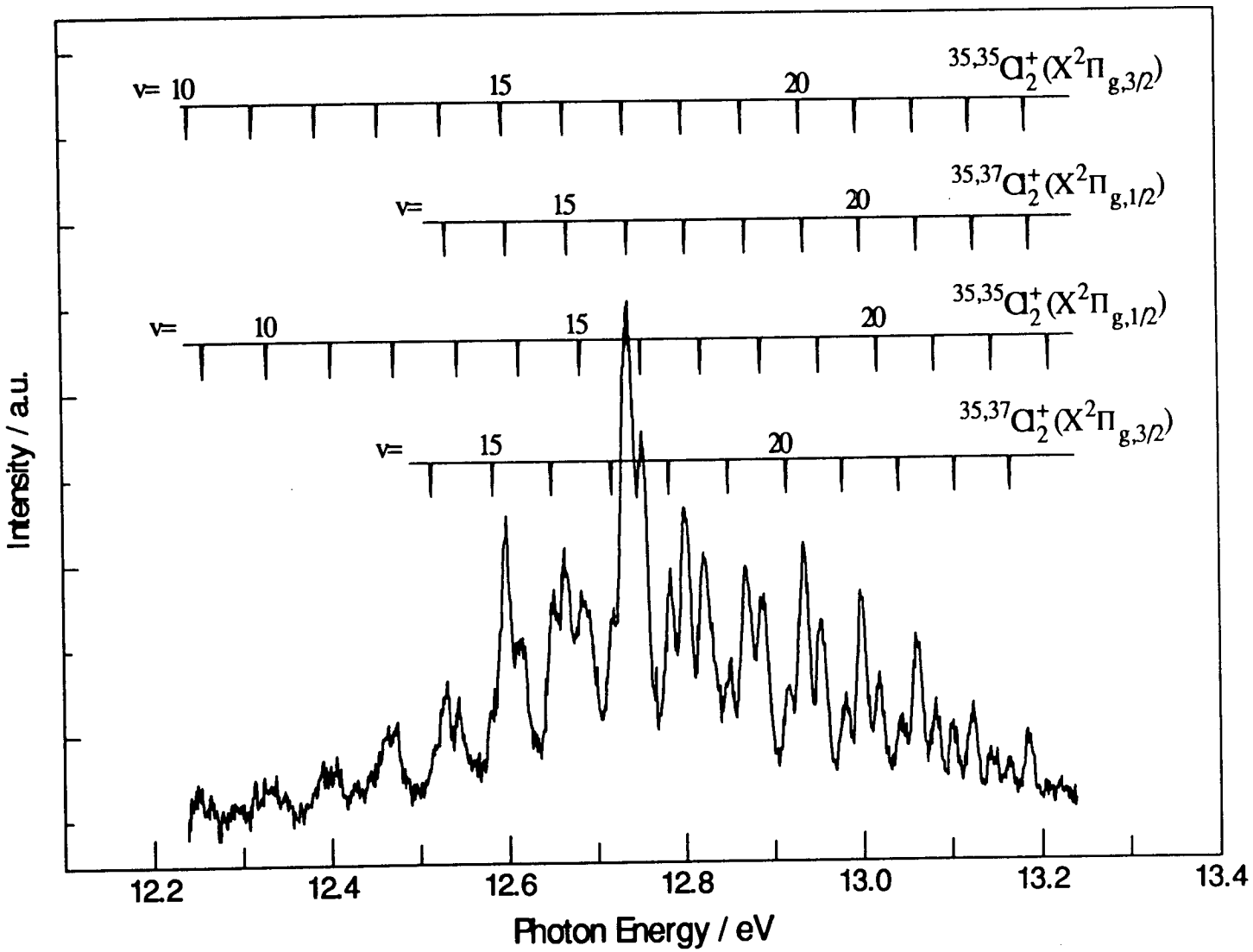

Figure 4.4 The extended vibrational structure of the two spin-orbit components of the $X\ ^2\Pi_{g,i}$ ionic state which arises as a result of autoionisation.

gaussian, the relative intensities of the individual vibrational bands are complicated by a number of factors. These include the natural abundance's of the molecular chlorine isotopomers, $^{35,35}Cl_2$ (~56%), $^{35,37}Cl_2$ (~38%) and $^{37,37}Cl_2$ (~6%), the overlapping vibrational bands and the efficiency of autoionisation from the different isotopomer Rydberg states.

Table 4.2 A comparison of the experimentally determined relative vibrational intensities in the X $^2\Pi_{g,i}$ ionic band of Cl_2 from TPES and He(I) PES with the calculated Franck-Condon factors (FCF) between Cl_2 (X $^1\Sigma_g^+$, v"=0) and Cl_2^+ (X $^2\Pi_{g,i}$, v')

Vibrational band (v', v") of X ($^2\Pi_{g,3/2}$) [a]	Relative vibrational intensities		FCF [b]
	TPES [c]	He(I) PES [d]	
(0,0)	82	37	44
(1,0)	100	89	100
(2,0)	77	100	90
(3,0)	46	60	47
(4,0)	19	23	15
(5,0)	9	8	2

[a] Vibrational bands after the (0,0) band of the X $^2\Pi_{g,3/2}$ state are blended with vibrational bands of the X $^2\Pi_{g,1/2}$ state.

[b] Sum of the relative Franck-Condon factors calculated for both spin-orbit states using known spectroscopic constants [1] and assuming that the spin-orbit splitting equals one vibrational quantum and equal weighting is taken for both spin-orbit components.

[c] Measured band intensities of superimposed spin-orbit components.

[d] Band intensities (areas) of unresolved spin-orbit components determined from Figure 4 of Reference [17].

Table 4.3 Experimental and calculated transition energies for the X $^2\Pi_{g,3/2}$ and X $^2\Pi_{g,1/2}$ ionic states of $^{35,35}Cl_2$.

v'	$^{35,35}Cl_2^+$ X $^2\Pi_{g,3/2}$ transition energy / eV		$^{35,35}Cl_2^+$ X $^2\Pi_{g,1/2}$ transition energy / eV	
	Experimental [a]	Calculated [b]	Experimental [a]	Calculated [b]
0	11.481	11.483	–	11.576
1	–	11.562	11.652	11.654
2	11.644	11.641	11.733	11.732
3	–	11.719	11.809	11.809
4	–	11.796	11.886	11.885
5	–	11.873	–	11.961
6	–	11.948	–	12.036
7	–	12.023	–	12.111
8	–	12.098	–	12.184
9	–	12.171	–	12.258
10	–	12.244	–	12.330
11	–	12.316	–	12.402
12	–	12.387	12.472	12.473
13	–	12.458	12.543	12.544
14	12.528	12.528	12.613	12.614
15	12.597	12.597	12.686	12.683
16	12.666	12.666	12.752	12.751
17	12.736	12.733	12.822	12.819
18	12.801	12.800	12.887	12.886
19	12.869	12.867	12.952	12.952
20	12.933	12.932	13.018	13.018
21	12.998	12.997	13.081	13.082
22	13.060	13.061	13.145	13.147
23	13.122	13.124	–	13.210
24	13.185	13.187	13.267	13.272
25	13.246	13.248	13.333	13.334
26	13.308	13.309	13.393	13.395
27	13.369	13.370	–	13.455
28	13.432	13.429	13.516	13.514
29	13.491	13.488	13.577	13.573
30	13.550	13.547	13.635	13.631
31	13.606	13.604	13.689	13.688
32	13.663	13.660	13.747	13.744
33	13.714	13.716	13.800	13.799
34	13.774	13.771	13.854	13.853
35	13.827	13.825	13.905	13.907
36	13.878	13.879	13.958	13.959
37	13.932	13.932	–	–
38	13.981	13.984	–	–
39	14.040	14.036	–	–
40	–	14.086	–	–
41	14.136	14.136	–	–

[a] Uncertainty ± 0.003 eV.

[b] Calculated from a third order Dunham fit of the experimental vibrational band positions, uncertainty ± 0.003 eV

Table 4.4 Experimental and calculated transition energies for the X $^2\Pi_{g,3/2}$ and X $^2\Pi_{g,1/2}$ ionic states of $^{35,37}Cl_2$.

v'	$^{35,37}Cl_2^+$ X $^2\Pi_{g,3/2}$ transition energy / eV		$^{35,37}Cl_2^+$ X $^2\Pi_{g,1/2}$ transition energy / eV	
	Experimental [a]	Calculated [c]	Experimental [a,b]	Calculated [c]
13	–	12.445	12.530	12.531
14	12.516	12.514	12.599	12.600
15	12.579	12.583	12.665	12.668
16	12.651	12.650	12.736	12.736
17	12.719	12.717	12.801	12.803
18	12.784	12.783	12.868	12.869
19	12.850	12.849	12.933	12.935
20	12.915	12.914	12.998	12.999
21	12.980	12.978	12.061	13.064
22	13.042	13.041	12.122	13.127
23	13.101	13.104	12.185	13.190
24	13.165	13.166	–	–

[a] Uncertainty ± 0.003 eV.

[b] The $^{35,37}Cl_2^+$ X $^2\Pi_{g,1/2}$ vibrational bands overlay the $^{35,35}Cl_2^+$ X $^2\Pi_{g,3/2}$ vibrational bands and some uncertainty is therefore present in these values.

[c] These values are calculated from the $^{35,35}Cl_2^+$ X $^2\Pi_{g,i}$ Dunham expressions by introducing the reduced mass dependence.

4.3.3 The TPE Spectrum of Cl_2 between 13.15 and 15.0 eV

The TPE spectrum of Cl_2 in the 13.15-15.0 eV range, shows two highly structured vibrational band systems, the higher energy one of which is associated with the first excited A $^2\Pi_{u,i}$ ionic state of Cl_2, as identified in Figure 4.5. The vibrational structure below the A $^2\Pi_{u,i}$ ionic state can again be assigned to high vibrational levels associated with the two spin-orbit components of the X $^2\Pi_{g,i}$ ionic state. The simplified appearance of this vibrational structure compared to the triplet structure observed to lower energy arises through the complete overlap of the two spin-orbit components of the $^{35,37}Cl_2$ isotopomer with the two spin-orbit components of the more intense $^{35,35}Cl_2$ isotopomer. The $^{35,35}Cl_2$ isotopomer vibrational band positions of the two spin-orbit components of the X $^2\Pi_{g,i}$ ionic state in this region are tabulated in

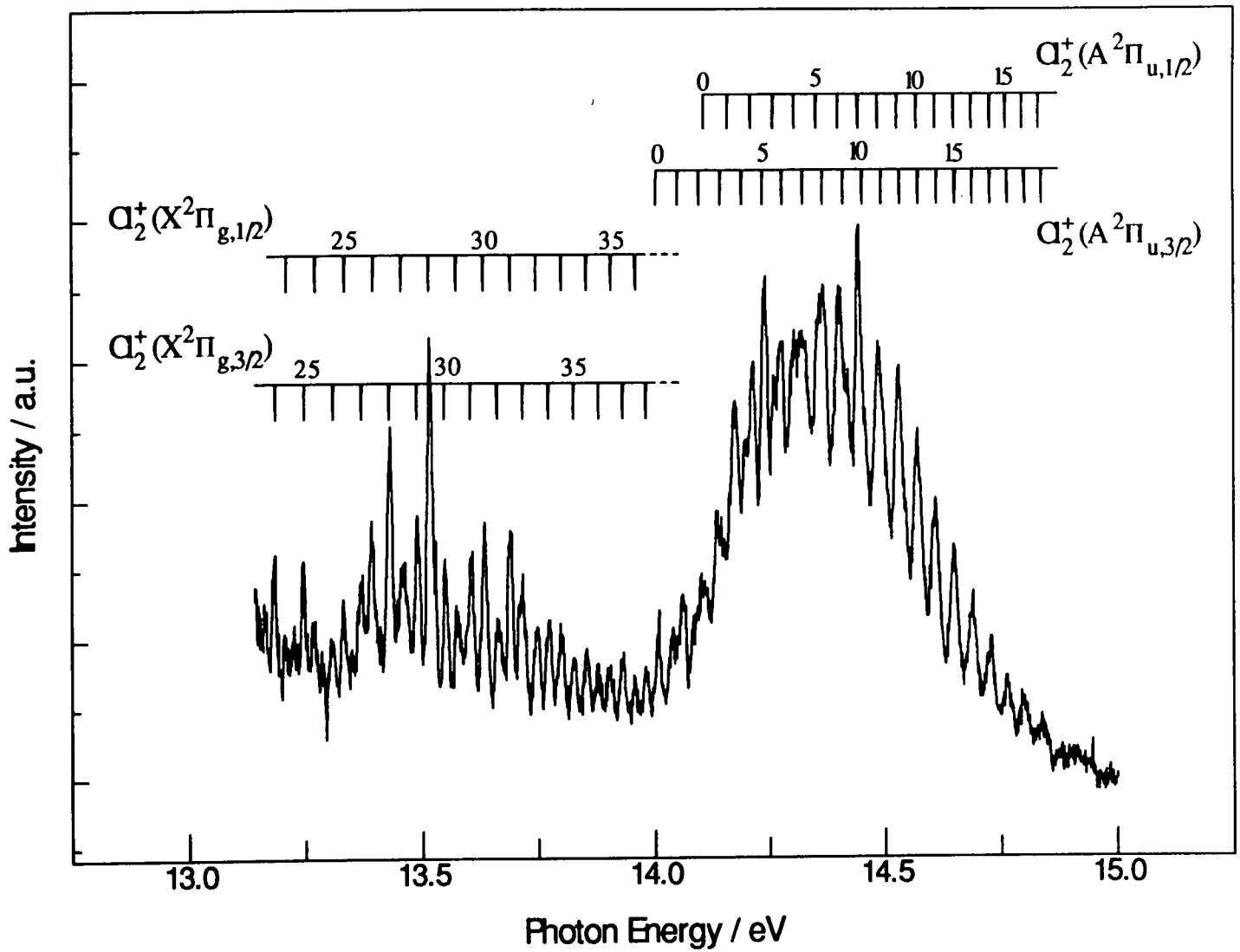

Figure 4.5 The threshold photoelectron spectrum of Cl_2 showing the A $^2\Pi_{u,i}$ band system of Cl_2^+ and high vibrational bands of the X $^2\Pi_{g,i}$ ionic state.

Table 4.3 along with the calculated peak positions from a third order Dunham fit of all the vibrational data. The third order Dunham fits generate ω_e values of 80.1 meV (646.0 cm^{-1}) for the X $^2\Pi_{g,3/2}$ spin-orbit component and 78.7 meV (634.8 cm^{-1}) for the X $^2\Pi_{g,1/2}$ spin-orbit component. These vibrational constants, along with all the other spectroscopic constants derived from the analysis of the vibrational data for the X $^2\Pi_{g,i}$ ionic states are given in Table 4.8. A summary of relevant spectroscopic data from optical emission studies and previous photoelectron studies is also included in Table 4.8.

The TPE spectrum of the A $^2\Pi_{u,i}$ vibrational band shown in Figure 4.5 has very similar vibrational structure to that observed in both He(Iα) and Ne(Iβ) photoelectron investigations of Cl_2 [17]. The band can be split into two sections; the lower energy side of which consists of congested irregular vibrational structure whereas the higher energy side seemingly consists of a single vibrational progression. This has been attributed by de Lange and van Lonkhuyzen [17] to the overlapping vibrational progressions of the $^2\Pi_{u,3/2}$ and $^2\Pi_{u,1/2}$ spin-orbit components, whose spin-orbit splitting coincides closely with an integral number of vibrational quanta. A high resolution optical emission study of the A $^2\Pi_{u,i}$ - X $^2\Pi_{g,i}$ transition by Tuckett and Peyerimhoff [23] resulted in the construction of Deslandres tables for both spin-orbit components. However, they were unable to assign vibrational quantum numbers due to the irregularity of the vibrational spacings. A very early emission study of Cl_2^+ by Huberman [20] had also found the vibrational structure to be irregular, even though the rotational structure was characteristic of a pure Π - Π transition. Huberman suggested that ionic states arising from the configuration $(\sigma_g)^2(\pi_u)^4(\pi_g^*)^2(\sigma_u^*)^1$ i.e. $^2\Sigma_u^+$ and $^2\Delta_u$ states, could be responsible for the extensive vibrational perturbations. Further detailed calculations by Tuckett and Peyerimhoff [23] and Boerrigter et al. [28] have shown that the A $^2\Pi_u$ ionic state is crossed near its origin by some states arising from the configuration above and that the localised spin-orbit interactions between the crossing states was likely to be vibrational in nature.

Van Lonkhuyzen and de Lange, in a conventional photoelectron study of Cl_2 [17], were successful in assigning vibrational quantum numbers to Tuckett and Peyerimhoff's Deslandres tables [23] using a knowledge of the term values, T_e, for both emission components. Their assignment placed the first row of Tuckett and Peyerimhoff's $^2\Pi_{u,3/2}$ Deslandres table equal to $v' = 4$ and the first row of the $^2\Pi_{u,1/2}$ Deslandres table equal to $v' = 2$, with a possible error of one in each of the quantum numbers. These assignments placed the band origin of the A $^2\Pi_{u,3/2}$ spin-orbit component very near the onset of their photoelectron band, at 14.049 eV. Although the high resolution threshold photoelectron spectrum shown in Figure 4.5, is very similar to van Lonkhuyzen and de Lange's photoelectron spectrum and the vibrational assignments agree, it also includes a very narrow vibrational peak at 14.008 eV which does not fit into an extension of either of the two X $^2\Pi_{g,i}$ ionic state vibrational progressions. Assigning this as the new band origin of the X $^2\Pi_{u,3/2}$ ionic state would necessitate an increase of one in the vibrational numbering compared with that suggested by van Lonkhuyzen and de Lange [17]. With this new vibrational assignment, a second order Dunham expression was fitted to the emission data of Tuckett and Peyerimhoff [23] as tabulated in Table 4.5. Although the threshold experimental data could have been used in a vibrational fit, it was decided that the limited number of resolved vibrational bands (v'=0-7) in the threshold spectrum would reduce the accuracy of the fit compared with the wavenumber resolution and wide range of vibrational levels (v'=5-20) available in the emission data. The vibrational perturbations present in the system, however, do add some uncertainty to the constants. Table 4.5 shows the vibrationally reassigned emission data belonging to Tuckett and Peyerimhoff along with the resolved threshold vibrational band positions and the calculated band positions from the constants obtained from the second order Dunham fit (see Table 4.8). The new vibrational assignment results in an experimental adiabatic ionisation potential of 14.008 ± 0.003 eV for the A $^2\Pi_{u,3/2}$ spin-orbit component and a calculated ω_e of 48.1 meV (388 cm^{-1}). These spectroscopic constants are listed along with the other derived constants for this state in Table 4.8. The calculated vibrational band positions have been used to make the vibrational band assignment in the A $^2\Pi_{u,3/2}$ spin-orbit component, as shown in Figure 4.5.

Table 4.5 Experimental and calculated transition energies of the A $^2\Pi_{u,3/2}$ ionic state of Cl_2.

v'	Tuckett and Peyerimhoff's emission transition energies / eV [a]	Calculated transition energies / eV	Threshold transition energies / eV [b] [c]
0	–	14.002	14.008
1	–	14.049	14.058
2	–	14.096	14.101
3	–	14.142	14.145
4	–	14.188	14.196
5	14.235	14.233	14.238
6	14.272	14.277	14.276
7	14.328	14.321	14.320
8	14.366	14.364	
9	14.403	14.407	
10	14.455	14.448	
11	14.491	14.490	
12	14.528	14.531	
13	14.576	14.571	
14	14.612	14.610	
15	14.646	14.649	
16	14.692	14.687	
17	14.72	14.725	
18	–	14.762	
19	14.802	14.798	
20	14.836	14.834	

[a] Tuckett and Peyerimhoff's reassigned emission transition energies are combined with the calculated term values of the vibrational levels of the X $^2\Pi_{g,3/2}$ spin-orbit component given in Table 4.3 to generate the values shown here.

[b] The vibrational bands of the A $^2\Pi_{u,3/2}$ spin-orbit component after v'=7 are blended with the vibrational bands of the A $^2\Pi_{u,1/2}$ spin-orbit component.

[c] Uncertainty ± 0.003 eV.

The overlapping vibrational progressions in the A $^2\Pi_{u,i}$ band and the fact that the spin-orbit splitting is not well known, means that the band origin of the A $^2\Pi_{u,1/2}$ spin-orbit vibrational progression is impossible to identify in the threshold spectrum shown in Figure 4.5. It is therefore not clear whether a similar reassignment of the vibrational numbering is required. However, by comparing the spin-orbit splitting in the A $^2\Pi_{u,i}$ ionic state calculated using the two possible vibrational assignments for the A $^2\Pi_{u,1/2}$ spin-orbit component, with the 766 cm^{-1} spin-orbit splitting in the X $^2\Pi_{g,i}$ ionic state of Cl_2 determined in this study, it may be possible to shed some light on the possible origin. Using the original vibrational quantum number assignment of van Lonkhuyzen and de Lange [17] for the A $^2\Pi_{u,1/2}$ spin-orbit component and our new vibrational assignment in the A $^2\Pi_{u,3/2}$ spin-orbit component, the spin-orbit splitting is calculated to be 790 cm^{-1}, an increase of 3 % compared with the ground state. Alternatively, if the vibrational numbering of the A $^2\Pi_{u,1/2}$ spin-orbit component is increased by +1 in accord with the lower spin-orbit component, the spin-orbit splitting is calculated to be 476 cm^{-1}, a decrease of 38 % compared with the ground state. These results can be compared with the spin-orbit splittings and percentage changes in the X $^2\Pi_{g,i}$ and A $^2\Pi_{u,i}$ ionic states of the other halogen systems shown in Table 4.6 to see if a trend is exhibited.

Table 4.6 The spin-orbit splittings and percentage changes in the X $^2\Pi_{g,i}$ and A $^2\Pi_{u,i}$ states of the halogens.

	Spin-orbit splitting in the X $^2\Pi_{g,i}$ ionic state	Spin-orbit splitting in the A $^2\Pi_{u,i}$ ionic state	% change	Ref.
Iodine	5130 cm^{-1}	6694 cm^{-1} [a)]	~ +30%	This work
Bromine	2815 cm^{-1}	3420 cm^{-1}	+21%	This work
Chlorine	766 cm^{-1}	790 cm^{-1}	+3%	This work
"	"	476 cm^{-1}	-38%	This work
Fluorine	337 cm^{-1}	252 cm^{-1}	-25%	[22]

[a)] Spin-orbit splitting measured between vertical ionisation energies.

The overall trend suggests a spin-orbit splitting of 790 cm^{-1} in the A $^2\Pi_{u,i}$ ionic state of Cl_2, favouring the original vibrational numbering of van Lonkhuyzen and de Lange [17]. This therefore makes the spin-orbit splitting approximately equal to two vibrational quanta of the A $^2\Pi_{u,i}$ ionic state in agreement with previous predictions. Based on the above discussion and using the same method as outlined above for the A $^2\Pi_{u,3/2}$ spin-orbit component, a second order Dunham fit generated an adiabatic ionisation potential of 14.106 ± 0.003 eV along with an ω_e of 52.2 meV (421 cm^{-1}) for the A $^2\Pi_{u,1/2}$ ionic state. These spectroscopic vibrational constants are given in Table 4.8. However, it should be noted that the vibrational perturbations present in the system do add some uncertainty to the vibrational Dunham constants derived from the fit.

4.3.4 The TPE Spectrum of Cl_2 between 15.0 and 17.0 eV

The TPE spectrum between 15 and 17 eV shown in Figure 4.6 shows a broad band with resolved vibrational structure in the region of the band maximum which represents the B $^2\Sigma_g^+$ ionic state of Cl_2^+. The most recently reported He(I) photoelectron study [17] included a very similar band profile for this state. Theory indicates that this state arises from an avoided crossing of two $^2\Sigma_g^+$ diabatic potentials [27] and it is therefore possible that the appearance of this band may result from a superposition of the vibrational bands of both states. Approximately seven vibrational levels are identified around the band maximum with an average vibrational spacing of 30 meV (242 cm^{-1}). No attempt to identify the vibrational numbering was made and the transition energies are tabulated in Table 4.7. The adiabatic ionisation energy of 15.70 eV, determined by van Lonkhuyzen and de Lange [17], appears to lie in a region of the TPE spectrum which has an underlying background connected to an extension of the A $^2\Pi_{u,i}$ ionic state (see Figure 4.2). This background signal is the result of the autoionisation of Rydberg states converging on the B $^2\Sigma_g^+$ ionic state which populate high vibrational levels of the A $^2\Pi_{u,i}$ ionic state. Evidence for the presence of these autoionising Rydberg states is discussed below. The spectroscopic constants for this state are given in Table 4.8.

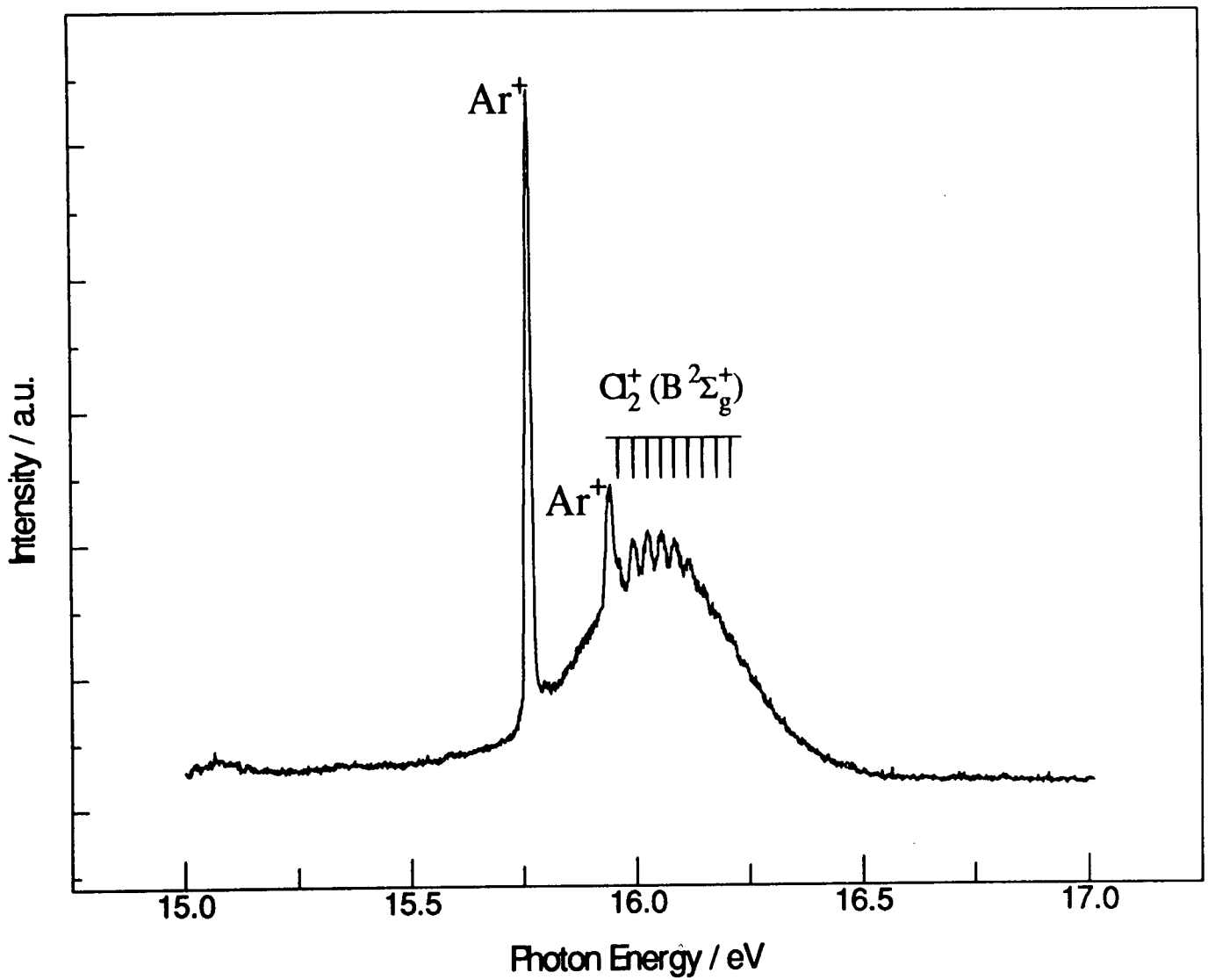

Figure 4.6 The threshold photoelectron spectrum of Cl_2 showing the $B\ ^2\Sigma_g^+$ ionic band of Cl_2 with resolved vibrational structure. The Ar^+ lines were used for calibration.

Table 4.7 Experimental vibrational transition energies for the B $^2\Sigma_g^+$ ionic state of Cl_2.

Vibrational peak No.	Experimental B $^2\Sigma_g^+$ state
1	15.961
2	15.992
3	16.024
4	16.054
5	16.084
6	16.114
7	16.145

[a] Uncertainty ± 0.004 eV.

4.3.5 The Origin of the Observed Autoionising Structure between 11.4 and 17 eV

The main autoionising structure in the valence ionisation region of Cl_2 occurs between the main X $^2\Pi_{g,i}$ and A $^2\Pi_{u,i}$ ionic bands and involves the population of high vibrational levels of the ground X $^2\Pi_{g,i}$ ionic state of Cl_2. Vibrational structure has previously been observed in this region of the spectrum by Reddish et al. [33] in a photoelectron investigation utilising synchrotron excitation radiation between 13.6-15.0 eV. From the appearance of the band structure in Figure 4.2, there is a clear indication of the presence of several band systems. Since this structure is believed to arise through both vibrational and spin-orbit autoionisation of neutral Rydberg states coupled to the ionisation continuum, it is possible to make an attempt to identify the Rydberg states responsible. The intensity profile of the autoionising vibrational structure indicates the Franck-Condon factors for the autoionising Rydberg states, which are in general very similar to those of the ionic state to which the Rydberg converges. The vibrational peak positions within the profile, on the other hand, yield the term values for the final vibrational states of the X $^2\Pi_{g,i}$ ionic state. From an inspection of the autoionising vibrational structure lying between the main X $^2\Pi_{g,i}$ and A $^2\Pi_{u,i}$ ionic bands, there appears to be four visible band profiles which have been

Table 4.8 Summary of the spectroscopic constants for the valence ionic states of Cl_2.

Molecule Cl_2	AIE (eV)	VIE (eV)	ω_e (cm^{-1})	$\omega_e x_e$ (cm^{-1})	$\omega_e y_e$ $x10^{-3}$ (cm^{-1})	r_e (Å)	Spin-orbit splitting (cm^{-1})	Ref.
Cl_2 ($X\ ^1\Sigma_g^+$)	–	–	559.72	-2.675	–	1.9879	–	[1]
($X\ ^2\Pi_{g,3/2}$)	11.481 [a] ±0.003	11.481 ±0.003	646.0	-2.9	-0.9	–	766±48 [b]	this work
	11.480 ±0.005	11.559 ±0.005	~645	~-3	–	1.890 ±0.010	725±25	[17]
	–	–	645.61	-3.015	–	1.8917	–	[20]
	11.49	–	645±40	–	–	1.892	645±40	[14] [c]
	11.51 ±0.01	11.59 ±0.01	645±20	–	–	–	645±16	[15] [c]
	11.490	–	639	2.7	–	–	6949	[33]
($X\ ^2\Pi_{g,1/2}$)	11.576 [d] ±0.003	–	634.8	-2.3	-11.3	–	766±48 [b]	this work
	11.520 ±0.005	11.559 ±0.005	~645	~-3	–	1.890	725±25	[17]
	–	–	644.77	-2.988	–	1.8910	–	[20]
	11.577	–	639	2.7	–	–	694±9	[33]
($A\ ^2\Pi_{u,3/2}$)	14.008 [a] ±0.003	–	388	-2.5	–	–	790±48	this work
	14.04 ±0.05	14.393 ±0.003	~370	~-2	–	2.21 ±0.02	550±100	[17]
	–	–	~310	–	–	~2.25	–	[20]
	14.0 [e]	~14.43	–	–	–	–	–	[14] [c]
	13.96 ±0.02	14.40 ±0.02	323±20	–	–	–	~645	[15] [c]
($A\ ^2\Pi_{u,1/2}$)	14.106 [d] ±0.003	–	421	-4.2	–	–	790±48	this work
	–	–	~310	–	–	~2.25	–	[20]
($B\ ^2\Sigma_g^+$)	–	16.041 ±0.01	~240 [f]	–		–	–	this work
	15.70 ±0.02	16.082 ±0.005	~280	~-2	–	2.30 ±0.01	–	[17]
	15.8 [e]	~16.10	–	–		–	–	[14]
	15.72 ±0.02	16.08 ±0.02	–	–		–	–	[15]

[a] Experimental adiabatic ionisation energy. [b] Spin-orbit splitting measured between v'=0 bands.
[c] Average values over both spin-orbit components. [d] Calculated value from Dunham expression, see text. [e] Band onset. [f] Average value.

labelled J, K, L and M in Figure 4.2. The labelling is based on similar labelling of identified $[(\sigma_g)^2(\pi_u)^3(\pi_g^*)^4]$ $ns\sigma_g$ $^1\Pi_u$ Rydberg states converging on the A $^2\Pi_{u,i}$ ionic state of Cl_2 which were detected in a Cl_2 energy loss spectrum by Stubbs et al. [34].

An investigation of the photoionisation spectrum of Cl_2 by monitoring both ion-pair mass channels (Cl^++Cl^-) and the molecular ion (Cl_2^+) mass channel, revealed band profiles which closely resembled those exhibited in the threshold spectrum between 12.3 and 14.0 eV [35]. The close correlation between the structural features in the photoionisation spectra recorded by Berkowitz et al. [35] and the autoionising structure in the threshold photoelectron spectrum suggests that the Rydberg states responsible for these features are the same as the Rydberg states detected in the energy loss spectrum. However, there is not an exact correlation between the peak positions within the overall band profiles of the threshold spectrum and the other spectra. This is because the peaks in the threshold spectra reflect the term values of vibrational levels of the ground state of the molecular ion, whereas those in the energy loss spectrum and molecular ionisation yield spectrum, for example, represent the term values of the vibrational levels of the neutral Rydberg states converging on the A $^2\Pi_{u,i}$ ionic state of Cl_2.

With this information it is now possible to attempt an assignment of the Rydberg states detected indirectly in our TPE spectrum with those observed directly by other methods. A schematic potential energy diagram of the X and A ionic states of Cl_2 along with the Rydberg states based on the analysis of Stubbs et al. is shown in Figure 4.7. The A $^2\Pi_{u,i}$ ionic state potential is described by a Morse potential with an assumed dissociation energy of ~1.85 eV and an ω_e of 388 cm^{-1} (see Table 4.8) whereas the X $^2\Pi_{g,i}$ ionic state potential was derived from the data of Huberman [20]. The A state Rydberg potentials are identical to the A state ionic potential but with T_e values defined by Stubbs et al. [34]. The vibrational J, L and M-series, in the energy loss spectra, were identified by Stubbs et al. [34] as the 5, 6 and 7$s\sigma_g$ $^1\Pi_u$ Rydberg states converging on the A $^2\Pi_{u,i}$ ionic state through their average vibrational spacings and quantum defects. This assignment was later confirmed by Berkowitz et al. [35]

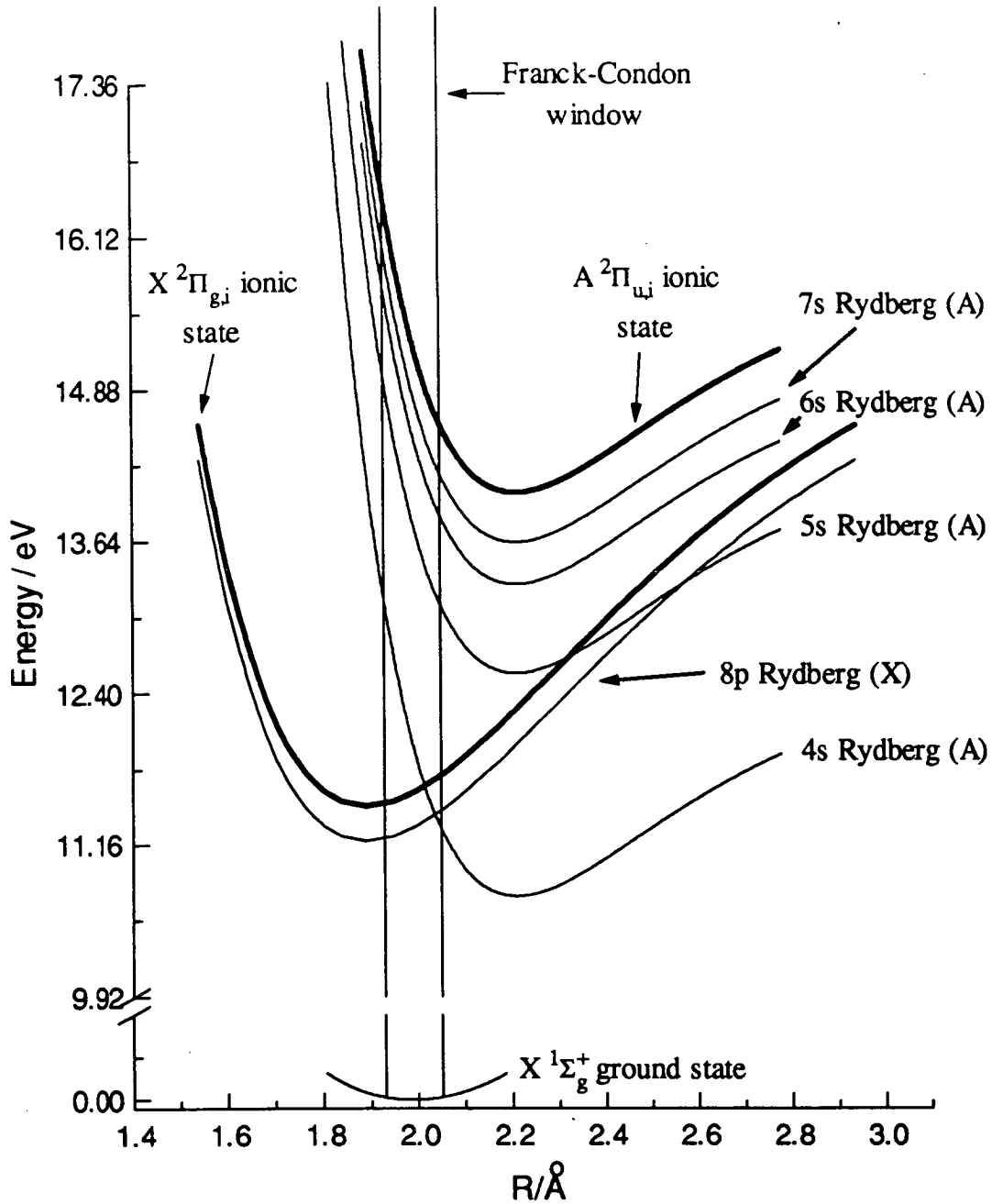

Figure 4.7

A schematic potential energy diagram of some of the $ns\sigma_g$ $^1\Pi_u$ Rydberg states converging on the A $^2\Pi_{u,i}$ ionic state of Cl_2. The 5s, 6s and 7s Rydbergs are proposed to be involved in producing the autoionising structure observed in the threshold spectrum between the X and A ionic states.

using the higher resolution photoelectron data of van Lonkhuyzen and de Lange [17]. The vibrational K-series, which was not assigned in the energy loss study [34], was proposed by Berkowitz et al. [35] to be related to the J-series. The fact that there are Rydberg series converging on both the A $^2\Pi_{u,3/2}$ and A $^2\Pi_{u,1/2}$ spin-orbit states suggests that the K-series represents a Rydberg state converging on the A $^2\Pi_{u,1/2}$ state of the ion, while the J-series represents a Rydberg converging on the lower A $^2\Pi_{u,3/2}$ spin-orbit component. It is interesting to note that the K-series is weaker in intensity than the J-series in both the energy loss spectrum and the threshold spectrum (see Figure 4.2), reflecting the differences in transition probabilities for excitation of the individual Rydberg states.

The intensity profile and width of the J-series in the energy loss spectrum of Stubbs et al. [34], raises two additional points. Firstly, the most intense peak in the J-series in the energy loss spectrum occurs at 12.834 eV, while the maximum in the threshold photoelectron profile occurs at 12.736 eV. Secondly, the band onset in the energy loss spectrum profile (12.565 eV), which is assigned as the band origin, is significantly higher than the band onset in the threshold photoelectron profile (~12.24 eV). If the assignment of the J-series to the $5s\sigma_g$ $^1\Pi_u$ Rydberg state is assumed to be correct, then the $4s\sigma_g$ $^1\Pi_u$ Rydberg state which would have a band maximum at ~10.08 eV can be discounted as causing the observed differences. With Berkowitz et al. [35] having already questioned the Rydberg vibrational assignments of Stubbs et al. and the fact that there is this large discrepancy between the band onset in the threshold spectrum and the band onset in the energy loss spectrum, it is suggested that the onset of the Rydberg series is shifted to 12.244 eV. This is the onset of the threshold photoelectron band and is equivalent to a shift of approximately seven vibrational quanta from that reported by Stubbs et al. [34]. With an adiabatic ionisation potential of the A $^2\Pi_{u,3/2}$ ionic state of 14.008 eV and the suggested value for the onset of the J-series Rydberg state, an effective quantum number of 2.777 can be calculated. For a principal quantum number of 5 this yields a quantum defect of 2.223, which is reasonable for an s-type Rydberg electron. Therefore the "extended" J-series and K-series can be assigned to the Rydberg states, $[(\sigma_g)^2(\pi_u)^3(\pi_g^*)^4]_{3/2}$ $5s\sigma_g$

($^1\Pi_u$) and $[(\sigma_g)^2(\pi_u)^3(\pi_g^*)^4]_{1/2}$ $5s\sigma_g$ ($^1\Pi_u$), respectively. A possible reason for the incorrect assignment of the vibrational progression by Stubbs et al. is the low anharmonicity constant of the progression which makes it very difficult to determine accurate vibrational numbering. It is very probable that vibrational assignments given by Stubbs et al. for the K, L and M Rydbergs also require to be shifted. However, a reassignment is impossible due to the fact that the band onsets for these series cannot be determined from the threshold spectrum. The L- and M-series have been assigned by both Berkowitz et al. and Stubbs et al. to the $6s\sigma_g$ ($^1\Pi_u$) and the $7s\sigma_g$ ($^1\Pi_u$) Rydberg states, respectively. However, based on the similar intensity profiles between the J- and K-series and between the L- and M-series and the similar overall width compared with the $^2\Pi_{u,i}$ band, it is tempting to suggest that the L- and M-series in both the energy loss spectrum and the TPE spectrum are related in the same sense as the J- and K-series, i.e. the same type of Rydberg state ($6s\sigma_g$) with differing core configurations (3/2 and 1/2, respectively).

The origin of the background signal in the threshold photoelectron spectrum between the A and B bands appears to be connected with Rydberg states converging on the B $^2\Sigma_g^+$ state. In the study of ion-pair formation [35], a broad feature was observed with some structure superimposed on it at the peak maximum (~16.1-16.2 eV), reminiscent of the B state band in the He(I) study of van Lonkhuyzen and de Lange [17]. However, the ion-pair spectrum also exhibited a very long tail to lower energy which extended down to and merged with the high-energy tail of the structured region at ~ 14.4 eV. The similarity between the ion-pair spectrum and the threshold spectrum again points to the involvement of the same Rydberg states even though the species detected are quite different. The broad nature of the signals in both types of spectra precludes any identification of the Rydberg states, except that they would necessarily be of $^1\Sigma_g^+$ or $^1\Pi_g$ symmetry.

A wide variety of autoionising Rydberg states could be involved in enhancing the low vibrational bands of the X $^2\Pi_{g,i}$ ionic state in the 11.4-12.0 eV range. However, the obvious candidate by analogy with the series producing the

extensive structure between the X and A bands would be the $4s\sigma_g$ ($^1\Pi_u$) Rydberg state converging on the A $^2\Pi_{u,i}$ ionic state. With an adiabatic ionisation potential of 14.008 eV for the A $^2\Pi_{u,3/2}$ state and a quantum defect of 2.223, the band origin of the $4s\sigma_g$ ($^1\Pi_u$) Rydberg state is calculated to be 9.699 eV, well below the energy region under consideration. However, theory [27] predicts that this $^1\Pi_u$ Rydberg state interacts strongly with a $^1\Pi_u$ ion-pair state with a $(\sigma_g)^1(\pi_u)^3(\pi_g)^4(\sigma_u)^2$ configuration, resulting in an avoided crossing. At higher energy this mixed Rydberg/ion-pair potential experiences a further avoided crossing with a $5p\sigma_g$ Rydberg state and the p-character of the mixed Rydberg/ion-pair state in the energy region of the X $^2\Pi_{g,i}$ ionic state of Cl_2 might well be responsible for it's role in producing autoionising structure. Alternatively, *n*p and *n*f Rydberg states converging on the X $^2\Pi_{g,i}$ ionic state could be involved. These Rydberg states have very similar potentials to the X $^2\Pi_{g,i}$ ionic state which means that only their low vibrational levels will be populated. Autoionisation into the low vibrational levels (v=0,1 and 2) of the ion, as observed experimentally (see the vibrational band intensities shown in Table 4.2), would therefore require the low Rydberg vibrational levels to be isoenergetic with the low vibrational levels in the ion. This of course places restrictions on the Rydbergs involved and as a result of Franck-Condon factors, implies that only Rydberg states with band origins, one or two vibrational quanta below the adiabatic ionisation limit would be involved in the autoionisation process. In fact the most likely Rydbergs involved are those converging on the higher $^2\Pi_{g,1/2}$ spin-orbit component which spin-orbit autoionise into low vibrational levels of the X $^2\Pi_{g,3/2}$ ionic state. One possible Rydberg state converging on the ionisation threshold was observed in the energy loss study of Stubbs et al. [34] and assigned to the $[(\sigma_g)^2(\pi_u)^4(\pi_g^*)^3]$ $8p\sigma_u$ ($^1\Pi_u$) Rydberg state. However, energetically it was deemed to be too far below the ionisation limit to be involved in the autoionisation process.

A comparison of the relative intensities of the three main ionic bands in this threshold photoelectron study (see Figure 4.2) with those recorded in a He(I) photoelectron study [32] reveals that the relative intensity of the X $^2\Pi_{g,i}$ band is dramatically increased, compared with the two higher energy bands in the threshold

study. However, this can probably be put down to the effects of autoionisation enhancing the X band. This is supported by the fact that the intensity of the autoionising structure between the X and A bands is almost as intense as the A $^2\Pi_{u,i}$ band. However, this is not easily verified when the He(I) PES and threshold techniques have different photoionisation cross sections $\sigma(h\nu\text{-}E_j)$.

4.4 The Threshold Photoelectron Spectrum of Br_2

In many respects, the TPE spectrum of Br_2 parallels that of Cl_2, as might be expected. The complete valence ionisation threshold photoelectron spectrum of Br_2 (10.3-15.0 eV) is shown in Figure 4.8. The X $^2\Pi_{g,i}$, A $^2\Pi_{u,i}$, and B $^2\Sigma_g^+$ bands, familiar from conventional He(I) PE spectra [14,17,32] are labelled in the figure. The larger spin-orbit splitting in Br_2 allows the individual spin-orbit components of the X $^2\Pi_{g,i}$ ionic state to be well separated compared with Cl_2. One of the most striking features of the band structure in this spectrum is the well-resolved vibrational structure associated with the A $^2\Pi_{u,i}$ band compared to the very weak structure observed in the Ne(Iβ) photoelectron spectrum of van Lonkhuyzen and de Lange [17]. In addition, there is the clear presence of resolved autoionising structure running from the X $^2\Pi_{g,i}$ band into the onset of the A $^2\Pi_{u,i}$ band as found in Cl_2. However, the individual band profiles (I and II) are not as pronounced as in Cl_2. To a lesser extent, there also appears to be some contribution to the photoelectron signal between the A $^2\Pi_{u,i}$ and B $^2\Sigma_g^+$ bands due to autoionisation. A detailed analysis of all features found in the valence ionisation region of Br_2 are described below.

4.4.1 The TPE Spectrum of Br_2 between 10.3 and 12.4 eV

Figure 4.9 shows the high-resolution (~ 8 meV) TPE spectrum of Br_2 in the 10.3-12.4 eV range. The two well resolved vibrational progressions associated with the direct excitation of the two spin-orbit components of the X $^2\Pi_{g,i}$ state of Br_2^+ are

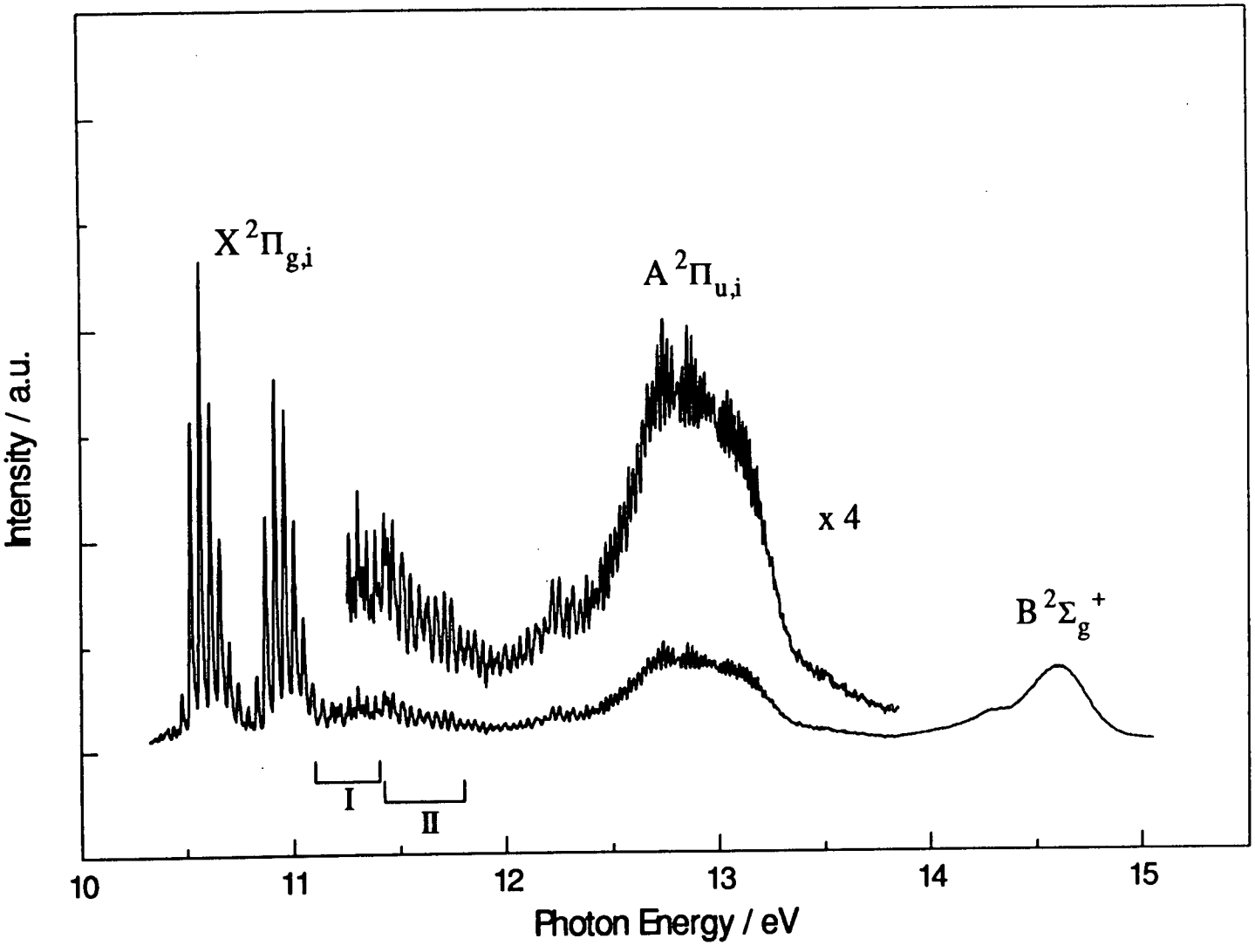

Figure 4.8 The threshold photoelectron spectrum of the valence ionisation region of Br_2 showing the X $^2\Pi_{g,i}$, A $^2\Pi_{u,i}$ and B $^2\Sigma_g^+$ bands of Br_2^+. The vibrational structure, identified by the bracketed regions I and II, is due to autoionisation processes and is discussed in the text.

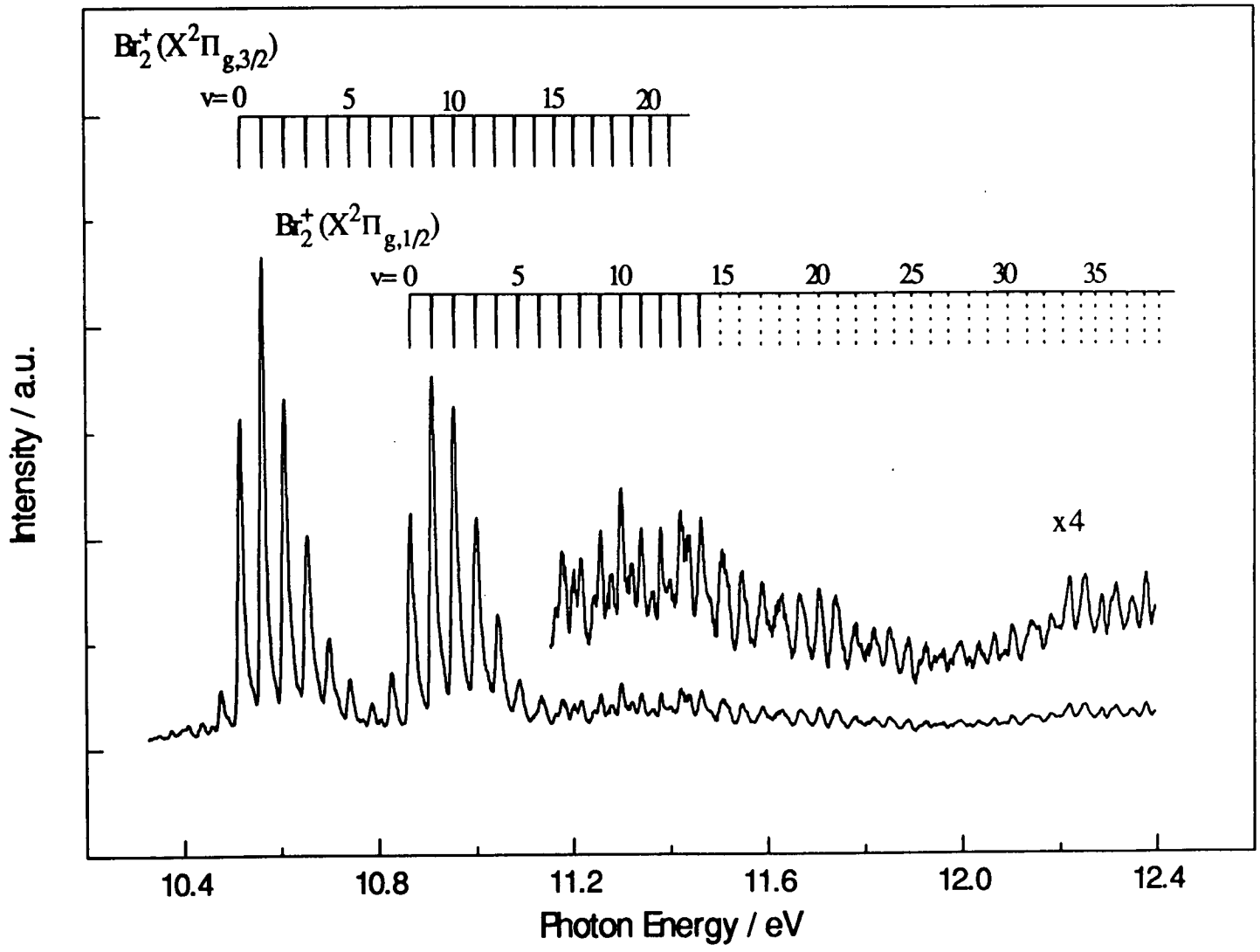

Figure 4.9 The high resolution (~8 meV at 10.6 eV) threshold photoelectron spectrum of Br_2 showing the assignment of the vibrational bands in the X $^2\Pi_{g,i}$ ionic state of Br_2, including the higher vibrational bands produced through autoionisation processes. The solid lines are based on Dunham expressions, while the dashed lines are based on observed peak positions.

very similar to those found in conventional photoelectron studies [17] although their intensities are reversed. The adiabatic ionisation energy of the lower X $^2\Pi_{g,3/2}$ spin-orbit state is measured as 10.518 ± 0.003 eV whereas it is 10.867 ± 0.003 eV for the higher X $^2\Pi_{g,1/2}$ spin-orbit state. From these values the spin-orbit splitting is determined to be 0.349 ± 0.006 eV (2815 cm^{-1}). Above these two bands, in the Franck-Condon region where the probability for direct transitions into vibrational levels of the X $^2\Pi_{g,i}$ ionic state is exceedingly small, is found extended vibrational structure associated with the X $^2\Pi_{g,i}$ ionic state. This extra vibrational structure arises through autoionisation processes, similar to those found in Cl_2. The assignments given in Figure 4.9 (solid lines) are based on fitting a third order Dunham expression to the resolved vibrational bands, v' = 0-6, 15-21 in the X $^2\Pi_{g,3/2}$ spin-orbit component and a second order Dunham expression to the resolved vibrational bands v' = 0-14 in the X $^2\Pi_{g,1/2}$ spin-orbit component. These two fits give rise to very similar vibrational frequencies in the two spin-orbit components; 46.2 meV (372.6 cm^{-1}) for the X $^2\Pi_{g,3/2}$ state and 45.7 meV (368.6 cm^{-1}) for the X $^2\Pi_{g,1/2}$ state. The measured and calculated peak positions for the two spin-orbit components are given in Table 4.9.

The autoionising structure between ~11.1 and 11.8 eV can be identified as consisting of two bands as indicated in Figure 4.8. These are not as pronounced as in Cl_2 but can still be assigned to two Rydberg states converging on the A $^2\Pi_{u,i}$ ionic state. The first band between ~11.1 and ~11.4 eV contains two resolved vibrational progressions from which the X $^2\Pi_{g,1/2}$ spin-orbit component can be identified as being the more intense. Beyond ~11.4 eV (i.e. at the start of the second band), no clear indication of the individual spin-orbit vibrational progressions can be found. Based on the dominance of the X $^2\Pi_{g,1/2}$ spin-orbit component at lower energies it is felt that the vibrational bands beyond this point can be assigned predominantly to the higher spin-orbit component. The assignment of the extended X $^2\Pi_{g,1/2}$ spin-orbit component vibrational bands (v' = 15-40) in Figure 4.9 (dashed lines), is based on the position of the peak centroids. In contrast to the TPE spectrum of Cl_2, isotopic splitting is not

Table 4.9 Experimental and calculated transition energies for the X $^2\Pi_{g,3/2}$ and X $^2\Pi_{g,1/2}$ ionic states of Br_2.

v'	Br_2^+ X $^2\Pi_{g,3/2}$ transition energy / eV			Br_2^+ X $^2\Pi_{g,1/2}$ transition energy / eV	
	Experimental [a]	Calculated		Experimental [b]	Calculated [c]
0	10.518	10.518		10.867	10.866
1	10.563	10.564		10.911	10.911
2	10.608	10.609		10.955	10.956
3	10.654	10.654		11.000	11.000
4	10.698	10.699		11.045	11.044
5	10.741	10.743		11.088	11.088
6	10.786	10.786		11.134	11.131
7	–	10.830		11.179	11.174
8	–	10.873		11.217	11.216
9	–	10.915		11.257	11.258
10	–	10.957		11.299	11.300
11	–	10.999		11.340	11.341
12	–	11.041		11.382	11.382
13	–	11.082		11.424	11.422
14	–	11.123		11.464	11.462
15	11.164	11.164		11.508	
16	11.202	11.204		11.547	
17	11.244	11.244		11.589	
18	11.280	11.284		11.629	
19	11.322	11.324		11.667	
20	11.364	11.363		11.706	
21	11.400	11.402		11.740	
22				11.779	
23				11.816	
24				11.850	
25				11.889	
26				11.924	
27				–	
28				11.993	
29				12.030	
30				12.064	
31				12.102	
32				12.140	
33				12.180	
34				12.218	
35				12.250	
36				12.285	
37				12.313	
38				12.346	
39				12.375	
40				12.402	

[a] Uncertainty ± 0.003 eV.

[b] Uncertainty ± 0.003 eV (v'=0-14); ± 0.005 eV (v'=15-40).

[c] Only v'=0-14 of the experimental X $^2\Pi_{g,1/2}$ ionic state are used in the second order Dunham fit.

observed in the vibrational bands due to the extremely small rotational constant in this state [24]. The three isotopomer bands in bromine therefore merge together and the peaks become broadened, especially at higher v', making an exact assignment difficult. The spectroscopic constants derived from the vibrational structure in this region are given in Table 4.11. The origin of the extended vibrational structure and the neutral excited Rydberg states involved is discussed in section 4.4.4.

4.4.2 The TPE Spectrum of Br_2 between 12.2 and 13.8 eV

The threshold photoelectron spectrum of Br_2 in Figure 4.10 shows the A $^2\Pi_{u,i}$ band of Br_2^+ in which, unlike the ground state, the two spin-orbit vibrational bands are partially overlapped. Besides the obvious extended vibrational structure compared with Ne(Iβ) photoelectron spectrum [17], two intensity dips can also be observed in the vibrational progression. The second dip at ~13 eV, coincides with an abrupt change in vibrational frequency and peak width. Such a vibrational spacing anomaly has been previously noted in the analysis of the A $^2\Pi_{u,i}$ - X $^2\Pi_{g,i}$ emission spectrum of Br_2^+ [24] where the A $^2\Pi_{u,1/2}$ spin-orbit component was found to have a vibrational frequency ~25% lower than that measured in the A $^2\Pi_{u,3/2}$ spin-orbit component. Recent theoretical calculations on the electronic states of Br_2^+, in which spin-orbit interactions were included, have backed up the experimental findings [28,29]. The calculations show that an avoided crossing between the A $^2\Pi_{u,1/2}$ state and the $^4\Sigma_{u,1/2}^-$ state is the explanation for the reduced vibrational frequency in the A $^2\Pi_{u,3/2}$ state, compared with that in the A $^2\Pi_{u,3/2}$ state. The calculations also show that the interaction results in a reduction in the internuclear equilibrium distance in the A $^2\Pi_{u,1/2}$ state by 0.02 Å, compared with the A $^2\Pi_{u,3/2}$ state.

Based on the appearance of the vibrational peaks on the low-energy side of the A $^2\Pi_{u,i}$ band shown in Figure 4.10, and in light of the findings in the analysis of the same system in Cl_2^+, the band origin of the A $^2\Pi_{u,3/2}$ spin-orbit component is placed at 2.444 eV. There are two reasons for this assignment. Firstly, this peak is the first in

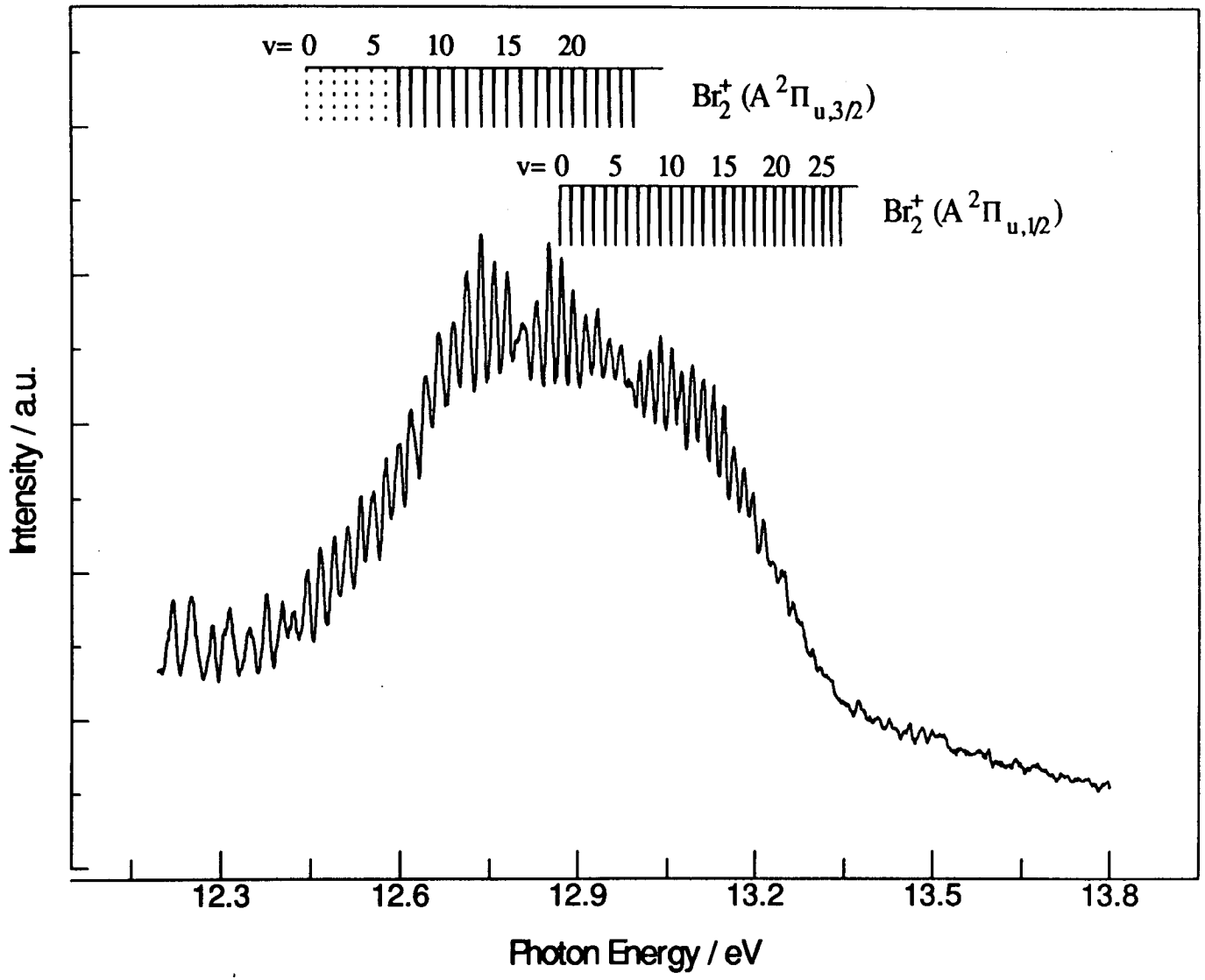

Figure 4.10 The threshold photoelectron spectrum of the $A\,^2\Pi_{u,j}$ ionic band of Br_2 showing the assignment of the vibrational bands. The solid lines are derived from Dunham expressions, while the dashed lines are based on observed peak positions.

the discernible vibrational structure at the onset of the band system with the approximate vibrational spacing of peaks to higher energy and secondly, it's intensity profile is similar to the peaks directly following. This assignment differs substantially from that given by Harris et al. [24] in their analysis of the high-resolution A $^2\Pi_{u,i}$ - X $^2\Pi_{g,i}$ emission spectrum of Br_2^+. Their assignment would place the band origin of the A $^2\Pi_{u,3/2}$ spin-orbit component midway up the low-energy side of the A $^2\Pi_{u,i}$ band system at 12.568 eV, as illustrated in Figure 7 of reference [17]. Van Lonkhuyzen and de Lange [17] attributed the ~0.2 eV difference between their photoelectron band onset and the adiabatic ionisation potential of Harris et al. to hot band contributions. However, this is not supported by their stated neutral ground state vibrational populations which would give them a band onset ~0.08 eV below the adiabatic ionisation potential of Harris et al.

The large difference in the position of the band origins can be largely reconciled if the assignment by Harris et al. [24] of the band origins of the two A $^2\Pi_{u,i}$ - X $^2\Pi_{g,i}$ emission systems is reversed. The band origins were derived from the intercepts of two parallel lines generated by plotting the isotopic splitting dependence against transition energy. If these band origin assignments of Harris et al. are reversed, then the term value of the band origin of the A $^2\Pi_{u,3/2}$ spin-orbit component would be 12.489 eV necessitating a change of +4 in the vibrational numbering of Harris et al.'s Deslandres table for the (3/2-3/2) emission system. A further shift in the vibrational numbering of +2 is also suggested such that it coincides with our assigned band origin. If the vibrationally reassigned (v' = 11-41) A $^2\Pi_{u,3/2} \rightarrow$ X $^2\Pi_{g,3/2}$ transition energies in Harris et al.'s Deslandres table are then combined with the experimental transition energies for the vibrational levels of the X $^2\Pi_{g,3/2}$ spin-orbit component shown in Table 4.9, the threshold spectral peak positions are regenerated to within ± 3 meV, as shown in Table 4.10. A third order Dunham expression was then fitted to Harris et al.'s vibrationally reassigned, v' = 11-41, transition energies which generated an ω_e of 27.2 meV (219.4 cm^{-1}). The calculated peak positions are tabulated in Table 4.10 and were used to determine the peak positions for the vibrational assignment (solid lines) in the A $^2\Pi_{u,3/2}$ spin-orbit component, as shown in

the upper portion of Figure 4.10. The threshold data for $v' = 0$-10 was not included in the Dunham fit for two reasons. Firstly, it would have had a very low weighting to take account of the large uncertainty in the vibrational band energies compared with the emission data and secondly, from the fit of Harris et al.'s data it was found that these peak positions were increasingly perturbed as $v' \rightarrow 0$, as can be seen by comparing the measured and calculated peak positions given in Table 4.10. The origin of this perturbation is at present unknown, but from Franck-Condon calculations for the $X\ ^1\Sigma_g^+ \rightarrow A\ ^2\Pi_{u,3/2}$ transition, the first observable vibrational band in the $A\ ^2\Pi_{u,3/2}$ spin-orbit component would be expected to be $v' = 4$. The $A\ ^2\Pi_{u,1/2}$ spin-orbit component is already known to be perturbed from both theory [29] and experiment [24] (see above), but theory [29] also suggests that there is a weak interaction in the $A\ ^2\Pi_{u,3/2}$ spin-orbit component with a $^4\Sigma_{u,3/2}^-$ state, and it may be this interaction which is causing the observed energy perturbations found in this spin-orbit component. The dashed lines in the vibrational assignment (v'=0-7) of the $A\ ^2\Pi_{u,3/2}$ spin-orbit component in Figure 4.10 therefore indicate the experimentally determined peak positions rather than the calculated peak positions.

The reversal of the band origin assignments in the emission spectra of Harris et al. requires the vibrational progression in the higher spin-orbit component to also be reassigned. Unfortunately the band origin of the $A\ ^2\Pi_{u,1/2}$ spin-orbit component is hidden within the $A\ ^2\Pi_{u,3/2}$ vibrational progression. Therefore, the approximate spin-orbit splitting determined by Harris et al. of 0.429 eV is applied to our experimental $A\ ^2\Pi_{u,3/2}$ band origin to generate a band origin for the $A\ ^2\Pi_{u,1/2}$ spin-orbit component of 12.873 eV. To assign Harris et al.'s data to this new band origin necessitated a vibrational numbering change of -2, with a possible error of ± 1. A third order Dunham fit of this reassigned vibrational data was then carried out using the same procedure as employed for the lower spin-orbit component i.e. using the new vibrational assignment in the Deslandres table ($v' = 3$-31) and Harris et al.'s

Table 4.10 Experimental and calculated transition energies for the A $^2\Pi_{u,3/2}$ and A $^2\Pi_{u,1/2}$ ionic states of Br_2.

v'	Br_2^+ A $^2\Pi_{u,3/2}$ transition energy / eV				Br_2^+ A $^2\Pi_{u,1/2}$ transition energy / eV		
	Exper. [a]	Calc. [b]	Harris et al.		Exper. [a]	Calc. [b]	Harris et al.
0	12.444	12.412	–		–	12.868	–
1	12.466	12.439	–		–	12.887	–
2	12.489	12.466	–		–	12.906	–
3	12.510	12.492	–		–	12.925	12.924
4	12.532	12.518	–		–	12.944	12.943
5	12.553	12.543	–		–	12.963	12.968
6	12.574	12.569	–		–	12.981	12.980
7	12.597	12.594	–		13.002	13.000	12.999
8	12.617	12.618	–		13.020	13.018	13.017
9	12.641	12.642	–		13.037	13.037	13.035
10	12.665	12.666	–		13.056	13.055	13.054
11	12.689	12.690	12.690		13.072	13.073	13.072
12	12.712	12.714	12.714		13.090	13.091	13.090
13	12.736	12.737	12.737		13.109	13.109	13.108
14	12.757	12.759	12.760		13.126	13.127	13.126
15	12.780	12.782	12.782		13.144	13.145	13.143
16	–	12.804	12.805		13.162	13.162	13.161
17	12.829	12.826	12.826		13.179	13.179	13.178
18	12.850	12.848	12.848		13.194	13.197	13.195
19	12.871	12.869	12.870		13.214	13.214	13.213
20	12.890	12.891	12.891		13.229	13.231	13.230
21	12.911	12.912	12.912		13.246	13.247	13.246
22	12.931	12.932	12.932		13.263	13.264	13.263
23	12.952	12.953	12.953		13.278	13.280	13.279
24		12.973	12.973		13.296	13.297	13.295
25		12.993	12.993			13.313	13.312
26		13.013	13.013			13.329	13.327
27		13.032	–			13.344	13.343
28		13.051	13.052			13.360	13.358
29		13.070	13.071			13.375	13.374
30		13.089	13.090			13.390	13.389
31		13.108	13.108			13.405	13.403
32		13.126	13.127				
33		13.145	13.145				
34		13.163	13.163				
35		13.180	13.181				
36		13.198	13.199				
37		13.216	–				
38		13.233	13.234				
39		13.250	13.251				
40		13.267	13.267				
41		13.284	13.284				

[a] Uncertainty ± 0.003 eV. [b] The calculated transition energies are generated from a third order Dunham fit of the data presented in the column of Harris et al. [c] Harris et al.'s emission transition energies combined with the calculated term values of the vibrational levels of the X $^2\Pi_{g,i}$ spin-orbit component given in Table 4.9.

transition energies combined with our X $^2\Pi_{g,1/2}$ vibrational band positions. From this fit an ω_e of 19.1 meV (154.1 cm^{-1}) was derived which agrees well with theory and is presented along with all the other spectroscopic data in Table 4.11. The calculated band positions shown in Table 4.10 were used to determine the peak positions of the A $^2\Pi_{u,1/2}$ spin-orbit component shown in the upper portion of Figure 4.10.

The reassignment of the band origins of the (3/2-3/2) and (1/2-1/2) emission bands has the effect of changing the spin-orbit splitting within the A $^2\Pi_{u,i}$ state of Br_2^+. Based on the re-evaluation of the emission data of Harris et al. and the threshold data, the spin-orbit splitting is now determined to be 0.424 eV (3420 cm^{-1}), which can be compared with the splitting measured for the X $^2\Pi_{g,i}$ state of 0.349 eV (2815 cm^{-1}). These two values are in reasonable accord with the calculated splittings of 3308 cm^{-1} in the A $^2\Pi_{u,i}$ state and 3030 cm^{-1} in the X $^2\Pi_{g,i}$. state, based on vertical transition energies [29].

The discussion and spectral assignments made above were primarily based on the reassignment of the band origins of the (3/2-3/2) and (1/2-1/2) emission spectra calculated by Harris et al. [24]. The reasoning behind their incorrect assignment must now be addressed. Harris et al. employed argon metastables to produce ground state Br_2^+ ions by Penning ionisation. These were then excited using several lines of an Ar^+ laser, and the laser induced fluorescence (LIF) from the A $^2\Pi_{u,i}$ state detected. They argued that, due to relaxation processes in the relatively high pressure Br_2/Ar^* afterglow system, the emission bands they observed using LIF "must belong to the lower ionic ground-state component." [24]. This, of course, implies that spin-orbit relaxation occurs between both spin-orbit components produced by the Penning ionisation process, an argument explicitly made by Hamilton [36] in his laser excitation study of Br_2^+. However, there is considerable experimental evidence [37-42] to suggest that spin-orbit relaxation is not a particularly fast process in either atomic or molecular systems with large spin-orbit splittings. For example, a rate constant for the quenching of HTe (X $^2\Pi_{1/2}$) to its ground state (X $^2\Pi_{3/2}$) by argon is k = 2.1 X 10^{-15} $cm^3molecule^{-1}s^{-1}$, while the quenching rate constants for Br ($4^2P_{1/2}$) and I

($5^2P_{1/2}$) atoms by argon are two and three orders of magnitude slower, respectively [37].

In an attempt to reconcile the LIF results of Harris et al., the following explanation is offered. It is well know that Penning ionisation is a highly efficient collision process [43], but there are always competing processes that must be considered in the overall quenching of metastable rare gas atoms. For example, excitation transfer, which is a resonance process, can effectively compete with Penning ionisation, as has been recently demonstrated in the Penning ionisation investigations of HCl [44], HBr [45] and HI [46]. Based on results presented here for the autoionisation of Rydberg states lying within the energy range of the $X\ ^2\Pi_{g,i}$ ionic state of Br_2^+ (see above), it is clear that Rydberg states of Br_2 can readily be populated. In fact, at the energies of the argon metastables, ($^3P_2$, 11.548 eV and $^3P_0$, 11.723 eV), autoionisation structure is evident in the TPE spectrum of Br_2 (see Figure 4.9 and Table 4.9). Thus, there are clearly Rydberg states present in Br_2 that are resonant or in near resonance with both argon metastables. Furthermore, autoionisation structure has been identified in this energy region as arising from the formation of vibrationally excited Br_2^+ in the $X\ ^2\Pi_{g,1/2}$ state. It is therefore postulated, that when argon metastables collide with bromine molecules, the following collision-induced quenching processes are important:

$$Br_2 + Ar(^3P_{2,0}) \rightarrow Br_2^*(Ryd) + Ar \qquad \text{resonant excitation transfer} \qquad 4.3$$

$$Br_2^*(Ryd) \rightarrow Br_2^+ (X\ ^2\Pi_{g,1/2}, v') + e^- \qquad \text{autoionisation} \qquad 4.4$$

where both excitation transfer (Equation. 4.3) and autoionisation (Equation 4.4) are highly probable processes, effectively competing with Penning ionisation (Equation. 4.5):

$$Br_2 + Ar(^3P_{2,0}) \rightarrow Br_2^+ (X\ ^2\Pi_{g,3/2,1/2}, v') + e^- \qquad \text{Penning ionisation} \qquad 4.5$$

If this is the case, then the formation of Br_2^+ in the X $^2\Pi_{g,1/2}$ spin-orbit ionic state may well be the dominant (although not necessarily the exclusive) spin-orbit component species present in the Br_2/Ar^* afterglow probed in the LIF study of Harris et al.

4.4.3 The TPE Spectrum of Br_2 between 13.7 - 15.0 eV

Figure 4.11 shows the TPE spectrum of Br_2 in the 13.7-15.0 eV range. A broad band representing the B $^2\Sigma_g^+$ ionic state of Br_2, with some weakly resolved vibrational structure at the band maximum (ω_e ~12 meV) is observed. As was found in the TPE spectrum of the B $^2\Sigma_g^+$ ionic state of Cl_2, this band in Br_2 also exhibits a long, low energy tail which connects to the high-energy tail of the A $^2\Pi_{u,1/2}$ band (see Figure 4.8). This tail arises through autoionisation processes and obstructs the true onset of the B $^2\Sigma_g^+$ band. An apparent difference between the B $^2\Sigma_g^+$ bands of Br_2^+ and Cl_2^+ is the appearance in the former of a pronounced broad shoulder on the low energy side of the band at ~14.3 eV. This feature along with the long low energy tail will be discussed further below.

4.4.4 Origin of the Observed Autoionising Structure between 10.3 - 15.0 eV

In contrast to the situation in chlorine, very much less is known about the Rydberg states of bromine above the lowest ionisation potential. Therefore, to analyse the autoionising features within the TPE spectrum of Br_2 we must rely upon our knowledge of these states in Cl_2. Since the number and type of Rydberg states residing in the energy region beyond the lowest ionisation potential in Br_2 are many, only the *n*sσ Rydberg states that appear to be important in Cl_2 will be considered. The adiabatic ionisation potentials of the A $^2\Pi_{u,3/2}$, A $^2\Pi_{u,1/2}$ and B $^2\Sigma_g^+$ states of Br_2^+ will be employed along with a quantum defect of 2.2, characteristic of an *n*s Rydberg electron. From Table 4.11 the ionisation potentials of the A $^2\Pi_{u,3/2}$ and A $^2\Pi_{u,1/2}$ components are 12.444 and 12.868 eV, respectively whereas the ionisation potential of the B $^2\Sigma_g^+$ is taken as the onset peak value of 14.3 eV [14]. It is well known that

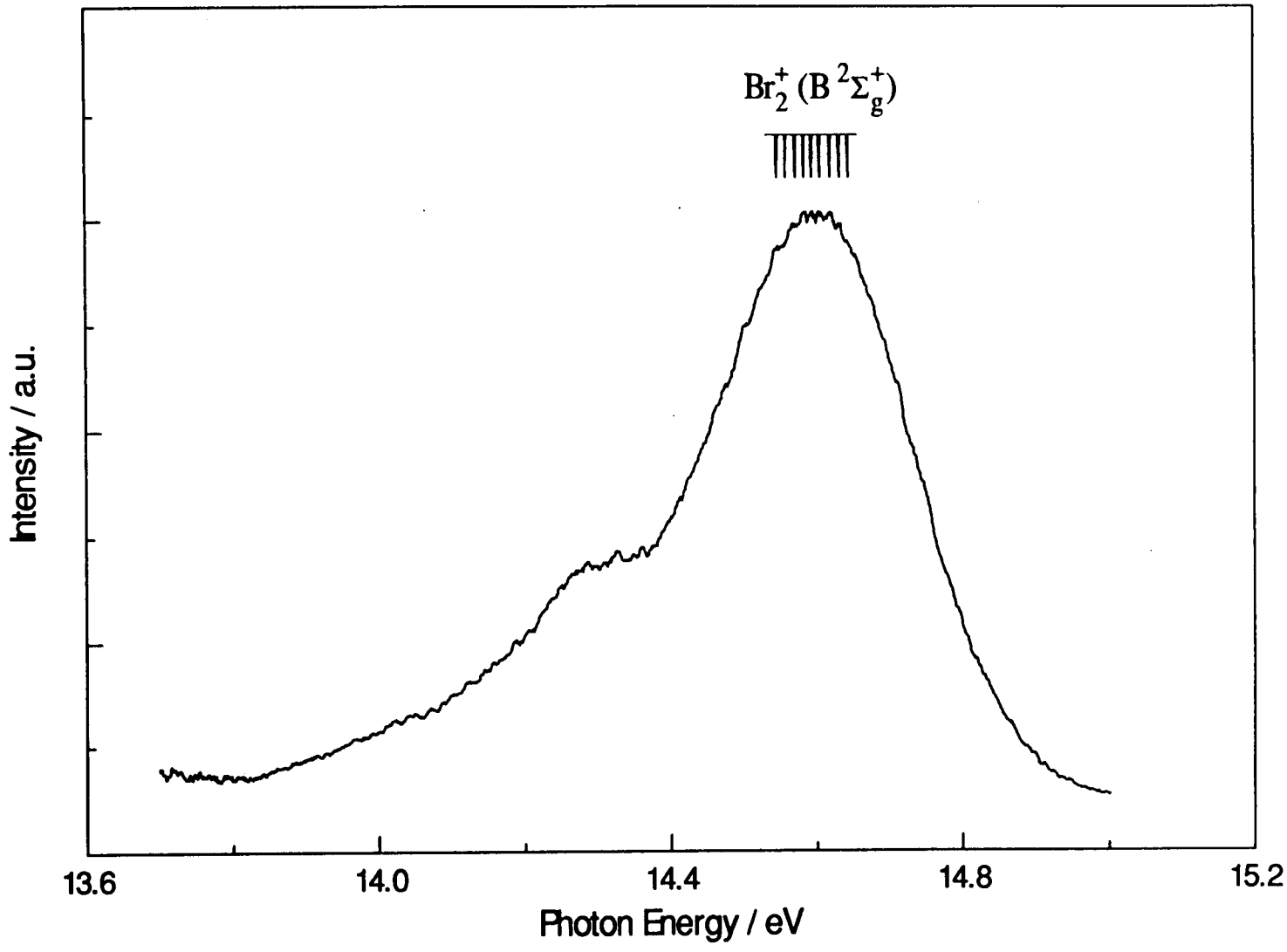

Figure 4.11 The threshold photoelectron spectrum of Br_2 showing the $B\ ^2\Sigma_g^+$ band system with resolved vibrational structure. The pronounced shoulder at ~14.3 eV and the long tail extending to lower energy are due to autoionisation processes and obscure the onset of the $B\ ^2\Sigma_g^+$ ionic state.

Table 4.11 A summary of the spectroscopic constants for the valence ionic states of Br_2.

Molecule Br_2	AIE (eV)	VIE (eV)	ω_e (cm^{-1})	$\omega_e x_e$ (cm^{-1})	$\omega_e y_e$ $x10^{-3}$ (cm^{-1})	r_e (Å)	Spin-orbit splitting (cm^{-1})	Ref.
($X\ ^1\Sigma_g^+$)	–	–	325.321	-1.0774	–	2.2810	–	[1]
($X\ ^2\Pi_{g,3/2}$)	10.518[a] ±0.003	10.563 ±0.003	372.6	-1.8	14.6	–	2815±48[b]	this work
	10.515 ±0.005	–	–	–	–	–	2822±81	[17]
	–	–	364.9 ±0.3	-1.13 ±0.03	–	2.18 ±0.01	–	[24]
	–	–	366.020 ±0.084	-1.2176 ±0.010	–	–	–	[36]
	10.51	–	360–40	–	–	–	2820±40	[14]
	10.51 ±0.01	10.56 ±0.01	355±20	–	–	–	2823±32	[15]
($X\ ^2\Pi_{g,1/2}$)	10.867[a] ±0.003	10.911 ±0.003	368.6	-1.7	–	–	2815±48[b]	this work
	10.865 ±0.005	–	–	–	–	–	2822±81	[17]
	–	–	361.2 ±0.2	-1.10 ±0.03	–	2.18 ±0.01	–	[24]
($A\ ^2\Pi_{u,3/2}$)	12.444[a] ±0.003	–	219.7	-1.4	6.0	–	3420±48	this work
	–	–	~ 180	–	–	–	–	[17]
	–	–	204.0 ±0.2	-1.31 ±0.02	6.5 ±0.2	2.54 ±0.02	–	[24]
	–	–	207.225 ±.200	-1.3997 ±0.009	87.595 ±0.022	–	–	[36]
	12.5[c]	13.08	–	–	–	–	2100±100	[14][d]
	12.41 ±0.02	12.77 ±0.02	~187	–	–	–	~2742	[15][d]
($A\ ^2\Pi_{u,1/2}$)	12.868[e] ±0.003	–	153.9	-0.2	-7.2	–	3420±48	this work
	–	–	154.1 ±0.4	-0.13 ±0.03	-8.1 ±0.4	2.56 ±0.02	–	[24]
($B\ ^2\Sigma_g^+$)	–	14.597[e]	(~97)[f]	–	–	–	–	this work
	14.3[c]	14.60	–	–	–	–	–	[14]
	14.28 ±0.02	14.56 ±0.03	–	–	–	–	–	[15]

[a] Experimental adiabatic ionisation energy. [b] Spin-orbit splitting measured between v'=0 bands.

[c] Band onset. [d] Average values over both spin-orbit components. [e] Calculated value from Dunham expression. [f] Average value.

the oscillator strength (I) for transitions to Rydberg states declines very steeply with increasing principal quantum number (i.e $I \approx 1/n^3$) [47] due to the increasingly diffuse nature of the electronic wavefunction and the resulting poor overlap with the ground state wavefunction. Rydberg states with the lowest possible value of principal quantum number (n) are therefore strongly favoured and as such our calculations are restricted to n = 5, 6, and 7. The results of these calculations are given in Table 4.12, and clearly indicate that these Rydberg states could account for the autoionising structure found in the TPE spectrum of Br_2, as shown in Figure 4.8. In visualising the profiles of these Rydberg states, it must be kept in mind that the maximum in the Franck-Condon envelope will lie to a higher energy than the values quoted in Table 4.12 and that these are only tentative calculations based on a quantum defect taken from Cl_2. In particular, the double band profile in the autoionising structure located between 11 and 12 eV is well positioned for being due to 5sσ and 6sσ Rydberg states converging on the A $^2\Pi_{u,3/2}$ spin-orbit component and a 5sσ Rydberg state converging on the A $^2\Pi_{u,1/2}$ spin-orbit component. The stepped band profile at about 12.2 eV, on the other hand, may be due to the 6sσ Rydberg state converging on the A $^2\Pi_{u,1/2}$ spin-orbit component. The unusual double dip within the A $^2\Pi_{u,i}$ ionic band and its long tail to higher energy can be assigned to the 5sσ, 6sσ, and 7sσ Rydberg states converging on the B $^2\Sigma_g^+$ ion state.

Table 4.12 Calculated adiabatic term values, in eV, for nsσ Rydberg states of Br_2 using a quantum defect of 2.2 and the values of 12.444, 12.868 and 14.3 eV for the I.P.'s of Br_2^+ (A $^2\Pi_{u,3/2}$), (A $^2\Pi_{u,1/2}$) and (B $^2\Sigma_g^+$), respectively.

n	$[(\sigma_g)^2(\pi_u)^3(\pi_g^*)^4]_{3/2}\ n s\sigma_g$ $^1\Pi_u$	$[(\sigma_g)^2(\pi_u)^3(\pi_g^*)^4]_{1/2}\ n s\sigma_g$ $^1\Pi_u$	$[(\sigma_g)^1(\pi_u)^4(\pi_g^*)^4]_{1/2}\ n s\sigma_g$ $^1\Sigma_g$
5	10.71	11.13	12.56
6	11.50	11.93	13.36
7	11.85	12.28	13.71

The observation of two dips in the vibrational structure on top of the A $^2\Pi_{u,i}$ ionic band shown in Figure 4.10 is intriguing. No double-dip feature is observed in the Ne(Iα) photoelectron spectrum of the A $^2\Pi_{u,i}$ band shown in figure 7 of Ref. [17] and the overall profile is significantly different with the intensities of the two spin-orbit components reversed. The first dip in the threshold spectrum at ~12.81 eV occurs amongst vibrational bands that all appear to belong to the A $^2\Pi_{u,3/2}$ spin-orbit component, whereas the second dip at ~12.98 eV marks the separation between vibrational bands belonging to the A $^2\Pi_{u,3/2}$ spin-orbit component and those belonging to the A $^2\Pi_{u,1/2}$ spin-orbit component. From Franck-Condon factor calculations based on Harris et al.'s spectroscopic constants, excitation from the neutral ground state would populate the vibrational levels, v' = 4-22, in the A $^2\Pi_{u,3/2}$ spin-orbit component. However, v' = 0-25 are clearly observed and it is therefore suggested that the origin of the unusual double-dip feature is a result of the enhancement of high vibrational levels (v' = 17-25) via autoionisation (e.g., by the 5sσ Rydberg state converging on the B $^2\Sigma_g^+$ ion state, see Table 4.12). It is also very likely that the low (v' = 0-4) perturbed vibrational bands of the A $^2\Pi_{u,3/2}$ spin-orbit component are also enhanced through autoionisation. In this case the neutral Rydberg state involved could be the 7sσ_g converging on the A $^2\Pi_{u,1/2}$ spin-orbit component, enhancement occurring through spin-orbit autoionisation.

The broad shoulder in Figure 4.11 with its long tail extending to lower energy occurs in the energy region just preceding the onset of the B $^2\Sigma_g^+$ band. These autoionising features are likely to be due to Rydberg states of high principal quantum numbers converging on the B $^2\Sigma_g^+$ state and by virtue of the high density of these states have a finite transition probability.

4.5 The Two-Electron Excitation Region between ~17 and 35 eV in Cl_2 and Br_2

4.5.1 General Considerations

The ground state electron configuration of the diatomic halogens is $(\sigma_g)^2(\sigma_u^*)^2(\sigma_g)^2(\pi_u)^4(\pi_g^*)^4$ and in the energy region between the end of valence ionisation and the start of double ionisation, e.g., between approximately 17 eV and 30 eV in chlorine and bromine, core ionisation processes can occur. Core ionisation results in the removal of an electron from the σ_u or σ_g molecular orbitals which are largely localised on one of the halogen atoms. However, the independent-particle model approximation which is applicable to valence electron ionisation, breaks down when core electrons are removed and requires correlation effects to be taken into account. This breakdown of the independent-particle model leads to the formation of satellite states, in which one or more valence electrons are simultaneously excited in the core ionisation process, in addition to the pure core ionisation band. Although these satellite ionic states involve two or more electron promotion schemes, their band intensities can be comparable to that of the main core electron band. This has been observed, for example, in the ionisation of the inner valence electron $(s\sigma)^{-1}$ in HCl [48] and HBr [49]. In fact, in some cases the main core ionisation band may not even be detected [50], all of the intensity being shared amongst the satellite bands. The fact that both of the core sigma orbitals are largely nonbonding in a molecular orbital sense, might lead one to expect that many ionic states based on these hole configurations would have bound, stable potentials and hence discrete band structure. In the context of the present work, the importance of these ionic states is due, firstly, to their direct photoionisation cross sections, and secondly, to their participation in the autoionisation of highly-excited Rydberg states of the neutral molecule. These Rydberg states may of course involve convergence to any singly- or doubly-charged ionic state in the general energy range being studied. Because of the method of detecting the presence of such Rydberg states in this study, namely threshold photoelectron spectroscopy, a severe restriction is placed on the Rydberg states

undergoing autoionisation, although as was found in the valence ionisation region, this does not seem to limit the resultant structure. In addition, the Rydberg states must survive long enough for autoionisation to occur, and, of course, the Rydberg states must lie within the Franck-Condon region for excitation from the lowest vibrational level of the ground state of the molecule.

4.5.2 The TPE Spectrum of Cl_2 between 17 and 35 eV

The TPE spectrum of Cl_2 in the energy range 17.0-35.0 eV is shown in Figure 4.12 and consists of several broad but defined peaks. It should be noted that the intensity scale shown in Figure 4.12 was multiplied by a factor of 200 compared to the intensity scale of the TPE spectrum shown in Figure 4.2. Theoretical calculations [51] show that in this energy range the $(\sigma_u^*)^{-1}$ and $(\sigma_g)^{-1}$ core ionic states are expected at 23.15 eV and 31.17 eV, respectively, together with several associated satellite states which are listed in Table 4.13. The spectrum has been divided into six regions roughly corresponding to the broad peak regions observed in the $(3s\sigma)^{-1}$ inner-valence ionisation spectrum of HCl [48], which on an electron-structural basis, may be considered as a corollary system to $(\sigma_u^*)^{-1}$ ionisation in Cl_2. These regions, with their mid-energy values, together with observed peak energy positions, are listed in Table 4.13. From Figure 4.12, all of the observed peaks precede the onset of double ionisation at 31.13 eV, recently measured in a threshold photoelectron coincidence study [52]. It should be noted that the intensity of the peaks in Figure 4.12 are considerably below what might be expected for σ-core electron ionisation [48]. In spite of this, the most intense regions in Figure 4.12 are believed to represent direct photoionisation of a σ_u^* core electron. The peak structure in Figure 4.12 is not believed to correspond to vibrational structure because the magnitude of vibrational frequencies in chlorine are much smaller than the resolution available to us in this region (~190 meV at 25 eV). By analogy with HCl [53], peak 1 of region B is assigned to the main $(\sigma_u^*)^{-1}$ band, with the peaks in region A due to direct ionisation processes involving repulsive ionic states. Regions C, D, E, and F may then be

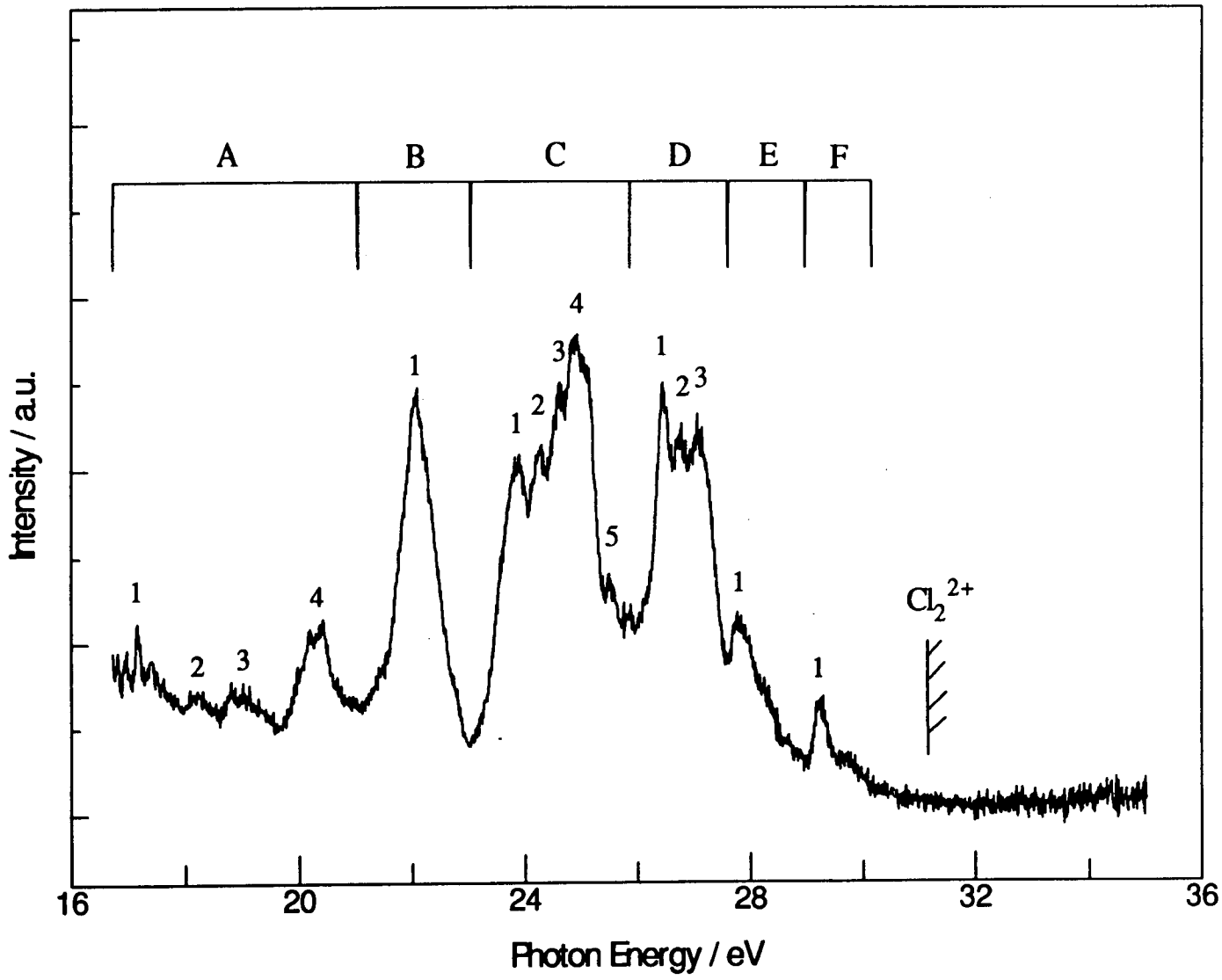

Figure 4.12 The threshold photoelectron spectrum of Cl_2 in the core ionisation region between 17 and 35 eV. The regions A-F and the peak numbers are described in the text.

associated with satellite states of the $(\sigma_u^*)^{-1}$ ionisation. Individual peaks contained within the regions most likely represent the influence of resonant autoionising processes involving Rydberg states of the neutral Cl_2 molecule. The identity of these Rydberg states is unknown and must await a comprehensive theoretical treatment of the highly excited states of Cl_2.

Table 4.13 Experimental band energies and peak positions for the $(\sigma_u^*)^{-1}$ core ionisation region of the TPE spectrum of Cl_2 as identified in Figure 4.12. The calculated binding energies for core ionisation in Cl_2 are also given.

Hole state	Experiment / eV [a]				Theory / eV [b]
	Band		Peak		Binding energy
	region	energy	no.	energy	
$(\sigma_u^*)^{-1}$	A	18.88	1	17.16	
			2	18.23	
			3	18.93	
			4	20.30	
	B	22.03	1	22.06	23.15
	C	24.43	1	23.87	25.33
			2	24.25	
			3	24.61	
			4	24.87	
			5	25.51	
	D	26.72	1	26.47	27.26
			2	26.74	
			3	27.08	
	E	28.27	1	27.83	
	F	30.04	1	29.24	
$(\sigma_g)^{-1}$					31.17
					39.18
					39.87

[a] This work.

[b] Reference [48].

4.5.3 The TPE Spectrum of Br_2 between 15 and 35 eV

Figure 4.13 shows the TPE spectrum of Br_2 in the high-energy region (15-35 eV). As was the case in Cl_2, extensive structure is also found, but in contrast the spectrum is more congested and the peaks less well defined. The intensity scale in this figure was also multiplied by a factor of 200 compared with the TPE spectrum of the valence ionisation region shown in Figure 4.8. Following the procedure used in interpreting the high energy TPE spectrum of Cl_2, the peaks in this energy range have been divided up into six band regions corresponding roughly to the main broad bands observed in the XPS of HBr [49]. The mid-energy value of these band regions and the peak energy positions contained within them are given in Table 4.14 together with calculated values for $(\sigma_u^*)^{-1}$ and $(\sigma_g)^{-1}$ core ionisation in Br_2 and associated satellite states [51]. The estimated double ionisation onset in Br_2 (~28.7 eV) derived from similar values known for HBr, HCl, and Cl_2 is shown in Figure 4.13. It is not clear whether the main $(\sigma_u^*)^{-1}$ band is located in region A or B, but based on the fact that the calculated core ionisation values in Cl_2 appear at a greater energy than found experimentally, peak 2 in region A is assigned to the main $(\sigma_u^*)^{-1}$ core ionisation band. The more intense peaks in band region D and E may indicate the presence of $(\sigma_g)^{-1}$ core ionisation. Again, as was found in Cl_2, the peak structure within a band region, in particular in band region B, is believed to represent the influence of autoionising Rydberg states of neutral Br_2. Further analysis of the structure in Figure 4.13 must await a higher resolution TPE study and in depth theoretical calculations of both neutral and ionic states of Br_2 in this energy region..

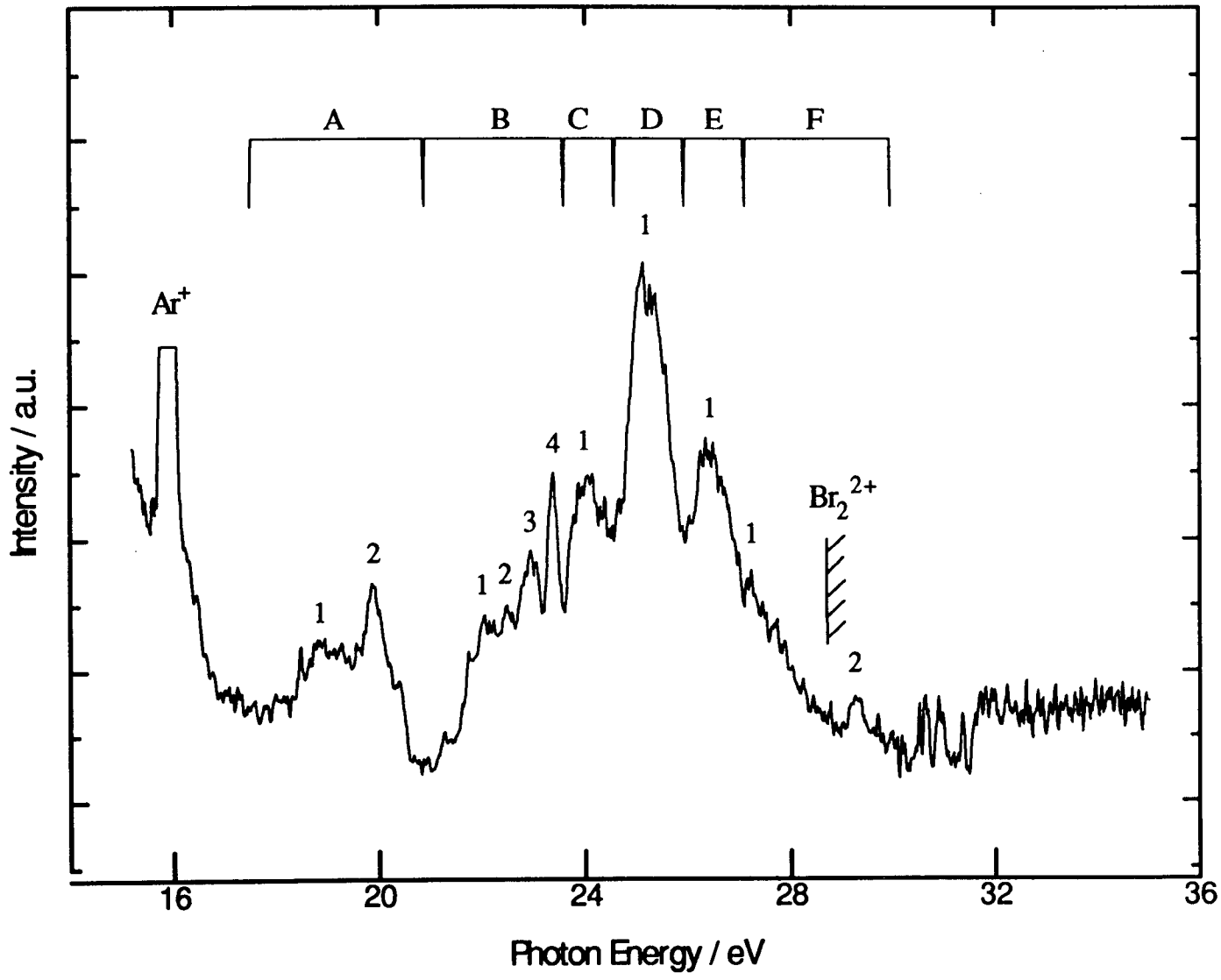

Figure 4.13 The threshold photoelectron spectrum of Br_2 in the core ionisation region between 15 and 35 eV. The regions A-F and the peak numbers are described in the text.

Table 4.14 Experimental band energies and peak positions for the $(\sigma_u^*)^{-1}$ core ionisation region of the TPE spectrum of Br_2 as identified in Figure 4.13. The calculated binding energies for core ionisation in Br_2 are also given.

Hole state	Experiment / eV [a]				Theory / eV [b]
	Band		Peak		Binding energy
	region	energy	no.	energy	
$(\sigma_u^*)^{-1}$	A	19.19	1	18.87	
			2	19.89	20.66
	B	22.23	1	22.04	22.19
			2	22.48	
			3	22.92	
			4	23.39	
	C	24.08	1	24.01	25.06
	D	25.25	1	25.19	27.97
$(\sigma_g)^{-1}$	E	26.52	1	26.41	28.46
	F	28.53	1	27.22	33.76
			2	29.26	

[a] This work.

[b] Reference [48].

4.6 The Threshold Photoelectron Spectrum of I_2

The threshold photoelectron spectrum of I_2 spanning the valence ionisation region (9.2 - 13.75 eV) is shown in Figure 4.14. It consists of five distinct bands, in contrast to the number of bands observed in chlorine and bromine, due to the increased spin-orbit splitting. The main band contours are very similar to those observed in conventional He(I) photoelectron investigations [14,15,32], with the exception that there appears to be an intensity reversal in the two spin-orbit components of the X $^2\Pi_{g,i}$ ionic state. In addition there is a significant amount of extra vibrational structure to the blue of each of the X $^2\Pi_{g,i}$ spin-orbit bands that has not been observed previously in any He(I) photoelectron investigation. Vibrational structure is also resolved for the first time on each of the A $^2\Pi_{u,i}$ spin-orbit bands. All these features will be discussed in detail below.

4.6.1 The TPE Spectrum of I_2 between 9.2 and 10.6 eV

The threshold photoelectron spectrum of I_2 in the range 9.2-10.6 eV covering the two spin-orbit components of the X $^2\Pi_{g,i}$ ionic state is shown in Figure 4.15. Additional vibrational structure is also observed on the high energy side of each of the direct ionisation bands which, as in Cl_2 and Br_2, can be assigned to a continuation of the spin-orbit vibrational progressions as indicated in the figure. The vibrational band at 9.311 ± 0.002 eV is assigned as the adiabatic ionisation potential of the X $^2\Pi_{g,3/2}$ ionic state of I_2 which is in exact agreement with the value reported by Higginson et al. [16] in their vibrationally resolved Ne(I) PE spectrum. However, the value for the adiabatic ionisation potential of the X $^2\Pi_{g,1/2}$ ionic state of 9.947 ± 0.003 eV, differs slightly from Higginson et al.'s value of 9.953 eV. The vibrational band positions of both spin-orbit vibrational progressions shown in Figure 4.15 are detailed in Table 4.15. The vibrational anharmonicity constants of both X $^2\Pi_{g,i}$ vibrational progressions are so small that only average vibrational spacings have been determined. These are calculated to be 27.3 meV (220 cm^{-1}) for the X $^2\Pi_{g,3/2}$ spin-orbit component

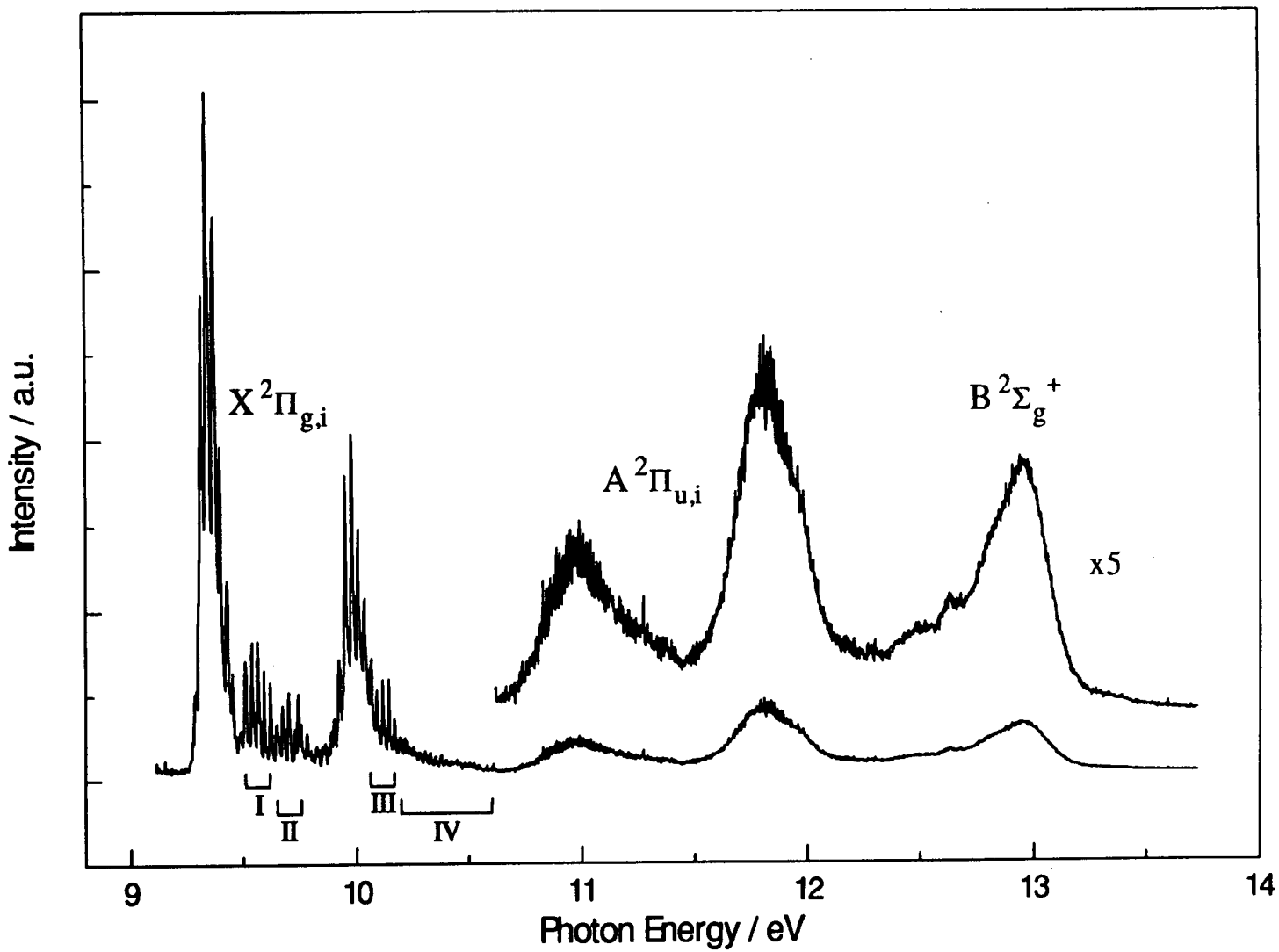

Figure 4.14 The threshold photoelectron spectrum of the valence ionisation region of I_2 showing the X $^2\Pi_{g,i}$, A $^2\Pi_{u,i}$ and B $^2\Sigma_g^+$ bands of I_2^+. The vibrational structure identified by the bracketed regions I - IV is due to autoionisation processes and is discussed in the text.

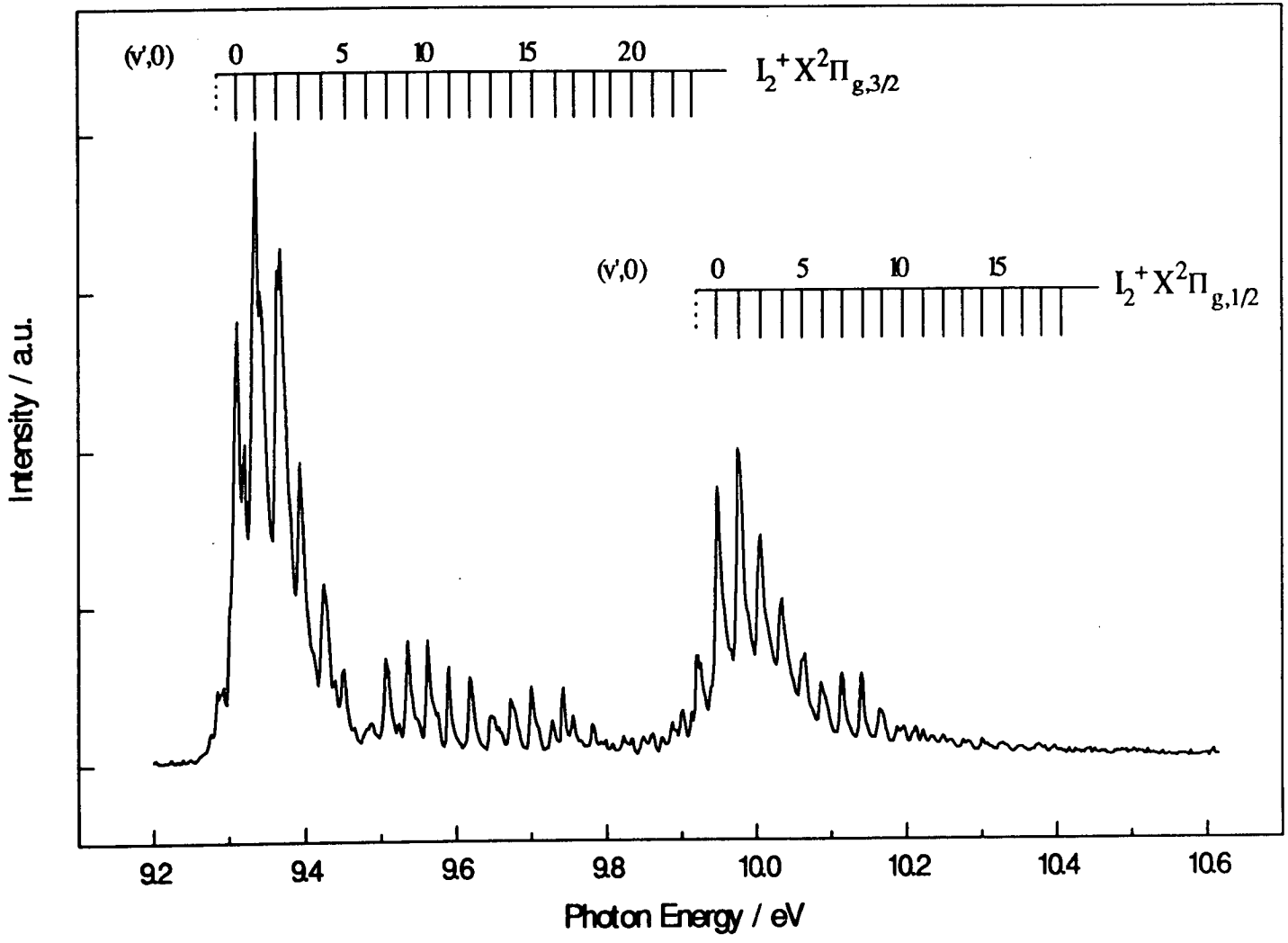

Figure 4.15 The high resolution (~6 meV at 9.7 eV) threshold photoelectron spectrum of I_2 indicating the vibrational assignment of the two spin-orbit components of the $X\ ^2\Pi_{g,i}$ ionic state.

and 26.5 meV (214 cm^{-1}) for the X $^2\Pi_{g,1/2}$ spin-orbit component. The spectroscopic constants derived from the threshold spectrum are shown in table 4.17.

Some well defined peaks are also observed to the high energy side of each of the (0,0), (1,0) and (2,0) vibrational bands of the X $^2\Pi_{g,3/2}$ spin-orbit component, displaced by 10, 6 and 4 meV, respectively. An initial assignment of these features to sequence bands was discounted because the difference in the vibrational frequency of the neutral ground state (214 cm^{-1}) [1] and the ground ionic state is so small that the sequence bands would not have been resolvable with the experimental electron resolution. A possible explanation for these features is that they arise from the autoionisation of an underlying Rydberg state yielding an enhanced rotational branch within the individual vibrational bands. The presence of an underlying Rydberg state in the region of the X $^2\Pi_{g,3/2}$ spin-orbit component is supported by the spin-orbit branching ratio found in the threshold investigation compared with that found in conventional He(I) PES [14,15,32].

4.6.2 The TPE Spectrum of I_2 between 10.6 and 12.3 eV

The threshold photoelectron spectrum of I_2 between 10.6 and 12.3 eV containing the two spin-orbit bands of the A $^2\Pi_{u,i}$ valence ionic state is shown in Figure 4.16. Low frequency vibrational structure is resolved on both spin-orbit components, although to varying degrees. Although vibrational resolution has been achieved in the A $^2\Pi_{u,i}$ - X $^2\Pi_{g,i}$ emission spectrum of I_2^+ [25,54], this is the first time it has been observed in a photoelectron investigation. Unfortunately a vibrational number assignment was not possible in the emission spectrum, partly because the emission was very weak and partly because the spectrum was complicated by

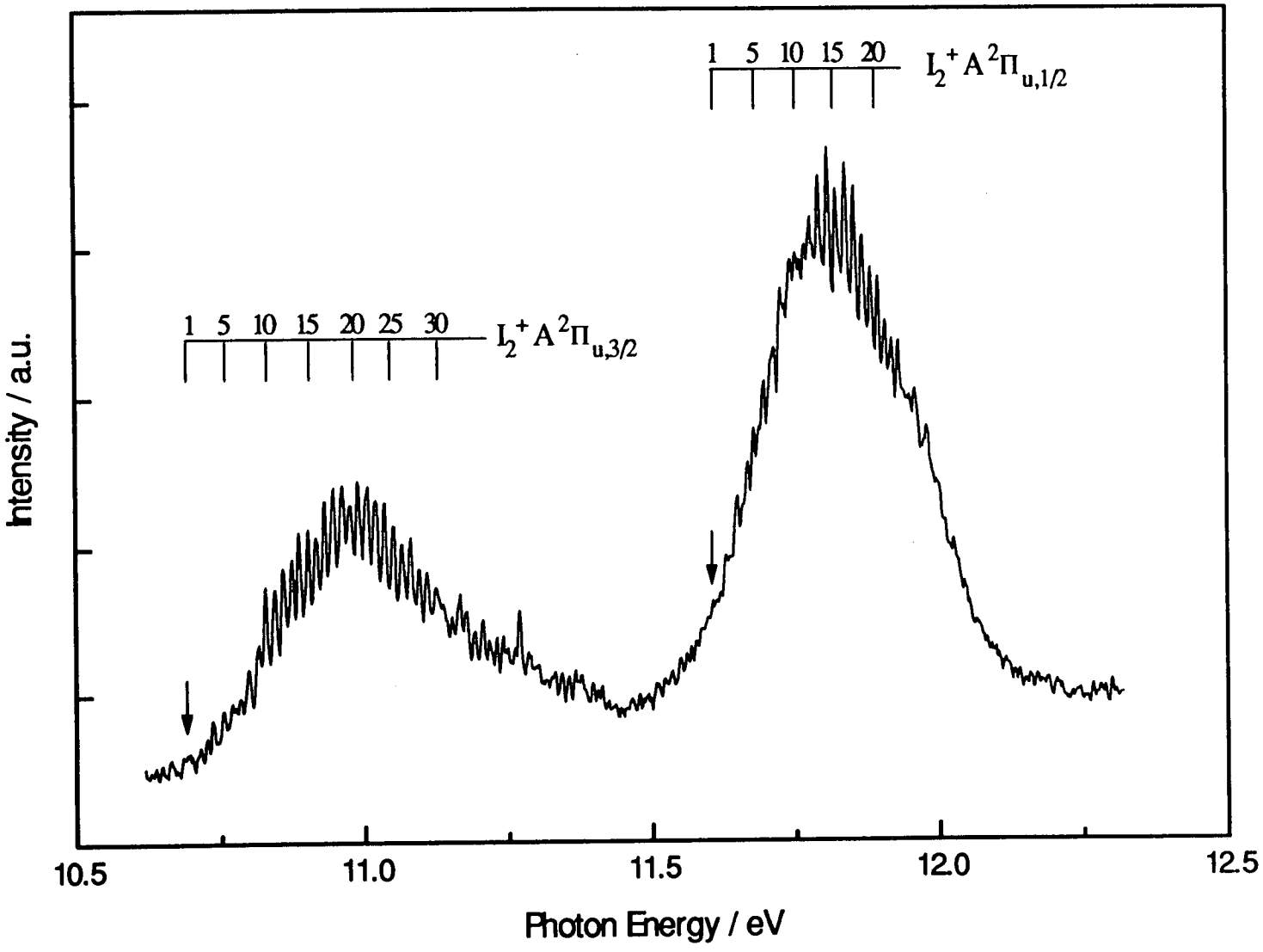

Figure 4.16 The threshold photoelectron spectrum of I_2 incorporating the band structure associated with the two-spin-orbit components of the $A\,^2\Pi_{u,i}$ ionic state. The assignment is based on peak number rather than vibrational quantum number.

Table 4.15 Experimental transition energies for the X $^2\Pi_{g,3/2}$ and X $^2\Pi_{g,1/2}$ ionic states of I_2.

v'	I_2^+ X $^2\Pi_{g,3/2}$ transition energy / eV [a)]	I_2^+ X $^2\Pi_{g,1/2}$ transition energy / eV [a)]
0	9.311	9.947
1	9.335	9.976
2	9.363	10.004
3	9.394	10.032
4	9.426	10.060
5	9.451	10.088
6	–	10.115
7	9.508	10.140
8	9.536	10.116
9	9.562	10.196
10	9.590	10.222
11	9.619	10.248
12	9.648	10.275
13	9.674	10.300
14	9.700	10.328
15	9.729	10.352
16	9.756	10.376
17	9.782	10.398
18	9.808	
19	9.834	
20	9.861	
21	9.887	
22	9.913	

[a)] Uncertainty ± 0.002 eV.

overlapping vibrational bands. This inability to vibrationally assign the structure in the two A $^2\Pi_{u,i}$ spin-orbit bands is also applicable to the threshold spectrum. The lack of a discernible band origin in both spin-orbit bands makes it impossible to assign vibrational quantum numbers. For convenience, therefore, peak numbers have been assigned, beginning with the band identified by the arrow in Figure 4.16, which correspond to the transition energies given in Table 4.16. The average vibrational spacing over both spin-orbit components is measured to be 14.8 meV (120 cm^{-1}). The prominence of some vibrational bands clustered together is reminiscent of similar

structure found in the TPE spectrum of bromine. In that case the enhanced vibrational behaviour was attributed to the autoionisation of neutral Rydbergs, the underlying main bands being due to direct ionisation processes. The possible neutral autoionising Rydberg states involved in enhancing the vibrational structure in the A $^2\Pi_{u,i}$ spin-orbit components is discussed below.

4.6.3 The TPE Spectrum of I_2 between 12.3 and 13.7 eV

The region of the threshold spectrum containing the B $^2\Sigma_g^+$ state of I_2^+ is shown in Figure 4.17. The broad band has a band maximum of 12.95 eV, although there is a hint of vibrational structure on the low energy side of this band with a vibrational spacing of ~16 meV. The resolution, however, is insufficient to positively identify this structure. The onset of the band is obscured by the presence of broad autoionising features with band maxima at ~12.48 eV and ~12.63 eV. These probably arise from the population of high vibrational levels of the A $^2\Pi_{u,i}$ state through autoionisation of Rydberg states converging on the B $^2\Sigma_g^+$ state. These features are similar to those observed in Cl_2 and Br_2.

4.6.4 Origin of the Observed Autoionising Structure between 9.2 - 13.7 eV

The vibrational structure appearing to the blue of the main spin-orbit component bands can, as in Cl_2 and Br_2, be explained by the autoionisation of neutral Rydberg states. Two distinctive autoionisation vibrational band profiles appear above each main X $^2\Pi_{g,i}$ spin-orbit band, labelled I and II for the X $^2\Pi_{g,3/2}$ spin-orbit component and III and IV for the X $^2\Pi_{g,1/2}$ spin-orbit component as shown in Figure 4.14. The vibrational structure in bands I and II could arise from neutral Rydberg states converging on the X $^2\Pi_{g,1/2}$ spin-orbit component, the A $^2\Pi_{u,i}$ state, or a higher energy state. If it arose from Rydberg states converging on the A $^2\Pi_{u,3/2}$ ionic state, then the most likely candidate would be the 7s Rydberg state (see Table 4.19). However, the similarity between the profiles of bands I and II and that of the main

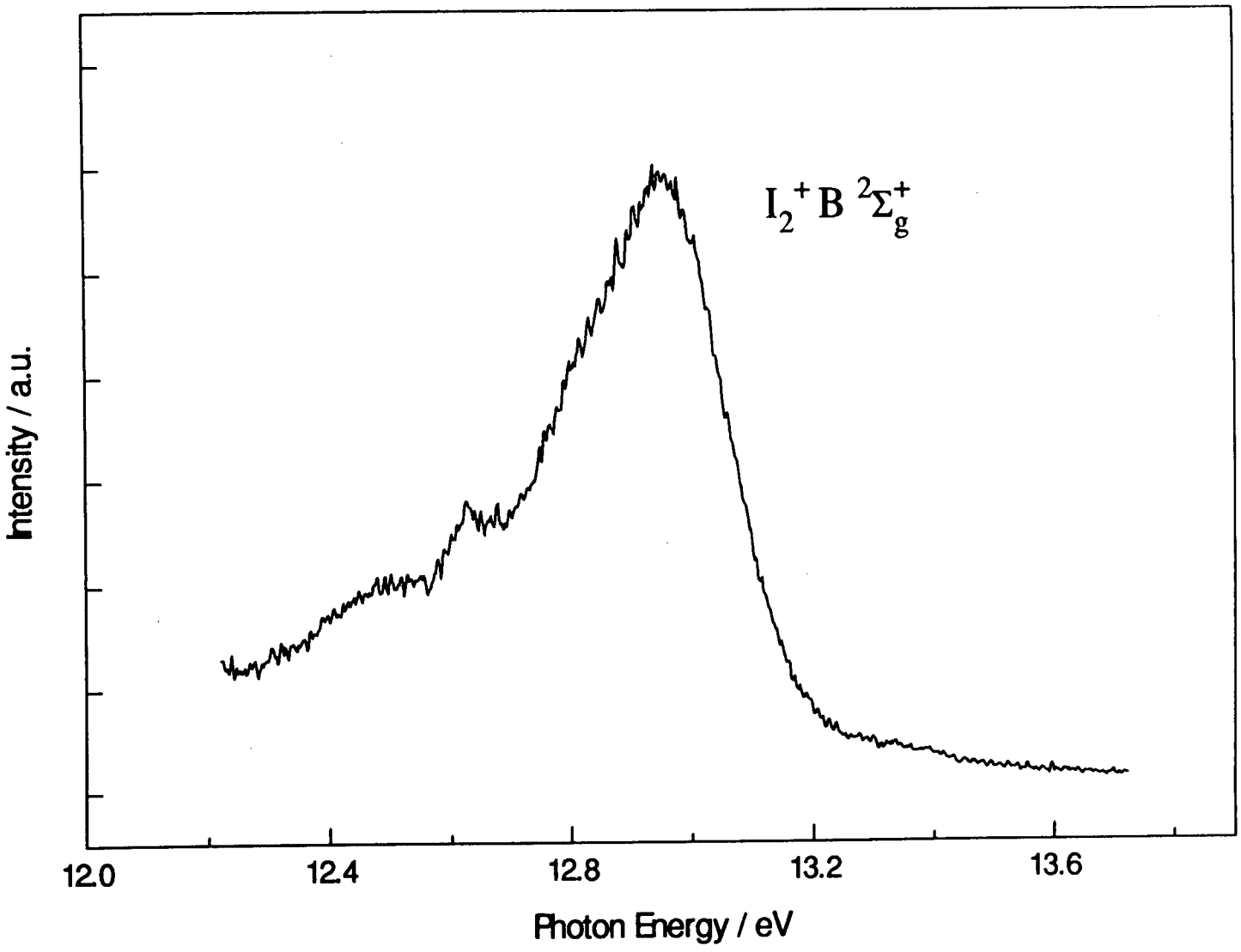

Figure 4.17 The threshold photoelectron spectrum of I_2 showing the B $^2\Sigma_g^+$ band system. The pronounced shoulder at ~12.5 eV and the long tail extending to lower energy are due to autoionisation processes and obscure the onset of the band.

Table 4.16 Experimental transition energies for the A $^2\Pi_{u,3/2}$ and A $^2\Pi_{u,1/2}$ ionic states of I_2.

Peak No. [a]	I_2^+ A $^2\Pi_{u,3/2}$ transition energy / eV [b]	I_2^+ A $^2\Pi_{u,1/2}$ transition energy / eV [b]
1	10.691	11.608
2	10.713	11.630
3	10.727	11.649
4	10.736	11.668
5	10.756	11.679
6	10.770	11.695
7	10.785	11.710
8	10.800	11.727
9	10.816	11.742
10	10.828	11.757
11	10.844	11.768
12	10.858	11.777
13	10.874	11.791
14	10.886	11.807
15	10.902	11.822
16	10.916	11.837
17	10.930	11.853
18	10.946	11.867
19	10.962	11.880
20	10.976	11.893
21	10.990	11.905
22	11.006	11.917
23	11.020	11.929
24	11.035	
25	11.050	
26	11.066	
27	11.081	
28	11.096	
29	11.109	
30	11.127	

[a] See the text.

[b] Uncertainty ± 0.002 eV.

Table 4.17 Summary of the spectroscopic constants for the valence ionic states of I_2.

Molecule I_2	AIE (eV)	VIE (eV)	ω_e (cm^{-1})	$\omega_e x_e$ (cm^{-1})	r_e (Å)	Spin-orbit splitting (cm^{-1})	Ref.
($X\ ^1\Sigma_g^+$)	–	–	214.502	-0.6147	2.666	–	[1]
($X\ ^2\Pi_{g,3/2}$)	9.311[a] ±0.002	9.335 ±0.002	220[b]	–	–	5130±32[c]	this work
	–	–	242±15	~-1	–	–	[17][d]
	9.311 ±0.002	9.34 ±0.01	240 ±10	–	–	5178±32[c]	[16]
	–	9.34	~220	–	–	5125±40	[14]
	9.22 ±0.01	9.35 ±0.01	~236	–	–	5243±40	[15]
($X\ ^2\Pi_{g,1/2}$)	9.947[a] ±0.002	9.976 ±0.002	214[b]	–	–	5130±32[c]	this work
	–	–	242±15	~-1	–	–	[17][d]
	9.953 ±0.002	9.98 ±0.01	220±10	–	–	5178±32[c]	[16]
	–	9.97	~220	–	–	5125±40	[14]
($A\ ^2\Pi_{u,3/2}$)	–	10.98 ±0.01	~120[d]	–	–	6694±160[e]	this work
	–	–	~130[d]	–	–	–	[54]
	–	–	~122[d]	–	–	–	[25]
	10.8[f]	11.03	–	–	–	~6400	[14]
	10.74	11.01	~125	–	–	6452±160	[15]
($A\ ^2\Pi_{u,1/2}$)	–	11.81 ±0.01	~120[d]	–	–	6694±160[e]	this work
	11.6[f]	11.82	–	–	–	~6400	[14]
($B\ ^2\Sigma_g^+$)	–	12.95 ±0.01	–	–	–	–	this work
	12.7[f]	12.95	–	–	–	–	[14]
	12.66 ±0.02	12.95 ±0.02	–	–	–	–	[15]

[a] Experimental adiabatic ionisation energy, uncertainty. [b] Average vibrational spacing. [c] Spin-orbit splitting measured between v=0 bands. [d] Average values over both spin-orbit components. [e] Vertical I.P. spin-orbit splitting. [f] Band onset.

$X\ ^2\Pi_{g,1/2}$ spin-orbit component, suggests that Rydbergs converging on this state are responsible. The most likely candidates are therefore the *n*p and *n*f Rydberg states. However, since exact quantum defects for these Rydberg series are unknown, averaged, atomic *n*p (3.58) and *n*f (0.1) quantum defect values [55] are used, along with a value of 9.947 eV for the adiabatic ionisation potential of the $X\ ^2\Pi_{g,1/2}$ ionic state, to calculate the Rydberg band origins shown in Table 4.18. From the calculations, the most likely candidates for the two band profiles, labelled I and II, are the 9p and 10p Rydberg states. Based on the identification of these Rydbergs series in autoionisation structure found in the molecular ion excitation function at approximately the same energies [56], these Rydbergs are likely to be pπ in character rather than pσ. Table 4.18 also suggests that the 8p Rydberg may be responsible for the reversed spin-orbit branching ratio's observed in the main $X\ ^2\Pi_{g,i}$ bands. Similar Rydberg states have been identified as resulting in the formation of free pairs of ions in this energy range [57] and it is therefore fairly clear that autoionisation and ion-pair formation can occur in competition from the same Rydberg state [58] as was found in the threshold study of Cl_2.

Table 4.18 Calculated adiabatic term values in eV for *n*p and *n*f Rydberg states of I_2 converging on the $X\ ^2\Pi_{g,1/2}$ spin-orbit component.

n	$[(\sigma_g)^2(\pi_u)^4(\pi_g^*)^3]_{1/2}$ *n*p	$[(\sigma_g)^2(\pi_u)^4(\pi_g^*)^3]_{1/2}$ *n*f
6	7.62	9.56
7	8.78	9.66
8	9.25	9.73
9	9.48	9.78
10	9.62	9.81

The extended vibrational structure in the X $^2\Pi_{g,1/2}$ spin-orbit component suggests that Rydberg states converging on the A $^2\Pi_{u,i}$ ionic state or a higher energy state are likely to be responsible. However, the profile of band III in Figure 4.14 and its breadth is more in line with that of bands I and II. Hence band III is likely to arise from autoionisation of a Rydberg state whose electronic character is very similar to that of the X $^2\Pi_{g,1/2}$ ionic spin-orbit component, although at present the exact identity of this state remains a mystery. In contrast, the shape and width of band IV has the general appearance of one of the A $^2\Pi_{u,i}$ spin-orbit band profiles. A tentative identification of this band can be made in a similar manner to above. As was the case in Cl_2 and Br_2, only the *n*sσ Rydberg states converging on the A $^2\Pi_{u,i}$ ionic bands will be considered. The exact quantum defect is unknown so an average atomic *n*s quantum defect of 4.04 [55] is used in the calculation. Due to the uncertainty in the adiabatic ionisation potentials for the A $^2\Pi_{u,i}$ spin-orbit states, the vertical ionisation potentials are employed (see Table 4.17) to calculate the Rydberg band maximums shown in Table 4.19. These calculations suggest that either the 9sσ Rydberg state converging on the A $^2\Pi_{u,3/2}$ spin-orbit component or the 7sσ Rydberg state converging on the A $^2\Pi_{u,1/2}$ spin-orbit component may be responsible for band IV.

Table 4.19 Calculated adiabatic term values in eV for *n*sσ Rydberg states of I_2 converging on the A $^2\Pi_{u,i}$ spin-orbit components.

n	$[(\sigma_g)^2(\pi_u)^3(\pi_g^*)^4]_{3/2}$ *n*sσ	$[(\sigma_g)^2(\pi_u)^3(\pi_g^*)^4]_{1/2}$ *n*sσ
6	7.44	8.27
7	9.43	10.25
8	10.11	10.94
9	10.43	11.26

The enhanced vibrational structure within both spin-orbit components of the A $^2\Pi_{u,i}$ ionic band is very likely to be due to Rydbergs converging on higher states. By analogy with the calculations carried out for the X $^2\Pi_{g,3/2}$ band, it would seem likely that the enhanced structure in the A $^2\Pi_{u,3/2}$ spin-orbit component arises from autoionisation of a Rydberg converging on the A $^2\Pi_{u,1/2}$ spin-orbit component. Using the results of the Rydberg calculations shown in Table 4.19, it would seem as though the vibrationally enhanced structure could arise through the 8sσ Rydberg state which is predicted to have a band maximum at 10.94 eV. This fits in very nicely with the almost symmetric vibrational structure around the band maximum (10.98 eV) of the A $^2\Pi_{u,3/2}$ spin-orbit band. This band also contains a very long tail which continues into the higher spin-orbit component and which could arise from the 9sσ Rydberg state which is predicted to be found at 11.26 eV. The most likely candidate, on the other hand, to explain the enhanced structure on the A $^2\Pi_{u,1/2}$ spin-orbit band is probably a Rydberg state converging to the B $^2\Sigma_g^+$ state. However, the identification of this Rydberg will have to await further work.

4.7 References

[1] K.P. Huber and G. Herzberg, Molecular Spectra and Molecular Structure, Vol. 4, Constants of diatomic molecules, Van Nostrand Reinhold Company, New York (1979)

[2] Ch. A. Brau, Excimer Lasers, edited by Ch. K. Rhodes, Springer, Berlin (1984)

[3] M. Diegelmann, K. Hohla, F. Rebentrost and K.L. Kompa, J. Chem. Phys. **76** (1982) 1233

[4] H.A. Bethe and E.E. Salpeter, Quantum mechanics of one- and two- electron atoms, Springer-Verlag, Berlin (1957)

[5] E.U. Condon and H. Odabasi, Atomic Structure, Cambridge University Press, Cambridge 1980

[6] R.S. Mulliken, Rev. Mod. Phys. **2** (1930) 60

[7] J.H.D. Eland, Photoelectron Spectroscopy, Butterworth & Co., England (1974)

[8] C.E. Moore, Atomic Energy Levels, Vol. I (1949), Vol. II (1952), Vol. III (1957), National Bureau of Standards, Washington

[9] D.W. Turner, C. Baker, A.D. Baker and C.R. Brundle, Molecular Photoelectron Spectroscopy, Wiley-Interscience, London (1970)

[10] D.C. Frost and C.A. McDowell, J. Chem. Phys. **38** (1960) 407

[11] K. Watanabe, J. Chem. Phys. **26** (1957) 542

[12] J.D. Morrison, H. Hurzeler, M.G. Inghram and H.E. Stanton, J. Chem. Phys. **33** (1960) 821

[13] D.C. Frost, C.A. McDowell and D.A. Vroom, J. Chem. Phys. **46** (1967) 4255

[14] A.B. Cornford, D.C. Frost, C.A. McDowell, J.L. Ragle and I.A. Stenhouse, J. Chem. Phys. **54** (1971) 2651

[15] A.W. Potts and W.C. Price, Trans. Faraday Soc. **67** (1972) 1242

[16] B.R. Higginson, D.R. Lloyd and P.J. Roberts, Chem. Phys. Lett. **19** (1973) 480

[17] H. van Lonkhuyzen and C.A. de Lange, Chem. Phys. **89** (1984) 313

[18] T.L. Porter, J. Chem. Phys. **48** (1968) 2071

[19] V.V. Rao and P.T. Rao, Can. J. Phys. **36** (1958) 1557

[20] F.P. Huberman, J. Mol. Spec. **20** (1966) 29

[21] P.B.V. Haranath and P.T. Rao, Indian J. Phys. **29** (1955) 205

[22] R.P. Tuckett, A.R. Dale, D.M. Jaffey, P.S. Jarret and T. Kelly, Mol. Phys. **49** (1983) 475

[23] R.P. Tuckett and S.D. Peyerimhoff, Chem. Phys. **83** (1984) 203

[24] T. Harris, J.H.D. Eland and R.P. Tuckett, J. Mol. Spec. **98** (1983) 269

[25] S.M. Mason and R.P. Tuckett, Chem. Phys. Lett. **160** (1989) 575

[26] D.C. Cartwright and P.J. Hay, J. Chem. Phys. **114** (1987) 305

[27] S.D. Peyerimhoff and R.J. Buenker, Chem. Phys. **57** (1981) 279

[28] P.M. Boerrigter, M.A. Buijse and J.G. Snijders, Chem. Phys. **111** (1987) 47

[29] K. Balasubramanian, Chem. Phys. **119** (1988) 41

[30] J. Li and K. Balasubramanian, J. Mol. Spec. **138** (1989) 162

[31] P.M. Guyon, R.Spohr, W.A. Chupka and J. Berkowitz, J. Chem. Phys. **65** (1976) 1650

[32] K. Kimura, S. Katsumata, Y. Achiba, T. Yamazaki and S. Iwata, Handbook of He(I) Photoelectron Spectra of Fundamental Organic Molecules, Halsted Press, New York (1981)

[33] T. Reddish, A.A. Cafolla and J. Comer, Chem. Phys. **120** (1988) 149

[34] R.J. Stubbs, T.A. York and J. Comer, J. Phys. B: At. Mol. Phys. **18** (1985) 3229

[35] J. Berkowitz, C.A. Mayhew and B. Ruščic, Chem. Phys. **123** (1988) 317

[36] P.A. Hamilton, Chem. Phys. Lett. **140** (1987) 591

[37] D.J. Little, R.J. Donovan and R.J. Butcher, J. Photochem. **2** (1973) 451

[38] R.H. Strain, J. McLean and R.J. Donovan, Chem. Phys. Lett. **20** (1973) 504

[39] K.H. Kompa and K. Hohla, Chem. Phys. Lett. **14** (1972) 445

[40] R.J. Donovan and D. Husain, A. Rep. Chem. Soc. **123** (1971)

[41] D. Husain and R.J. Donovan, Adv. Photochem. **8** (1971) 1

[42] R.J. Donovan and D. Husain, Chem. Rev. **70** (1970) 489

[43] A.J. Yencha, "Penning Ionisation and Related Processes", in Electron Spectroscopy: Theory, Techniques and Applications, edited by C.R. Brundle, and A.D. Baker, Academic Press, London **5** (1984) 197

[44] A.J. Yencha, J. Ganz, M-W. Ruf and H. Hotop, Z. Phys. D. **14** (1989) 57

[45] A.J. Yencha, M-W. Ruf and H. Hotop, Z. Phys. D. **21** (1991) 113

[46] A.J. Yencha, M-W. Ruf and H. Hotop, Z. Phys. D. **29** (1994) 163

[47] J. Berkowitz, Photoabsorption, Photoionisation, and Photoelectron Spectroscopy, Academic Press, London (1979)

[48] M.Y. Adam, Phys. Scr. **35** (1987) 477

[49] M.Y. Adam, M.P. Keane, A. Naves de Brito, N. Correia, P. Baltzer, B. Wannberg, L. Karlson and S. Svensson, J. Electron Spectrosc. Relat. Phenom. **27** (1982) 129

[50] W. von Neissen, L.S. Cederbaum, W. Domcke and G.H.F. Dierckson, Chem. Phys. **56** (1981) 43

[51] G. Bieri, L. Asbrink and W. von Neissen, J. Electron Spectrosc. Relat. Phenom. **27** (1982) 129

[52] A.G. McConkey, G. Dawber, L. Avaldi, M.A. MacDonald, G.C. King and R.I. Hall, J. Phys. B. **27** (1994) 271

[53] S. Svensson, L. Karlsson, P. Baltzer, B. Wannberg, U. Gelius and M.Y. Adam, J. Chem. Phys. **89** (1988) 7193

[54] J.P. Horner and J.H.D. Eland, Chem. Phys. Lett. **110** (1984) 29

[55] C.C. Kiess and C.H. Corliss, J. Research of the Nat. Bur. Stand.-A. Phys. and Chem. Vol 63A, July-August (1959)

[56] D. Kaur-Kela, Ph.D. Thesis, State University of New York at Albany (1991)

[57] A. Kvaran, A.J. Yencha, D.K. Kela, R.J. Donovan and A. Hopkirk, Chem. Phys. Lett. **179** (1991) 263

[58] A.J. Yencha, D. Kaur, R.J. Donovan, A. Kvaran, A. Hopkirk, H. Lefebvre-Brion and F. Keller, J. Chem. Phys. **99** (1993) 4986

Chapter 5

The *Gerade* Rydberg States and Ground Ionic State of I_2

5.1 Introduction

Spectroscopic interest in the diatomic halogens has been ongoing ever since the dense manifold of electronic states predicted to be present in these molecules [1,2] were discovered experimentally [3]. Optical spectroscopic techniques, such as fluorescence and REMPI spectroscopy have proven to be the best methods of investigating the many Rydberg and ion-pair states found in the UV and VUV regions of these halogens. However, the presence of both Rydberg and ion-pair states (see below) in the same spectral regions can induce many spectral perturbations and although an explicit understanding of these interactions is still to be established, progress is being made in certain cases [4-,5,6].

5.2 Rydberg and Ion-pair States

Rydberg states are a distinct group of electronically excited states in which an electron with angular momentum l, is promoted to an orbital with a principal quantum number, n, greater than that characteristic of the valence shell (i.e. n>5 for I_2) [7]. Excitation of the electron to progressively larger n constitutes a Rydberg series and as $n \rightarrow \infty$ the series converges to the limit of the atomic/molecular ion core, corresponding to the complete removal of the Rydberg electron. To a first approximation the Rydberg electron experiences an isotropic Coulomb attraction and

is largely unaffected by the rotational and vibrational motion of the molecular ion core. Molecular Rydberg series for an individual l are described by

$$T_{nl} = \text{I.P.}[\text{core}^+] - \frac{R}{(n-\delta(l))^2} \qquad 5.1$$

where I.P.[core$^+$] is the energy of the ionic core to which the Rydberg series converges, n is the principle quantum number of the Rydberg electron, R is the Rydberg constant (109737.3 cm^{-1}) and δ is the quantum defect associated with a particular Rydberg electron. The quantum defect, $\delta(l)$, measures the departure of the orbitals of such electrons from hydrogenic orbitals, for which $\delta(l)$=0. This arises because the presence of core electrons means the Rydberg electron experiences a shielded Coulomb potential that falls off more rapidly with distance than the pure Coulomb potential. The magnitude of $\delta(l)$ is mainly dependent on how deeply the Rydberg electrons radial wavefunction penetrates the core region as a function of *nl*. For a given n, δ for different l values increases in the order s>p>d>f. However, $\delta(l)$ is found to experimentally remain nearly constant with increasing n. It has been shown for many molecules that the quantum defect of an electron in a particular Rydberg orbital is virtually the same whether the orbital is associated with a molecular core or an atomic core [8]. A knowledge of atomic quantum defect values can therefore be used to assign Rydberg electronic band origins in molecular species. An infinite number of Rydberg states converging on every ionisation limit can lead to many problems in identifying individual states. However, low n Rydberg states tend to be energetically well separated making them relatively easy to identify. In contrast, the fact that the intensity of transitions to high-n states falls off as n^{-3} [9] and the fact that the energetic separation between individual high-n Rydberg states reduces can make the identification of high-n Rydberg states increasingly difficult.

In contrast to Rydberg states, whose potentials are very similar to the ionic state to which they converge, ion-pair state potentials are essentially Coulombic in nature [10,11]. They are characterised by deeply bound potentials with large

internuclear separations which can support a high density of vibrational levels. The spectroscopic characteristics of ion-pair states, such as large dissociation energies and small vibrational and rotational constants are therefore unusual compared with conventional valence states. As the name suggests ion-pair states correlate at dissociation with two oppositely charged ions, which in the diabatic approximation corresponds to the closed shell ground state $^1S_0$ of the halide anion and a low lying cationic state; $^3P_2$, $^3P_1$, $^3P_0$, $^1D_2$ and $^1S_0$. Since the halogen cation has several spectroscopic states, the potentials correlating with each ionic asymptote run parallel to eachother giving rise to clusters (or tiers) of ion-pair states. In I_2, because of the strong spin-orbit coupling in the cation, there is a clear clustering of the T_e values at R_e into three groups with spacings similar to those between the corresponding cationic states, as shown in Table 5.1. The molecular orbital configuration of an ion-pair state is generally characterised by the fact that the number of electrons present in the antibonding σ_u orbital is equal to or greater than the number of bonding σ_g electrons, such as [1441], [2332] and [1432].

5.2.1 The Rydberg Excited States of I_2

The spectroscopic study of the Rydberg states of the homonuclear diatomic halogens has been focused on those Rydberg states which converge on the positive molecular ion in its lowest electronic configuration, $[\sigma_g^2\pi_u^4\pi_g^3\sigma_u^0]$ (X $^2\Pi_{g,3/2}$, X $^2\Pi_{g,1/2}$). One of the first studies of the Rydberg states of I_2 was by Venkateswarlu in which the *n*p and *n*f Rydbergs were investigated using high resolution vacuum ultraviolet absorption spectroscopy [12]. More recently, however, the one colour (2+1) REMPI excitation scheme has become the main technique employed to investigate the Rydberg states of I_2 [13-19]. In contrast to Venkateswarlu's single photon excitation scheme, a two photon transition from the totally symmetric ground state of I_2 can only access the *n*s and *n*d *gerade* Rydberg states. This arises due to the fact that the promotion of an electron from a *gerade* (anti-bonding) π orbital to a Rydberg orbital leaves the ionic core with *gerade* symmetry. To maintain the overall

gerade symmetry after a two photon transition, the Rydberg electron must be s or d in character.

Table 5.1 A summary of the principle spectroscopic constants for the ion-pair states of molecular iodine.

Ion-Pair state	T_e / cm^{-1}	ω_e / cm^{-1}	R_e / Å	Dissociation limits ($I^- + I^+$)	Refs.
First Tier					
D 0_u^+	41028.6	95.0	3.58	$^1S_0 + {}^3P_2$	[20,21]
E 0_g^+	41411.8	101.4	3.65	$^1S_0 + {}^3P_2$	[22]
γ 1_u	41621.3	95.0	3.67	$^1S_0 + {}^3P_2$	[23]
β 1_g	40821.0	105.0	3.61	$^1S_0 + {}^3P_2$	[24]
δ 2_u	41689	100.2	(4.0)	$^1S_0 + {}^3P_2$	[25,23]
D' 2_g	40388.3	104.0	3.60	$^1S_0 + {}^3P_2$	[26,27]
2nd Tier					
F 0_u^+	47217.4	96.3	3.60	$^1S_0 + {}^3P_0$	[28,29]
f 0_g^+	47025.9	104.2	3.57	$^1S_0 + {}^3P_0$	[30]
g 0_g^-	(47070)	(105.7)	(3.55)	$^1S_0 + {}^3P_1$	[31]
G 1_g	47559.1	106.6	3.53	$^1S_0 + {}^3P_1$	[32]
H 1_u	48280.3	107.7	3.63	$^1S_0 + {}^3P_1$	[33]
3rd Tier					
1_g	53216.3	106.9	3.52	$^1S_0 + {}^1D_2$	[34]
f' 0_g^+	55409.9	97.0	3.83	$^1S_0 + {}^1D_2$	[5]
F' 0_u^+	51706.2	131.0	3.48	$^1S_0 + {}^1D_2$	[35,36]

The notation used to describe the Rydberg states of I_2 is $[^{2S+1}\Lambda_\Omega]_c$ *n*l; Ω_g, where the square brackets contain a Hund's case (a) description of the spin, orbital and total angular momenta of the ionic core to which the Rydberg state converges. The principal quantum number, *n*, and angular momentum of the Rydberg electron, l, along with the total angular momentum of the molecule, Ω_g are described outside the brackets. In Hund's case (c) notation Ω_g, which is the sum of the angular momentum

of the Rydberg electron, ω_{Ry}, and the total angular momentum of the ionic core, Ω_c, is a good quantum number.

$$\Omega_g = \Omega_c + \omega_{Ry} \qquad 5.2$$

However, Ω_c and ω_{Ry} may additionally be taken as good quantum numbers in I_2, as the coupling between the core and the Rydberg electron through electron exchange is fairly small compared with spin-orbit coupling within the core. Furthermore, the separation of the valence 5pσ and 5pπ orbitals in I_2 is sufficiently large for the dominant configuration of the ground state of I_2^+, $[\sigma_g^2\pi_u^4\pi_g^3\sigma_u^0]$, to contribute over 90% [37] with configurations such as $[\sigma_g^0\pi_u^4\pi_g^3\sigma_u^2]$ playing very little part. In the (2+1) REMPI spectrum, four Rydberg series are expected to converge on the positive molecular ion; $[^2\Pi_{3/2}]_c$ *n*s, $[^2\Pi_{1/2}]_c$ *n*s, $[^2\Pi_{3/2}]_c$ *n*d and $[^2\Pi_{1/2}]_c$ *n*d. As a result of the coupling between the Rydberg electron and the ionic core, each Rydberg state is split into a number of components. The $[^2\Pi_{3/2}]_c$ *n*s term splits into two states yielding Ω=2,1 components while each $[^2\Pi_{1/2}]_c$ *n*s has three components $\Omega=0^+,0^-,1$. The $[^2\Pi_{3/2}]_c$ *n*d series is split into 12 components having Ω=4(1), 3(2), 2(2), 1(3), 0^+(2) and 0^-(2) and the $[^2\Pi_{1/2}]_c$ *n*d is similarly split into 12 states (Ω=3(1), 2(3), 1(4), 0^+(2) and 0^-(2)). For a single *n* this amounts to a total of 29 Rydberg states. However, only Rydberg states with $\Omega\leq2$ can be accessed in a two photon transition from the totally symmetric $^1\Sigma_{0_g^+}$ ground state of I_2. With the electric dipole selection rules also forbidding $\Omega=0^-$ states, the actual spectrum is significantly simpler than the density of states would suggest.

The application of the (2+1) REMPI technique to I_2 by Dalby et al in 1977 provided the first coherent two-photon transitions to *gerade* Rydberg states [14]. From the vibrational spacings, polarisation data and rotational band contour analysis, the Rydberg state accessed was assigned $[^2\Pi_{1/2}]_c$ 6s; 1_g with an origin at 53560 cm^{-1}. In 1978, Lehmann et al. [15] observed a Rydberg state with an origin at 48400 cm^{-1} and assigned it as the other spin-orbit partner of the Dalby system, $[^2\Pi_{3/2}]_c$ 6s; 2_g.

Recently, however, Dasari et al. reassigned it as the $[^2\Pi_{3/2}]_c$ 6s; 1_g state based on rotational contour analysis [18]. The observation and assignment of the $[^2\Pi_{1/2}]_c$ 6s; 0_g^+ Rydberg state was reported by Miller in 1987 using mass-selective (2+1) REMPI [16]. Wu and Johnson [17] employed the same technique over the energy range 62000-64500 cm^{-1} and 67600-70000 cm^{-1} and observed four *n*d Rydberg states. However, Wu and Johnsons assignments were shown to be incorrect in the most recent complete (2+1) REMPI study by Donovan et al. [19]. The room temperature investigation by Donovan et al. reported a total of 12 new band systems in the two-photon energy region 48000-75300 cm^{-1}. These included *n*s Rydberg states up to n=11 based upon the $[^2\Pi_{3/2}]$ ion core and up to n=8 based on the $[^2\Pi_{1/2}]$ ion core with in addition at least three 5d Rydberg excited states based upon both cores. A schematic potential energy diagram of the known *n*s and *n*d Rydberg states above 53000 cm^{-1} is shown in Figure 5.1. The assignment of the Rydberg states of I_2 observed by Donovan et al. was based on determining a value for n-δ in Equation 5.1, at the electronic band origin of the Rydberg state. These calculations employed the ionisation potentials of I_2^+ given by Higginson et al. [38] and by Kvaran et al. [39] for the X $^2\Pi_{g,3/2}$ and X $^2\Pi_{g,1/2}$ spin-orbit states of 75093 and 80271 cm^{-1}, respectively.

5.3 The (2+1) Mass Resolved REMPI Excitation Spectra of the *n*s and *n*d Rydberg Excited States of Jet Cooled I_2 between 53000 and 70000 cm^{-1}

The emphasis of this investigation was to record mass resolved one colour (2+1) REMPI excitation spectra of the Rydberg excited states of jet-cooled I_2 which improved upon on the previous room temperature spectra. The study was also to act as a basis for a number of other investigations which required detailed spectral information on the Rydberg states of I_2. These included a (2+1') ZEKE-PFI investigation of the iodine molecular ion using a Rydberg intermediate state and an investigation of the Rydberg excited states of the I_2–Ar van der Waals complex. The (2+1) mass resolved REMPI excitation spectra of jet cooled I_2 has in fact managed to

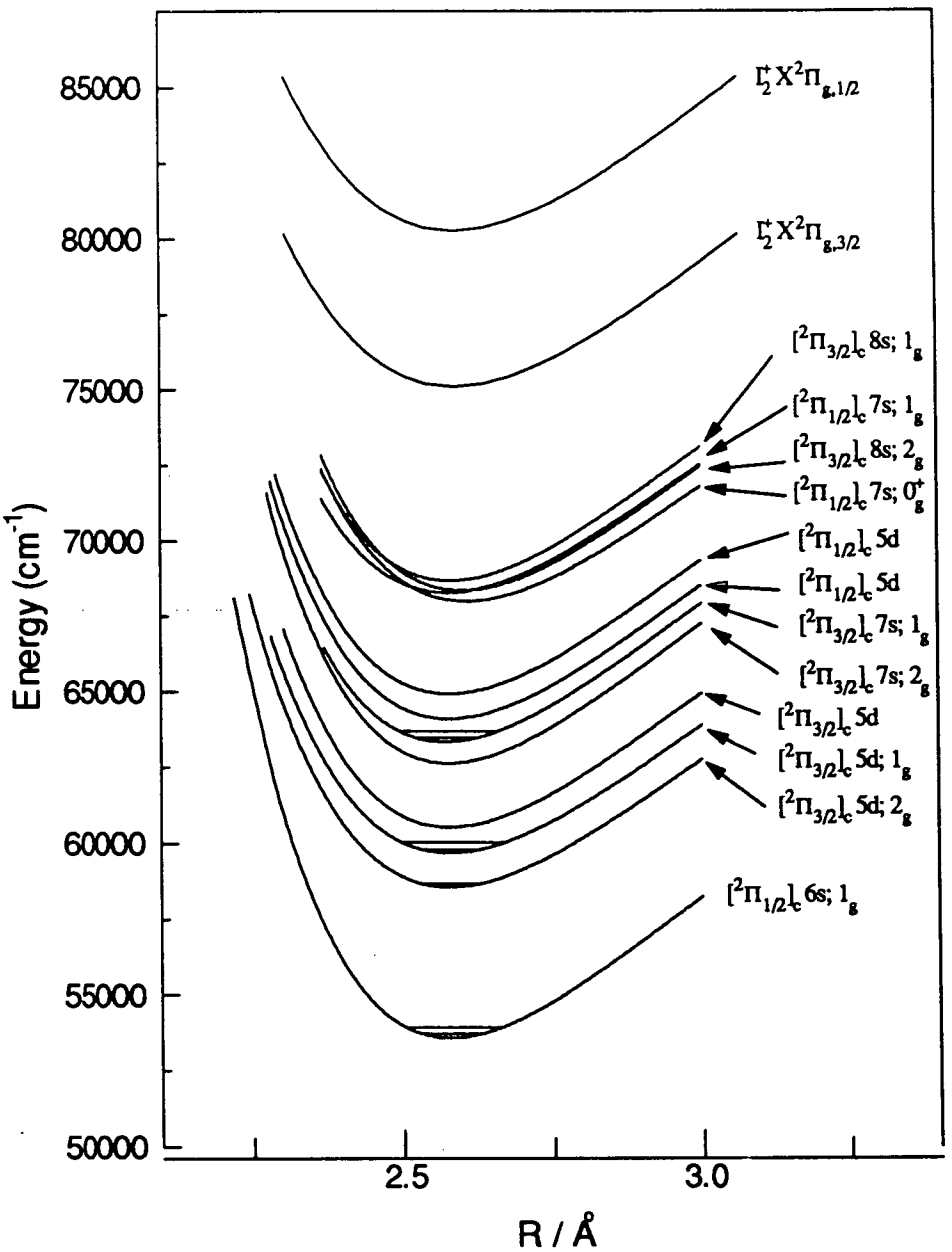

Figure 5.1

A schematic potential energy diagram of the known *n*s and *n*d Rydberg states above 53000 cm^{-1} converging on the X $^2\Pi_{g,3/2}$ and X $^2\Pi_{g,1/2}$ ionic states of I_2.

resolve ion-pair fine structure in a number of the ion-pair/Rydberg mixed states enabling the Ω quantum number of the Rydberg state to be determined and shown that a proposal put forward by Donovan et al. [19] to explain their polarisation results is incorrect. Throughout this investigation the assignments of Donovan et al. have not been changed. The iodine sample (Fisons) employed in this investigation was heated to approximately 100 ^{0}C and an argon carrier gas at pressures of 400-600 Torr was employed. The results are presented in order of increasing Rydberg principal quantum number.

5.3.1 The $[^2\Pi_{1/2}]_{c,g}$ 6s Rydberg System

The (2+1) mass resolved REMPI excitation spectrum recorded in the range 53200–55300 cm^{-1} two photon energy by monitoring the I_2^+ and I^+ mass channels is shown in Figure 5.2. The $[^2\Pi_{1/2}]_c$ 6s; 1_g and $[^2\Pi_{1/2}]_c$ 6s; 0_g^+ Rydberg states both give rise to regularly spaced progressions with narrow rotational contours and appear in both the I^+ and I_2^+ mass channels. These Rydberg states have previously been observed by both Dalby et al. [14] and Donovan et al. [19] in room temperature studies and Miller [16], both in a room temperature study and via jet-cooling. Vibrational bands up to v'=8 have been observed for the 1_g state with a vibrational frequency, ω_e= 244 ± 1 cm^{-1}, and up to v'=4 for the 0_g^+ state with a vibrational frequency, ω_e= 243 ± 1 cm^{-1}. These can both be compared with an ω_e of 214.5 cm^{-1} for the ground state of the neutral [40]. Up to three sequence bands are also observed to the blue of each of the (v',0) vibrational bands in the 1_g progression in the I^+ mass channel. The peak positions for the two Rydberg vibrational progressions, accurate to ± 2 cm^{-1}, are given in Table 5.2. A comparison with the previous study by Dalby et al. [14] reveals that the present values are consistently 7 cm^{-1} higher in energy. This is probably due to the lower rotational temperature (~15 K, cf. ~300K) and narrower laser bandwidth (0.4 cm^{-1} cf. 2 cm^{-1}) used in the present work. Although the peak positions and vibrational spacings of the 1_g progression are identical for the I^+ and I_2^+ mass channel spectra, the relative intensities within the

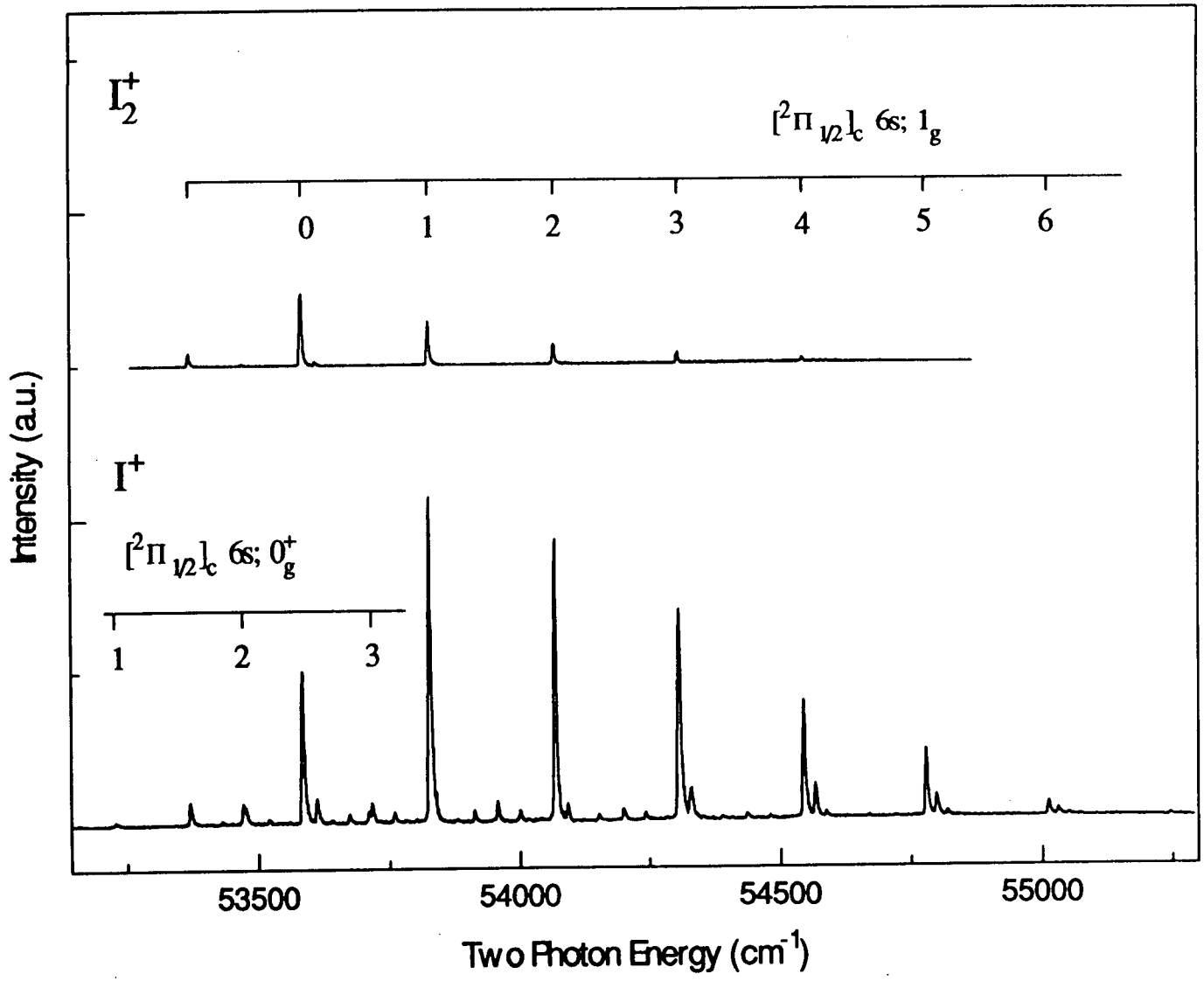

Figure 5.2 The (2+1) mass resolved REMPI excitation spectrum of jet-cooled I_2 recorded in the range 53200-55300 cm^{-1} by monitoring the I_2^+ and I^+ mass channels.

progressions are quite different. This is in agreement with previous results [16,41] which have shown that the I_2^+/I^+ ratio in the 1_g state decreases as v' increases. The exact value of this ratio has been found to be power dependant which suggests that although the production of I_2^+ is a three-photon process, the production of I^+ requires a fourth photon. The observation of a decrease in intensity in the I_2^+ mass channel with increasing vibrational quantum number suggests that the absorption of a fourth photon takes the molecular ion to a dissociative ionic state. Increasing the vibrational level in the Rydberg state improves the vibrational Franck-Condon overlap with the dissociative state, such that by the time v' =4 is reached, dissociation of I_2^+ is almost complete. One further point of note for this system is its behaviour with circularly polarised light. Both the I^+ and I_2^+ mass channel spectra display net increases in intensity in agreement with the room temperature observations of Donovan et al. [19] and theory [42]. The weak vibrational structure appearing between the Rydberg vibrational bands in the I^+ mass channel arises from the I_2–Ar van der Waals complex and will be discussed in the following chapter.

5.3.2 The $[^2\Pi_{3/2}]_{c,g}$ 7s Rydberg System

The (2+1) REMPI excitation spectrum of I_2 in the range 62500-64500 cm^{-1} has been reported by Wu and Johnson [17] using jet-cooling and time-of-flight mass spectrometric (TOFMS) detection. The observed bands, in that case, were assigned to a single *n*d Rydberg state progression. However, in a recent room temperature study of the *gerade* Rydberg states of iodine, Donovan et al. [19] reassigned the progression using polarisation data to the $[^2\Pi_{3/2}]_c$ 7s; 2_g and $[^2\Pi_{3/2}]_c$ 7s; 1_g overlapping Rydberg states. The mass resolved REMPI spectrum in the range 62250-64200 cm^{-1} is shown in Figure 5.3. Clearly, the presence of two states is confirmed with the lower energy 2_g state appearing in both the I_2^+ and I^+ mass channels, whereas the 1_g state is only observed when collecting I^+. The peak positions accurate to ± 2 cm^{-1} are given in Table 5.2. The vibrational bands associated with the progression in the 2_g state (up to v'=4) have an ω_e=234 ± 1 cm^{-1}. The vibrational bands of the 1_g

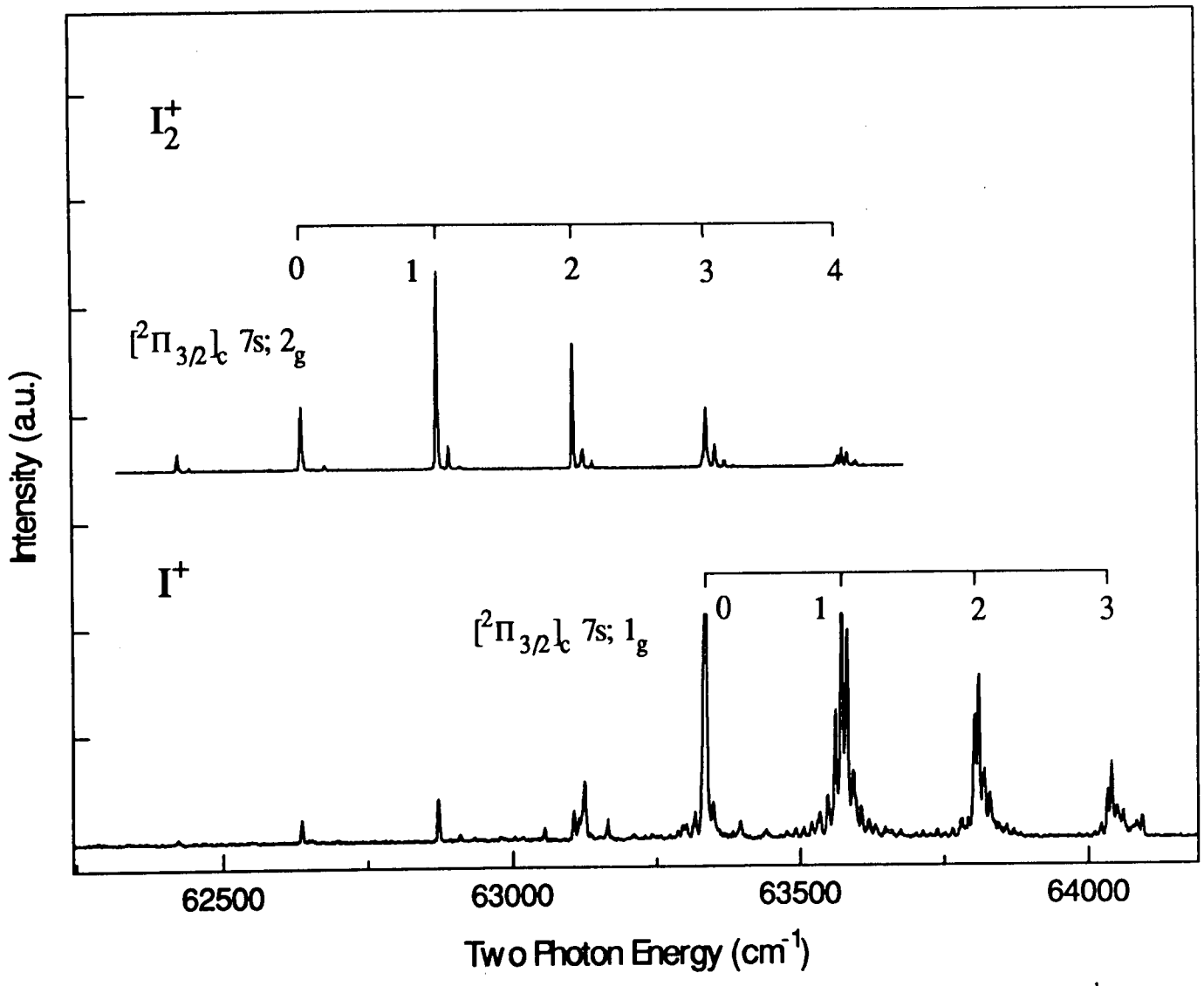

Figure 5.3 The (2+1) mass resolved REMPI excitation spectrum of jet-cooled I_2 recorded in the range 62250-64200 cm^{-1} by monitoring both the I_2^+ and I^+ mass channels. Note that the v=0 band of the $[^2\Pi_{3/2}]_c$ 7s; 1_g progression is off scale.

Rydberg state, however, are heavily perturbed by an ion-pair state such that only an approximate ω_e of 242 ± 5 cm^{-1} can be determined. The fact that the vibrational band intensities in the I^+ and I_2^+ mass channels in Figure 5.3 are directly comparable makes it possible to ascertain that the parent molecular ion (I_2^+) is the dominant ionisation product in the 2_g Rydberg state whereas the fragment I^+, is only a minor product. One further point of note is the behaviour of these two Rydberg states with circularly polarised light. The 1_g Rydberg state displays an almost complete loss of intensity whereas the 2_g state displays a net increase in intensity. The observed spectral differences with circularly and linearly polarised light will be discussed further below.

Table 5.2 Spectral peak positions and assignments for the (2+1) REMPI excitation spectra of I_2.

$[\Omega_c]nl$; Ω_g	(v',v'') [a]						
	(0,1)	(0,0)	(1,0)	(2,0)	(3,0)	(4,0)	(5,0)
$[^2\Pi_{1/2}]_c$ 6s; 0_g^+		52988	53229	53471	53709	53948	
$[^2\Pi_{1/2}]_c$ 6s; 1_g	53369	53582	53824	54064	54302	54538	54773
$[^2\Pi_{3/2}]_c$ 5d; 2_g [b]	58361	58577	58778	59023			
$[^2\Pi_{3/2}]_c$ 5d; 1_g		59695	59942	60187	60418	60689	60915
$[^2\Pi_{3/2}]_c$ 5d	60323	60536					
$[^2\Pi_{3/2}]_c$ 7s; 2_g	62424	62639	62872	63104	63335	63565	
$[^2\Pi_{3/2}]_c$ 7s; 1_g [b]	63118	63332	63576	63806	64037	64269	
$[^2\Pi_{1/2}]_c$ 5d		64098	64280				
$[^2\Pi_{1/2}]_c$ 5d		64927	65155	65410	65646	65886	
$[^2\Pi_{1/2}]_c$ 7s; 0_g^+	67778	67992	68218	68441	68660		
$[^2\Pi_{1/2}]_c$ 7s; 1_g	68059	68274	68499	68716	68934	69160	69388
$[^2\Pi_{3/2}]_c$ 8s; 2_g	68129	68343	68577	68805	69030		
$[^2\Pi_{3/2}]_c$ 8s; 1_g	68456	68668	68900	69128	69360		

[a] Uncertainty ± 2 cm^{-1}.

[b] Strong interaction with an ion-pair state. Values are therefore estimated unperturbed levels.

An expanded spectrum of the 1_g vibrational progression from v'=0-3, observed by monitoring I^+ is shown in Figure 5.4. The multiplet structure centred on v'=1,2 and 3 is assigned to ion-pair structure and arises from a coupling of an ion-pair state with the 1_g Rydberg state. The measured average vibrational spacing of ~14 cm^{-1} enables us to unambiguously assign the ion-pair state as belonging to the first tier of states which dissociate to I^+ ($^3P_2$) and I^- ($^1S_0$) (see Table 5.1). The strong coupling between the states suggests that it is homogeneous in nature and further labels the ion-pair state as 1_g. Consequently, we can assign it to the β state since this is the only first tier ion-pair state of 1_g symmetry (see Table 5.1). Only weak ion-pair structure is observed around v'=0 of the Rydberg state while it appears at its strongest around v'=1 indicating that the potentials cross in this region. The irregular nature of the structure near each of the band maxima results from a Fermi resonance of the unperturbed Rydberg level with a near degenerate ion-pair level. A full simulation of the interaction between the $[^2\Pi_{3/2}]_c$ 7s; 1_g Rydberg state and the $\beta(1_g)$ ion-pair state has been carried out by Al-Kahali et al. [43]. The $\beta(1_g)$ ion-pair state band positions accurate to ± 2 cm^{-1} are given in Table 5.3 and an indication of the position of the unperturbed Rydberg vibrational levels is given in the Figure 5.4. The vibrational numbering of the $\beta(1_g)$ ion-pair state levels is taken form Ref. [43].

5.3.3 The $[^2\Pi_{1/2}]_{c,g}$ 7s and $[^2\Pi_{3/2}]_{c,g}$ 8s Rydberg Systems

The (2+1) REMPI excitation spectrum of I_2 in the range 67800-69950 cm^{-1} has been previously reported by Wu and Johnson [17]. The observed vibrational bands in that case were assigned to at least three *n*d Rydberg state progressions but the complexity of the spectrum made a precise assignment impossible. The recent room temperature study by Donovan et al. [19] reassigned the vibrational bands to four *n*s Rydberg states based on quantum defect assignments and polarisation data. The four overlapping Rydberg vibrational progressions were assigned to the $[^2\Pi_{1/2}]_c$ 7s; 0_g^+ and 1_g and $[^2\Pi_{3/2}]_c$ 8s; 2_g and 1_g Rydberg states.

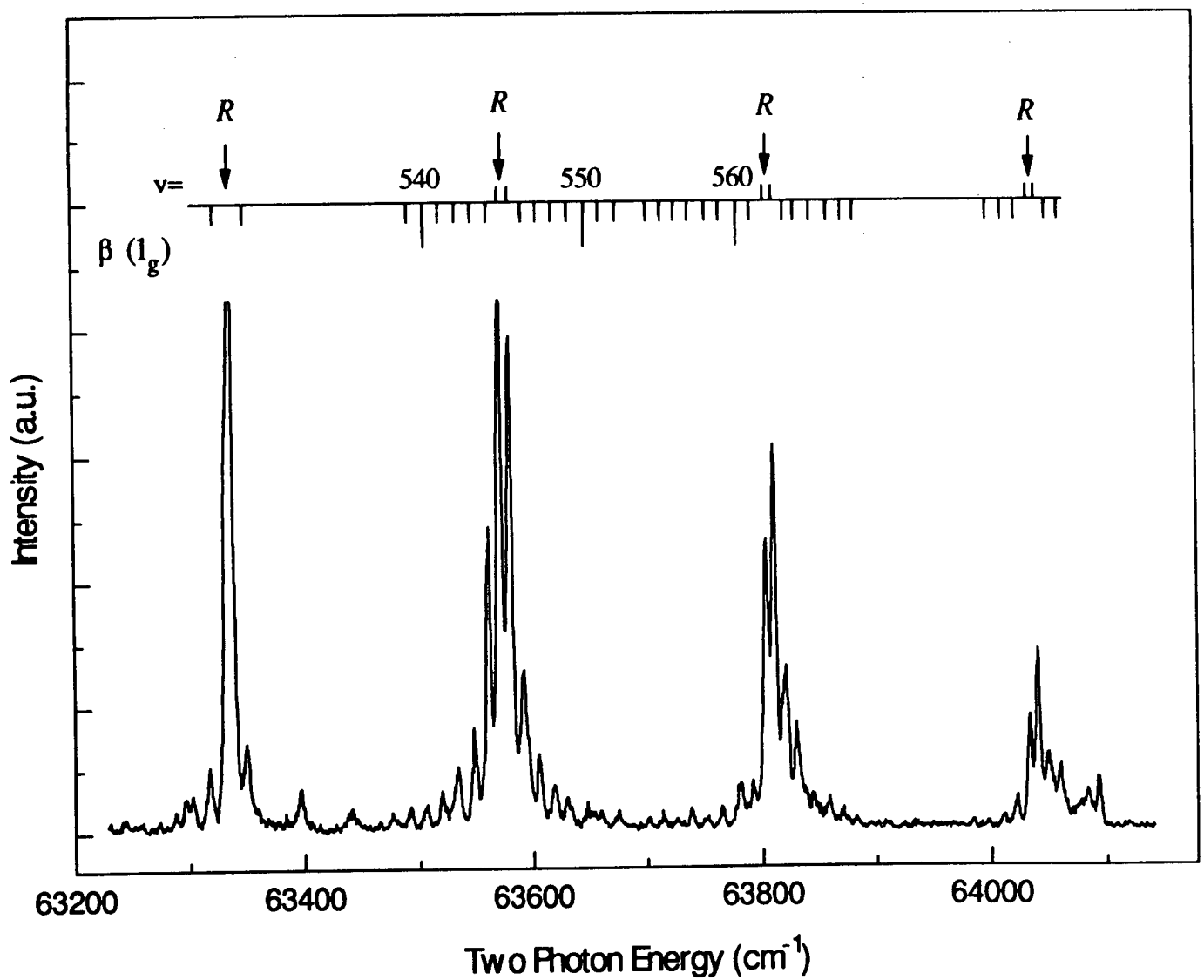

Figure 5.4 An expanded scan of the (2+1) REMPI excitation spectrum of jet-cooled I_2 recorded in the range 63200-64200 cm^{-1} showing rich ion-pair vibrational structure arising from an interaction of the $[^2\Pi_{3/2}]_c$ 7s; 1_g Rydberg state with the $\beta(1_g)$ ion-pair state, R denotes the position of the unperturbed Rydberg vibrational levels.

Table 5.3 Spectral peak positions and assignments for the $\beta(1_g)$ ion-pair state coupled to the $[^2\Pi_{3/2}]_c 7s;\ 1_g$ Rydberg state.

(v',0) [a]	Transition energy / cm^{-1} [b]	(v',0) [a]	Transition energy / cm^{-1} [b]
523	63273	559	63765
524	63287	560	63781
525	63302	561	63793
526	63317	562	63802/63809
539	63492	563	63820
540	63505	564	–
541	63520	565	63845
542	63535	566	63858
543	63549	567	63870
544	63562	568	63882
545	63572/63582	569	63897
546	63591	570	63909
547	63605	571	–
548	63620	572	63934
549	63633	577	63997
550	63647	578	64010
551	63662	579	64023
552	63675	580	64034/64041
553	–	581	64050
554	63700	582	64062
555	63713	598	64260
556	63727	599	64274
557	63739	600	64288
558	63753		

[a] Vibrational numbering taken from Ref. [43].

[b] Uncertainty $\pm 2\ cm^{-1}$.

The mass resolved (2+1) REMPI spectrum of I_2 recorded in the two-photon energy range 67250 to 70000 cm^{-1} is shown in Figure 5.5. It should be noted that the I^+ mass channel must be scaled by a factor of approximately four when making intensity comparisons between the two mass channels. The peak positions of the four Rydberg states resolved in Figure 5.5 accurate to ± 2 cm^{-1} are given in Table 5.2. The two 1_g states again dominate the I^+ mass channel in agreement with the behaviour observed in the lower energy $[^2\Pi_{3/2}]_c$ 7s system. However, in contrast to the $[^2\Pi_{3/2}]_c$ 7s system, the two 1_g states also appear in the I_2^+ mass channel with comparable intensities to the 0_g^+ and 2_g states. The intensity ratio (I_2^+/I^+) of the vibrational bands of the 2_g and 0_g^+ Rydberg states as the Rydberg vibrational quantum number increases shows a broad similarity to that observed for the $[^2\Pi_{1/2}]_c$ 6s; 1_g Rydberg state. This would suggest that these Rydberg states also undergo the absorption a fourth photon to a dissociative state where the vibrational Franck-Condon overlap with the dissociative state improves with increasing vibrational quantum number in the Rydberg state. The $[^2\Pi_{1/2}]_c$ 7s; 0_g^+ Rydberg state has an ω_e of 230 ± 1 cm^{-1} whereas the $[^2\Pi_{3/2}]_c$ 8s; 2_g state has an ω_e of 238 ± 1 cm^{-1}. In contrast to the 0_g^+ and 2_g Rydberg states, both the 1_g Rydberg vibrational progressions are observed predominantly in the I^+ mass channel and show anomalous vibrational intensity distributions. The $[^2\Pi_{1/2}]_c$ 7s; 1_g Rydberg state has an ω_e of 217 ± 4 cm^{-1} whereas the $[^2\Pi_{3/2}]_c$ 8s; 1_g Rydberg state has an ω_e of 230 ± 4 cm^{-1}. The large uncertainties in the vibrational frequencies of the two 1_g states along with the anomalous intensities support some form of perturbation in the neutral Rydberg states and/or in the ionisation continuum. The (2+1) REMPI spectra of the I^+ and I_2^+ mass channels recorded between 68100 and 69250 cm^{-1} with linearly and circularly polarised light are shown in Figures 5.6 and 5.7, respectively. Both mass channels demonstrate a loss of intensity in the 1_g Rydberg vibrational bands only. This point will be discussed further in a later section.

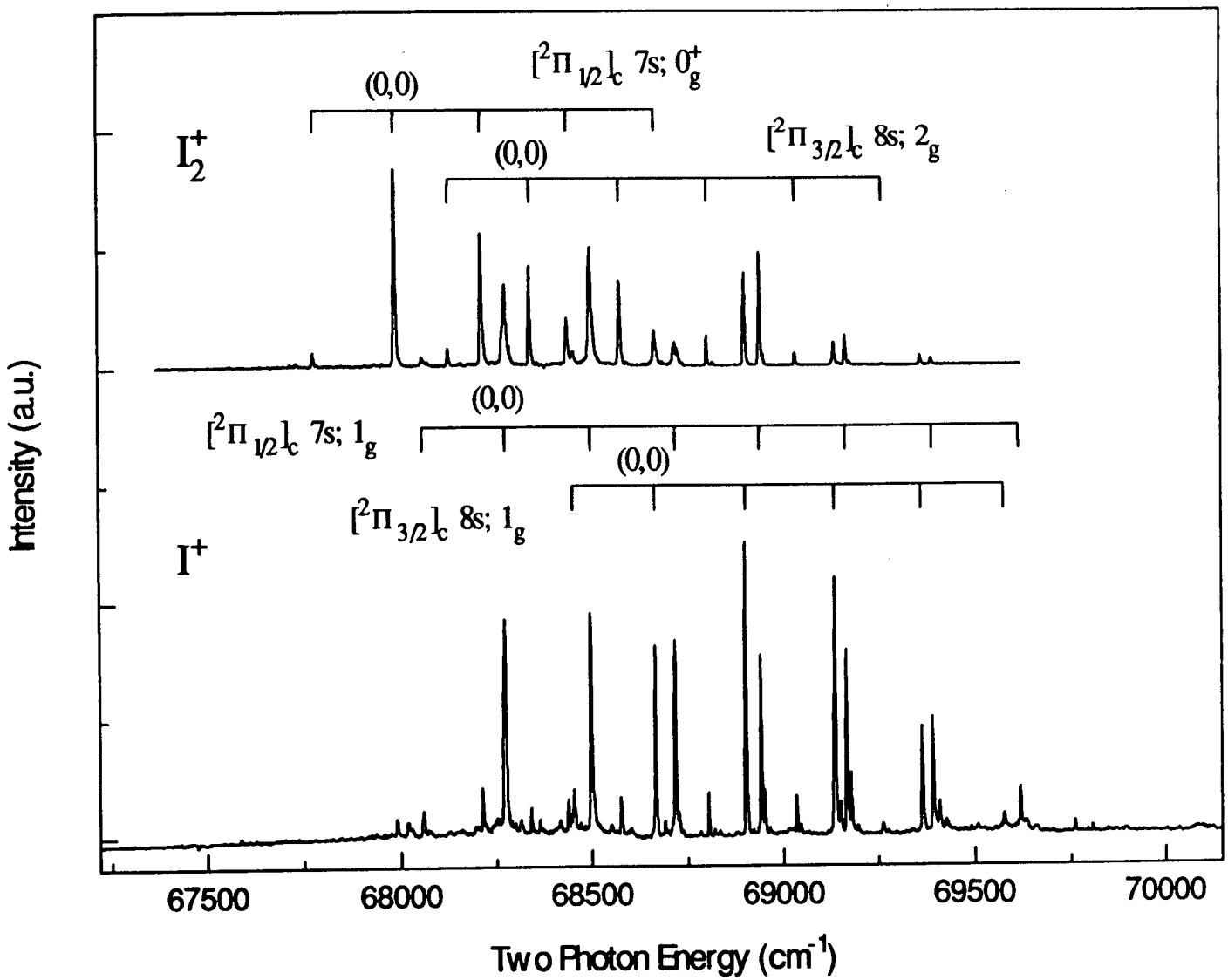

Figure 5.5 The (2+1) mass resolved REMPI excitation spectrum of jet-cooled I_2 recorded in the range 67250-70000 cm^{-1} by monitoring both the I_2^+ and I^+ mass channels. Note that in the upper spectrum, all four Rydberg states appear with comparable intensity whilst in the lower spectrum the 1_g states dominate.

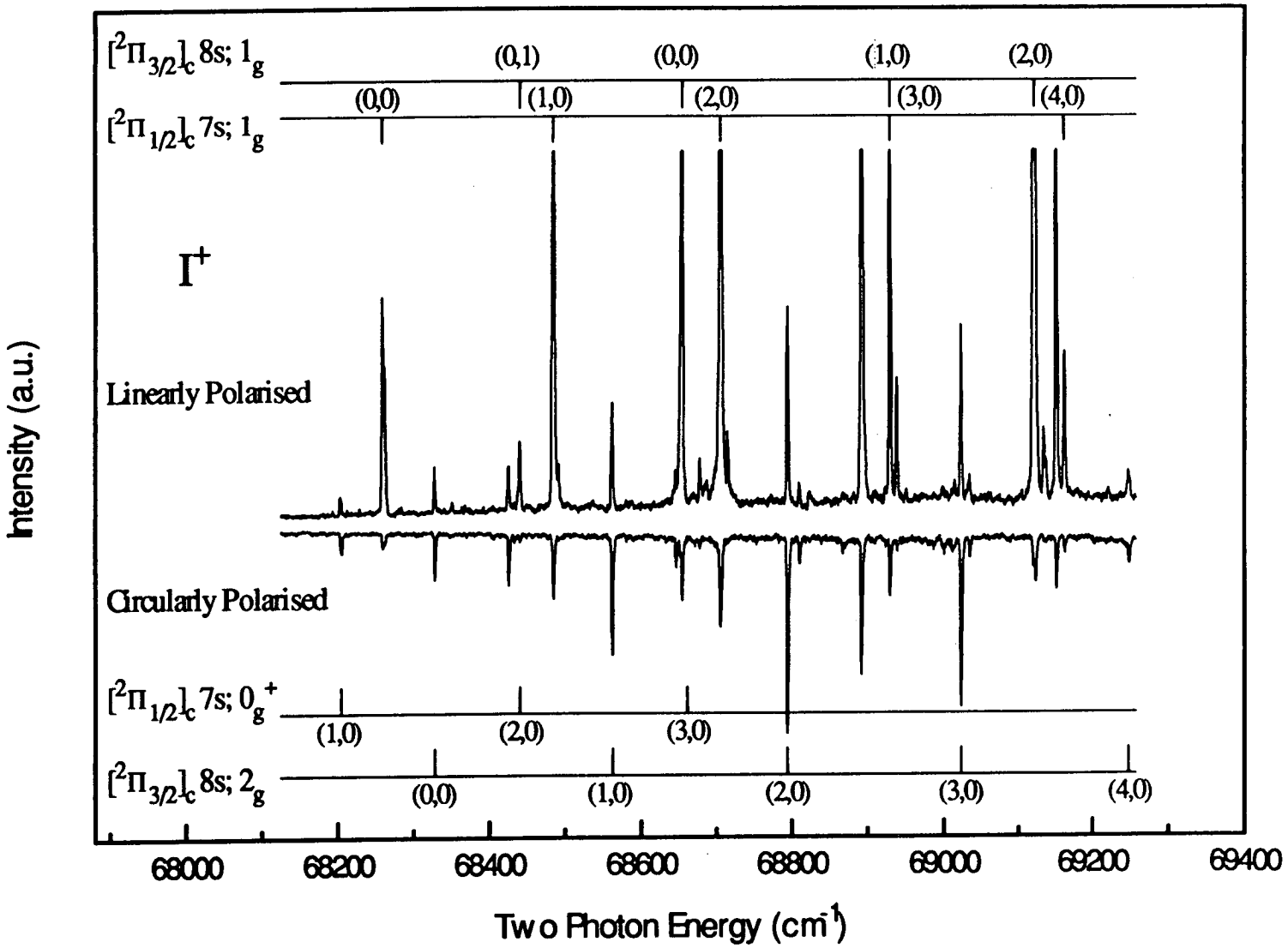

Figure 5.6 The (2+1) mass resolved REMPI excitation spectrum of jet-cooled I_2 recorded in the range 68100-69250 cm^{-1} by monitoring the I^+ mass channel with both linearly and circularly polarised light. Some of the 1_g vibrational peak maxima have been removed from the figure to enhance the weaker vibrational structure.

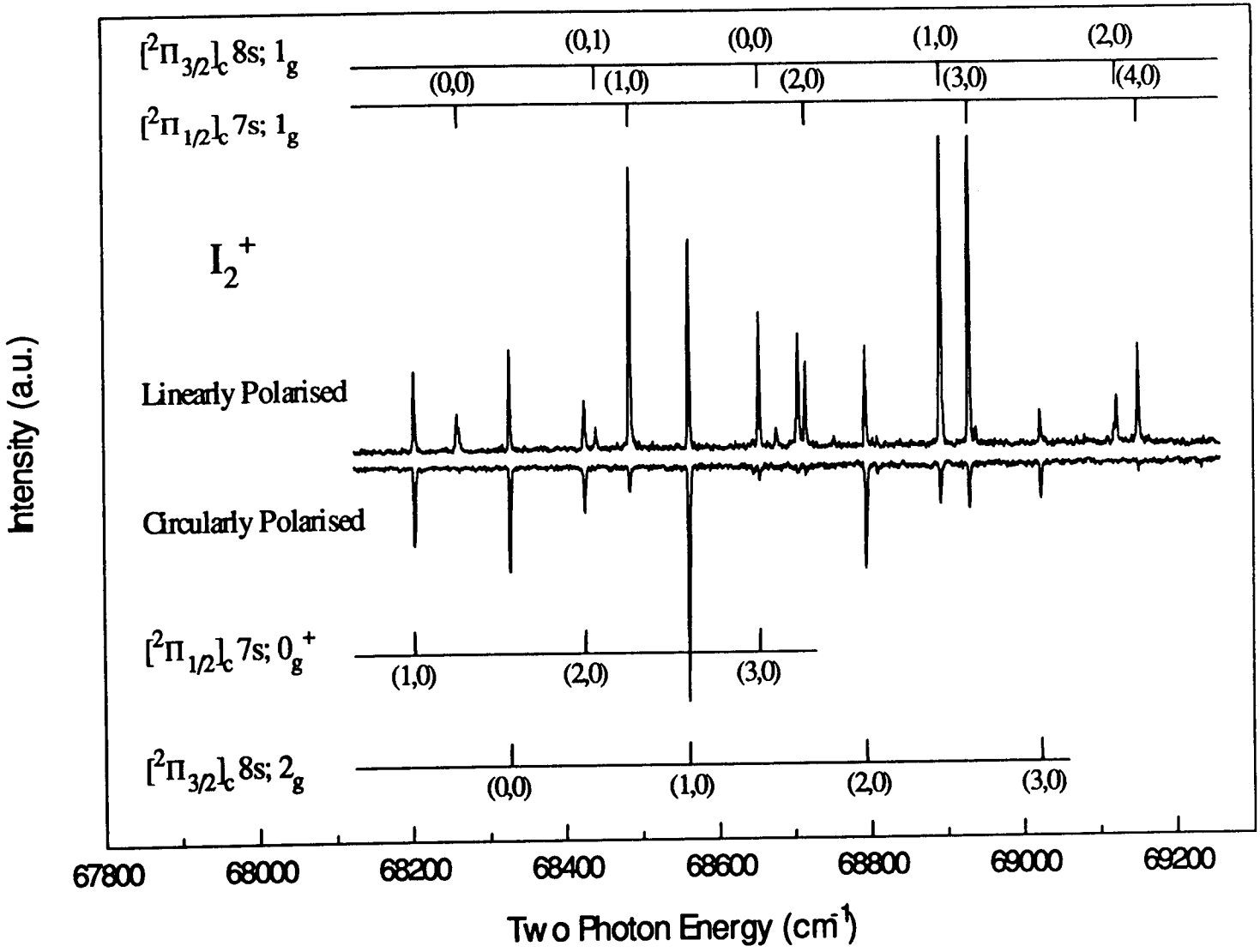

Figure 5.7 The (2+1) mass resolved REMPI excitation spectrum of jet-cooled I_2 recorded in the range 68100-69250 cm^{-1} monitoring the I_2^+ mass channel with both linearly and circularly polarised light. The 1_g vibrational peak maxima are off scale to enhance the weaker vibrational structure.

5.3.4 The $[^2\Pi_{3/2}]_{c,g}$ 5d Rydberg States

In the room temperature study of Donovan et al., three weak 5d states associated with the $[^2\Pi_{3/2}]$ core were observed. The lowest energy of these was observed in the region between 58000 and 59500 cm^{-1} and consisted of five broad features with Rydberg like spacings and a band origin at 58580 cm^{-1}. The jet-cooled (2+1) mass resolved REMPI spectrum in the same region (see Figure 5.8) reveals extensive vibrational structure in the I^+ mass channel associated with each of the Rydberg bands. This structure extends more than two thousand wavenumbers below the origin of the Rydberg progression. The I_2^+ mass channel in comparison, displays significantly less vibrational structure associated with each of the Rydberg bands. The low frequency structure can be assigned to an ion-pair progression similar to that observed in the $[^2\Pi_{3/2}]_c$ 7s system. The ion-pair vibrational band assignments and positions are given in Table 5.4. The Rydberg vibrational level observed at ~58577 cm^{-1} is assigned to the band origin, the 216 cm^{-1} separation between this band and the one to lower energy being indicative of a hot band. The strong ion-pair intensity can again be assumed to be induced by homogeneous mixing between an ion-pair state and this 5d Rydberg state. The ion-pair vibrational structure forms a rather irregular progression whose average vibrational spacing of ~25 cm^{-1} once again suggests that it must be a first tier state. One possibility as to the identity of this ion-pair state is the $E(0_g^+)$ state which has been observed by Double Resonance Ionisation Nozzle Cooled Spectroscopy (DRINCS) and was found to consist of a regular progression (to within $\pm$ 0.5 cm^{-1}) [5]. However, any perturbation in the ion-pair structure should also show up in the DRINCS spectrum which suggests that the present ion-pair structure cannot be assigned to the E state. An identification of this state will be made in section 5.4.

Two further 5d $[^2\Pi_{3/2}]_c$ progressions were observed by Donovan et al. in the region between 59500 and 61000 cm^{-1}. The lower energy vibrational progression was observed up to v'=3 and was assigned as having 1_g symmetry on the basis of a rotational band contour analysis [19] whereas the higher energy vibrational

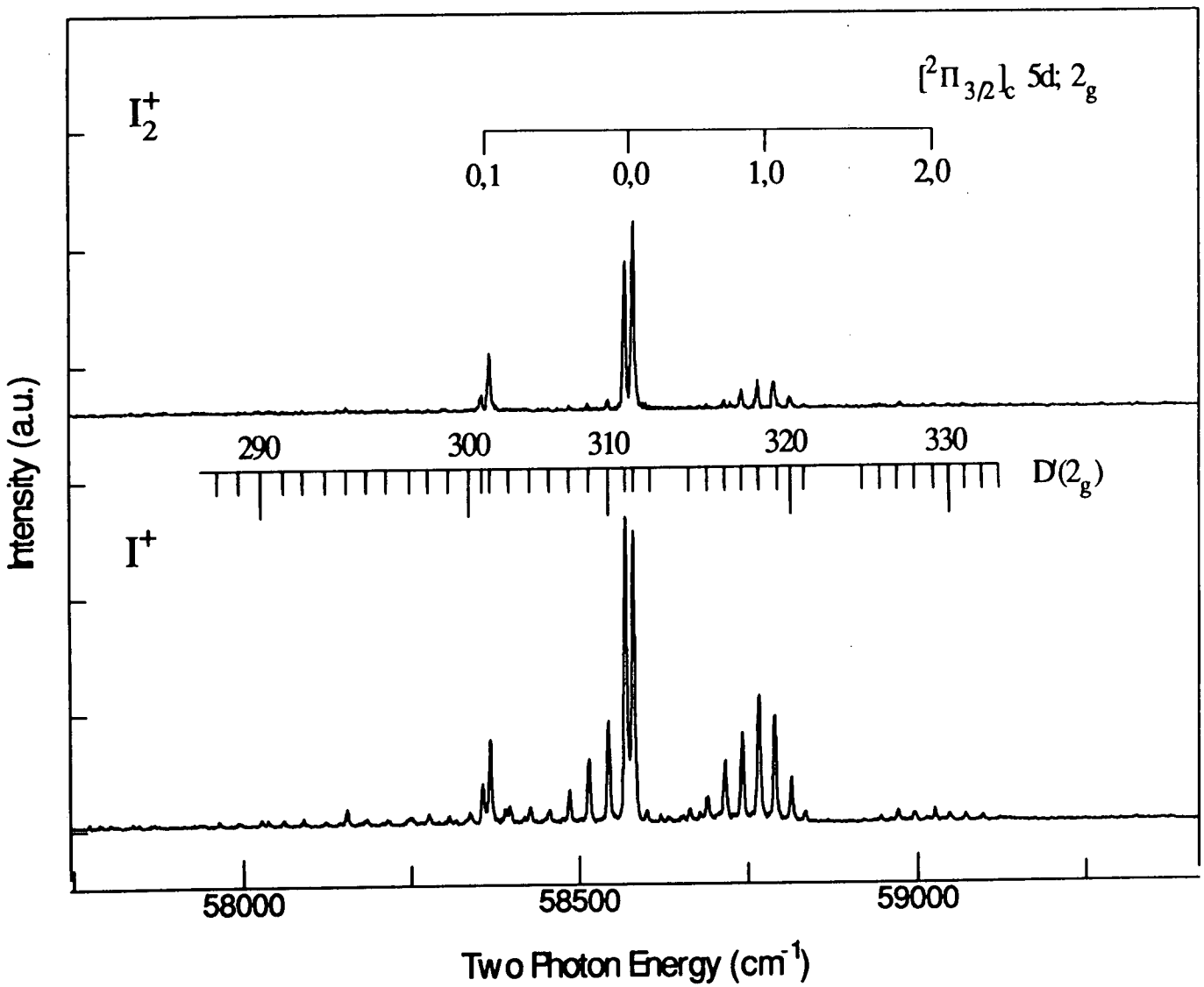

Figure 5.8 The (2+1) mass resolved REMPI excitation spectrum of jet-cooled I_2 recorded in the range 57750-59500 cm^{-1} by monitoring both the I_2^+ and I^+ mass channels. Both spectra display rich ion-pair structure arising from an interaction of the $[^2\Pi_{3/2}]_c$ 5d; 2_g Rydberg state with the D'(2_g) ion-pair state.

progression only consisted of two bands (v'=0 and 1) and was assigned a band origin of 60316 cm^{-1}. The equivalent jet-cooled spectrum is shown in Figure 5.9. The 1_g progression which dominates the I_2^+ mass channel spectrum extends up to v'=7 and shows rather irregular vibrational spacings (see Table 5.2). The sudden drop in intensity observed above v'=3 is the result of a weak avoided crossing with the $\beta(1_g)$ ion-pair state. The avoided crossing also displaces the v'=3 and v'=4 levels by ~20 cm^{-1}. This 5d Rydberg state and the ion-pair/Rydberg interaction has been investigated in more detail in a room temperature study by Kvaran et al. [44]. The lower spectrum in Figure 5.9 was recorded by monitoring the I^+ mass channel. Although the 1_g progression is present, two multiplet features are also observed, the most intense of which lies at 60536 cm^{-1}. The enhancement of these features in the I^+ spectrum relative to the I_2^+ spectrum suggests that they originate from a different Rydberg state to that which dominates the I_2^+ mass channel spectrum. The separation of these features is about 213 cm^{-1} which labels the lower energy band as a hot band. This disagrees, however, with Donovan et al.'s assignment which placed the band origin at 60316 cm^{-1}. The multiplet structure, which is basically composed of two side peaks and a single more intense central peak, arises from a crossing of the Rydberg state vibrational levels with one of the first tier ion-pair states. The central peak in this case is the unperturbed Rydberg level and the two side peaks are ion-pair levels. An appropriate pair of $E(0_g^+)$ state ion-pair levels have been observed by DRINCS [5] and although the two sets of data lie within the experimental error of $\pm$ 2 cm^{-1} an unambiguous assignment cannot be made in this case.

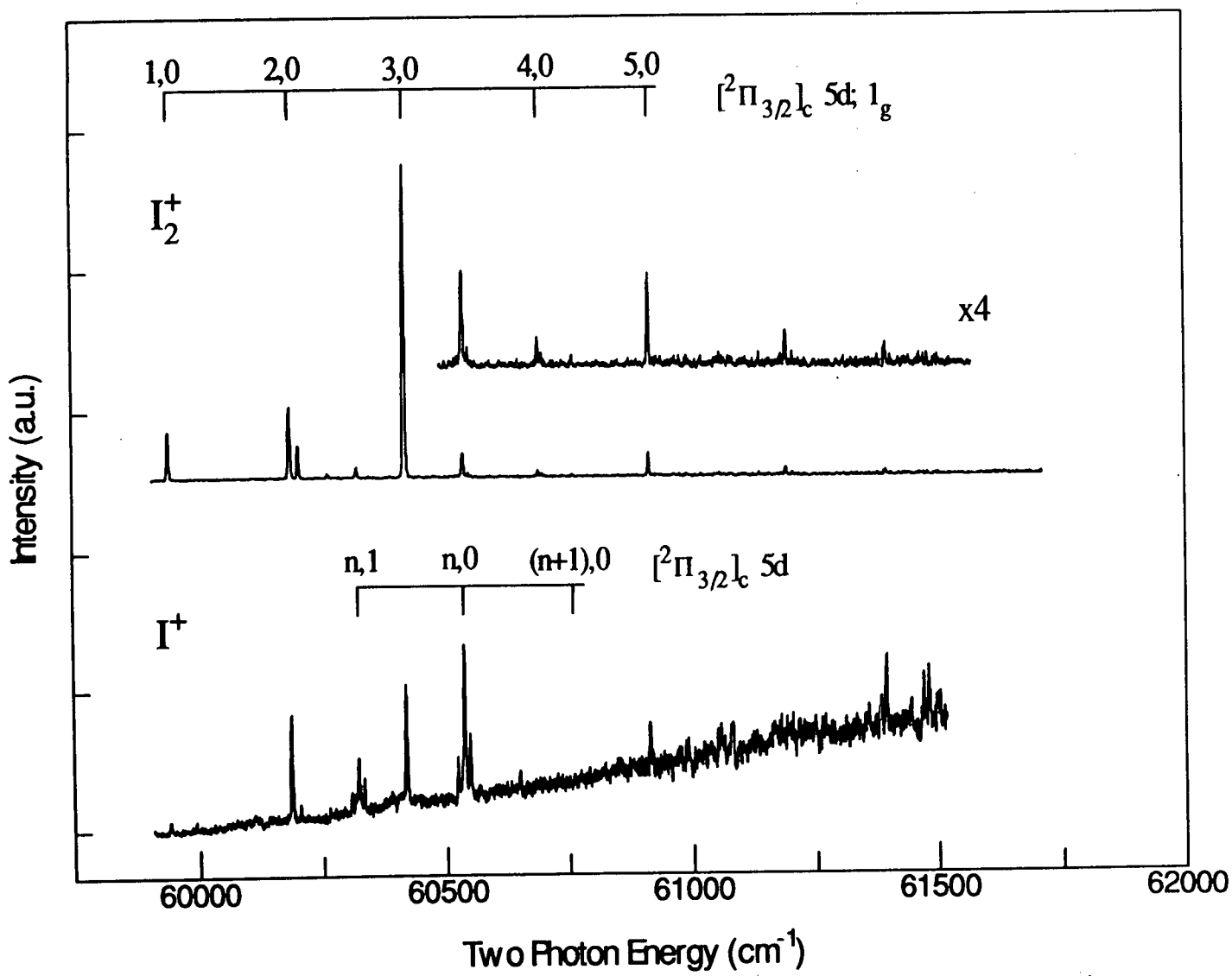

Figure 5.9 The (2+1) mass resolved REMPI excitation spectrum of jet-cooled I_2 recorded in the range 59750-61750 cm^{-1} by monitoring both the I_2^+ and I^+ mass channels. An avoided crossing between the $[^2\Pi_{3/2}]_c$ 5d; 1_g state and the $\beta(1_g)$ state results in irregular vibrational spacings in the upper figure whilst an interaction between another $[^2\Pi_{3/2}]_c$ 5d Rydberg state and an ion-pair state results in the appearance of weak ion-pair vibrational structure in the lower spectrum.

Table 5.4 Spectral peak positions and assignments for the D'(2_g) ion-pair state coupled to the $[^2\Pi_{3/2}]_c$ 5d; 2_g Rydberg state.

(v',0) [a]	Transition energy / cm^{-1} [b]	(v',0) [a]	Transition energy / cm^{-1} [b]	(v',0) [a]	Transition energy / cm^{-1} [b]
267	57174	293	58032	319	58769
268	57208	294	58062	320	58792
269	57241	295	58093	321	58816
270	57275	296	58126	322	58836
271	57309	297	58158	323	58868
272	57348	298	58187	324	–
273	57379	299	58217	325	58920
274	57412	300	58248	326	58947
275	57446	301	58279	327	58972
276	57480	302	58308	328	58997
277	57513	303	58339	329	59027
278	57546	304	58370	330	59048
279	57580	305	58398	331	59073
280	57613	306	58430	332	59098
281	57646	307	58459	333	59125
282	57678	308	58489	334	59150
283	57710	309	58519	335	59175
284	57742	310	58547	336	–
285	57777	311	58571	337	59225
286	57809	312	58583	338	59251
287	57841	313	–	339	59276
288	57872	314	–	340	59301
289	57902	315	58660	341	59326
290	57939	316	58693	342	59350
291	57979	317	58719	343	59371
292	58002	318	58744	344	59403

[a] Vibrational numbering taken from Ref. [45].

[b] Uncertainty ± 2 cm^{-1}.

5.3.5 The $[^2\Pi_{1/2}]_{c,g}$ 5d Rydberg States

Three $[^2\Pi_{1/2}]_{c,g}$ 5d progressions were identified in the room temperature spectrum in Ref. [19] between 64000 and 66000 cm^{-1}. Due to the fact that none of the 5d Rydberg states displayed the same polarisation behaviour as the *n*s Rydbergs above 62000 cm^{-1}, the Ω values of these Rydbergs could not be determined. The jet cooled spectrum between 63900 and 64300 cm^{-1} contains two vibrational bands identical to those observed in the room temperature study with the band origin assigned as 64098 cm^{-1}, in agreement with Donovan et al. (see Table 5.2). Each Rydberg vibrational band also had a number of ion-pair bands surrounding it with separations of ~ 30 cm^{-1}. This separation is characteristic of a second tier ion-pair state, i.e. a 0_g^+ or 1_g state, since no 2_g second tier state exists, but other than that the exact assignment of the symmetry of this Rydberg state can not be determined. The two higher energy $[^2\Pi_{1/2}]_c$ 5d progressions observed in the room temperature spectrum are observed as a single progression in the mass resolved jet-cooled spectrum shown in Figure 5.10 with an origin at 64927 cm^{-1} (see Table 5.2). Irregularly spaced vibrational bands are observed in the I_2^+ mass channel with the v'=1 and v'=2 levels displaced by about 13 cm^{-1} from their expected positions. All the vibrational bands are significantly broader in the spectrum which may be due to an interaction with an ion-pair, state such as the $E(0_g^+)$, which has a high density of ion-pair levels in this region. The I^+ mass channel spectrum in contrast to the I_2^+ mass channel spectrum contains numerous atomic I^+ lines which were identified in Ref. [19], some of which overlap the Rydberg vibrational bands (e.g. v'=3).

5.4 Discussion

One of the most interesting effects observed in this investigation of the Rydberg states of I_2 was the behaviour of the individual ion products (I_2^+ and I^+) when the Rydberg states were excited with circularly polarised light. In a two photon transition, a net increase in intensity of 1.5 is expected with circularly polarised light

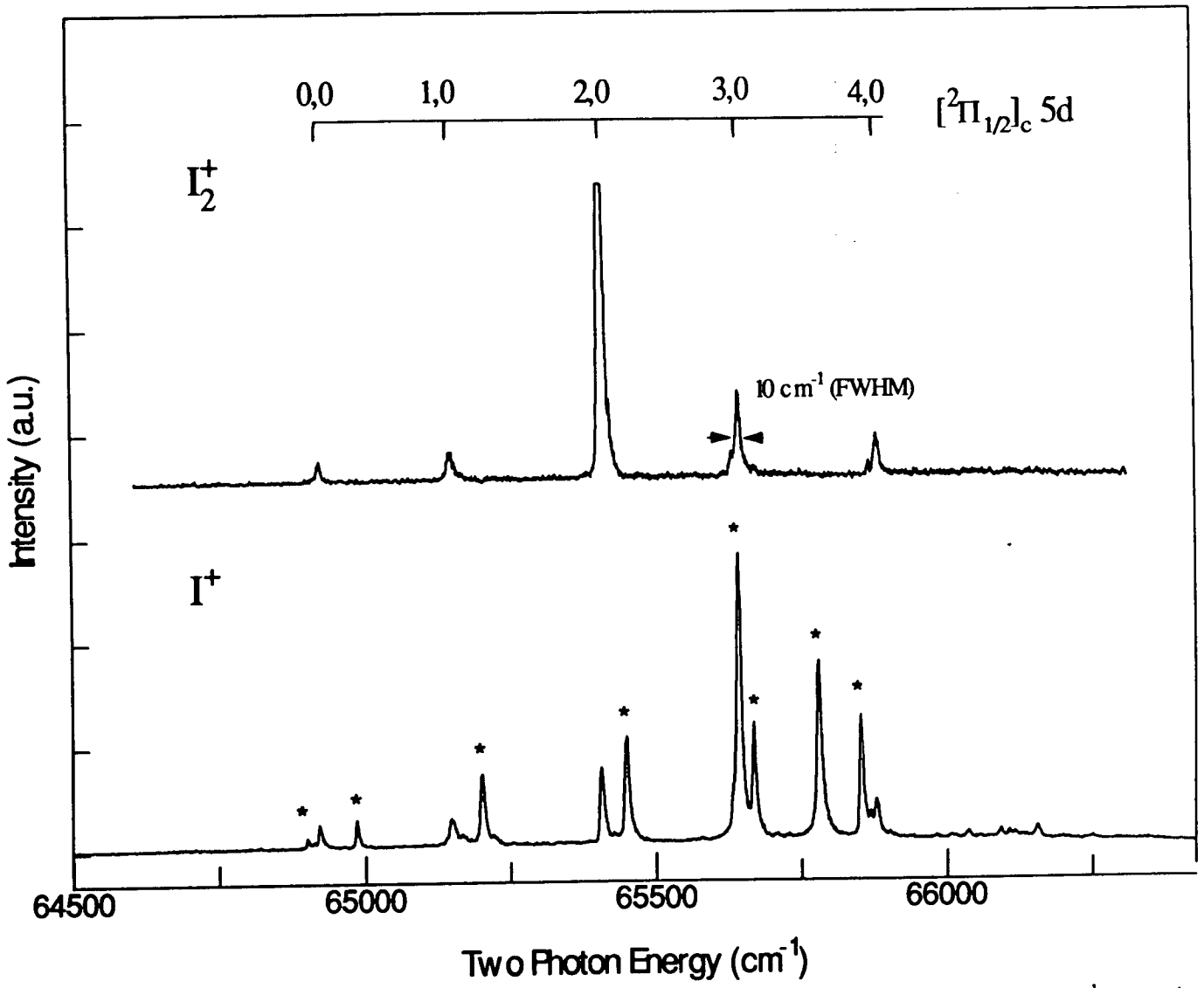

Figure 5.10 The (2+1) mass resolved REMPI excitation spectrum of jet-cooled I_2 recorded in the range 64500-66300 cm^{-1} by monitoring both the I_2^+ and I^+ mass channels. Note the broadness of the peaks in the $[^2\Pi_{1/2}]_c$ 5d Rydberg state. The starred peaks in the lower spectrum are due to atomic iodine.

for all rotational branches with $\Delta\Omega=0, \pm1$, and ±2 except for the Q branch of a $\Delta\Omega=0$ transition which is J dependant and can range from 0 to 0.25 [42]. In the case of molecular I_2, the two photon transition originates in the totally symmetric $X\ ^1\Sigma_{0_g^+}$ ground electronic state and therefore a $\Delta\Omega=0$ transition must terminate on a 0_g^+ state. However, Donovan et al. [19] discovered that the band intensity of all the 1_g *ns* Rydberg states above 62000 cm^{-1} was almost completely reduced to zero when excited with circularly polarised light. The 0_g^+ and 2_g Rydberg states on the other hand displayed a net increase in intensity. It was proposed that this observed loss in intensity in the 1_g bands resulted from the 1_g Rydberg states being predissociated by a repulsive valence state to give ground state atoms which in turn were ionised via a coherent three photon process. It is well known that the yield for non-resonant ion formation in atoms can be dramatically reduced with circularly polarised light compared with linearly polarised light [46,47]. This proposal, however, could not be confirmed with total ion current measurements.

The mass resolved (2+1) REMPI excitation spectra of these Rydberg states offered the opportunity to establish whether the model correctly explained the observed behaviour. The observation of the $[^2\Pi_{3/2}]_c$ 7s; 1_g Rydberg state in only the I^+ mass channel (see Figure 5.3) and its loss of intensity with circularly polarised light would seem to confirm the model proposed by Donovan et al. However, the behaviour of $[^2\Pi_{1/2}]_c$ 7s; 1_g and $[^2\Pi_{3/2}]_c$ 8s; 1_g Rydberg states disagrees with these observations. The I^+ mass channel spectra of the four Rydberg states is shown in Figure 5.6 and as proposed the 1_g vibrational bands are the only ones to lose their intensity with circularly polarised light. However, Figure 5.7 shows that this loss of intensity in the 1_g states is not limited to the I^+ mass channel but is also observed in the parent molecular ion (I_2^+) mass channel. These observations would therefore seem to suggest that the existence of a neutral 1_g predissociation channel cannot be the correct explanation for the behaviour of the 1_g states with circularly polarised light. This unusual polarisation phenomenon has recently been supported by similar

observations in a (2+1) REMPI study of the Rydberg states of Cl_2 [48], in which all the high lying *n*s Rydberg states with $n>4$, were also found to lose their intensity with circularly polarised light. The observations in Cl_2 support an idea that it may in fact be the lowest Rydberg state in both Cl_2 ($n=4$) and I_2 ($n=6$) which is not behaving as expected with circularly polarised light, rather than the higher Rydberg states. However, given the obvious inapplicability of the theoretical explanation to account for the behaviour of the *n*s Rydberg states ($n>6$ for I_2) with circularly polarised light, an adequate explanation for the observations cannot be found at present.

The present study of the jet-cooled (2+1) mass resolved REMPI spectra of I_2 permit some observations to be made concerning the interactions between Rydberg and ion-pair states. An interaction between an ion-pair state and a Rydberg state is favoured if their molecular orbital configurations differ by no more than one, two electron excitation e.g. the [1432] $\beta(1_g)$ and $D'(2_g)$ ion-pair states might be expected to mix with the [2430] Rydberg states, whereas the [2242] $E(0_g^+)$ ion-pair state would not. It has, however, been noted that in certain cases, such as the $E(0_g^+)$ ion-pair state [5], [1432] character can be gained from some of the other ion-pair states, in this example the $f(0_g^+)$ state, allowing them to interact with Rydberg states. However, even using this criterion many crossings which might be expected to involve interactions are not observed in the REMPI spectra. Clearly the interactions between Rydberg and ion-pair states are very complex and cannot be fully explained at present.

To clarify the situation for I_2 within the bounds of the experimental observations, a schematic representation of the electronic state potentials which explain the experimental observations most effectively is shown in Figure 5.11. The Rydberg states are described by Morse potentials all of which have an assumed average dissociation energy of ~15000 cm^{-1}. The T_e values are calculated from the experimental results and the r_e values are for the most part derived from Franck-Condon calculations. A value for r_e derived in this way for the $[^2\Pi_{1/2}]_c$ 6s; 1_g Dalby

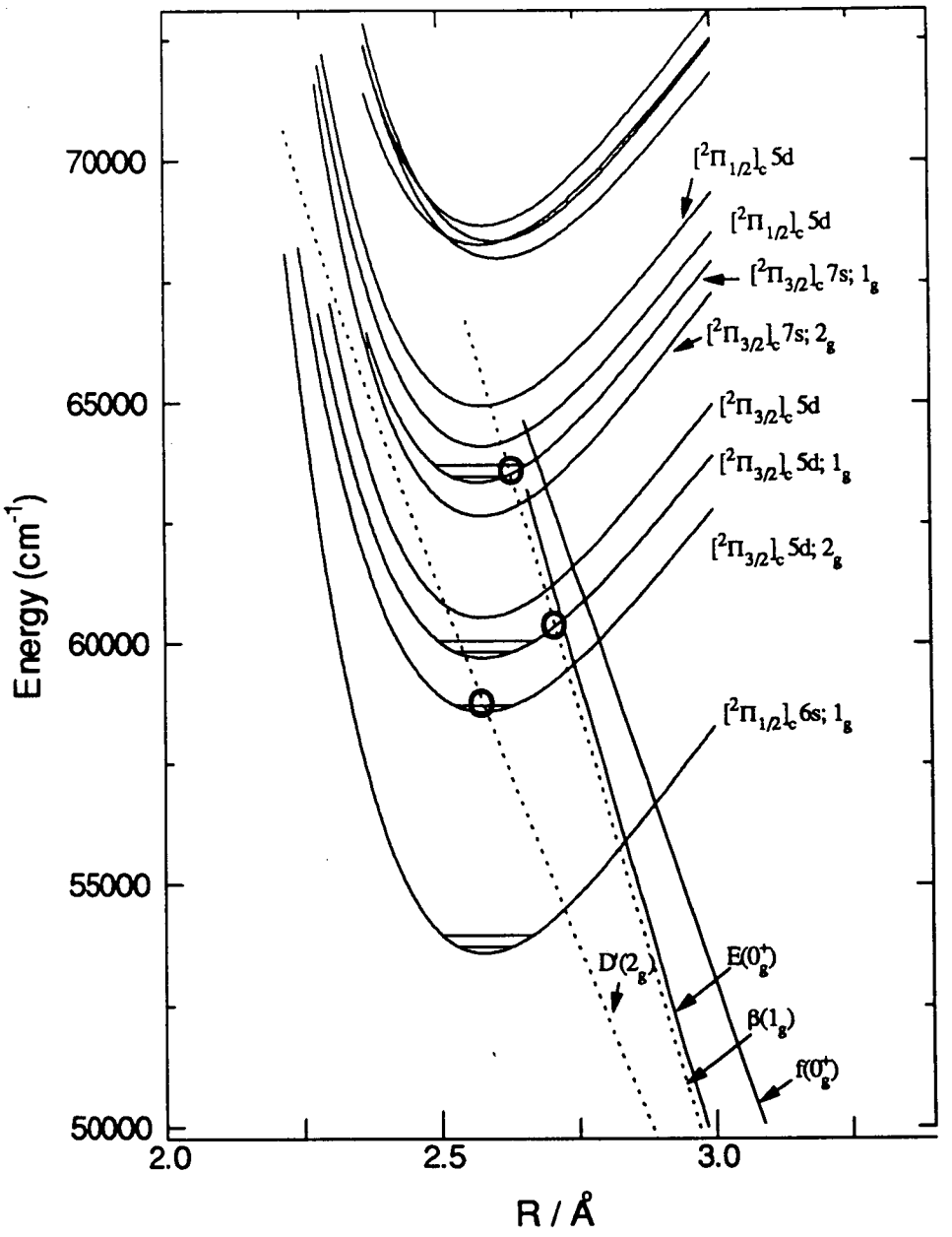

Figure 5.11

A schematic potential energy diagram of I_2 depicting the possible Rydberg/ion-pair interactions. The ion-pair potentials drawn with solid lines are taken from experimentally fitted data, whereas the dotted ion-pair potentials are fitted to the observed interactions. The crossings of states which result in an observable interaction are indicated by circles.

system (2.577 Å) compares very favourably with a value determined from a rotational band contour analysis of the v'=0 band of 2.566 Å [49]. An r_e value of 2.56 Å has been assumed for all the 5d Rydberg states based on a recent room temperature study of the $[^2\Pi_{3/2}]_c$ 5d; 1_g Rydberg state of I_2 by Kvaran et al. [44]. Franck-Condon calculations of the 5d Rydberg states would have been meaningless as the vibrational bands gain most of their intensity from ion-pair interactions. The ion-pair potentials are, with the exception of the $\beta(1_g)$ and $D'(2_g)$ states, taken from Ref. [5]. The $\beta(1_g)$ ion-pair state potential was drawn to fit the assumed interactions with Rydberg states, i.e. the $[^2\Pi_{3/2}]_c$ 5d; 1_g state at v'=3 as proposed by Kvaran et al. [44] and the $[^2\Pi_{3/2}]_c$ 7s; 1_g state at v'=1, as observed experimentally. The crossings of states which result in an observable interaction are indicated by circles. Obviously there are other ion-pair states of the correct symmetry which have not been considered such as the $G(1_g)$ in the second tier and the $f'(0_g^+)$ in the third tier (see Table 5.1). However, at present it is impossible to say to what extent these influence the observed REMPI spectra.

The potentials shown in Figure 5.11 can be used to propose a possible assignment for the lowest energy $[^2\Pi_{3/2}]_{c,g}$ 5d Rydberg state discussed in section 5.3.4 and the ion-pair state with which it interacts. Based on the knowledge that the $\beta(1_g)$ ion-pair state crosses the $[^2\Pi_{3/2}]_c$ 5d; 1_g state at v'=3 and crosses the $[^2\Pi_{3/2}]_c$ 7s; 1_g state at v'=1, it cannot therefore cross the $[^2\Pi_{3/2}]_{c,g}$ 5d state near it's band origin which lies at 58577 cm^{-1}, as shown in Figure 5.11. From the vibrational spacing the ion-pair state is a first tier state and from Table 5.1 the only other ion-pair states which are accessible in a two photon transition are the $E(0_g^+)$ and $D'(2_g)$. The $E(0_g^+)$ has already been dismissed as the interacting ion-pair state so the only remaining possibility is the $D'(2_g)$ ion-pair state. Consequently we can assign the lowest lying $[^2\Pi_{3/2}]_{c,g}$ 5d state whose origin lies at 58577 cm^{-1} as having 2_g symmetry and the $D'(2_g)$ can be drawn as in Figure 5.11 to cross near the band origin. A full simulation of this mixed Rydberg/ion-pair spectrum has been carried out by in Ref. [43].

Theoretically, a two-photon transition from the ground state can access sixteen 5d Rydberg states; seven converging on the $[^2\Pi_{3/2}]$ ionic core and nine converging to the $[^2\Pi_{1/2}]$ ionic core. The fact that only five of these sixteen 5d Rydberg states are observed in the (2+1) REMPI spectrum of I_2 is very surprising. Those 5d Rydbergs which are observed, however, are heavily perturbed in some way, either having identifiable ion-pair structure or irregularly spaced and incomplete progressions with anomalous intensity distributions. This would seem to imply that these 5d Rydberg states are only observed as a result of an interaction with an ion-pair state. The (2+1) REMPI excitation spectra recorded in this study and shown in Ref. [19] also indicate that no ion-pair structure is observed unless it is mixed with a Rydberg state, be it an *n*s or an *n*d Rydberg state. It can therefore be concluded that the 5d Rydbergs observed in the (2+1) REMPI spectra gain their two-photon intensity from the Rydberg character of the state and acquire greatly increased ionisation efficiency from the ion-pair character. It is well known that ionisation of unperturbed ion-pair states is a facile process [5]. The lack of spectral evidence for the other eleven 5d Rydberg states suggests that they are either crossed by an ion-pair state outside the Franck-Condon allowed region or, more probably, are not mixed with an ion-pair state giving them a route to the ionisation continuum.

The dominance of Rydberg states rather than the ion-pair states in (2+1) REMPI spectra of the diatomic halogens has proved quite surprising [50]. Various theories have therefore been put forward to explain this lack of ion-pair structure. One possibility concerns an energetic limitation which makes it difficult to ionise out of an ion-pair state with its large equilibrium bond length. However, the $E(0^+)$ ion-pair state of ICl [51] has recently been observed in a (2+1) REMPI study, proving that energetic requirements are not a limitation to the observation of ion-pair states. A proposal, involving the two-photon excitation path to the ion-pair state, was also put forward to explain why the $E(0^+)$ ion-pair state was the only one to be observed in the (2+1) REMPI study of ICl [51]. Exactly why no ion-pair states are observed directly in a (2+1) REMPI investigation of the diatomic homonuclear halogens and only one has been observed in a (2+1) REMPI investigation of the heteronuclear

diatomic halogens is still unclear. They are certainly not predissociated as evidenced by their abundance in two colour optical double resonance investigations [4,52,53].

One important general observation which can be made about these *gerade* Rydberg states is that, with the exception of the $[^2\Pi_{3/2}]_c$ 7s; 1_g state, all states with an *n*s Rydberg electron have reasonably regular unperturbed vibrational progressions. In contrast, all the observed 5d states are heavily perturbed either having identifiable ion-pair structure or irregular intensities and vibrational separations.

5.5 ZEKE-PFI Photoelectron Spectroscopy of Rydberg Excited I_2

The ionic states of the homonuclear diatomic halogens have been studied in detail with conventional PES [54] and as was shown in the previous chapter, threshold photoelectron spectroscopy. However, the only halogen containing diatomics which have been studied with ZEKE-PFI photoelectron spectroscopy are the halogen acids, HF [55], HCl [56] and HI [57]. Their large rotational constants making them very suitable candidates for investigation. Ideally it would be nice to carry out a ZEKE-PFI investigation of the diatomic halogen cations with a two colour (1+1') ionisation scheme. However, the halogens and more specifically I_2, lack suitably positioned bound valence states in the UV. An alternative excitation scheme in I_2 is to use the low lying valence B $^3\Pi_{0_u^+}$ state. Unfortunately, the possibility of accidental ion-pair resonances at the second photon level in a (1+2') experiment makes this excitation scheme unreliable. The only option therefore, is to use some of the bound *gerade* Rydberg states previously characterised, as intermediates in a (2+1') excitation scheme. A number of experimental restrictions are, however, placed on the choice of the Rydberg intermediate state for the two colour ZEKE-PFI experiments. A (2+1') experiment requires high photon fluxes in both the pump and probe lasers and consequently this limits the choice of laser dyes. In this respect it is a considerable advantage if we can use the fundamental wavelength of a particular dye for the probe laser rather than generating the second harmonic as is often the case. Secondly, the wavelength of the probe laser is restricted by the dyes available, which

in practice limits us to the generation of light with a wavelength less than 900 nm. This confines the possible Rydberg intermediates to those with a principle quantum number less than 8. Assuming that core preservation holds upon ionisation, the choice of Rydberg intermediates is therefore restricted to the $[^2\Pi_{3/2}]_{c,g}$ 7s and $[^2\Pi_{1/2}]_{c,g}$ 7s Rydberg states for ionisation into their respective ionic spin-orbit components.

The ZEKE-PFI spectra of the $[^2\Pi_{3/2}]$ ionic core presented in section 5.6.2 via v'=0-2 of the $[^2\Pi_{3/2}]_c$ 7s; 2_g Rydberg state were recorded with an extraction potential of 5.32 V/cm whereas the ZEKE-PFI spectrum recorded via v'=3 employed an extraction potential of 1 V/cm. The ZEKE-PFI spectra of the $[^2\Pi_{1/2}]$ ionic core presented in section 5.7.2 via v'=0-1 of the $[^2\Pi_{1/2}]_c$ 7s; 0_g^+ Rydberg state were recorded with an extraction potential of 5.32 V/cm whereas the ZEKE-PFI spectrum recorded via v'=2 employed an extraction potential of 2 V/cm. All the ZEKE-PFI spectra were recorded with a delay of 586 ns.

5.6 The X $^2\Pi_{g,3/2}$ Ionic State of I_2

5.6.1 The (2+1) REMPI Spectrum of I_2 in the Range 62250 to 64250 cm^{-1}

Ionisation into the lower X $^2\Pi_{g,3/2}$ spin-orbit ionic state of I_2^+ is nominally favoured for a transition *via* a Rydberg state having a $[^2\Pi_{3/2}]$ core. The most suitable system from the point of experimental convenience is the $[^2\Pi_{3/2}]_{c,g}$ 7s system at around 63000 cm^{-1} which is composed of two overlapping states i.e. $[^2\Pi_{3/2}]_c$ 7s; 1_g and $[^2\Pi_{3/2}]_c$ 7s; 2_g. The mass resolved (2+1) REMPI excitation spectrum of jet-cooled I_2 in this region is presented in Figure 5.3 and has been discussed in section 5.3.2.

5.6.2 The (2+1') ZEKE-PFI Spectrum of I_2 Ionised *via* the $[^2\Pi_{3/2}]_c$ 7s; 2_g Rydberg State

The two colour (2+1') ZEKE-PFI spectra of I_2 ionised *via* the band origin of the $[^2\Pi_{3/2}]_c$ 7s; 2_g Rydberg state at 62639 cm^{-1} as well as *via* the first three vibrationally excited levels are presented in Figure 5.12. In the spectrum recorded *via* the band origin (Figure 5.12(a)), the most intense peak corresponds to the $\Delta v=0$ transition to the $v^+=0$ level in the ion. The total indicated transition energy to this level is 75066 ± 2 cm^{-1} which nominally represents the adiabatic ionisation energy of the X $^2\Pi_{g,3/2}$ state. However, in order to determine the true ionisation energy, the effects of field ionisation need to be corrected for. The equation describing field ionisation in I_2 was determined in chapter 3 to be $(1.60 \pm 0.3)\sqrt{F(V/cm}$, which with an extraction potential of 5.32 V/cm, results in a field free ionisation energy of 75069 ± 2 cm^{-1}. This compares with the previous value determined in the threshold study and the Ne(I) photoelectron spectrum of Higginson et al. [38] of 75098 ± 16 cm^{-1}.

A weak vibrational progression built upon the origin band extends up to $v^+=4$. The dominance of the origin peak in the spectrum reflects the minimal geometry change experienced by the molecule upon ionisation. This is to be expected given that ionisation occurs from a Rydberg state whose potential is very similar to the X $^2\Pi_{g,3/2}$ ionic state potential to which it converges. However, the progression does extend to rather higher v than would be expected on the basis of Franck-Condon factors. This behaviour is even more marked in the spectrum in Figure 5.12(b) recorded *via* v=1 in the $[^2\Pi_{3/2}]_c$ 7s; 2_g state. Here, once again the $\Delta v=0$ transition dominates the spectrum, but the $v^+=0$ peak appears this time with an intensity almost matching that of $v^+=1$. Even more remarkable is that the I_2 stretching progression can be followed as high as $v^+=7$. This behaviour continues in Figure 5.12(c) and (d) as the level of vibrational excitation in the intermediate Rydberg state is increased. Although all the spectra show a broadly $\Delta v=0$ propensity, the distribution of peak intensities is clearly not classically Franck-Condon in nature.

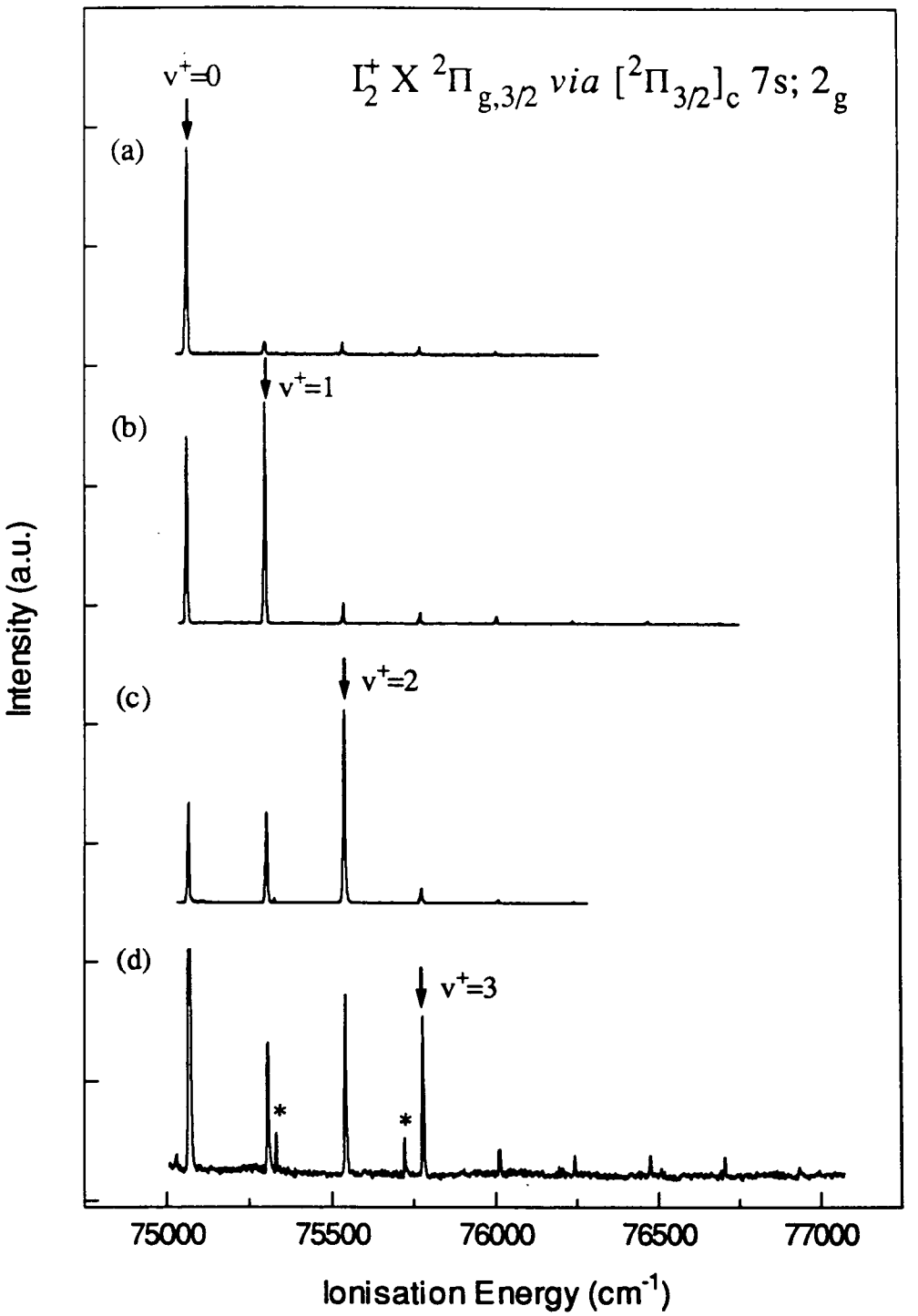

Figure 5.12

The (2+1') ZEKE-PFI photoelectron spectra of I_2 recorded *via* the $[^2\Pi_{3/2}]_c$ 7s; 2_g Rydberg excited state. The vertical arrows indicate the $\Delta v=0$ transitions and the small peaks marked with a * indicate accidental A←X neutral state resonance's.

The large intensity of the $v^+=0$ peak in Figure 5.12(d) is due to an overlap of the v=3 level of the $[^2\Pi_{3/2}]_c$ 7s; 2_g state with the band origin of the $[^2\Pi_{3/2}]_c$ 7s; 1_g state (see Figure 5.3) which results in a superposition of two ZEKE-PFI spectra. However, since most of the transition intensity arising from ionisation of the band origin of the $[^2\Pi_{3/2}]_c$ 7s; 1_g state will probably be concentrated in the $v^+=0$ peak (by analogy with the ZEKE-PFI spectrum in Figure 5.12(a)), we can be fairly confident that the peak intensity distribution to higher v in the ion essentially reflects that which would arise mainly from ionisation of v=3 of the $[^2\Pi_{3/2}]_c$ 7s; 2_g state.

A plot of $\Delta G_{v+1/2}$ *vs* v from Figure 5.12(b) yields values for ω_e and $\omega_e x_e$ of I_2^+ X $^2\Pi_{g,3/2}$ of 240 ± 1 cm^{-1} and 0.77 ± 0.05 cm^{-1}, respectively, in good agreement with the values determined by van Lonkhuyzen and de Lange [54] in their H-Lyman α study of 242 ± 15 cm^{-1} and ~1 cm^{-1}, respectively. The field free peak positions accurate to ± 2 cm^{-1} for the X $^2\Pi_{g,3/2}$ ionic state pumping v=1 of the $[^2\Pi_{3/2}]_c$ 7s; 2_g Rydberg state are given in Table 5.5.

One final point of note is the appearance of some weak peaks in Figure 5.12(c) and (d) which cannot be assigned to any vibrational progression in I_2^+. The linewidths of these peaks are significantly narrower than the other peaks in the ZEKE-PFI spectrum which is strongly suggestive of an accidental neutral state resonance which gives rise to the production of ZEKE electrons. In fact all these extra peaks can be assigned to valence A←X transitions [32] in neutral I_2 promoted by absorption of a probe laser infrared photon. The A $^3\Pi_{1_u}$ state level populated in this process then absorbs one of the pump laser photons in a second accidental resonant transition to an ion-pair state which in turn absorbs further photons ultimately resulting in ionisation. The exact process which creates ZEKE electrons from this excitation scheme is unknown although it is believed to involve repulsive ionic states.

Table 5.5 The field free peak positions for the X $^2\Pi_{g,3/2}$ ionic state pumping v=1 of the $[^2\Pi_{3/2}]_c$ 7s; 2_g Rydberg state and the X $^2\Pi_{g,1/2}$ ionic state pumping v=1 of the $[^2\Pi_{1/2}]_c$ 7s; 0_g^+ Rydberg state

$(v^+,0)$	Transition energy for the X $^2\Pi_{g,3/2}$ ionic state / cm^{-1} [a)]	Transition energy for the X $^2\Pi_{g,1/2}$ ionic state / cm^{-1} [a)]
0	75069	80266
1	75308	80494
2	75545	80720
3	75780	80942
4	76014	–
5	76246	–
6	76477	–

[a)] Uncertainty ± 2 cm^{-1}.

5.6.3 The (2+1') ZEKE-PFI Spectrum of I_2 Ionised *via* the $[^2\Pi_{3/2}]_c$ 7s; 1_g Rydberg State

An expanded (2+1) REMPI excitation spectrum of the v=1 level of the $[^2\Pi_{3/2}]_c$ 7s; 1_g state is shown in Figure 5.13. As discussed in section 5.3.2, the fine structure in the spectrum, which has a vibrational spacing of approximately 14 cm^{-1}, arises from a crossing of the repulsive limb of the $\beta(1_g)$ ion-pair state with the 1_g Rydberg state and can readily be assigned to very high vibrational levels of the ion-pair state (see Table 5.3). In general, there is little to be gained in terms of ionic state spectroscopy from using the 1_g state as a resonant intermediate state in addition to the 2_g state. However, the ZEKE-PFI spectra recorded by selectively exciting individual

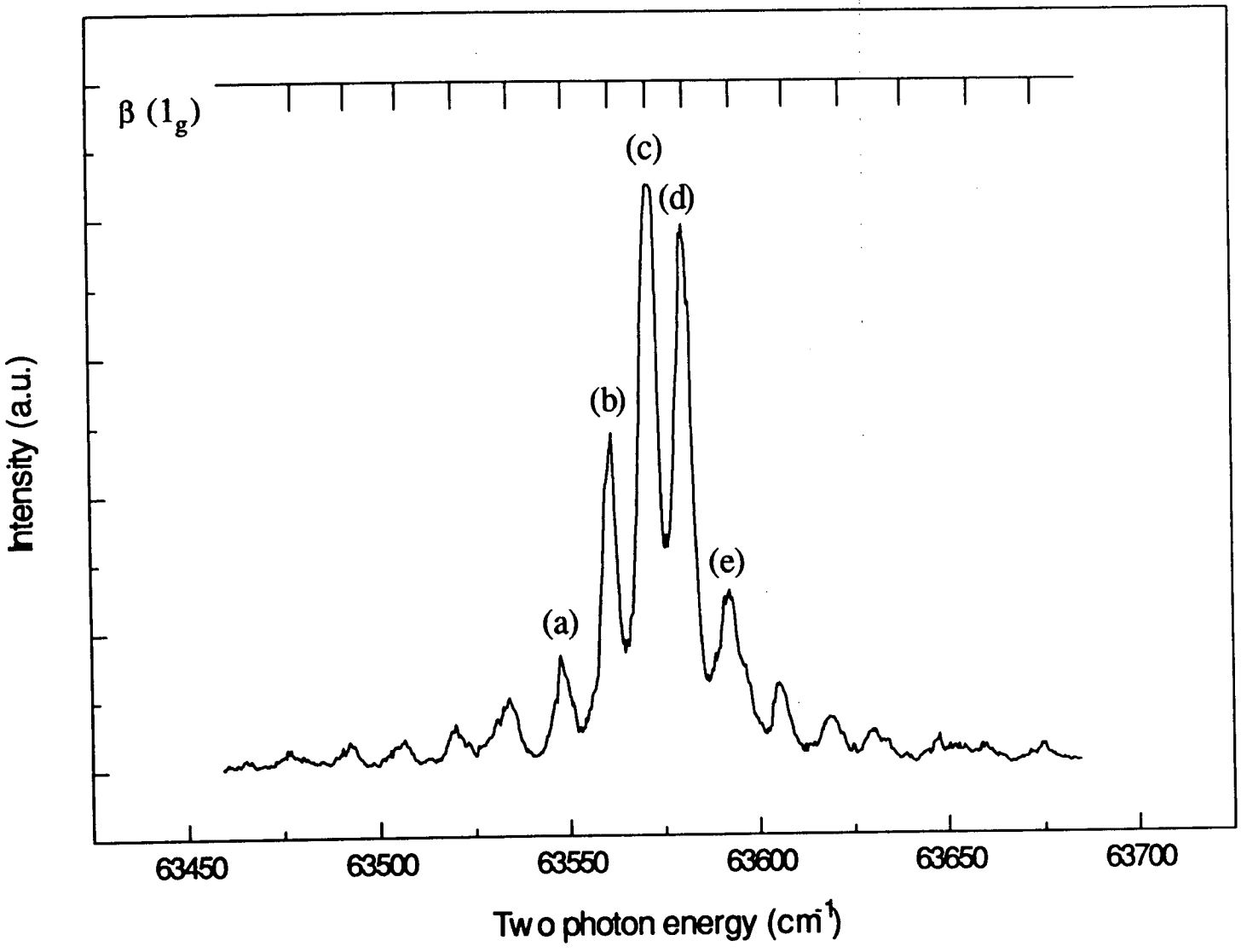

Figure 5.13 An expanded scan of the (2+1) REMPI excitation spectrum of I_2 in the range 63450-63700 cm^{-1}. The extended low frequency progression is associated with the $\beta(1_g)$ ion-pair state which interacts strongly in the region of the v=1 peak of the $[^2\Pi_{3/2}]_c$ 7s; 1_g state progression. The peaks labeled (a) to (e) have been used as resonant intermediate levels for the ZEKE-PFI spectra shown in Figure 5.14.

ion-pair bands within the overall Rydberg state vibrational band envelope should provide an indication of the character of the mixed intermediate state.

The ZEKE-PFI spectra depicted in Figure 5.14(a) to (e) were obtained by selectively exciting the ion-pair peaks (a) to (e) in Figure 5.13. The region of the ZEKE-PFI spectrum being scanned in each case extends from the v^+=1 peak to the v^+=2 peak (extended scans to v^+=3 are given as insets in spectra (c) to (e)). Two things are immediately apparent from the spectra; firstly the FWHM of the v^+=1 ZEKE-PFI peaks progressively decrease from around 8.4 cm^{-1} in spectrum (a) to 4.9 cm^{-1} in spectrum (c) and then increase to 6.7 cm^{-1} in (d) and again to 8.7 cm^{-1} in spectrum (e). Secondly, the intensity of the v^+=2 (and v^+=3) peaks gradually decreases from (a) to (c) but thereafter increases again from (c) to (e) (see insets to Figures (c) to (e) for extended scans to v^+=3). It is suggested that both trends are indicative of the relative amounts of Rydberg and ion-pair character in the intermediate state as the pump laser is scanned through the Rydberg state vibrational band envelope. At the wings of the envelope the ion-pair character is more dominant than at the peak where the electronic wavefunction acquires more Rydberg character.

5.7 The X $^2\Pi_{g,1/2}$ Ionic State of I_2

5.7.1 The (2+1) REMPI Spectrum of I_2 in the Range 67500 to 69000 cm^{-1}

The mass resolved (2+1) REMPI spectrum of I_2 in the range 67500 to 69000 cm^{-1} two photon energy is presented in Figure 5.15. For the sake of clarity the spectrum was recorded with circularly polarised light to exclude contributions from 1_g states. The two states which dominate the spectrum in the I_2^+ mass channel are the $[^2\Pi_{1/2}]_c$ 7s; 0_g^+ state and the $[^2\Pi_{3/2}]_c$ 8s; 2_g state and have previously been discussed in section 5.3.3. However, it is the former which is of interest to us as an intermediate for ionisation into the X $^2\Pi_{g,1/2}$ spin-orbit state of I_2^+.

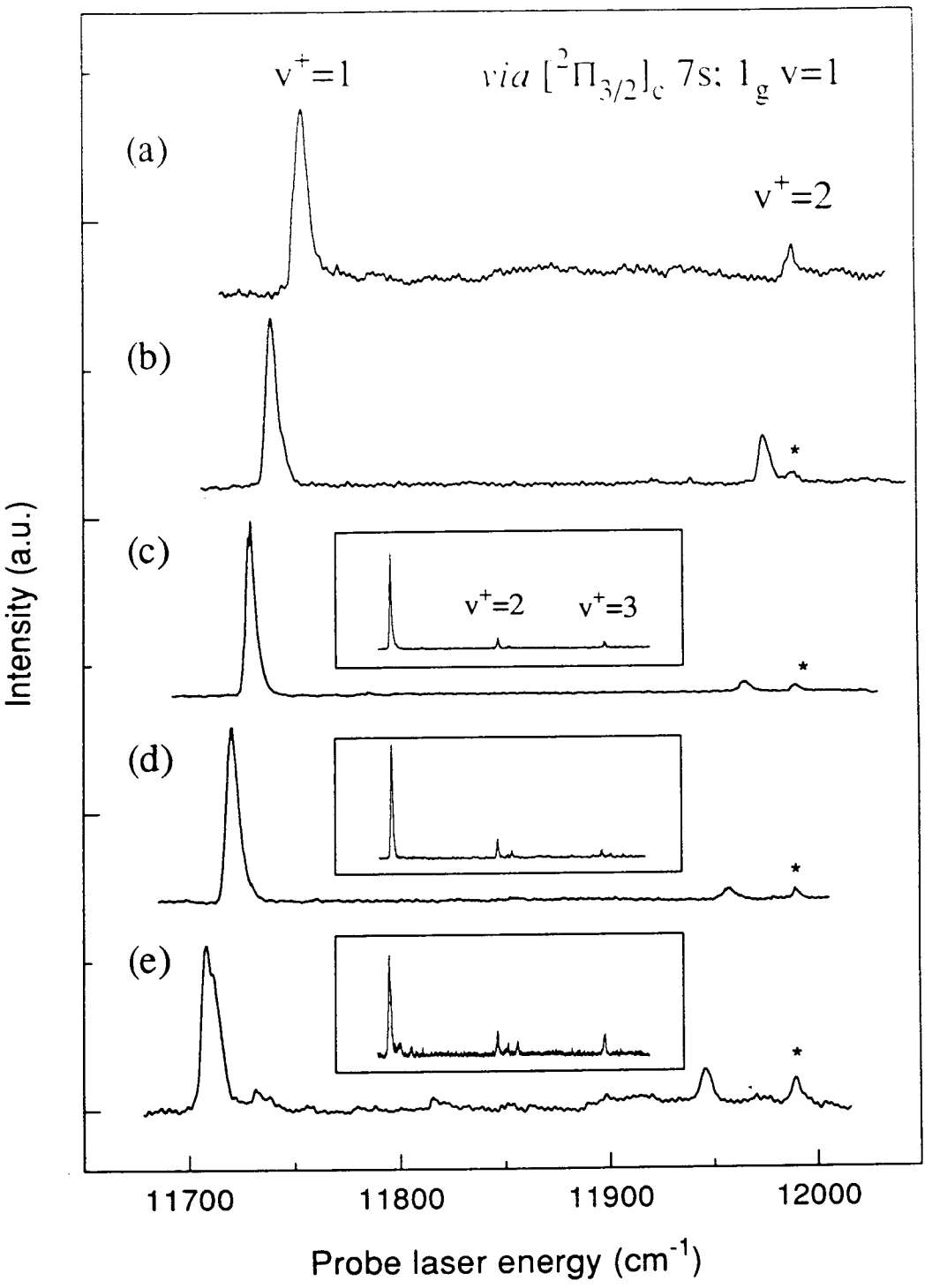

Figure 5.14

The (2+1') ZEKE-PFI photoelectron spectra of I_2 recorded by selectively exciting peaks labeled (a) to (e) in Figure 5.13. The region of the ZEKE-PFI spectrum being scanned in each case extends from the $v^+=1$ peak to the $v^+=2$ peak. The insets in spectra (c) to (e) show extended scans to $v^+=3$ for excitation of peaks (c) to (e) in Figure 5.13, respectively. The small peaks marked with a * indicate an accidental A←X neutral state resonance.

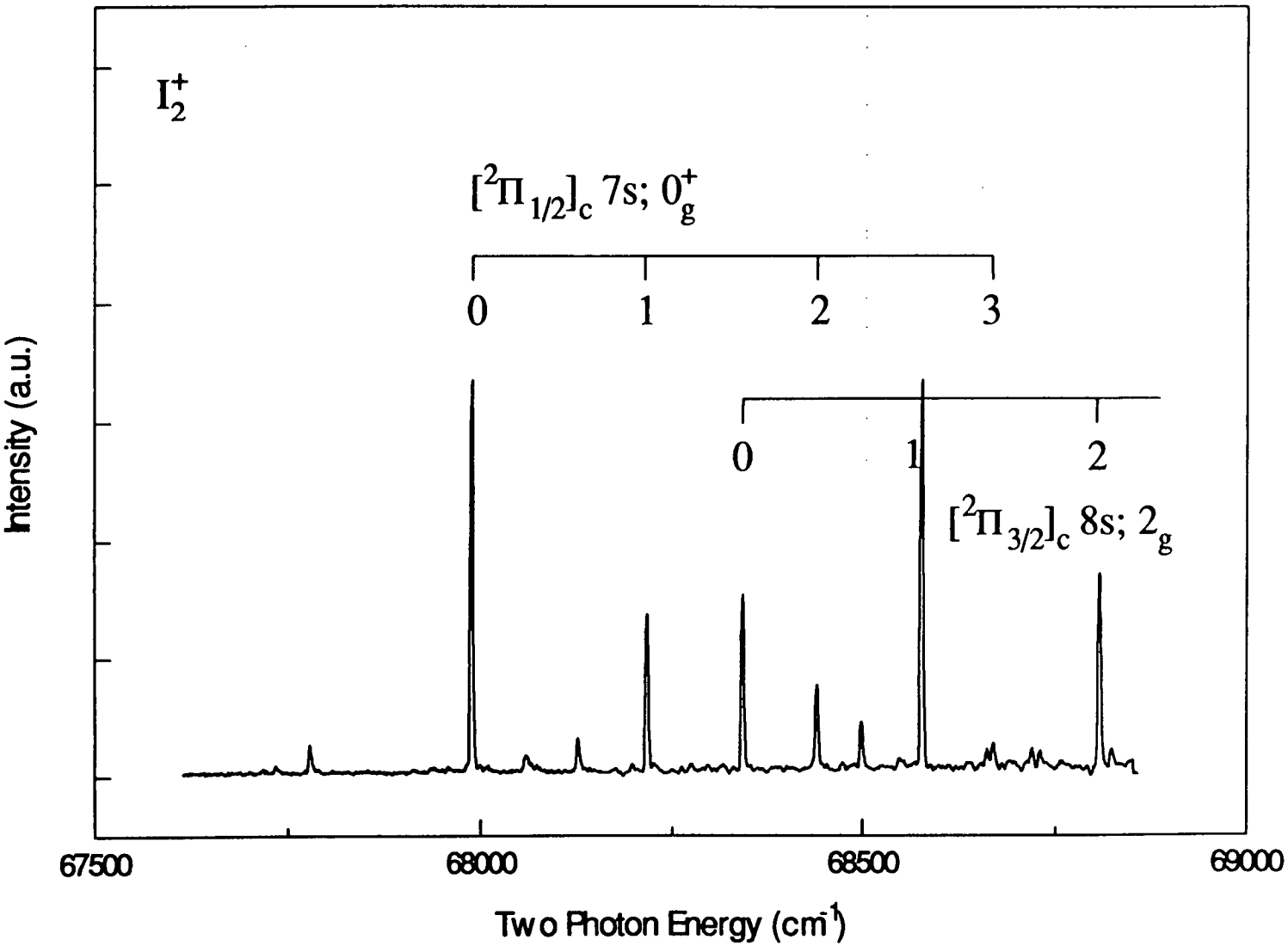

Figure 5.15 The (2+1) mass resolved REMPI excitation spectrum of I_2 in the range 67500-69000 cm^{-1} recorded by monitoring the I_2^+ mass channel. For the sake of clarity the spectrum was recorded with circularly polarised light to exclude contributions from 1_g states.

5.7.2 The (2+1') ZEKE-PFI Spectrum of I_2 Ionised *via* the $[^2\Pi_{1/2}]_c$ 7s; 0_g^+ Rydberg State

The two-colour (2+1') ZEKE-PFI spectra of I_2 ionised *via* the band origin of the $[^2\Pi_{1/2}]_c$ 7s; 0_g^+ Rydberg state at 67992 cm^{-1} as well as *via* the first two vibrational levels are presented in Figure 5.16(a) to (c). In the spectrum recorded *via* the band origin (Figure 5.16(a)), the most intense peak corresponds to the $\Delta v=0$ transition to the $v^+=0$ level of the ion. The total indicated transition energy to this level is 80263 ± 2 cm^{-1} which nominally represents the adiabatic ionisation energy to the X $^2\Pi_{g,1/2}$ state. However, correcting for the 5.32 V/cm extraction potential gives a field free adiabatic ionisation energy of 80266 ± 2 cm^{-1}. This compares with the previous value determined by Higginson et al. of 80276 ± 16 cm^{-1} from a Ne(I) photoelectron spectrum [38] and the threshold photoelectron value of 80228 ± 16 cm^{-1}. Having determined the field free adiabatic ionisation energies of the two spin-orbit components of the X $^2\Pi_{g,i}$ ionic state, a value of 5197 ± 4 cm^{-1} can now be calculated for the spin-orbit splitting in the ground electronic state of I_2^+.

As with the ZEKE-PFI spectra obtained for the X $^2\Pi_{g,3/2}$ state, increasing the level of vibrational excitation in the intermediate Rydberg state leads to an increase in the level of vibrational excitation in the product ion (see Figure 5.16(b) and (c)). However, this time the propensity for $\Delta v=0$ transitions is far more marked, with the distribution in peak intensities exhibiting classical Franck-Condon behaviour. The difference in the appearance of the spectra recorded in Figure 5.16 compared to those recorded for the X $^2\Pi_{g,3/2}$ state is of some significance and will be discussed in some detail below.

A plot of $\Delta G_{v+1/2}$ *vs* v from Figure 5.16(b) yields values for ω_e and $\omega_e x_e$ of I_2^+ X $^2\Pi_{g,1/2}$ of 229 ± 1 cm^{-1} and 0.69 ± 0.05 cm^{-1} respectively. This can be compared with values of 242 ± 15 cm^{-1} and ~1 cm^{-1}, obtained by van Lonkhuyzen and de Lange from their H-Lyman-α study [54]. The field free peak positions accurate to ± 2 cm^{-1}

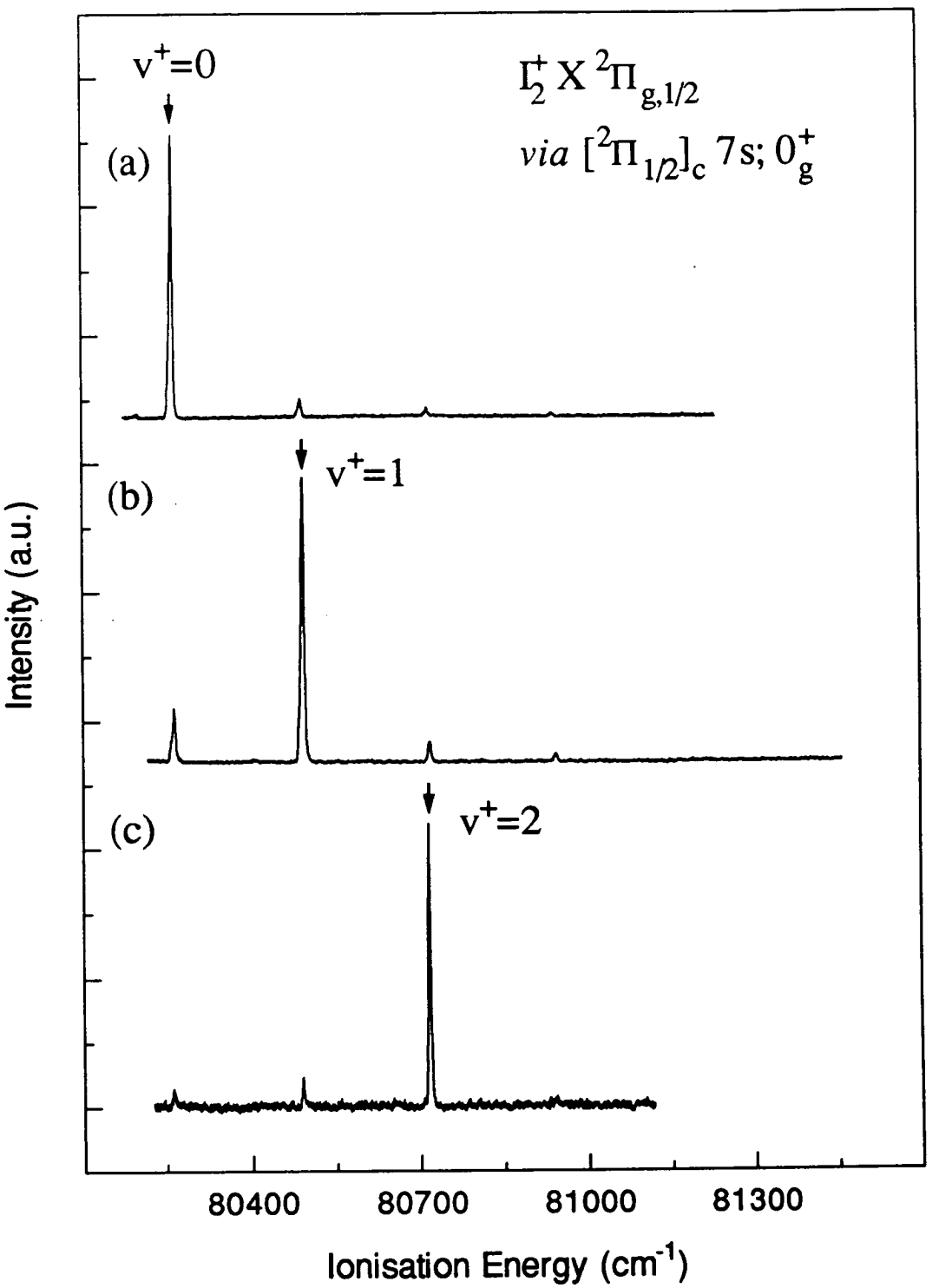

Figure 5.16

The (2+1') ZEKE-PFI photoelectron spectra of I_2 recorded *via* the $[^2\Pi_{1/2}]_c$ 7s; 0_g^+ Rydberg excited state. The vertical arrows indicate the $\Delta v=0$ transition.

for the X $^2\Pi_{g,1/2}$ ionic state pumping v=1 of the $[^2\Pi_{1/2}]_c$ 7s; 0_g^+ Rydberg state are given in Table 5.5. All the spectroscopic constants determined in this work are presented in Table 5.6.

Table 5.6 Spectroscopic data obtained for the X $^2\Pi_{g,i}$ ground electronic state of I_2^+

Spin-orbit component	Adiabatic I.P. / cm^{-1}	ω_e / cm^{-1}	$\omega_e x_e$ / cm^{-1}
X $^2\Pi_{g,3/2}$	75069 ± 2	240 ± 1	0.77 ± 0.05
X $^2\Pi_{g,1/2}$	80266 ± 2	229 ± 1	0.69 ± 0.05

5.8 Discussion

The marked deviation from Franck-Condon behaviour observed in the ZEKE-PFI spectra recorded for the lower spin-orbit state of I_2^+ is one of the main points of interest in the present work. Such effects in small molecules are usually the result either of perturbations to the resonant intermediate state or of autoionisation mechanisms in the ionic continuum. Given the apparently unperturbed nature of the $[^2\Pi_{3/2}]_c$ 7s; 2_g Rydberg state used in the stepwise ionisation to the X $^2\Pi_{g,3/2}$ state and its well defined total angular momentum, it would seem that autoionisation processes are probably responsible for the observed anomalous intensity distribution. The enhanced intensity of certain transitions can result from field-induced autoionisation processes occurring as a consequence of the pulsed field ionisation process employed in ZEKE-PFI spectroscopy [58-60]. The autoionising states responsible for these processes are usually low-*n* Rydberg states converging on some higher rovibronic limit which can interact with the near degenerate high-*n* Rydberg states (*n*>150) which are central to the PFI mechanism. The subsequent application of the pulsed electric field results in the field induced autoionisation of the low-*n* Rydbergs along with the field ionisation of the high-*n* Rydbergs.

The deviations from Franck-Condon behaviour observed in the ZEKE-PFI spectra of I_2 occur predominantly for transitions into the lower of the two spin-orbit components. One possibility which could explain this behaviour is the autoionisation of *n*p Rydberg states converging on the upper $^2\Pi_{g,1/2}$ spin-orbit state since there are no analogous Rydberg states available for autoionisation into the $^2\Pi_{g,1/2}$ ionic spin-orbit state (see Figure 5.17 for a schematic potential energy diagram showing possible autoionising Rydberg states). Such a process would initially require a single photon absorption from the $[^2\Pi_{3/2}]_c$ 7s; 2_g Rydberg intermediate state to an *n*p Rydberg state converging to the $^2\Pi_{g,1/2}$ limit. Calculations based on the Rydberg equation (Equation 5.1) taking the adiabatic ionisation energy of the X $^2\Pi_{g,1/2}$ state to be 80266 cm^{-1} and an average p Rydberg electron quantum defect of 3.58 [61] gives the band origins for a range of Rydberg principal quantum numbers shown in Table 5.7.

Table 5.7 Calculated band origins for the *n*p Rydbergs converging on the X $^2\Pi_{g,1/2}$ ionic state.

$[^2\Pi_{g,1/2}]_c$ *n*p	*n*=7	*n*=8	*n*=9	*n*=10
Band origin / cm^{-1}	70844	74649	76531	77604

Table 5.7 reveals that the most likely candidate on energetic grounds is the $[^2\Pi_{g,1/2}]_c$ 8p Rydberg state (see Figure 5.17) whose origin is calculated to lie 420 cm^{-1} below the band origin of the X $^2\Pi_{g,3/2}$ ionic state (75069 cm^{-1}). However, molecular *n*p Rydberg quantum defects can range from ~ 3.5 - 3.65 which could in principle shift the band origin of the $[^2\Pi_{g,1/2}]_c$ 8p Rydberg state anywhere between ~200-600 cm^{-1} below the band origin of the X $^2\Pi_{g,3/2}$ ionic state. Transitions to these high principal quantum number Rydbergs will probably not have a particularly large oscillator strength since a change in core is required in addition to the *n*s→*n*p transition. However, the inherent strength of $\Delta v=0$ transitions into the $[^2\Pi_{g,1/2}]_c$ 8p Rydberg state from the $[^2\Pi_{3/2}]_c$ 7s; 2_g Rydberg state could enhance the lower vibrational bands in the

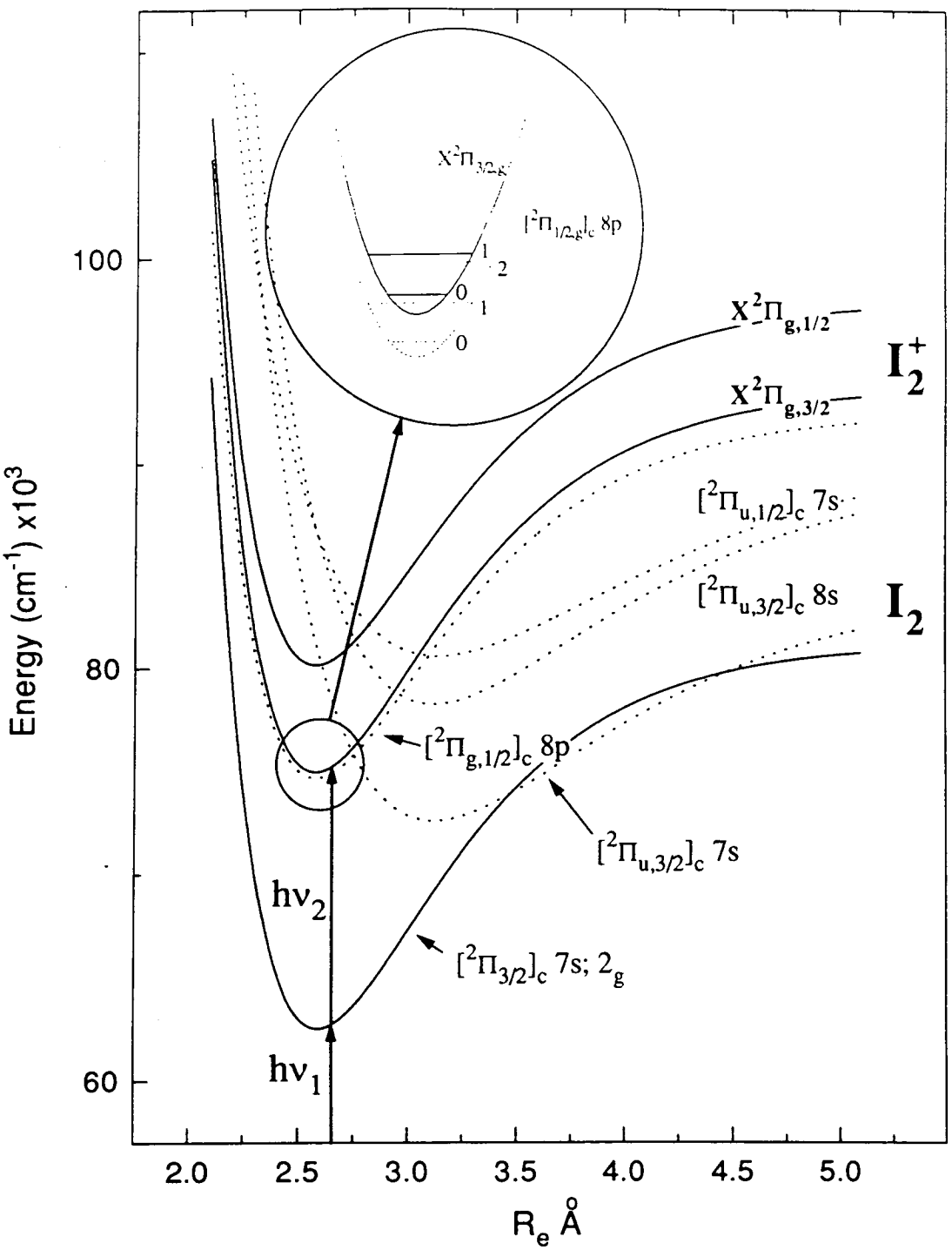

Figure 5.17

A schematic potential energy diagram showing the Rydberg states involved in the field induced autoionisation mechanism proposed to account for the non Franck-Condon distribution of peak intensities observed in the ZEKE-PFI spectra recorded for the X $^2\Pi_{g,3/2}$ state of I_2^+.

ZEKE-PFI spectrum. This would arise if the $[^2\Pi_{g,1/2}]_c$ 8p Rydberg band origin were displaced to lower energy by approximately the ionic state vibrational spacing (240 cm^{-1}) such that vibrational levels of the $[^2\Pi_{g,1/2}]_c$ 8p Rydberg state with vibrational quantum number, v, would tend to be nearly degenerate with ionic state vibrational levels with vibrational quantum numbers of v-1. For example, if we initially pump v=1 in the $[^2\Pi_{3/2}]_c$ 7s; 2_g Rydberg state then the similarity in the equilibrium geometry between the two states will tend to favour a transition into the $[^2\Pi_{g,1/2}]_c$ 8p v=1 level. This level could be nearly degenerate with v^+=0 in the ion which would lead to an enhancement of this peak in the ZEKE-PFI spectrum (see Figure 5.12(b)) through what might loosely be called 'spin orbit autoionisation'. The $[^2\Pi_{g,1/2}]_c$ 8p; v=1 level interacts and mixes with high-*n* Rydberg states converging to the v^+=0 level in the ion during the delay employed in the PFI mechanism and the subsequent application of the electric field pulse results in field induced autoionisation of the mixed $[^2\Pi_{g,1/2}]_c$ 8p vibronic state. This assignment must be qualified to some extent by acknowledging the inherently weak oscillator strength for transitions into the $[^2\Pi_{g,1/2}]_c$ *n*p Rydberg series. However, in their joint REMPI-PES and ZEKE-PFI study of HCl, de Beer et al. [56] found that transitions to the $^2\Pi_{1/2}$ ionic state had significant transition intensity (~10%) when a Rydberg state of nominal $^2\Pi_{3/2}$ core character was pumped. In fact, the $F\ ^1\Delta_2$ and $f\ ^3\Delta_2$ Rydberg intermediate states used to promote transitions into the $^2\Pi_{1/2}$ and $^2\Pi_{3/2}$ ionic states of HCl in that study can mix through spin-orbit coupling [62] and consequently, transitions nominally requiring a change in Ω_c will have significant transition probability. However, in the case of iodine, it would appear that the $[^2\Pi_{3/2}]_c$ 7s; 2_g state is a pure triplet (there being no $[^2\Pi_{1/2}]_c$ *n*s Ω=2 component to mix with) and such transitions may be less likely than is the case in HCl.

A second possibility is that the *n*s Rydberg series converging to the $A\ ^2\Pi_{u,i}$ ionic state may be the autoionising states responsible. A transition from the $[^2\Pi_{g,3/2}]_c$ 7s Rydberg state could be accomplished by a simple $\pi_u \rightarrow \pi_g$ transition in the core. Possible candidates are shown in Figure 5.17, although it should be noted that these potentials are drawn in their most likely positions since accurate r_e values and

adiabatic ionisation energies for the two A $^2\Pi_{u,i}$ spin-orbit components are unknown. These Rydberg states are predicted to be the $[^2\Pi_{u,3/2}]_c$ 7s state for autoionisation into the $^2\Pi_{g,3/2}$ spin-orbit ionic state and either the $[^2\Pi_{u,3/2}]_c$ 8s or $[^2\Pi_{u,1/2}]_c$ 7s states for autoionisation into $^2\Pi_{g,1/2}$ spin-orbit ionic state. The case for the $[^2\Pi_{u,3/2}]_c$ 7s state autoionising into the $^2\Pi_{g,3/2}$ spin-orbit ionic state would seem strong on grounds of initial transition probability. However, it would seem from Figure 5.17 that an autoionisation mechanism involving this state will tend to favour enhancement of transitions to higher v levels rather than the strong enhancement of transitions to low v levels observed in Figure 5.12. In addition we might reasonably expect a similar effect to arise from autoionisation of the $[^2\Pi_{u,3/2}]_c$ 8s state into the $^2\Pi_{g,1/2}$ spin-orbit ionic state but in fact this would appear to be very weak in our experiment. A more detailed knowledge of the potential curves is needed before firm conclusions can be drawn in this respect.

It seems reasonable to conclude that the non Franck-Condon distribution of intensities observed for ionisation into the $^2\Pi_{g,3/2}$ spin-orbit ionic state probably arises principally from 'spin-orbit autoionisation' although the second mechanism proposed above may also play a role. The enhancement of low v vibrational bands results from field induced autoionisation of the $[^2\Pi_{g,1/2}]_c$ 8p Rydberg state (i.e. field induced spin-orbit autoionisation) whilst the extended vibrational progression to high v may result from an autoionisation mechanism involving the *n*s Rydberg series converging to the A $^2\Pi_{u,i}$ ionic state.

Whilst it would seem that autoionisation mechanisms are contributing to the distribution of peak intensities observed in some of our ZEKE-PFI spectra, we cannot arrive at an unambiguous conclusion with regard to the extent to which the overall spin-orbit branching ratio differs from that observed in a conventional photoelectron experiment. In their ZEKE-PFI spectra of HCl, de Beer et al. [56] found that transitions to the lower $^2\Pi_{3/2}$ ionic spin-orbit state were apparently favoured over transitions into the $^2\Pi_{1/2}$ state regardless of the ionic core character of the intermediate Rydberg state. This was in marked contrast to the branching ratios

observed in their conventional REMPI photoelectron spectra in which transitions which preserved ionic core character were strongly favoured. They attributed their observations in the ZEKE-PFI spectra to spin-orbit autoionisation of the high n Rydberg states converging on the $^2\Pi_{1/2}$ ionic state which resulted in a loss in transition intensity to the upper spin-orbit state. A similar explanation was proposed by Mank et al. [55] in their VUV ZEKE-PFI study of HF to explain an 8:1 preference for transitions into the lower spin-orbit state of HF^+. In the case of iodine, the spin-orbit splitting in I_2^+ is considerably larger (5197 cm^{-1} as determined in the present work) than that in HCl^+ and HF^+ which means that we cannot make direct comparisons of absolute peak intensity for different spin-orbit states due to the large difference in laser dye output for different wavelength regions. In addition, the experimental restrictions placed on our choice of intermediate Rydberg states means that we were unable to ionise into the X $^2\Pi_{g,3/2}$ state by exciting a Rydberg having a $^2\Pi_{1/2}$ core. An attempt to record a ZEKE-PFI spectrum of the upper spin-orbit state in the ion by pumping the $[^2\Pi_{3/2}]_c$ 7s; 2_g Rydberg state proved inconclusive. Although a number of features did appear in the spectrum, these were mostly attributed to accidental neutral state resonance's and none could unambiguously be assigned to transitions into the upper ionic spin-orbit state.

The nature of a two-colour ZEKE-PFI experiment invites its use as a technique to probe the character of the intermediate states as well as looking at the spectroscopy of the final ionic state. The mixed Rydberg/ion-pair states observed in the (2+1) REMPI spectrum of iodine provide us with an ideal opportunity to make full use of this facility in order to investigate to what extent the Rydberg or ion-pair character of the mixed state changes across the Rydberg state vibrational band envelope. The results obtained here for ionisation of the $[^2\Pi_{3/2}]_c$ 7s; 1_g state are of considerable interest in this respect.

In the REMPI spectroscopy of vibronically mixed states, we can envisage two cases in which the appearance of the spectrum will depend on the relative transition oscillator strengths of the participating states. In the first case, in which

both the ion-pair and Rydberg states carry some oscillator strength in the excitation step we would expect the ion-pair progression to continue throughout the Rydberg progression with a mutual homogeneous perturbation at each near resonance between a particular Rydberg rovibrational level and a particular ion-pair rovibrational level. In the second case, only one of the two electronic components is accessed directly. The vibronically mixed state which is being probed in the present experiment is an example of the latter. In this case, the two-photon transition to the $[^2\Pi_{3/2}]_c$ 7s; 1_g Rydberg state carries all the oscillator strength and the characteristic ion-pair satellites associated with each of the main Rydberg vibrational levels appear solely as a consequence of intensity borrowing. The measured average vibrational spacing of this ion-pair structure in Figure 5.13 of ~14 cm^{-1} enables us to assign the ion-pair state as belonging to the first tier of states which dissociate to $I^+(^3P_2) + I^-(^1S_0)$. The strong coupling between the states suggests that it is homogenous in nature from which we can conclude that the ion-pair state is the $\beta(1_g)$ state which is the only first tier ion-pair state of 1_g symmetry. The irregular nature of the structure near each band maximum results from a resonance of the Rydberg level with a near degenerate ion-pair level (see Figure 5.18).

The ZEKE-PFI spectra recorded by exciting a number of the ion-pair lines which form part of the $[^2\Pi_{3/2}]_c$ 7s; 1_g $v=1$ Rydberg state vibrational band envelope (see Figure 5.13(a) to (e) for the REMPI spectrum of this vibronic state) should provide an indication of the extent of Rydberg and ion-pair character of the intermediate state (see Figure 5.14). Whilst the spectra in Figure 5.14 are generally similar in appearance to the same ion internal energy region in the ZEKE-PFI spectrum presented in Figure 5.12 (b), they do exhibit progressive changes in the peak width as well as an increased propensity for $\Delta v > 0$ transitions when ion-pair peaks lying in the wings of the Rydberg state vibrational envelope are pumped. The obvious conclusion in both cases is that as the ion-pair contribution to the intermediate state increases so the ZEKE-PFI spectra acquire characteristics which reflect the smaller

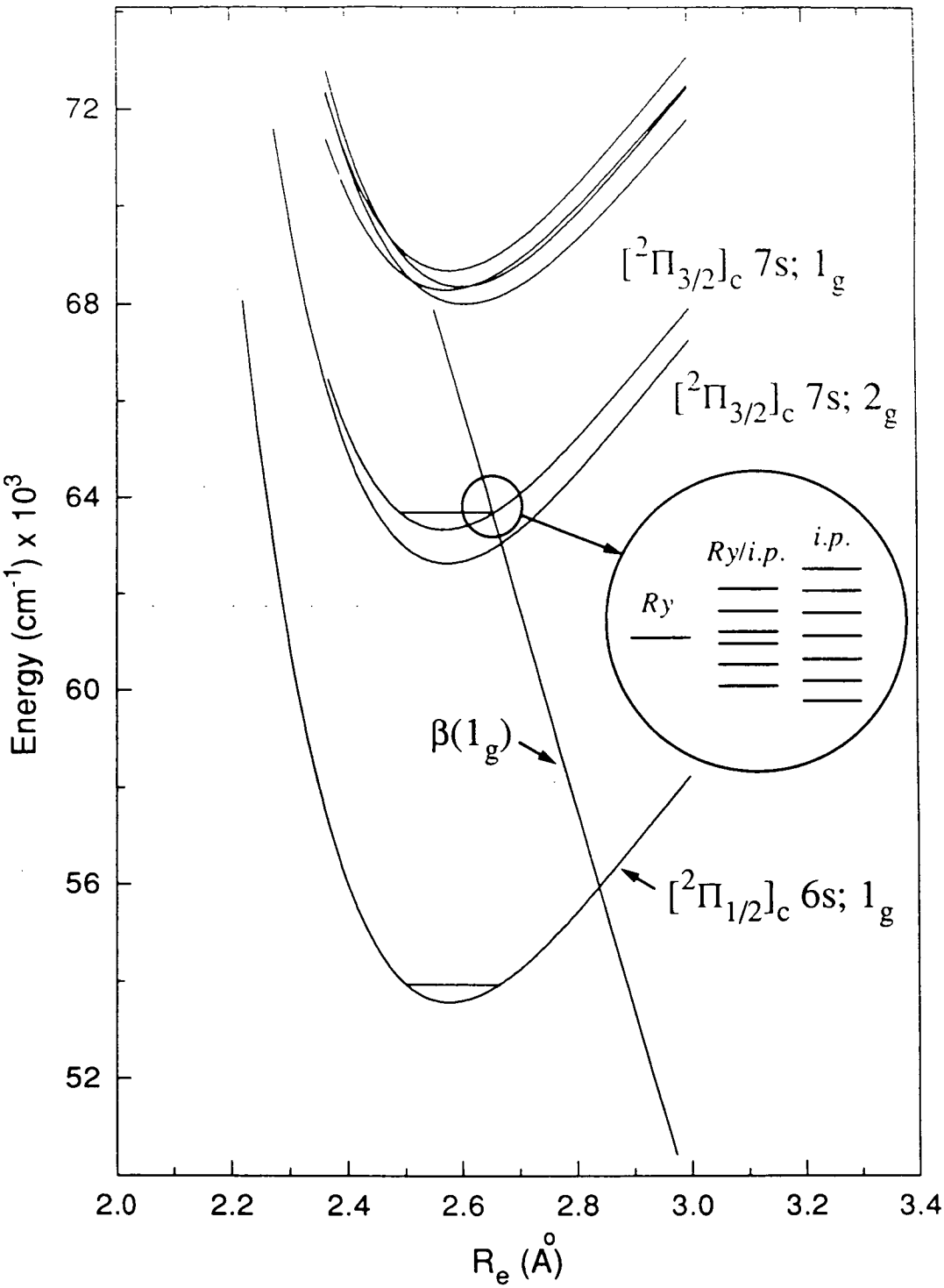

Figure 5.18

A schematic potential energy diagram showing the interaction of the $\beta(1_g)$ ion-pair state with the $[^2\Pi_{3/2}]_c$ 7s; 1_g state. *Ry* refers to a Rydberg state and *i.p.* refers to an ion-pair state.

rotational constant of the ion-pair state as well as the increased vibrational activity resulting from the subtle effect of the coupling of the Rydberg and ion-pair vibrational wavefunctions.

Ion-pair states are characterised by ω_e and B_e values which are substantially smaller than those of the Rydberg and ionic states. For the high v states in the region of the ion-pair/Rydberg interaction, B_v values of around 0.004 cm^{-1} for the ion-pair state, compared with typical values of around 0.04 cm^{-1} for the Rydberg state, may exert a considerable influence on the appearance of the ZEKE-PFI peak shape as the level of ion-pair character of the intermediate state increases. The rotational constant of the perturbed state is given by

$$B_v = C_1^2(v)B_{v,i.p.} + C_2^2(v)B_{v,Ry.} \qquad 5.3$$

where $B_{v,i.p.}$ and $B_{v,Ry.}$ are the rotational constants of the unperturbed ion-pair and Rydberg states respectively, and C_1 and C_2 are the coefficients of the ion-pair and Rydberg components of the vibronically mixed state such the $C_1^2 + C_2^2 = 1$. In this case, increased ion-pair character results in a reduction in the net B_v value for the perturbed state and a corresponding increase in the simulated ZEKE-PFI peak width (arising principally from a blue degraded rotational contour).

The possibility of lifetime broadening was also considered as an explanation for the change in peak shape but this seems unlikely as previous fluorescence studies on the ion-pair states in question show dips in the fluorescence quantum yield in regions where the ion-pair state crosses a Rydberg state [6]. This strongly suggests that it is the Rydberg state which is predissociated and not the ion-pair state. The trend observed in the spectra in Figure 5.14 would seem to indicate that the reverse is the case. Consequently, we discount lifetime broadening as the cause of our experimental observations.

In a similar vein, whilst the mixed Rydberg/ion-pair state probed by the ZEKE-PFI experiment will retain the electronic character of the Rydberg state, the vibrational amplitude may be extended by the interaction of the two vibrational wavefunctions. Stronger coupling can be regarded as introducing some $v_{Ry}=2$ character into what is nominally a $v_{Ry}=1$ level which results in v_{Ry} no longer being a good quantum number. The consequence of this will be to encourage a propensity for larger changes in vibrational quantum number upon ionisation. This is reflected in the insets to spectra (c) to (e) in Figure 5.14 which show increased intensity in the $v^+=2$ and $v^+=3$ peaks as the ion-pair character of the mixed intermediate state increases.

5.9 References

[1] R.S. Mulliken, Phys. Rev. **36** (1930) 699

[2] R.S. Mulliken, Phys. Rev. **57** (1940) 500

[3] For a summary see G. Herzberg, Spectra of Diatomic Molecules, 2nd Edition, Van Nostrand Reinhold and Co., New York (1950)

[4] R.J. Donovan, T. Ridley, K.P. Lawley and P.J. Wilson, Chem. Phys. Lett. **196** (1992) 173

[5] P.J. Wilson, T. Ridley, K.P. Lawley and R.J. Donovan, Chem. Phys. **182** (1994) 325

[6] A. Hiraya, K. Shobatake, R.J. Donovan and A. Hopkirk, J. Chem. Phys. **88** (1988) 52

[7] R.S. Mulliken, J. Am. Chem. Soc. **86** (1964) 3183

[8] T. Ridley, K.P. Lawley, R.J. Donovan and A.J. Yencha, Chem. Phys. **148** (1990) 315

[9] W.A. Chupka, J. Chem. Phys. **98** (1993) 4520

[10] J.C.D. Brand and A.R. Hoy, Appl. Spectrosc. Rev. **23** (1987) 285

[11] K.P. Lawley and R.J. Donovan, J. Chem. Soc. Faraday II **89** (1993) 1885

[12] P. Venkateswarlu, Can. J. Phys. **48** (1970) 1055

[13] G. Petty, C. Tai and F.W. Dalby, Phys. Rev. Lett. **34** (1975) 1207

[14] F.W. Dalby, G. Petty-Sil, M.H.L. Pryce and C. Tai, Can. J. Phys. **55** (1977) 1033

[15] K.K. Lehmann, J. Smolarek and L. Goodman, J. Chem. Phys. **69** (1978) 1569

[16] J.C. Miller, J. Phys. Chem. **91** (1987) 2589

[17] M. Wu and P.M. Johnson, J. Chem. Phys. **90** (1989) 74

[18] R.R. Desari and F.W. Dalby, J. Chem. Phys. **92** (1990) 3984

[19] R.J. Donovan, R.V. Flood, K.P. Lawley, A.J. Yencha and T. Ridley, Chem. Phys. **164** (1992) 439

[20] T. Ishiwata and I. Tanaka, Laser Chem. **7** (1987) 79

[21] A.R. Hoy and R.H. Lipson, Chem. Phys. **140** (1990) 187

[22] J.C.D. Brand, A.R. Hoy, A.K. Kalkar and A.B. Yamashita, J. Mol. Spec. **95** (1982) 350

[23] G.W. King, I.M. Littlewood and J.R. Robins, Chem. Phys. **56** (1981) 145

[24] J.P. Perrot, B. Femelat, M. Broyer and J. Chevaleyre. Mol. Phys. **61** (1987) 97

[25] K.P. Lawley, P.J. Jewsbury, T. Ridley, P.R.R. Langridge-Smith and R.J. Donovan, Mol. Phys. **75** (1992) 811

[26] J. Tellinghuisen, J. Mol. Spec. **94** (1982) 231

[27] J. Tellinghuisen, S. Fei, X. Zheng and M.C. Heaven, Chem. Phys. Lett. **176** (1991) 373

[28] T. Ishiwata, T. Kusayanagi, T. Hara and I. Tanaka, J. Mol. Spec. **119** (1986) 337

[29] A.R. Hoy and J.C.D. Brand, Chem. Phys. **109** (1986) 109

[30] J.S. Hickmann, C.R.M. de Oliveira and R.E. Francke, J. Mol. Spec. **127** (1988) 556

[31] K.S. Viswanathan and J. Tellinghuisen, J. Mol. Spec. **101** (1983) 285

[32] K.S. Viswanathan, A. Sur and J. Tellinghuisen, J. Mol. Spec. **86** (1981) 393

[33] P.J. Jewsbury, T. Ridley, K.P. Lawley and R.J. Donovan, J. Mol. Spec. **157** (1993) 33

[34] T. Ishiwata, H. Takekawa and K. Obi, J. Mol. Spec. **159** (1993) 443

[35] G.W. King and T.D. McLean, J. Mol. Spec. **135** (1989) 207

[36] T. Ishiwata, A. Tokunaga, T. Shinzawa and I. Tanaka, J. Mol. Spec. **117** (1986) 89

[37] J. Li and K. Balisubramanian, J. Mol. Spec. **138** (1989) 162

[38] B.R. Higginson, D.R. Lloyd and P.J. Roberts, Chem. Phys. Lett. **19** (1973) 480

[39] A. Kvaran, A.J. Yencha, D.K. Kela, R.J. Donovan and A. Hopkirk, Chem. Phys. Lett. **179** (1991) 263

[40] K.P. Huber and G. Herzberg, Constants of Diatomic Molecules, Van Nostrand, New York (1979)

[41] L. Zandee, R.B. Bernstein and D.A. Lichtin, J. Chem. Phys. **69** (1978) 3427

[42] R.G. Bray and R.M. Hochstrasser, Mol. Phys. **31** (1976) 1199

[43] M.S.N. Al-Kahali, R.J. Donovan, K.P. Lawley, Z. Min, T. Ridley and P.J. Wilson, *to be published*

[44] A. Kvaran, H. Wang, G.H. Johannesson and A.J. Yencha, Chem. Phys. Lett. **222** (1994) 436

[45] P.J. Wilson, Ph.D. Thesis, University of Edinburgh, 1994

[46] P.H. Bucksbaum, M. Bashkansky, R.R. Freeman, T.J. McIlraith and L.F. DiMauro, Phys. Rev. Lett. **56** (1986) 2590

[47] R. Hippler, H. Schwier, H.J. Humpert and H.O. Lutz, Z. Phys. D **5** (1987) 21

[48] M.S.N. Al-Kahali, R.J. Donovan, K.P. Lawley and T. Ridley, *to be published*

[49] A. Kvaran, H. Wang and J. Asgeirsson, J. Mol. Spec. **163** (1994) 541

[50] T. Ridley, K.P. Lawley, R.J. Donovan and A.J. Yencha, Chem. Phys. **148** (1990) 315

[51] R.J. Donovan, J.G. Goode, K.P. Lawley, T. Ridley and A.J. Yencha, J. Phys. Chem. **98** (1994) 2236

[52] R.J. Donovan, T. Ridley, K.P. Lawley and P.J. Wilson, Chem. Phys. Lett. **205** (1993) 129

[53] R.J. Donovan, T. Ridley, K.P. Lawley and P.J. Wilson, Chem. Phys. Lett. **207** (1993) 129

[54] H. van Lonkhuyzen and C.A. de Lange, Chem. Phys. **89** (1984) 313

[55] A. Mank, D. Rodgers and J.W. Hepburn, Chem. Phys. Lett. **219** (1994) 169

[56] E. de Beer, W.J. Buma and C.A. de Lange, J. Chem. Phys. **99** (1993) 3252

[57] S.T. Pratt, J. Chem. Phys. **101** (1994) 8302

[58] R.G. Tonkyn, R.T. Wiedmann and M.G. White, J. Chem. Phys. **96** (1992) 3696

[59] R.T. Wiedmann, M.G. White, K. Wang and V. McKoy, J. Chem. Phys. **98** (1993) 7673

[60] R.D. Gilbert and M.S. Child, Chem. Phys. Lett. **187** (1991) 153

[61] C.C. Kiess and C.H. Corliss, Journal of the National Bureau of Standards-A. Physics and Chemistry, Vol. 63A, July-August (1959)

[62] Y. Xie, P.T.A. Reilly, S. Chilukuri and R.J. Gordon, J. Chem. Phys. **95** (1991) 854

Chapter 6

The Rydberg States and Ground Ionic State of the I_2–Ar vdW Complex

6.1 Introduction

The general area of non-covalent (van der Waals) interactions between atoms, molecules and macromolecular structures has developed spectacularly in the past 20-25 years. Although the chemistry of individual molecules is generally dominated by covalent bonding, van der Waals forces govern the interactions within collections of molecules and are responsible for the stability of intermolecular complexes, surface bonding of solutions, and possible adsorbed species and even for the existence of the condensed liquid phase. Studying these van der Waals complexes, both experimentally and theoretically, can therefore bridge the gap between gas phase molecular interactions and the condensed phase [1].

One of the goals of a high resolution spectroscopic study of weakly bound molecular complexes has been a detailed understanding of the electrostatic interactions between the atoms and molecules which make up these complexes. Although a complete picture is still to evolve, an impressive volume of information on these weakly bound molecular species has been generated. The accumulation of this data has been achieved using a wide variety of spectroscopic techniques to investigate these weakly bound systems ranging from detailed microwave and infrared spectroscopic measurements to broader electronic spectroscopic measurements.

Theoretical calculations have also played a major part in understanding the role of the different interactions at work in these complexes.

Early attempts at spectroscopically investigating gas phase van der Waals complexes were only successful for very strongly bound complexes such as the HF dimer [2]. The binding energies of most complexes were so small compared with kT (when T is the temperature of the ordinary laboratory environment) that they were unstable with respect to two-body collisions and did not survive long enough to be studied [2-,3,4]. One solution which extended the lifetime of the complex was to trap it in an inert matrix. However, the matrix generally perturbed the complex such that a spectroscopic investigation was not representative of the gas phase complex. It was not until the advent of the supersonic expansion [5] that the lifetime of the complex in the gas phase was increased sufficiently to allow them to be probed spectroscopically. The cooling which occurs in a supersonic expansion generally results in a much lower value of kT (T in this case is the low translational temperature of the beam) compared to the binding energy of the complex such that the complex is stable to two body collisions. Disadvantages of supersonic expansions include the fact that the van der Waals complex usually constitutes only a very small percentage of the molecular beam and that there is also the possibility of forming more than one complex species in the beam. To maximise complex formation careful optimisation of the molecular beam by varying the expansion conditions, such as carrier gas, concentrations of reactants and backing gas pressure is required.

The low binding energy of vdW complexes leaves them with some unusual characteristics compared to chemically bound species. The weak vdW bond generally means that the vibrational modes of a vdW complex can be separated into a set of high frequency vibrational modes of the chemically bound substrate (if it is molecular in nature) plus a set of low frequency modes associated with the vdW bond. As a result of the large frequency mismatch between these vibrational modes there tends to be very little coupling between them. The weak binding energy of the complex also results in a large van der Waals bond length.

The attractive forces which bind neutral van der Waals molecules [6] consist of a number of individual, weak electrostatic interactions. In the case of neutral vdW complexes the electrostatic interactions depend on the charge distribution within the atomic or molecular species which constitute the complex. If one of the molecular constituents of the complex has a net charge distribution (i.e. quadrupole, octapole etc.), then the electric field generated by the charge distribution may induce small changes in the electron distribution of the nearby atom or molecule leading to an interaction energy called an induction energy. In general, however, the major source of attractive forces (excluding charged species and highly polar molecules) arises through the rather subtle dispersion effect in which instantaneous dipoles associated with the rapid movement of electrons in one molecule are correlated with those in a neighbour. If one of the constituents of the complex is charged (i.e. an ionic complex) or highly polar (i.e. Rydberg excited complex) then there is an additional strong electrostatic attraction which can significantly increase the binding energy of van der Waals complexes. This arises through charge induced dipole interactions.

6.2 The I_2–Ar van der Waals Complex

This chapter is primarily concerned with the gas phase spectroscopic study of the iodine-argon van der Waals complex in Rydberg excited electronic states and in its ground ionic state using both REMPI spectroscopy and ZEKE-PFI photoelectron spectroscopy. Diatomic and triatomic vdW complex species are particularly attractive to study as their spectral simplicity presents us with the possibility of achieving a real understanding of the perturbations which are induced in a solute molecule by the initial stages of solvation. Much of the pioneering work was carried out by Levy and co-workers on the I_2–He [7-,8,9,10] and I_2–Ar [11,12] vdW complexes using laser induced fluorescence (LIF) spectroscopy. However, since the original study of I_2–He [7], the number of diatomic–rare gas systems studied, remains quite small, the emphasis having shifted to larger systems such as those formed between mono- and

polycyclic aromatic molecules and various solvent species [13-,14,15]. Many of the diatomic–rare gas complex studies which have been undertaken, however, have concentrated on the electronic spectroscopy of various halogen and interhalogen–rare gas complexes, such as Rg–Cl_2 (Rg = He, Ar, Ne) [16-,17,18] and Ne–ICl [19,20], using techniques such as LIF and optical-optical double resonance (OODR).

Almost all the electronic state spectroscopic studies to date have concentrated on valence excited van der Waals complexes [3], Rydberg excited van der Waals complexes being poorly represented. Theoretically, Rydberg excited van der Waals complexes are more strongly bound than valence excited vdW complexes. For low-n Rydberg states this increase in binding energy arises as a result of the highly polarisable nature of the Rydberg excited state. In contrast, a large proportion of the increase in binding energy in high-n Rydberg states where the Rydberg electron orbits outside the vdW bond results from a charge induced dipole interaction. The first Rydberg excited vdW complex to be investigated was Ar–NO. The $\tilde{A}\ ^2\Sigma^+$ Rydberg state of Ar–NO was found to be repulsive, both in a LIF study by Langridge-Smith et al. [21] and a REMPI study by Miller and Cheng [22]. Recently, however, it has been found to be weakly bound in a high resolution REMPI study by Tsuji et al. [23]. The REMPI technique has also been applied by Sato et al. [24] to investigate the Rydberg excited $\tilde{C}\ ^2\Pi$ state of Ar–NO. Miller and Cheng [22] have extended the work on Ar-NO, to include the valence $\tilde{B}\ ^2\Pi$ and Rydberg $\tilde{D}\ ^2\Pi$ states as well as to the $\tilde{C}\ ^2\Pi$ state of Ne–NO and Kr–NO. Complexes between a metal atom and a rare gas atom have also been observed in Rydberg excited states. One example is the Hg–Rg complexes (Rg = Ar and Ne) [25].

The two main techniques which have been employed to study weakly bound complexes are REMPI and LIF. REMPI, however, has a number of distinct advantages over LIF including the positive identification of the complex species through mass analysis, whilst discriminating against other species, such as the parent molecule. This can allow excitation spectra to be recorded which are free of contributions from other species present in the molecular beam. REMPI spectroscopy

is also particularly appropriate for the study of Rydberg excited van der Waals complexes because their failure to fluoresce in many cases precludes the use of LIF spectroscopy.

In the case of I_2–Ar, spectroscopic studies have mainly concentrated on the valence $\tilde{B}\ ^3\Pi_{0_u^+} \leftarrow \tilde{X}\ ^1\Sigma_{0_g^+}$ system. The early laser induced fluorescence excitation spectra recorded for this system displayed discrete bands shifted by 14 cm^{-1} to the blue of each of the corresponding (v',0) bands of I_2 (B←X) [11]. Although nearly all the intensity in the I_2 vibronic bands observed in these fluorescence excitation spectra was concentrated in a single feature, Johnson et al. [26] managed to observe a series of weak fluorescence bands to the blue of the I_2 (21,0) and (22,0) bands which were tentatively assigned to excitation in the I_2···Ar vdW stretching and bending modes. However, intensity arguments and the band shift rule [26] could not be applied as successfully with the I_2–Ar complex as they were with the I_2–He and I_2–Ne complexes to obtain a definitive vibrational assignment.

In addition to the spectroscopic characterisation of the valence excited states of the I_2–Ar vdW complex, a significant amount of experimental effort has also been focused on the dynamics of the I_2–Ar complex in discrete electronic states. These investigations have been primarily concerned with the experimental and theoretical study of vibrational [27-,28,29,30,31] and electronic predissociation [32-,33,34] of the complex following discrete excitation to the $\tilde{B}\ ^3\Pi_{0_u^+}$ state. One study, by Burke and Klemperer [33], managed to successfully analyse resolved rotational structure associated with each of the vibrational bands observed in the fluorescence excitation spectrum. From the analysis they concluded that the I_2–Ar vdW complex has a T-shaped geometry in both the $\tilde{X}$ and the $\tilde{B}$ valence states and that only slight changes in geometry occur upon excitation. The small geometry changes would explain the short progressions and weak vibrational structure associated with the complex fluorescence bands. The ambiguous assignment of the vdW structure observed by Johnson et al. [26] combined with the very short vibrational progressions

made an accurate binding energy determination very difficult. A solution to this problem, however, was achieved by Blazy et al. [12] via the selective vibrational excitation of the I_2–Ar vdW complex in the $\tilde{B}\ ^3\Pi_{0_u^+}$ state. An upper and lower bound to the complex binding energy was determined by monitoring the product state distribution of the fragment I_2* after the I_2–Ar complex had vibrationally predissociated and assuming that the first energetically open dissociation channel was observed.

While most spectroscopic studies of I_2–Ar have concentrated on the valence excited $\tilde{B}\ ^3\Pi_{0_u^+}$ state, no successful observations have been made of Rydberg excited states using either LIF or REMPI. An unsuccessful (2+1) REMPI study by Miller [35] using nanosecond lasers, concluded that the I_2–Ar complex must undergo an extremely rapid dissociation process when excited to the region populated by Rydberg states of I_2. He proposed that this dissociation occurred either via the rapid dissociation of the two-photon state to a lower lying state or at the nominally virtual one-photon level. A subsequent non-resonant MPI experiment using the third harmonic of a picosecond Nd:YAG laser (355 nm) seemed to support this conclusion, with the observation of iodine-argon cluster ions in a time-of-flight mass spectrum [36]. The observed cluster ions were predominantly I^+–Ar_n rather than I_2^+–Ar_n which was explained by Smith and Miller [36] by invoking a number of possible mechanisms such as chemi-ionisation and intracluster ion-molecule reactions along with the possibility that the I_2–Ar was being excited to an autoionising state from which dissociative ionisation was occurring to I^+–Ar + I. Electron impact studies have also been carried out on iodine/argon mixtures in which mass spectra have shown the presence of I–Ar_n^+ (n<28) and I_2–Ar_n^+ (n<25) cluster species with various "magic" number stable configurations [37].

6.3 The (2+1) Mass Resolved REMPI Excitation Spectra of the *ns* Rydberg Excited States of Jet Cooled I_2–Ar between 53000 and 70000 cm^{-1}

The jet cooling of I_2 in an argon carrier gas which enabled the mass resolved (2+1) REMPI investigation of I_2 presented in the previous chapter, provided the ideal opportunity to locate and characterise the Rydberg excited states of the I_2–Ar van der Waals complex. The following sections present mass resolved one colour (2+1) REMPI excitation spectra of the *n*s Rydberg excited states of jet-cooled I_2–Ar lying in the region between 53000 and 70000 cm^{-1}. The assignments of the electronic character of the Rydberg excited states of the complex are based on those of I_2. The I_2–Ar complex acquires most of its character from the parent I_2 molecule and therefore many of the figures and spectroscopic values referred to, are to be found in the previous chapter. The iodine sample (Fisons) employed to study the complex was heated to approximately 100 ^0C to generate a sufficiently high vapour pressure to observe the complex. An argon carrier gas at pressures of 400-600 Torr was found to give the best complexation. The results are presented in order of increasing Rydberg principal quantum number.

6.3.1 The $[^2\Pi_{1/2}]_{c,g}$ 6s Rydberg State

During the analysis of the (2+1) mass resolved REMPI excitation spectrum of jet-cooled I_2 between 53200 and 55300 cm^{-1} shown in Figure 6.1, a number of weak peaks were identified in the I^+ mass channel spectrum which could not immediately be assigned to I_2 itself. These peaks can be clearly observed in groups of three between the intense vibrational peaks assigned to the 1_g Rydberg state. The intensity of these peaks was found to be dependant on the argon stagnation pressure, and when helium was used in place of argon the peaks disappeared completely. This enabled a provisional assignment of the peaks to iodine-argon van der Waals

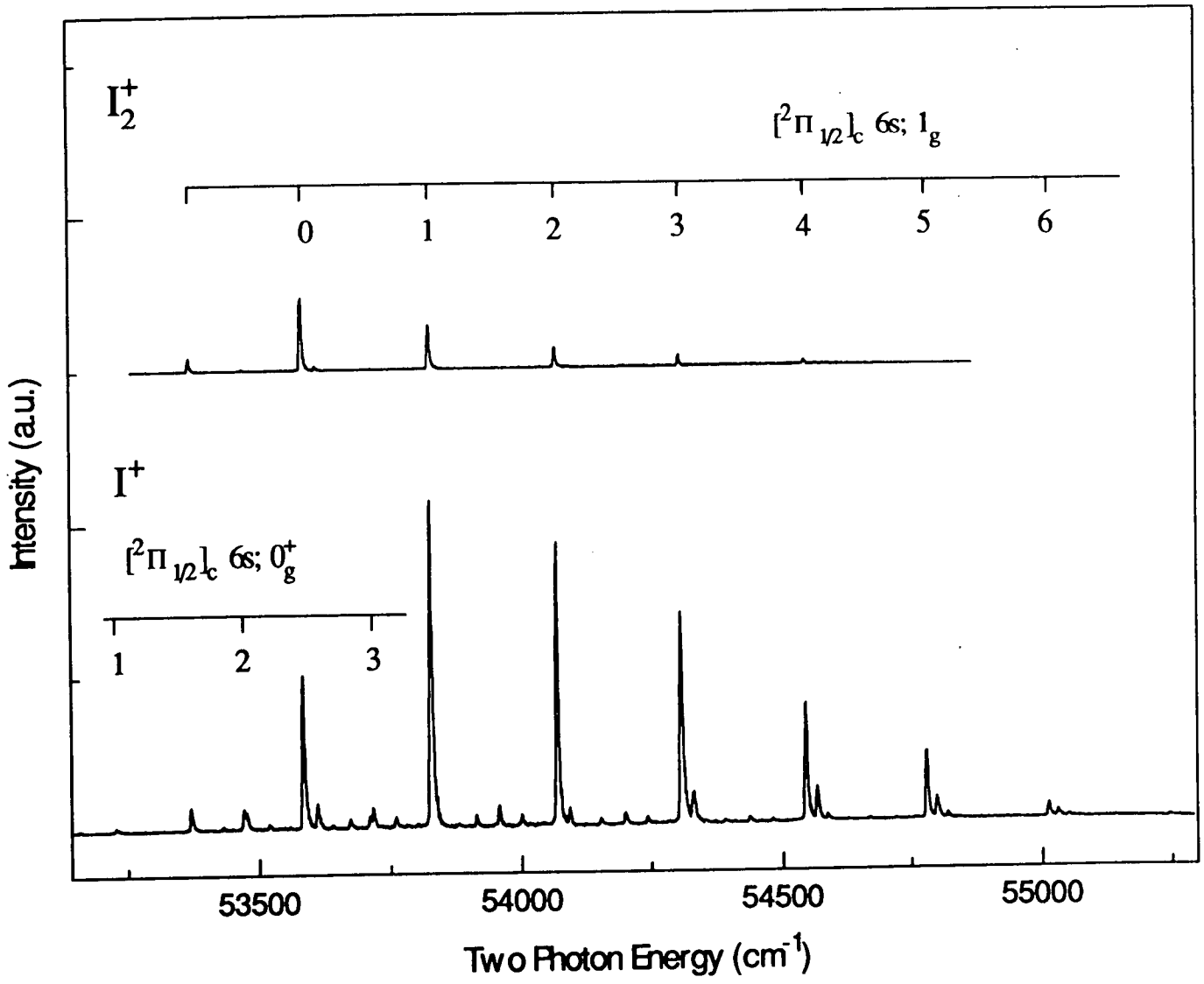

Figure 6.1 The (2+1) mass resolved REMPI excitation spectrum of jet-cooled I_2 recorded in the range 53200-55300 cm^{-1} by monitoring the I_2^+ and I^+ mass channels. Note the weak vibrational structure between the I_2 vibrational bands in the I^+ mass channel.

complexes. It is important to note that these complex peaks only appear in the I^+ mass channel spectrum and are completely absent from the I_2^+ mass channel spectrum.

To establish the identity of the species behind these peaks, the excitation laser wavelength was tuned to the most intense of these features at 53959 cm^{-1} and a time-of-flight mass spectrum recorded. The resulting mass spectrum is shown in Figure 6.2. The ringing in the time-of-flight mass spectrum is an instrumental artifact. The two most intense mass peaks to shorter flight time in the spectrum can readily be assigned to I^+ and I^+–Ar with the two much weaker peaks to longer flight time assigned to I_2^+ and I_2^+–Ar. The I_2^+ signal in this case forms a constant background and most probably arises from coherent three photon absorption of uncomplexed I_2 due to the tight focusing conditions (f=7.62 cm) of the laser beam. Similarly, part of the I^+ signal exists as a constant background which arises from subsequent fragmentation of the background I_2^+, the balance arising from fragmentation of the complex.

The (2+1) mass resolved REMPI excitation spectra recorded in the range 53300–54700 cm^{-1} two photon energy by simultaneously gating on both the I^+–Ar and I_2^+–Ar mass channels are presented in Figure 6.3. The vibrational peak positions accurate to $\pm$ 2 cm^{-1} and assignments are listed in Table 6.8. A comparison of the lower spectrum recorded by monitoring I^+–Ar with that recorded over the same region for I_2 by monitoring I^+ (see Figure 6.1) shows a similar overall Franck-Condon profile. Both the spectra shown in Figure 6.1 and those shown in Figure 6.3 were recorded with the same laser dye outputs and focusing conditions, although neither have been corrected for variations in laser intensity. Each of the vibronic bands labelled in the top spectrum in Figure 6.3 corresponds to excitation in the I_2 stretch and has a single low frequency progression built upon it which arises from excitation in one of the van der Waals vibrational modes. A comparison of the upper spectrum recorded by monitoring I_2^+–Ar again shows a very similar intensity distribution in the I_2 stretching progression as that in Figure 6.1 recorded by monitoring the I_2^+ mass channel. This striking observation would seem to imply that the addition of an argon

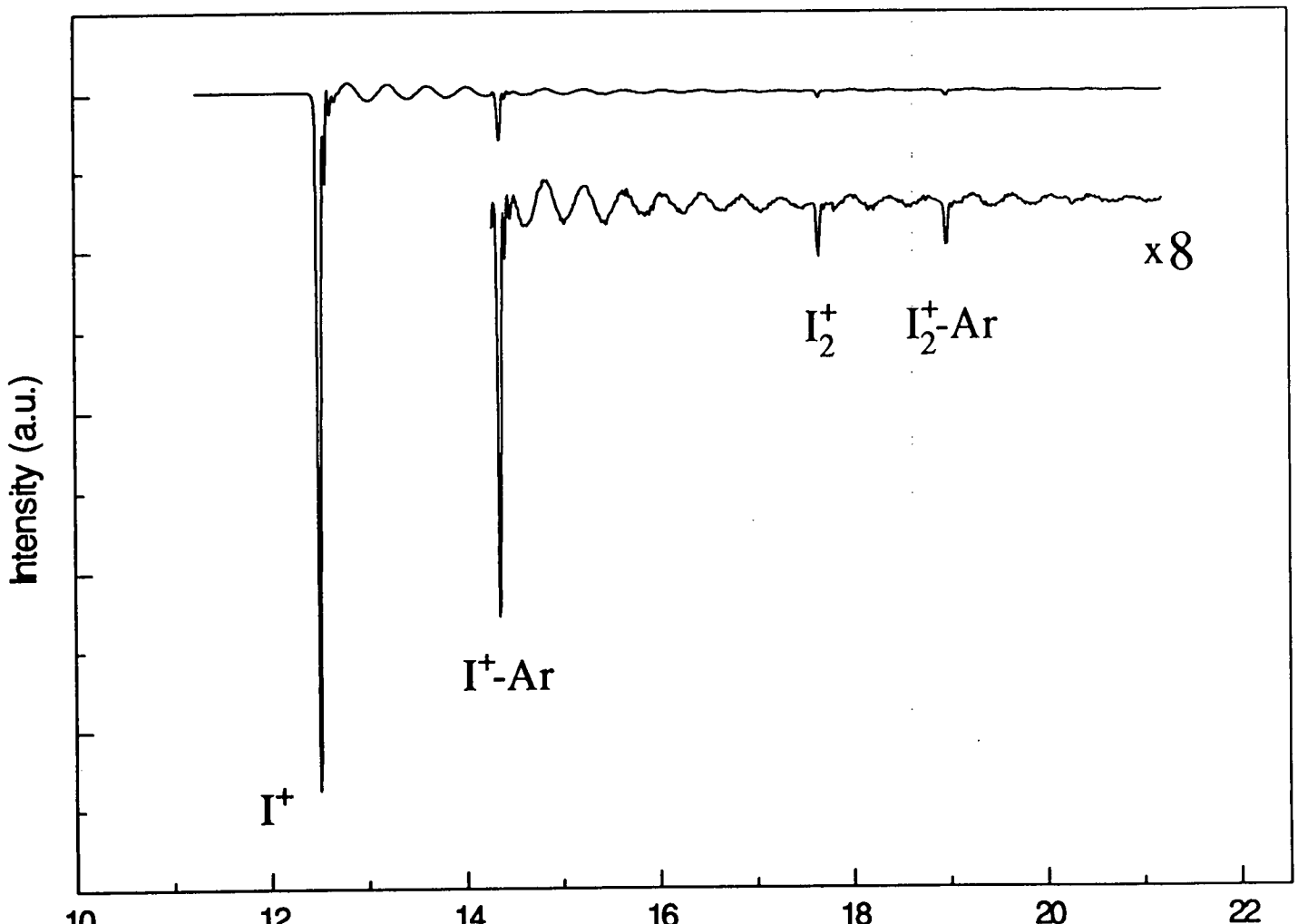

Figure 6.2 The time-of-flight mass spectrum of I_2 expanded in argon recorded by tuning the excitation laser to 53959 cm^{-1}.

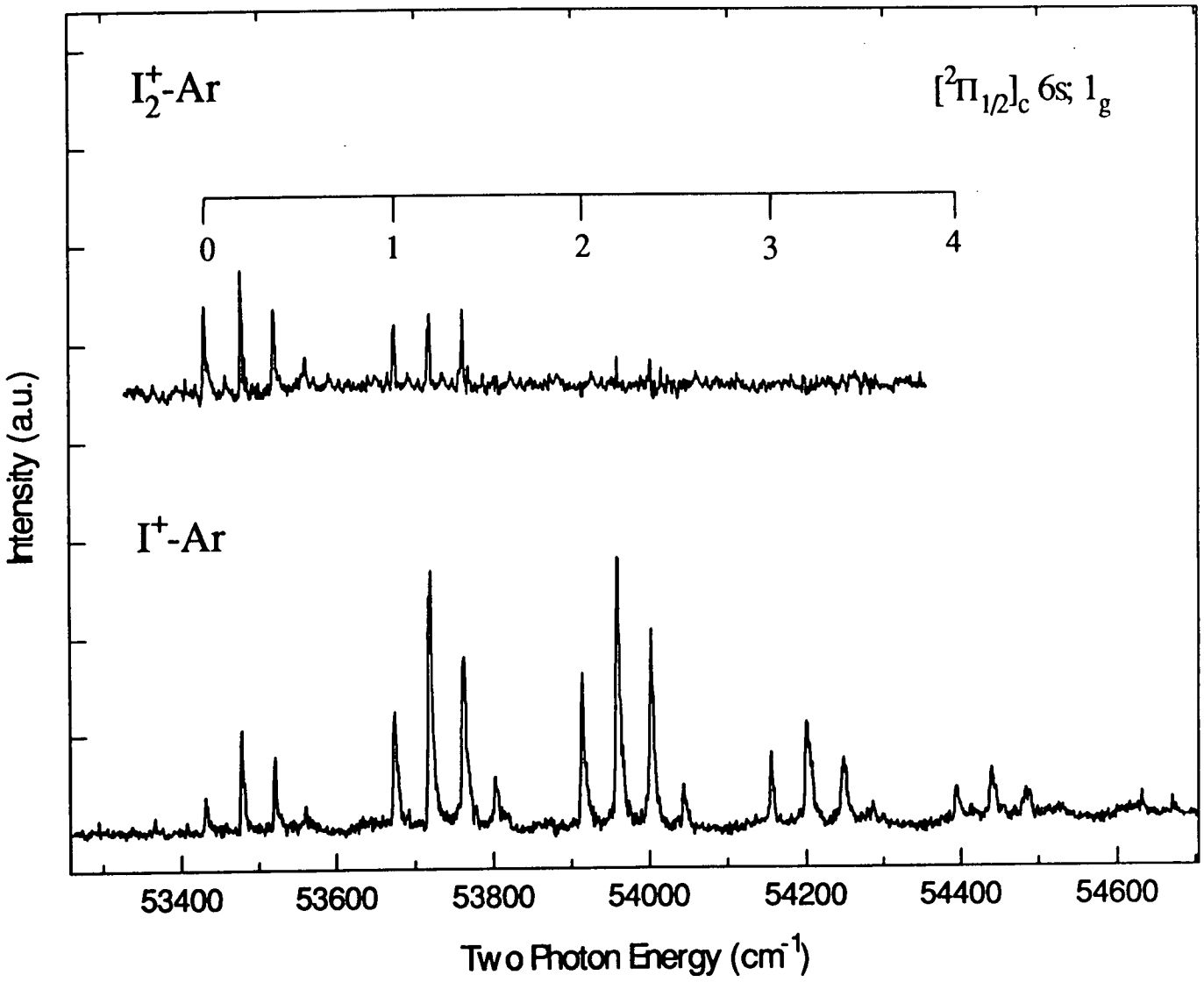

Figure 6.3 The (2+1) mass resolved REMPI excitation spectrum of jet-cooled I_2–Ar recorded in the range 53300-54700 cm^{-1} by monitoring both the I^+–Ar and I_2^+–Ar mass channels.

atom to the system does not influence the iodine fragmentation route. It would seem that after the I_2–Ar van der Waals complex has been ionised it favours a fast dissociation channel yielding I^+–Ar in preference to losing the argon atom. This dissociation channel can be followed by monitoring the ratio of I_2^+–Ar/ I^+–Ar as the level of vibrational excitation in the Rydberg state is increased. Clearly, by the time we reach two quanta in the I_2 stretch, the fragmentation of the complex is proceeding at an efficient rate and the v'=2 complex bands are only just discernible in the upper spectrum in Figure 6.3 while in the lower spectrum the complex bands are at their most intense.

The lowest energy peak in the spectrum appears at 53430 ± 2 cm^{-1} (Figure 6.3) and is assumed to be the band origin of the first progression in the series. In contrast to the I_2 spectrum in Figure 6.1, no evidence for hot band structure was observed. This might initially seem a little strange given that the binding energy of the complex in the ground electronic state is between 234.2–240.1 cm^{-1} [12] and the separation between v"=0 and v"=1 in the ground electronic state of I_2 is 214.5 cm^{-1} [38]. However, the intensity of the (0,1) vibrational hot band in the 1_g progression in the I^+ mass channel spectrum shown in Figure 6.1 is only ~15% of the band origin and if a similar hot band intensity is assumed in the I^+–Ar mass channel spectrum, then it is very likely that it would be too weak to observe. Therefore, from the lack of any other obvious features to lower energy a correspondence can be inferred between the band at 53430 cm^{-1} and the (0,0) band in the I_2 $[^2\Pi_{1/2}]_c$ 6s; 1_g Rydberg progression in Figure 6.1. The position of this peak represents a spectral red shift of 152 ± 2 cm^{-1}. This implies a significant strengthening in the van der Waals interaction with respect to that in the ground $\tilde{X}$ state which is what one would expect given the additional influence of the charge-induced dipole forces resulting from the positively charged ion core. Given a value for D_0 in the ground state of 237 ± 3 cm^{-1} determined experimentally by Blazy et al. [12], and assuming that the first spectral feature in the progression is the band origin, we can calculate a lower limit to D_0 in the $[^2\Pi_{1/2}]_c$ 6s; 1_g state of I_2–Ar of 389 ± 5 cm^{-1}. The beginning of the next band appears 244 cm^{-1} to

higher energy at 53674 ± 2 cm^{-1}. This separation is almost identical to that between v'=1 and v'=0 in Figure 6.1 (242 cm^{-1}) and consequently it can be assigned to one quantum excited in the I_2 stretching mode, ν_1. At least five quanta in ν_1 are observed which together with almost identical values for ν_1 in both I_2 and I_2–Ar suggests that there is very little coupling between the I_2 stretching mode and the van der Waals vibrational modes. In fact five quanta in the I_2 stretch lie at least 800 cm^{-1} above the dissociation energy of the complex (389 cm^{-1}).

As was mentioned earlier and can be seen in Figure 6.3, each of these bands consists of an anharmonic low frequency progression in one of the van der Waals modes. The average vibrational spacings in these progressions (~43 cm^{-1}) is consistent with single quanta excitation of the I_2···Ar stretching mode, ν_3. This represents a considerable increase in the stretching mode frequency over that determined in the ground state (26.3 cm^{-1}) [12] and is in agreement with the proposed strengthening of the vdW interaction based on the spectral red shift. The length of the progression (up to v'=3) and the propensity for Δv=+1 and +2 transitions would seem to indicate that a significant change in the I_2···Ar van der Waals bond length ($R_{Ar\cdots I_2}$) has occurred. From the increase in the vdW stretching frequency, ν_3, over that in the ground state it can be concluded that the bond has shortened. In order to quantify this geometry change, Franck-Condon band envelope simulations have been performed assuming that the potential curves following the I_2···Ar co-ordinate in both electronic states can adequately be described by a Morse potential, the functional form of which is given below

$$V(r)=D_e(1-\exp(-\alpha(r-r_e)))^2. \qquad 6.1$$

The Morse potential coefficients for the ground state van der Waals stretch were taken from Ref. [12] whereas those for the Rydberg state were derived from the v'=2 vibrational band. The dissociation energy (D_e) was taken as the binding energy i.e. 413 cm^{-1}, and the value of α was optimised until the Franck-Condon program

regenerated the eigenvalues of the v'=2 vdW stretching progression. The results of this simulation for the $[^2\Pi_{1/2}]_c$ 6s; 1_g Rydberg state are shown in Figure 6.4. They indicate that $R_{Ar\cdots I_2}$ is reduced by 0.29 Å upon electronic excitation from the ground state of the neutral to the $[^2\Pi_{1/2}]_c$ 6s; 1_g Rydberg state. The simulated band envelope and experimental band intensities have been normalised to the most intense band. All spectroscopic constants obtained from the spectrum are given in Table 6.8.

There still remains the possibility that some of the features in the spectrum may result from the fragmentation of higher clusters (I_2-Ar_n) in the same way that fragmentation of I_2-Ar eventually results in a contribution to the I^+ mass channel. However, no evidence of larger clusters is observed in the mass spectrum for this system at the stagnation pressures used (500 Torr) and it seems safe to conclude in this case that there are no contributions from higher clusters. Further evidence to support this conclusion will be presented below for the $[^2\Pi_{3/2}]_c$ 7s system.

One further point of note for this system is its behaviour with circularly polarised light. As with uncomplexed I_2, the intensity with circular polarisation shows a net increase of about 1.5 in agreement with that predicted by Bray and Hochstrasser [39] for all rotational branches with $\Delta\Omega=0, \pm1$ and ±2 except the Q branch of a $\Delta\Omega=0$ transition.

No evidence for the van der Waals complex in the $[^2\Pi_{1/2}]_c$ 6s; 0_g^+ Rydberg state was observed in either the I_2^+–Ar or I^+–Ar mass channels. If it is assumed that the transition probability to the $[^2\Pi_{1/2}]_c$ 6s; 1_g Rydberg state is similar in I_2-Ar and I_2, then the measured intensity ratio of vdW complex to I_2 was <5%. It is therefore not surprising that no complex bands of the $[^2\Pi_{1/2}]_c$ 6s; 0_g^+ Rydberg state are observed when the intensity of the I_2 $[^2\Pi_{1/2}]_c$ 6s; 0_g^+ Rydberg vibrational bands in Figure 6.1 are taken into consideration.

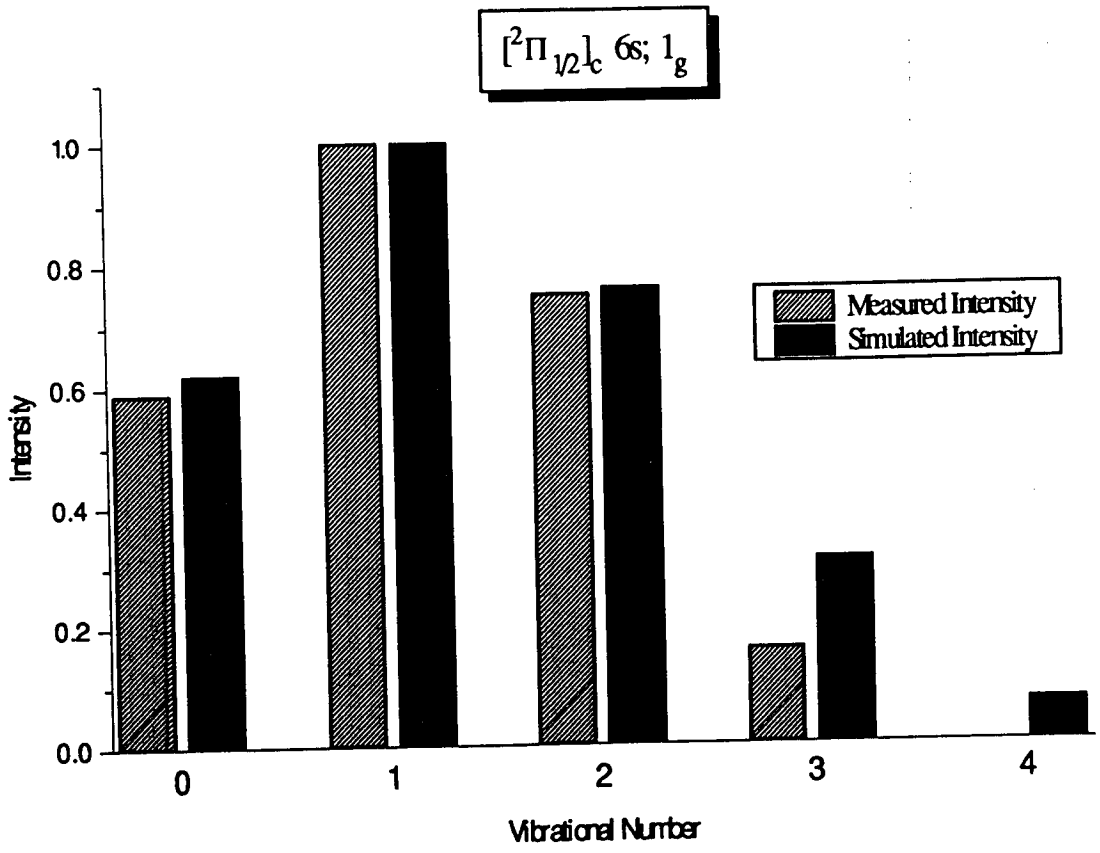

Figure 6.4 Observed and simulated Franck-Condon factors for the transition to the v'=2 band in the $[^2\Pi_{1/2}]_c$ 6s; 1_g state of I_2–Ar .

Table 6.1 Spectral peak position and assignments of the $[^2\Pi_{1/2}]_c\,6s;\ 1_g$ electronic state of I_2–Ar.

Transition energy / cm^{-1} [a]	Vibrational spacing / cm^{-1}		Assignment [b]
53430	0	0	0_0^0
53478	48		3_0^1
53521	43		3_0^2
53560	39		3_0^3
53674	0	244	1_0^1
53720	46		$3_0^1 1_0^1$
53762	42		$3_0^2 1_0^1$
53802	40		$3_0^3 1_0^1$
53914	0	240	1_0^2
53959	45		$3_0^1 1_0^2$
54003	44		$3_0^2 1_0^2$
54044	41		$3_0^3 1_0^2$
54154	0	240	1_0^3
54200	46		$3_0^1 1_0^3$
54244	44		$3_0^2 1_0^3$
54284	40		$3_0^3 1_0^3$
54392	0	238	1_0^4
54438	46		$3_0^1 1_0^4$
54482	44		$3_0^2 1_0^4$
54520	38		$3_0^3 1_0^4$
54631	0	239	1_0^5
54671	40		$3_0^1 1_0^5$

[a] Uncertainty $\pm 2\ cm^{-1}$.

[b] In this notation $3_0^n 1_0^m$ refers to m quanta excited in the I_2 stretch, ν_1, and n quanta excited in the I_2···Ar van der Waals stretch, ν_3.

6.3.2 The $[^2\Pi_{3/2}]_{c,g}$ 7s Rydberg System

As with the $[^2\Pi_{1/2}]_c$ 6s system, a number of peaks appeared in the (2+1) REMPI excitation spectrum shown in Figure 5.3 which could not be assigned to I_2. These peaks only appear in the I^+ mass channel and can be seen clearly either side of the v'=2 band of the I_2 $[^2\Pi_{3/2}]_c$ 7s; 2_g progression. The intensity of these peaks was found to be dependant on the argon stagnation pressure and consequently could be provisionally assigned to an iodine-argon van der Waals complex.

A time-of-flight mass spectrum recorded with the excitation laser wavelength tuned to the most intense of these features at 63114 cm^{-1} is shown in Figure 6.5. The three mass peaks in the spectrum can be readily assigned to I^+, I_2^+ and I_2^+–Ar with almost no I^+–Ar at the stagnation pressure used (500 Torr). In this respect the 7s system shows markedly different behaviour to the $[^2\Pi_{1/2}]_c$ 6s system in that the dominant complex ion is I_2^+–Ar rather than I^+–Ar.

In order to obtain a clearer view of the van der Waals spectrum a mass resolved (2+1) REMPI excitation spectrum of the complex was recorded by gating on the I_2^+-Ar mass channel. The (2+1) mass resolved REMPI excitation spectrum of I_2-Ar recorded in the range 62250 to 63750 cm^{-1} (two photon energy) using both linearly and circularly polarised light is presented in Figure 6.6 and the peak positions accurate to ± 2 cm^{-1} are listed in Table 6.2 and 6.3. The spectrum of the complex recorded with circular polarisation shows the same loss in intensity for the 1_g state which was found for I_2. Nevertheless, the observed behaviour provides us with a convenient way of deconvoluting the spectrum as well as assisting in its assignment. A comparison of the linearly polarised spectrum with the I^+ mass channel spectrum of I_2 in Figure 5.3 suggests that both of the Rydberg states in the iodine spectrum are observed in the complex spectrum. The subsequent loss of the higher energy progression with circular polarisation confirms this conclusion and further labels this state as having 1_g symmetry and the lower energy progression as 2_g. As with the

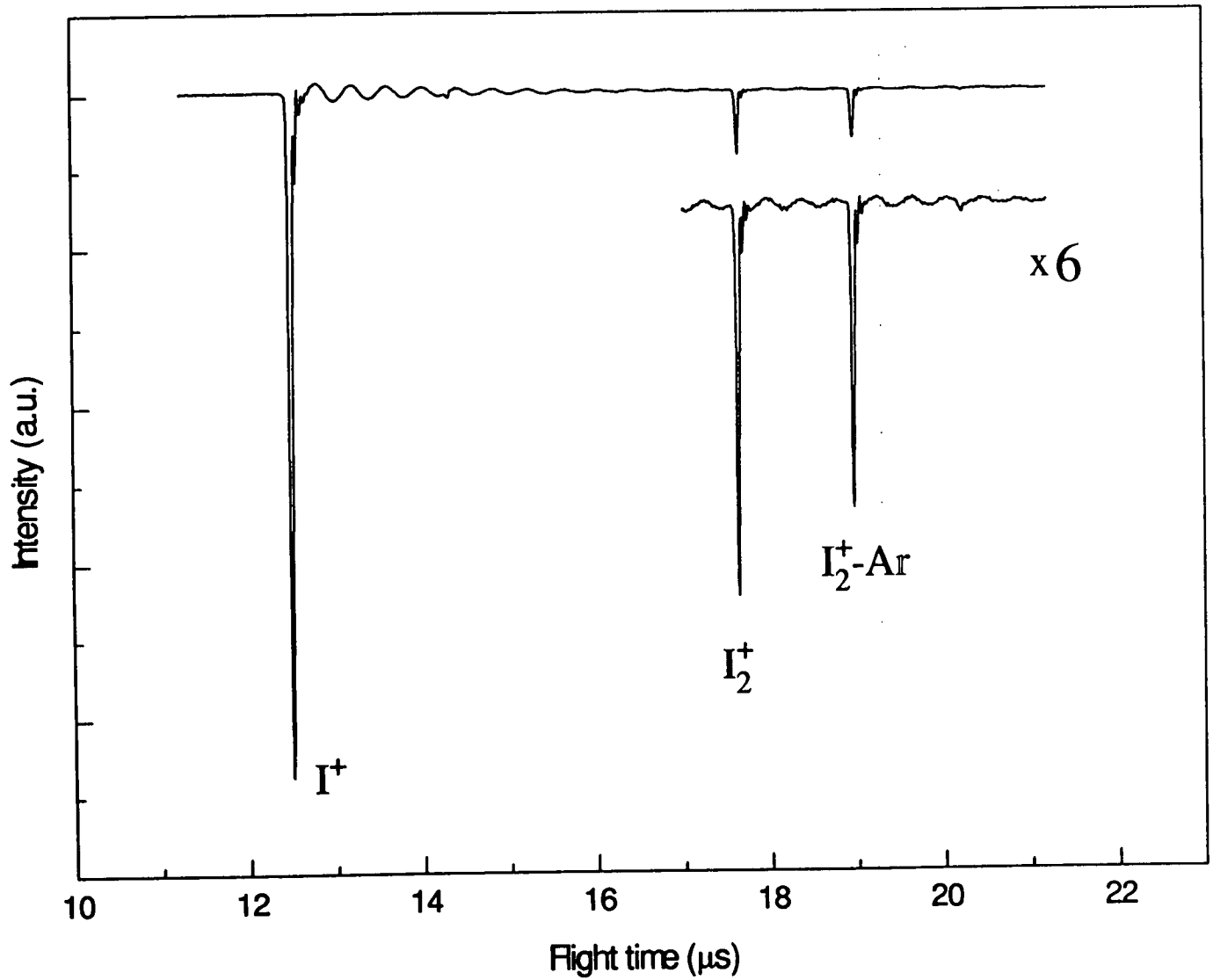

Figure 6.5 The time-of-flight mass spectrum of I_2 expanded in argon recorded by tuning the excitation laser to 63114 cm^{-1}.

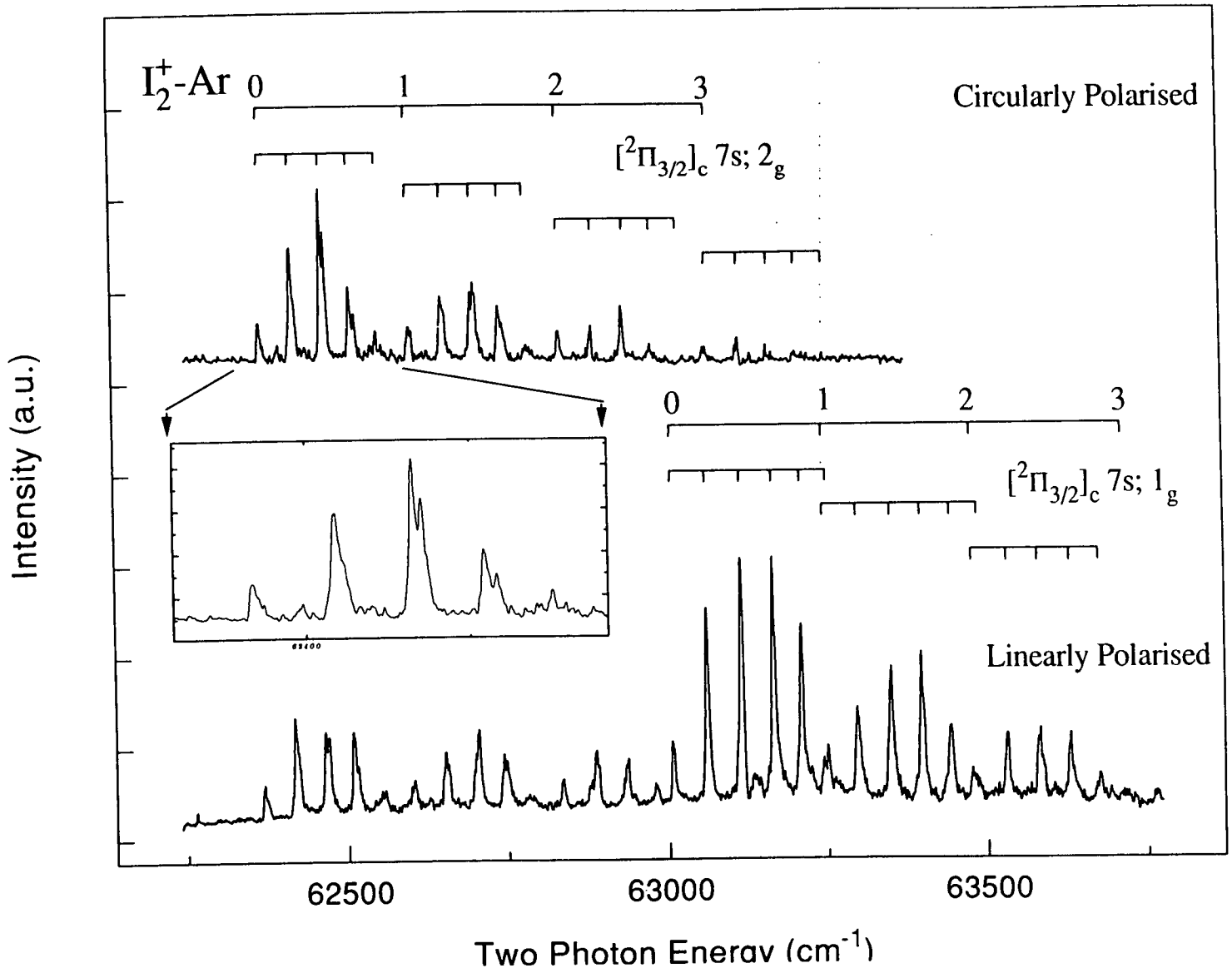

Figure 6.6 The (2+1) mass resolved REMPI excitation spectrum of jet-cooled I_2–Ar recorded in the range 62250-63750 cm^{-1} by monitoring the I_2^+–Ar mass channel with both linearly and circularly polarised light.

$[^2\Pi_{1/2}]_c$ 6s system, each of the vibronic bands corresponding to excitation in the I_2 stretch has a single anharmonic low frequency progression built upon them which arises from excitation in the van der Waals vibrational mode, ν_3. It is noticeable that the ion-pair structure present in the I_2 spectrum is absent from the complex spectrum. This will be discussed further in section 6.4.

The lowest energy peak in the spectrum appears at 62367 ± 2 cm^{-1} and is assumed to be the band origin of the first progression in the series. The lack of any other obvious spectral features to lower energy means that we can conclude that this band corresponds to the band origin of the I_2 $[^2\Pi_{3/2}]_c$ 7s; 2_g Rydberg progression in Figure 5.3. The position of this peak represents a spectral red shift of 272 ± 2 cm^{-1}. This value can be compared with a value of 152 cm^{-1} determined for the $[^2\Pi_{1/2}]_c$ 6s; 1_g Rydberg state and is consistent with a further strengthening in the van der Waals interaction which arises from a reduced level of shielding from the ionic core. Given a value for D_0 in the ground state of 237 ± 3 cm^{-1} [12], and assuming that the first spectral feature in the progression is the true band origin, we can calculate a lower limit to D_0 in the $[^2\Pi_{3/2}]_c$ 7s; 2_g state of I_2–Ar of 509 ± 5 cm^{-1}. The start of the next band appears 234 cm^{-1} to higher energy at 62601 ± 2 cm^{-1}. This separation is almost identical to that between v'=1 and v'=0 in Figure 5.3 (233 cm^{-1}) and consequently we can assign it to one quantum excited in the I_2 stretching mode, ν_1. The next band appears a further 234 cm^{-1} to higher energy and the one after that another 225 cm^{-1} although this latter band and its associated progression is partially obscured in the linearly polarised spectrum by the more intense band that marks the start of the $[^2\Pi_{3/2}]_c$ 7s; 1_g state of the complex.

The band origin of the first progression in the $[^2\Pi_{3/2}]_c$ 7s; 1_g state of the complex appears at 63006 ± 2 cm^{-1} which corresponds to a spectral red shift of 326 ± 2 cm^{-1}. Once again, however, we cannot be certain that this feature is the true origin of this series, but we can nevertheless determine a lower limit to D_0 in the $[^2\Pi_{3/2}]_c$ 7s;

1_g state of 563 ± 5 cm^{-1} which compares with a value of 509 ± 5 cm^{-1} determined for the $[^2\Pi_{3/2}]_c$ 7s; 2_g state.

As mentioned earlier, each of these bands consists of an anharmonic low frequency progression in one of the van der Waals vibrational modes. The average vibrational spacing in these progressions (~50 cm^{-1} for the $[^2\Pi_{3/2}]_c$ 7s; 1_g state and ~46 cm^{-1} for the $[^2\Pi_{3/2}]_c$ 7s; 2_g state) is consistent with single quanta excitation of the I_2···Ar stretching mode, ν_3. Both values are greater than that observed for the $[^2\Pi_{1/2}]_c$ 6s; 1_g Rydberg state which supports the conclusion of a progressive strengthening of the van der Waals bond as we proceed up the Rydberg manifold. The length of the progressions (up to v'=5 in the $[^2\Pi_{3/2}]_c$ 7s; 1_g state) indicates a substantial change in $R_{Ar\cdots I_2}$ and we can conclude from the increase in ν_3 that the bond has shortened. The results of Franck-Condon band envelope simulations on the v'=1 band in the $[^2\Pi_{3/2}]_c$ 7s; 2_g state and the v'=0 band in the $[^2\Pi_{3/2}]_c$ 7s; 1_g state, using the same procedure as laid out above, are shown in Figure 6.7(a) and (b). They indicate that $R_{Ar\cdots I_2}$ is reduced by 0.38 Å for the $[^2\Pi_{3/2}]_c$ 7s; 1_g state and 0.36 Å for the $[^2\Pi_{3/2}]_c$ 7s; 2_g state following electronic excitation from the ground state of the neutral. All spectroscopic constants obtained from the spectrum are given in Table 6.8.

One final point is the observation of a splitting of between 5 and 8 cm^{-1} for most of the peaks assigned to the $[^2\Pi_{3/2}]_c$ 7s; 2_g state (see inset to Figure 6.6). It seems likely that these doublets are either due to one of the van der Waals bending modes, possibly being excited according to the selection rule Δv=0, +2, or are partially resolved rotational branch heads. If the former is the case, then we can derive an approximate bending mode frequency of about 27 cm^{-1}. Similar splittings were observed in a REMPI study of the $\tilde{C}\ ^2\Pi$ state of Ar–NO [24] although no comment was made as to their origin

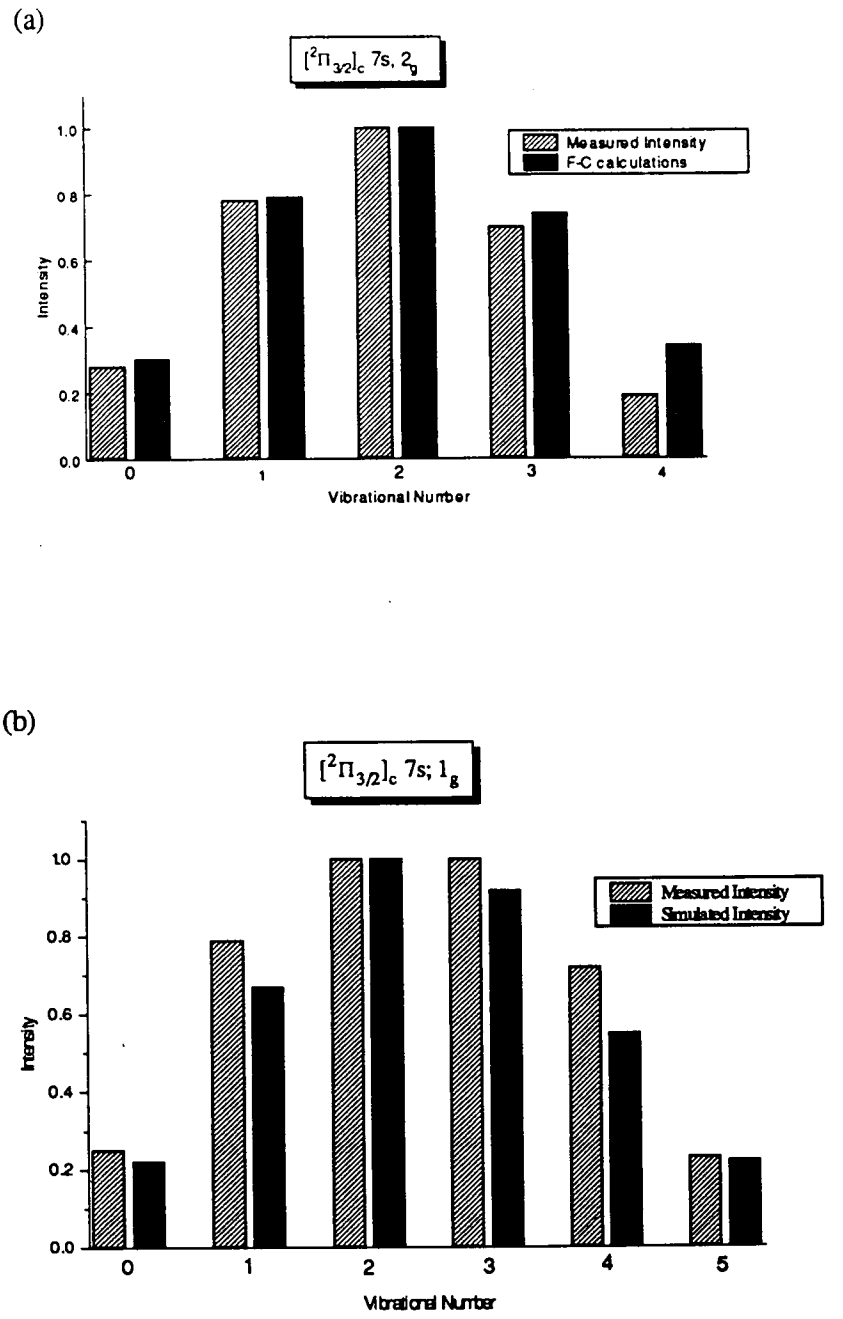

Figure 6.7

Observed and simulated Franck-Condon factors for the transition to (a) the v'=1 band in the $[^2\Pi_{3/2}]_c$ 7s; 2_g state and (b) the v'=0 band in the $[^2\Pi_{3/2}]_c$ 7s; 1_g state of I_2–Ar.

Table 6.2 Spectral peak positions and assignments of the $[^2\Pi_{3/2}]_c$ 7s; 2_g electronic state of I_2–Ar.

Transition energy / cm^{-1} [a]	Vibrational spacing / cm^{-1}		Assignment [b]
62367	0	0	0_0^0
62418	51		3_0^1
62465	47		3_0^2
62508	43		3_0^3
62550	42		3_0^4
62601	0	234	1_0^1
62651	50		$3_0^1 1_0^1$
62698	47		$3_0^2 1_0^1$
62741	43		$3_0^3 1_0^1$
62780	39		$3_0^4 1_0^1$
62835	0	234	1_0^2
62887	52		$3_0^1 1_0^2$
62933	46		$3_0^2 1_0^2$
62978	45		$3_0^3 1_0^2$
63021	43		$3_0^4 1_0^2$
63060	0	225	1_0^3
63111	51		$3_0^1 1_0^3$
63159	48		$3_0^2 1_0^3$
63204	45		$3_0^3 1_0^3$
63247	43		$3_0^4 1_0^3$

[a] Uncertainty ± 2 cm^{-1}.

[b] In this notation $3_0^n 1_0^m$ refers to m quanta excited in the I_2 stretch, ν_1, and n quanta excited in the I_2···Ar van der Waals stretch, ν_3.

Table 6.3 Spectral peak positions and assignments of the $[^2\Pi_{3/2}]_c 7s$; 1_g electronic state of I_2–Ar

Transition energy / cm^{-1} [a]	Vibrational spacing / cm^{-1}		Assignment [b]
63006	0	0	0_0^0
63059	53		3_0^1
63114	55		3_0^2
63164	50		3_0^3
63208	44		3_0^4
63249	41		3_0^5
63243	0	237	1_0^1
63295	52		$3_0^1 1_0^1$
63348	53		$3_0^2 1_0^1$
63396	48		$3_0^3 1_0^1$
63442	46		$3_0^4 1_0^1$
63485	43		$3_0^5 1_0^1$
63476	0	233	1_0^2
63530	54		$3_0^1 1_0^2$
63582	52		$3_0^2 1_0^2$
63629	47		$3_0^3 1_0^2$
63673	44		$3_0^4 1_0^2$
63702	0	226	1_0^3

[a] Uncertainty $\pm 2\ cm^{-1}$.

[b] In this notation $3_0^n 1_0^m$ refers to m quanta excited in the I_2 stretch, ν_1, and n quanta excited in the I_2···Ar van der Waals stretch, ν_3.

6.3.3 The $[^2\Pi_{3/2}]_{c,g}$ 7s Rydberg System in I_2-Ar_2

As with the $[^2\Pi_{1/2}]_c$ 6s system we have to consider the possibility that some of the features in the spectrum may result from fragmentation of higher clusters (I_2-Ar_n). However, in contrast to the $[^2\Pi_{1/2}]_c$ 6s system, however, I_2^+–Ar_2 ions were also observed in the TOF mass spectrum at well defined wavelengths. A time-of flight mass spectrum recorded with the excitation laser wavelength tuned to the most intense of these features at 62980 cm^{-1} is shown in Figure 6.8. The three most prominent mass peaks in the spectrum can be straightforwardly assigned to I^+, I_2^+ and I_2^+-Ar_2 with only very small contributions from I_2^+-Ar as well as I^+-Ar, which are both present this time only as background signals. A mass resolved (2+1) REMPI excitation spectrum of the complex, recorded by gating on the I_2^+-Ar_2 mass channel, is shown in Figure 6.9 while the peak positions are given in Table 6.4. None of the features observed in this spectrum appear in the I_2-Ar spectrum in Figure 6.6 which provides further evidence that fragmentation of higher clusters does not make any observable contribution to the I_2-Ar spectrum. A provisional assignment of the spectrum is relatively straightforward and we can immediately identify both electronic states by comparison with the I_2^+–Ar spectrum in Figure 6.6. The lower 2_g state, appearing at about 62322 cm^{-1} is rather weak compared with the 1_g state, as was found for I_2^+–Ar, and evidence of predissociation is also visible with only one quantum in the I_2 stretch being observed for each Rydberg state. However, rich vdW vibrational structure associated with each band appears in the spectrum for the 1_g state (see inset to Figure 6.9 for an expanded spectrum). This structure has been tentatively assigned to a progression in a vdW stretch having an average vibrational spacing of 40 cm^{-1} and a shorter bending mode progression appearing in combination with the vdW stretch having an average spacing of 15 cm^{-1} as shown in Table 6.4. The red shifts (317 cm^{-1} for the 2_g state and 392 cm^{-1} for the 1_g state) are only slightly greater than those observed for the monomeric clusters (272 cm^{-1} and 326 cm^{-1}, respectively) which implies that the stabilisation of the system brought about by the

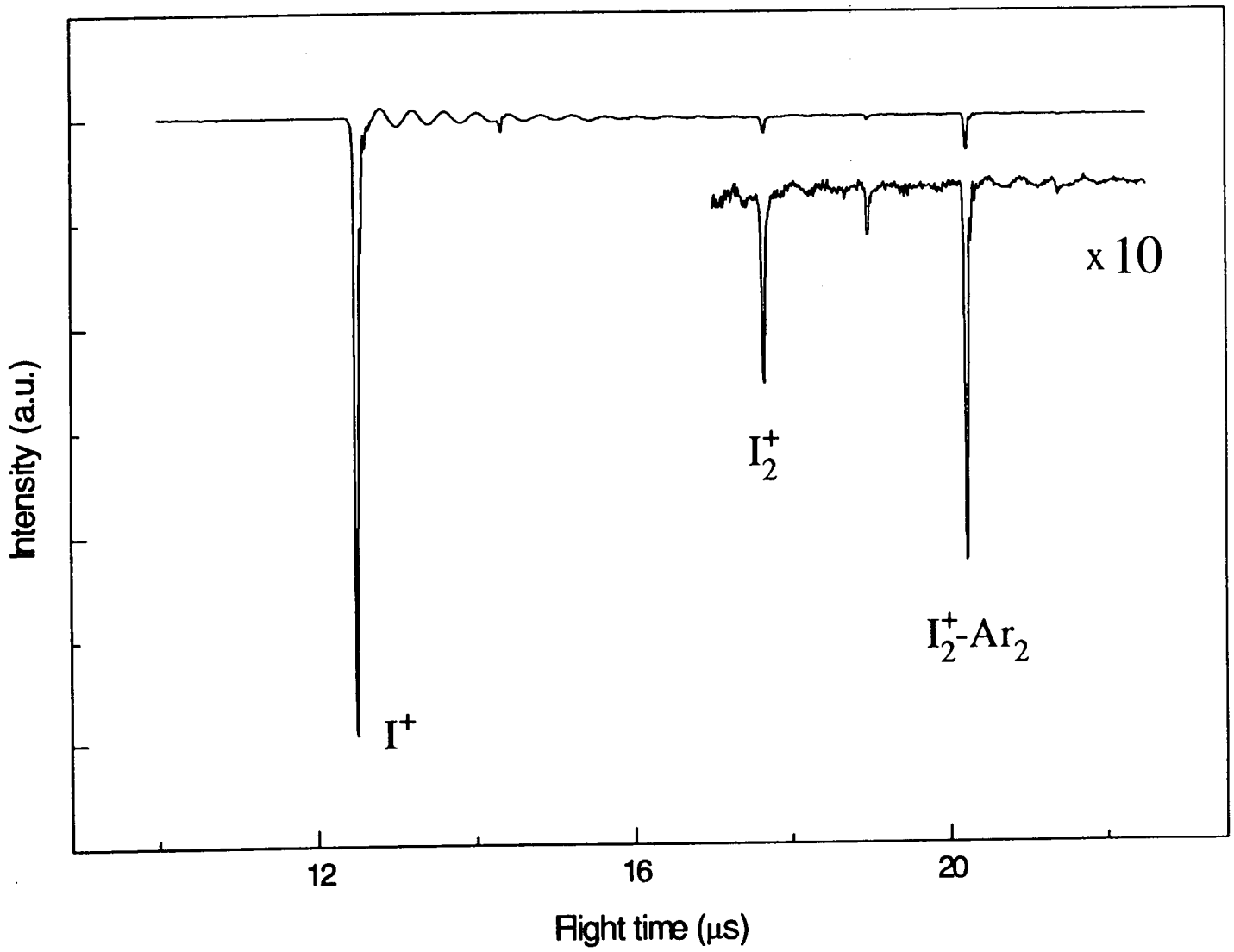

Figure 6.8 The time-of-flight mass spectrum of I_2 expanded in argon recorded by tuning the excitation laser to 62980 cm^{-1}.

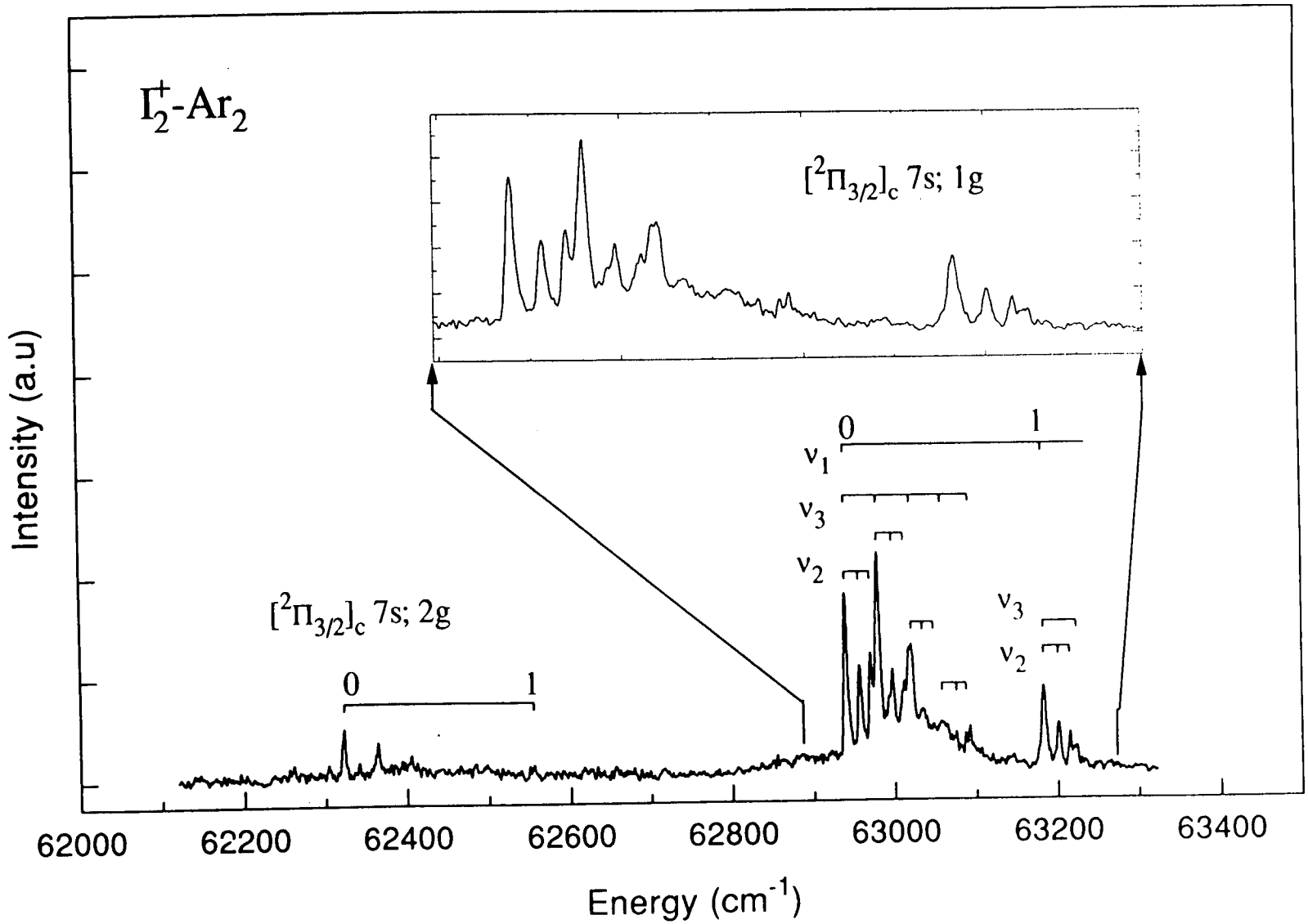

Figure 6.9 The (2+1) mass resolved REMPI excitation spectrum of jet-cooled I_2–Ar_2 recorded in the range 62100-63300 cm^{-1} by monitoring the I_2^+–Ar_2 mass channel.

addition of the second argon atom does not equal that of the first. This suggests that the position of the second Ar atom does not mirror that of the first in I_2-Ar, although beyond this we cannot come to any firm conclusion as to the geometry of the cluster.

Table 6.4 Spectral peak positions and assignments of the $[^2\Pi_{3/2}]_c$ 7s; 2_g and $[^2\Pi_{3/2}]_c$ 7s; 1_g electronic states of I_2–Ar_2.

Electronic state	Transition energy / cm^{-1} [a]	Vibrational spacing / cm^{-1}			Assignment [b]
$[^2\Pi_{3/2}]_c$ 7s; 2_g	62322	0	0	0	0_0^0
	62340			18	2_0^1
	62364		44	0	3_0^1
	62385			21	$2_0^1 3_0^1$
	62405		41		3_0^2
	62555	233			1_0^1
$[^2\Pi_{3/2}]_c$ 7s; 1_g	62940	0	0	0	0_0^0
	62957			17	2_0^1
	62970			13	2_0^2
	62980		40	0	3_0^1
	62997			17	$2_0^1 3_0^1$
	63012			15	$2_0^2 3_0^1$
	63020		40	0	3_0^2
	63034			14	$2_0^1 3_0^2$
	63060		40	0	3_0^3
	63075			15	$2_0^1 3_0^3$
	63088			13	$2_0^2 3_0^3$
	63092		32	0	3_0^4
	63182	242	0	0	1_0^1
	63201			19	$2_0^1 1_0^1$
	63215			14	$2_0^2 1_0^1$
	63221		39	0	$3_0^1 1_0^1$

[a] Uncertainty ± 2 cm^{-1}.

[b] In this notation $3_0^n 1_0^m 2_0^p$ refers to m quanta excited in the I_2 stretch, ν_1, n quanta excited in a van der Waals stretch, ν_3, and p quanta excited in one of the van der Waals bending modes, ν_2.

6.3.4 The $[^2\Pi_{1/2}]_{c,g}$ 7s and $[^2\Pi_{3/2}]_{c,g}$ 8s Rydberg Systems

As with the previous two Rydberg systems, peaks appeared in the I^+ mass channel of the I_2 REMPI spectrum, recorded in the energy range 67000-70000 cm^{-1} two photon energy (see Figure 5.5), which could be provisionally assigned to the van der Waals complex from their dependence on the argon stagnation pressure. No corresponding peaks were observed in the I_2^+ mass channel spectrum. The TOF mass spectrum recorded by tuning the laser to one of the more intense of these features revealed the presence of I_2^+–Ar ions but no evidence of any I^+–Ar could be found at the stagnation pressure used. It would seem that this system follows a similar fragmentation path to that of the 7s system based on the $[^2\Pi_{3/2}]$ ion core discussed above.

A mass resolved (2+1) REMPI excitation spectrum recorded with both linearly and circularly polarised light by gating on the I_2^+–Ar mass channel is presented in Figure 6.10. The presence of four electronic states makes for a substantially more complex spectrum with linear polarisation than those recorded for the other states. Unfortunately this also makes it more difficult to identify complete progressions and to make confident assignments. However, as with the $[^2\Pi_{3/2}]_c$ 7s system, the 1_g states lose practically all their intensity with circularly polarised light which makes it significantly easier to assign the spectrum than it would otherwise have been. These assignments are given in Figure 6.10 as well as in Tables 6.5, 6.6 and 6.7.

A reasonably straightforward assignment of the two lowest energy progressions to the $[^2\Pi_{1/2}]_c$ 7s; 0_g^+ and $[^2\Pi_{3/2}]_c$ 8s; 2_g states can be made since they are the only ones to appear in the upper spectrum in Figure 6.10, recorded with circularly polarised light. The lowest energy progression which starts at 67675 ± 2 cm^{-1} is assigned to the $[^2\Pi_{1/2}]_c$ 7s; 0_g^+ state which is the lowest energy state in this

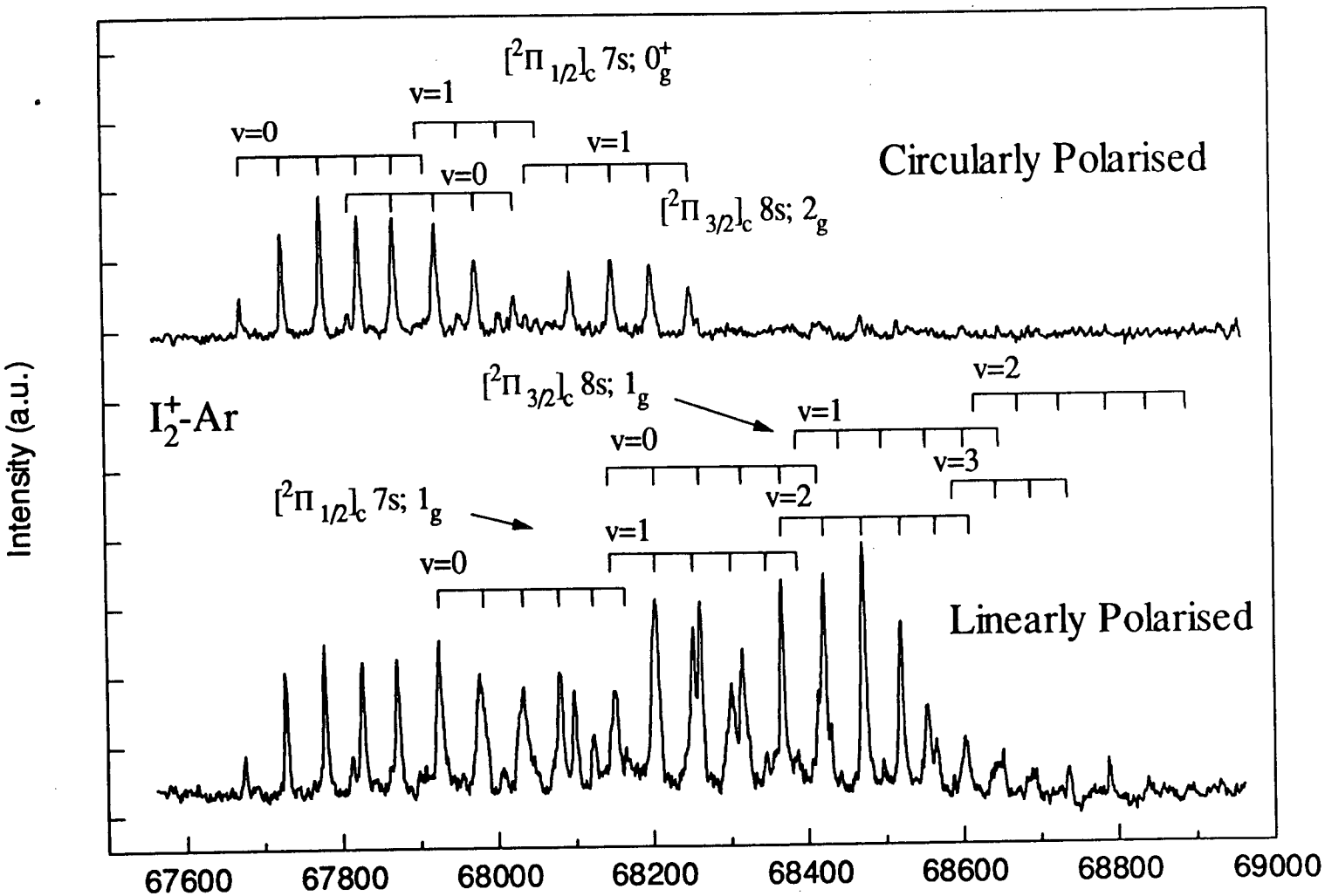

Figure 6.10 The (2+1) mass resolved REMPI excitation spectrum of jet-cooled I_2–Ar recorded in the range 67500-69000 cm^{-1} by monitoring the I_2^+–Ar mass channel with both linearly and circularly polarised light.

region for I_2. This would then represent a spectral red shift of 317 ± 2 cm^{-1} which although comparable with that obtained for the 7s system based on the $[^2\Pi_{3/2}]$ core is more than twice that of the $[^2\Pi_{1/2}]_c$ 6s system. This spectral red shift translates into a value for the dissociation energy D_0 of 554 ± 5 cm^{-1} which can be compared with a value determined for the $[^2\Pi_{1/2}]_c$ 6s; 1_g state of 389 ± 5 cm^{-1}. This increase in stability is matched by an increase in ω_e to 56 cm^{-1} (c.f. 49 cm^{-1} in the $[^2\Pi_{1/2}]_c$ 6s; 1_g state) for the vdW stretch, as well as a lengthening in the vdW progression. This state shows strong $\Delta v=0$ propensity in the I_2 stretching mode with the $v'=1$ band appearing very weakly, 227 cm^{-1} to higher energy.

The $[^2\Pi_{3/2}]_c$ 8s; 2_g state is the next to appear with two quanta in the I_2 stretch being observed. Whilst the $v'=0$ band is once again the most intense, this time the $v'=1$ band appears with comparable intensity in agreement with the intensities observed for these bands in the I_2^+ spectrum in Figure 5.5. These bands are separated by about 228 cm^{-1} which is consistent with excitation in the I_2 stretch. The onset of the $v'=0$ band can be tentatively assigned to a weak peak appearing at 67814 ± 2 cm^{-1} which represents a red shift of 529 ± 2 cm^{-1} and a lower limit to the dissociation energy D_0 of 766 ± 5 cm^{-1}. A comparison of this value for D_0 with that obtained for the $[^2\Pi_{3/2}]_c$ 7s; 2_g state (509 ± 5 cm^{-1}) shows an increase of about 50 % which is perhaps rather larger than we might have expected given that we are approaching the ionisation limit for the $[^2\Pi_{3/2}]$ core. However, it is, nonetheless, consistent with the general trend of increasing binding energy with increasing principle quantum number.

The $[^2\Pi_{1/2}]_c$ 7s; 1_g state shows considerable propensity for Δv = +1 and +2 transitions in the I_2 stretch with up to three quanta being observed. The band origin probably appears underneath the $[^2\Pi_{3/2}]_c$ 8s; 2_g state peak at 67925 ± 2 cm^{-1}. The $v'=1$ band appears with larger intensity, a further 222 cm^{-1} to higher energy and both bands show long progressions in the van der Waals stretch. The spectral red shift of this state is 349 ± 2 cm^{-1}, which corresponds to a binding energy of 586 ± 5 cm^{-1} and

is wholly consistent with that determined for the $[^2\Pi_{1/2}]_c$ 7s; 0_g^+ state (554 ± 5 cm^{-1}). An approximate value for ω_e of 59 cm^{-1} can also be determined, which again is reasonably consistent with the increase in binding energy observed over that in the $[^2\Pi_{1/2}]_c$ 6s system.

Having made provisional assignments for three of the four possible states, we can now assign the progression whose origin lies at 68145 cm^{-1} in the spectrum in Figure 6.10, to the $[^2\Pi_{3/2}]_c$ 8s; 1_g state. In this case we obtain a spectral red shift of 523 ± 2 cm^{-1} which corresponds to a dissociation energy D_0 of 760 ± 5 cm^{-1}. An ω_e for this progression of 62 cm^{-1} can also be derived which once again is reasonably consistent with the calculated dissociation energy. Both values are comparable to those obtained for the $[^2\Pi_{3/2}]_c$ 8s; 2_g state. All the spectroscopic data determined from this spectrum is listed in Table 6.8.

6.3.5 The 5d Rydberg States

In spite of a careful search, no van der Waals bands associated with any of the 5d systems were found. On intensity grounds alone, we might reasonably expect to observe the complex bands for these systems, given our ability to observe bands for the comparatively weak $[^2\Pi_{1/2}]_c$ 6s system. However, as we concluded in chapter 5, the 5d states are only observed as a result of interaction with ion-pair states. Since we have not observed any evidence of ion-pair interaction in any of the vdW complex spectra, it is perhaps not surprising that we are unable to observe the vdW 5d Rydberg states. This point will be addressed in detail below.

Table 6.5 Spectral peak positions and assignments of the $[^2\Pi_{1/2}]_c$ 7s; 0_g^+ and the $[^2\Pi_{3/2}]_c$ 8s; 2_g states of I_2–Ar.

Electronic state	Transition energy / cm^{-1} [a]	Vibrational spacing / cm^{-1}		Assignment [b]
$[^2\Pi_{1/2}]_c$ 7s; 0_g^+	67675	0	0	0_0^0
	67727	52		3_0^1
	67778	51		3_0^2
	67826	48		3_0^3
	67871	45		3_0^4
	67911	40		3_0^5
	67902	0	227	1_0^1
	67955	53		$3_0^1 1_0^1$
	68006	51		$3_0^2 1_0^1$
	68056	50		$3_0^3 1_0^1$
$[^2\Pi_{3/2}]_c$ 8s; 2_g	67814	0	0	0_0^0
	67871	57		3_0^1
	67925	54		3_0^2
	67976	51		3_0^3
	68026	50		3_0^4
	68042	0	228	1_0^1
	68098	56		$3_0^1 1_0^1$
	68152	54		$3_0^2 1_0^1$
	68202	50		$3_0^3 1_0^1$
	68252	50		$3_0^4 1_0^1$

[a] Uncertainty ± 2 cm^{-1}.

[b] In this notation $3_0^n 1_0^m$ refers to m quanta excited in the I_2 stretch, ν_1, and n quanta excited in the I_2···Ar van der Waals stretch, ν_3.

Table 6.6 Spectral peak positions and assignments of the $[^2\Pi_{1/2}]_c$ 7s; 1_g state of I_2–Ar.

Electronic state	Transition energy / cm^{-1} [a]	Vibrational spacing / cm^{-1}		Assignment [b]
$[^2\Pi_{1/2}]_c$ 7s; 1_g	67925	0	0	0_0^0
	67983	58		3_0^1
	68034	51		3_0^2
	68080	46		3_0^3
	68124	44		3_0^4
	68166	42		3_0^5
	68147	0	222	1_0^1
	68204	57		$3_0^1 1_0^1$
	68253	49		$3_0^2 1_0^1$
	68302	49		$3_0^3 1_0^1$
	68347	45		$3_0^4 1_0^1$
	68388	41		$3_0^5 1_0^1$
	68366	0	219	1_0^2
	68421	55		$3_0^1 1_0^2$
	68471	50		$3_0^2 1_0^2$
	68520	49		$3_0^3 1_0^2$
	68566	46		$3_0^4 1_0^2$
	68610	44		$3_0^5 1_0^2$
	68588	0	222	1_0^3
	68644	56		$3_0^1 1_0^3$
	68694	50		$3_0^2 1_0^3$
	68736	42		$3_0^3 1_0^3$

[a] Uncertainty ± 2 cm^{-1}.

[b] In this notation $3_0^n 1_0^m$ refers to m quanta excited in the I_2 stretch, ν_1, and n quanta excited in the I_2···Ar van der Waals stretch, ν_3.

Table 6.7 Spectral peak positions and assignments of the $[^2\Pi_{3/2}]_c$ 8s; 1_g state of I_2–Ar.

Electronic state	Transition energy / cm^{-1} [a]	Vibrational spacing / cm^{-1}		Assignment [b]
$[^2\Pi_{3/2}]_c$ 8s; 1_g	68145	0	0	0_0^0
	68204	59		3_0^1
	68261	57		3_0^2
	68316	55		3_0^3
	68366	50		3_0^4
	68414	48		3_0^5
	68387	0	242	1_0^1
	68442	55		$3_0^1 1_0^1$
	68497	55		$3_0^2 1_0^1$
	68554	57		$3_0^3 1_0^1$
	68603	49		$3_0^4 1_0^1$
	68648	45		$3_0^5 1_0^1$
	68617	0	230	1_0^2
	68673	56		$3_0^1 1_0^2$
	68726	53		$3_0^2 1_0^2$
	68785	59		$3_0^3 1_0^2$
	68837	52		$3_0^4 1_0^2$
	68888	51		$3_0^5 1_0^2$

[a] Uncertainty ± 2 cm^{-1}.

[b] In this notation $3_0^n 1_0^m$ refers to m quanta excited in the I_2 stretch, ν_1, and n quanta excited in the I_2···Ar van der Waals stretch, ν_3.

Table 6.8 Spectroscopic data obtained for the *n*s Rydberg states of I_2–Ar.

State	Band origin / cm^{-1}	Δv / cm^{-1}	D_0 / cm^{-1}	ω_e / cm^{-1}	$\omega_e x_e$ / cm^{-1}	G_0 / cm^{-1}	D_e / cm^{-1}
$[^2\Pi_{1/2}]_c$ 6s; 1_g	53430±2	152±2	389±5	49±2	1.50±0.1	24±4	413±9
$[^2\Pi_{3/2}]_c$ 7s; 2_g	62367±2	272±2	509±5	54±2	1.55±0.1	27±4	536±9
$[^2\Pi_{3/2}]_c$ 7s; 1_g	63006±2	326±2	563±5	59±2	1.75±0.1	29±4	592±9
$[^2\Pi_{1/2}]_c$ 7s; 0_g^+	67675±2	317±2	554±5	56±2	1.50±0.1	28±4	582±9
$[^2\Pi_{3/2}]_c$ 8s; 2_g	67814±2	529±2	766±5	59±2	1.20±0.1	29±4	795±9
$[^2\Pi_{1/2}]_c$ 7s; 1_g	67925±2	349±2	586±5	59±2	1.70±0.1	29±4	615±9
$[^2\Pi_{3/2}]_c$ 8s; 1_g	68145±2	523±2	760±5	62±2	1.45±0.1	31±4	791±9

6.4 Discussion

The present investigation of iodine-argon van der Waals complexes excited to a number of different Rydberg states based upon both spin-orbit components of the ionic core enables a number of general observations to be made. The first of these is the observation that as the principal quantum number of the Rydberg state increases, so does the binding energy of the van der Waals complex. This correlates with what one would intuitively expect given the progressive reduction in shielding of the effective ionic core charge by the Rydberg electron as it is excited into higher orbits. The increased effective charge of the core then exerts a greater attractive force on the polarisable argon atom through charge-induced dipole effects. This progressive strengthening of the bond is reflected in the experimentally observed increasing spectral red shifts and ω_e's, and the extension of the intermolecular vibrational progressions, which are all indicative of a shortening of the bond. The spectral red shifts determined in this work would appear to be consistent with a model of the Rydberg excited complex in which the Rydberg electron lies outside the boundaries of

the T-shaped complex. If we assume a model in which the argon atom is polarised by the full positive charge of I_2^+ (the charge situated at the centre of I-I bond) then we can calculate a polarisation energy of 575 cm^{-1} for an assumed vdW bond length of 3.6 Å. This can be compared to the experimentally determined red shift for the $[^2\Pi_{3/2}]_c$ 8s; 2_g state of 529 cm^{-1}.

The second, somewhat unexpected observation, was the rather puzzling fragmentation behaviour of the complexes. A general observation for all the Rydberg states described here was that fragmentation of the I_2-Ar complex always ultimately resulted in production of I^+ to the total exclusion of I_2^+; for all the Rydberg states for which we were able to record REMPI spectra of the complexes, we were unable to observe any evidence of complex bands in the I_2^+ mass channel spectra. However, for all the *n*s Rydberg states except the $[^2\Pi_{1/2}]_c$ 6s system, the primary complex ion was I_2^+-Ar. This suggests that either there is a competing fragmentation pathway in the neutral state which yields atomic iodine which is then ionised to give I^+ or that I_2^+-Ar can fragment completely ($I^+ + I + Ar$) following further absorption after ionisation, on a time scale far faster than fragmentation to I_2^+ and Ar. The first of these possibilities would seem to be supported by a rotational band contour analysis of the $[^2\Pi_{3/2}]_c$ 7s system in I_2 which shows clear evidence of lifetime broadening [40]. In contrast, the $[^2\Pi_{1/2}]_c$ 6s system exhibits completely different behaviour and provides us with a much more explicit picture of its fragmentation pathway. In this case the dominant product ion is I^+-Ar with I_2^+-Ar only being observed very weakly at the lowest level of vibrational excitation in the Rydberg state (see Figure 6.3). Although this observation initially seems to contradict what we might expect given the relative amount of energy required to break the I_2 bond versus that required to break the van der Waals bond, we can propose a number of possible explanations to account for this phenomenon. Firstly, the observation of I^+-Ar_n peaks in the mass spectrum would seem to be wholly consistent with the analogous one photon photodissociation of uncomplexed I_2^+ [41]. Fragmentation of the complex in the neutral state to give I-Ar through an interaction

of the Rydberg state with a repulsive valence state would appear to be unlikely. The point of interaction will lie some 38000 cm^{-1} above the likely dissociation products I (^2P) and this should impart sufficient acceleration to the products to make it unlikely that the van der Waals bond would survive the dissociation process. This conclusion is further supported by a rotational contour analysis of each of the bands in the $[^2\Pi_{1/2}]_c$ 6s system of I_2 which shows no evidence of any lifetime broadening [42]. However, if the primary ionic product, which in this case is I_2^+-Ar, absorbs a further photon to a weakly repulsive state of I_2^+, it could follow a much more gentle fragmentation path to give I^+-Ar which, as well as being electronically stable (i.e. isoelectronic with ICl), will be more strongly bound than I-Ar because of the charge-induced dipole component of the van der Waals bond. The apparent variation in fragmentation efficiency with vibrational excitation in the Rydberg state observed in the REMPI spectrum in Figure 6.3 can probably be attributed to progressively better Franck-Condon overlap between the vibrational wavefunction in the Rydberg state and the continuum wavefunction in the dissociative channel in the ion.

Other possibilities previously proposed to account for the observation of I^+-Ar_n clusters in mass spectrometric work [36] include excitation of the I_2-Ar complex to an autoionising state from which dissociative ionisation occurs to give I^+-Ar + I, as well as intracluster ion-molecule reactions of the type $I_2^+ + Ar \rightarrow I^+$-Ar + I. Given the dependence on laser wavelength of the relative amounts of I^+-Ar and I_2^+-Ar and the collision free environment inherent in a skimmed molecular beam, the latter explanation is fairly unlikely. Nevertheless, it is conceivable that the product ions may be undergoing collisions as they are accelerated through the molecular beam by the extraction field, but in this case we may expect some effect on the flight times of the ions perhaps in the form of a broadening in the peak shape. However, no observed broadening in the TOF peak shape between the uncomplexed I_2^+ and I^+ peaks and those of the complexes has been observed. Indeed, the complex peaks often appeared significantly narrower than those of the uncomplexed parent ions, so it seems safe to conclude that ion-molecule reactions are not contributing to the observed product ion

distributions. It is not so easy to discount the possibility of dissociative ionisation contributing to the ion intensity distribution but the experimental evidence seems to favour the provisional conclusion detailed above.

The behaviour of the van der Waals complex spectra above 62000 cm^{-1} when irradiated with circularly polarised light is found to be identical to that observed in I_2. Exactly the same loss in intensity was observed in all the 1_g states for the primary ion, I_2^+-Ar, rather than any of the subsequent products of fragmentation. These observations confirm the conclusions arrived at in chapter 5 regarding the explanation proposed by Donovan et al. [43]. The fact that the complex spectra show exactly the same behaviour with circularly polarised light as the uncomplexed I_2 suggests that the mechanism which accounts for this behaviour is the same in each case. However, even with this confirmatory data, a satisfactory explanation for these observations is at present unavailable. It is nonetheless fortunate that this phenomenon provides us with a means to deconvolute some of the more complicated spectra recorded for the I_2-Ar van der Waals complex (see for example Figure 6.10).

The apparent inhibition of ion-pair/Rydberg interaction in the complexes is a new phenomenon and is most explicitly demonstrated in the spectrum recorded for the $[^2\Pi_{3/2}]_c$ 7s; 1_g state in Figure 6.6. Clearly, the rich ion-pair structure apparent in the equivalent spectrum recorded for uncomplexed I_2, in Figures 5.3 and 5.4, has completely disappeared. The interacting Rydberg (*Ry*) and ion-pair (*i.p.*) states (the $\beta(1_g)$ ion-pair state in this case) differ by a two-electron configuration change and there is no reason to suppose that the electronic part of the interaction matrix element, $\langle Ry|\frac{1}{r_{12}}|i.p.\rangle$ is much affected by complexation. The extent of vibrational coupling in free I_2 is also governed by the Franck-Condon factor $\left\langle v^{Ry}\middle|v^{i.p.}\right\rangle$ where v^{Ry} is the vibrational wavefunction of the Rydberg state and $v^{i.p.}$ is the ion-pair state vibrational wavefunction. Similarly, in the complex, the Franck-Condon factor can be expressed by $\left\langle v_1^{Ry}v_3^{Ry}\middle|v_1^{i.p.}v_3^{i.p.}\right\rangle$ where v_1 and v_3 refer to the I_2 stretch and vdW stretch,

respectively. However, the vibrational motion on the 3-body ion-pair surface is extremely complex and the ν_1 and ν_3 modes cannot be treated as completely separable simple harmonic modes. Indeed, excimer formation, Ar^+I^-, becomes an open channel. Under these conditions, the effective Franck-Condon factor in the triatomic is much smaller than in the diatomic and the vibronic coupling will be effectively quenched. The second effect of complexation is to alter the relative energies of the Rydberg and ion-pair states, depending on the Ar···I_2 separation. It could well be that the position of the *i.p./Ry* curve crossing in the I···I co-ordinate is moved out of the Franck-Condon region accessible from the ground state.

The lack of any observable vibrational complex bands associated with the 5d states is not altogether unsurprising based on the discussion above and the fact that the 5d states in I_2 are only observed as a result of their interaction with ion-pair states. If the addition of an argon atom does indeed quench the vibronic coupling of the Rydberg state with an ion-pair state then the 5d Rydberg states would lose their route to ionisation and would not be observed. Another possibility for the lack of 5d Rydberg excited I_2–Ar, is that the level of vibrational excitation in the respective in-pair states, which at the point of interaction, represents at least 20000 cm^{-1} excess energy, would be such that the ion-pair van der Waals complex would almost certainly have dissociated.

6.5 ZEKE-PFI Photoelectron Spectroscopy of Rydberg Excited I_2–Ar

Over the last 5-10 years interest in the spectroscopic characterisation of ionic vdW clusters has increased as techniques such as zero kinetic energy pulsed field ionisation (ZEKE-PFI) photoelectron spectroscopy [44] have become capable of resolving the characteristic low frequency vibrational modes of vdW complexes [45]. Other techniques such as the resonance-enhanced photodissociation of mass selected ions have also permitted the selective study of ionic complexes [46]. Prior to these developments, interest had been primarily focused on the formation mechanisms and

reactivities of ionic vdW complexes and very few detailed gas phase spectroscopic measurements had been performed [47]. Ionic van der Waals complexes are in general more strongly bound than their neutral counterparts due to the addition of a charge induced dipolar interaction to the potential energy function and are found in any cool, ionised gas phase environment. However, as a general trend, ionic complexes are perhaps not bound as tightly as might be expected. It has been postulated in the case of vdW clusters consisting of an aromatic molecule and a rare gas atom [48] that this may be due to a decrease in the dispersive interaction upon ionisation through the reduced polarisability of the ion relative to the neutral.

The ionic potential of a vdW complex can be investigated by measuring the shift in the ionisation potential (which gives directly the change in bond strength) and the vibrational structure of the intermolecular modes. An analysis of the frequencies and line intensities of these modes can sensitively probe the intermolecular potential. For rare gas van der Waals cations it is reasonable to assume that the minimum in the ionic potential is not so far from the neutral to be unobservable. However, for species such as charge transfer complexes and higher clusters which may reorganise upon ionisation, it is possible that the neutral geometry does not have access to the potential minimum of the cation.

The electronic structure of the I_2–Ar van der Waals complex is very similar to that of I_2, and therefore there are no known suitable intermediate states in the UV for a (1+1') ZEKE-PFI study. The observation of the Rydberg excited states of the complex therefore provided the ideal intermediates for a (2+1') ZEKE-PFI study of the I_2–Ar vdW complex. A number of experimental limitations again constrained the possible Rydberg intermediate states which could be employed in a two colour ZEKE-PFI experiment. As was the case in I_2, the requirement for high photon fluxes in both the pump and probe lasers was of paramount importance and limited the probe laser output to a dye fundamental. The wavelength limit of the infra-red dyes (<900 nm) therefore constrained the intermediate Rydberg states to the $[^2\Pi_{3/2}]_{c,g}$ 7s and $[^2\Pi_{1/2}]_{c,g}$ 7s systems for ionisation into the respective ionic spin-orbit components.

However, in contrast to iodine other factors had to be taken into account when deciding which Ω state within the 7s systems was employed as the intermediate state of the complex. These included the relative intensity of the vibrational bands in the two Ω states in the $[^2\Pi_{3/2}]_{c,g}$ 7s system and the fact that in the $[^2\Pi_{1/2}]_{c,g}$ 7s system the 1_g vibrational bands are overlapped.

The ZEKE-PFI spectra of the $\tilde{X}\ ^2\Pi_{g,3/2}$ ionic state presented in section 6.7 via v'=0-4 of the $[^2\Pi_{3/2}]_c$ 7s; 1_g Rydberg state, were recorded with an extraction potential of 2.35 V/cm. The ZEKE-PFI spectrum of the $\tilde{X}\ ^2\Pi_{g,1/2}$ ionic state presented in section 6.8 via v'=2 of the $[^2\Pi_{1/2}]_c$ 7s; 0_g^+ Rydberg state, however, was recorded with an extraction potential of 2.27 V/cm. All the ZEKE-PFI spectra were recorded with a delay of 1.055 μs.

6.6 The $\tilde{X}\ ^2\Pi_{g,3/2}$ Ionic State of I_2–Ar

6.6.1 The (2+1) REMPI Spectrum of I_2–Ar in the Range 62250 to 63750 cm^{-1}

Ionisation into the lower $\tilde{X}\ ^2\Pi_{g,3/2}$ spin-orbit state of I_2^+-Ar is nominally favoured for a transition from a Rydberg state having a $[^2\Pi_{3/2}]$ core. The most experimentally convenient system for this purpose is the $[^2\Pi_{3/2}]_{c,g}$ 7s system at around 63000 cm^{-1} which is composed of two partially overlapping vibrational progressions arising from the $[^2\Pi_{3/2}]_c$ 7s; 2_g and the $[^2\Pi_{3/2}]_c$ 7s; 1_g Rydberg states of I_2-Ar as shown in Figure 6.6. The spectrum exhibits rich vibrational structure arising from simultaneous excitation of both the I···I stretch (ν_1) and the I_2···Ar van der Waals stretch (ν_3) for both Rydberg states. The high level of vibrational activity in the spectrum enables the optical preparation of a wide selection of vibrationally excited intermediate states. This greatly assists the assignment of the resulting ZEKE-PFI spectra since we can generally expect a direct correspondence between the level of vibrational excitation of the initially prepared state and that of the final ionic state.

The increased intensity of the 1_g vibrational bands compared with those of the 2_g make it the preferred intermediate Rydberg state.

6.6.2 The (2+1') ZEKE-PFI Spectrum of I_2-Ar Ionised *via* the $[^2\Pi_{3/2}]_c$ 7s; 1_g State

The two colour (2+1') ZEKE-PFI spectra of I_2-Ar *via* the band origin of the $[^2\Pi_{3/2}]_c$ 7s; 1_g Rydberg state at 63006 cm^{-1} as well as *via* the first four vibrationally excited levels in the I_2···Ar van der Waals stretching vibration, ν_3, are presented in Figure 6.11(a). A single peak is observed at 74520 ± 2 cm^{-1} in the spectrum recorded *via* the band origin (*via* ν_3=0) which can be provisionally assigned to the $\Delta\nu$=0 transition to the ν^+=0 level in the ion. No other obvious spectral features were observed scanning to lower energy so we can be reasonably confident that the peak at 74520 cm^{-1} corresponds to the band origin of the $\tilde{X}\ ^2\Pi_{g,3/2}$ state of I_2^+-Ar. A correction must be applied to this measured value to take account of the field ionisation shift. In the case of the van der Waals complex, the equation describing the field ionisation shift is assumed to be the same as that determined for molecular iodine ($\Delta E = 1.60\sqrt{F(V/cm)}$). This results in an adiabatic ionisation energy of 74523 ± 2 cm^{-1} and represents an ionisation energy red-shift of 546 ± 4 cm^{-1} with respect to the $\tilde{X}\ ^2\Pi_{g,3/2}$ spin-orbit state of molecular iodine (75069 ± 2 cm^{-1}) determined in the previous chapter. A lower limit to D_0 in the $\tilde{X}\ ^2\Pi_{g,3/2}$ spin-orbit state can therefore be calculated to be 783 ± 5 cm^{-1}, using a value for D_0 in the neutral ground state of I_2-Ar of 237 ± 3 cm^{-1} determined experimentally by Blazy et al. [12]. This compares with a value of D_0 determined previously for the $[^2\Pi_{3/2}]_c$ 8s; 2_g Rydberg state of 766 ± 5 cm^{-1}.

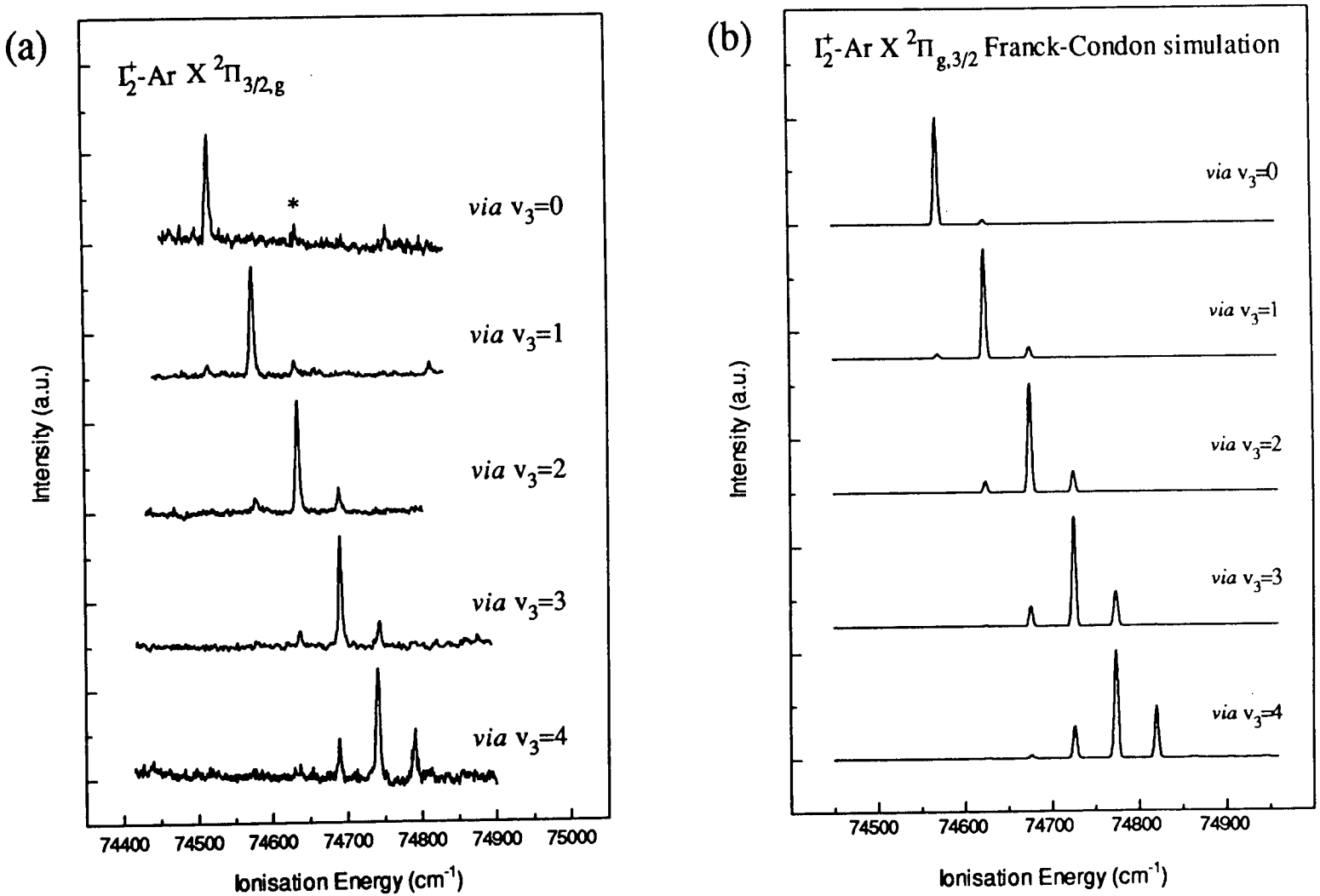

Figure 6.11 (a) The (2+1') ZEKE-PFI spectra of the $\tilde{X}\ ^2\Pi_{g,3/2}$ state of I_2^+–Ar recorded *via* the band origin of the $[^2\Pi_{3/2}]_c$ 7s; 1_g Rydberg state at 63006 cm^{-1} as well as *via* the first four vibrationally excited levels in the I_2···Ar vdW stretching vibration, v_3. In these spectra, * denotes an accidental A←X neutral state resonance in I_2. (b) Franck-Condon simulations of the ZEKE-PFI spectra shown in (a).

There is very little evidence in the spectrum recorded *via* the band origin of the $[^2\Pi_{3/2}]_c$ 7s; 1_g Rydberg state of any van der Waals stretching excitation. This is wholly consistent with the assumed similarities in equilibrium geometries of the Rydberg and ionic states. However, there is some intensity in a band appearing 238 cm^{-1} to higher ion internal energy which can be compared with a $v^+=0$ to $v^+=1$ vibrational separation of 239 cm^{-1} determined for the $\tilde{X}\ ^2\Pi_{g,3/2}$ ionic state of molecular iodine. This band can therefore be assigned to one quantum excited in the I_2 stretching mode, ν_1, of the complex. Clearly, the presence of the argon atom in the ionic complex has very little effect on the I_2 stretching frequency. The peak lying 117 cm^{-1} to higher energy of the band origin does not arise from direct (2+1') photoionisation of the complex but is due to an accidental resonance of the probe laser wavelength with an $A\,^3\Pi_{1_u} \leftarrow X\,^1\Sigma_{0_g^+}$ neutral state transition in I_2 which shows up in the ZEKE channel via a mechanism involving a further pump photon resonance with an ion-pair state.

The ZEKE-PFI spectrum recorded by exciting one quantum in the van der Waals stretching mode, ν_3, (i.e. *via* 3_0^1) in the $[^2\Pi_{3/2}]_c$ 7s; 1_g Rydberg state at 63059 cm^{-1} is also shown in Figure 6.11(a). Once again there is a strong propensity for the $\Delta v=0$ transition which results in most of the intensity appearing in the 3_0^{+1} band which lies 60 cm^{-1} above the band origin at 74583 ± 2 cm^{-1} (i.e. one quantum excited in the van der Waals stretching mode in the ion). However, this time we also observe some intensity in the $\Delta v = \pm 1$ transitions due to the improved vibrational wavefunction overlap between the Rydberg and ionic states. As in the spectrum recorded *via* the band origin a band appears ~237 cm^{-1} to the blue of the main 3_0^{+1} band. This feature can be straightforwardly assigned to a combination band corresponding to excitation of one quantum in the van der Waals stretching mode, ν_3, and one quantum in the I_2 stretching mode, ν_1 (i.e. $3_0^{+1}1_0^{+1}$).

Further increases in the level of vibrational excitation in the van der Waals stretching mode in the intermediate Rydberg state results in corresponding increases in the level of vibrational excitation in the ion (see Figure 6.11(a)) with each of the ZEKE-PFI spectra showing clear propensity for the $\Delta v=0$ transition. The progressive increase in intensity of the $\Delta v = \pm 1$ transitions, as the level of vibrational excitation in ν_3 is increased in the intermediate Rydberg state, provides us with a classic example of Franck-Condon behaviour. A plot of $\Delta G_{v+1/2}$ against v yields values for ω_e and $\omega_e x_e$ of 62 ± 2 cm^{-1} and 1.2 ± 0.1 cm^{-1} respectively. These can be compared with corresponding values determined for the $[^2\Pi_{3/2}]_c$ 8s; 2_g state of 59 ± 2 cm^{-1} and 1.2 ± 0.1 cm^{-1}. All ionic state spectroscopic constants determined in the present work are detailed in Table 6.9.

The obvious lack of vibrational structure in the ZEKE-PFI spectrum recorded *via* the band origin of the $[^2\Pi_{3/2}]_c$ 7s; 1_g Rydberg state and the clear propensity for the $\Delta v=0$ transition in each case strongly suggests that the geometry change between the Rydberg state and the ion along the van der Waals co-ordinate is small. In order to quantify this geometry change a series of Franck-Condon calculations were performed to simulate the experimentally observed band envelopes. In performing these calculations it has been assumed that the potential curve along the I_2···Ar co-ordinate can adequately be described by a Morse potential for both of the electronic states. The Rydberg state spectroscopic constants were taken from the results in section 6.2.2. The results of these simulations are shown in Figure 6.11(b) and display a very good agreement with the experimental data. The best fit to the experimental data was obtained for a reduction in the van der Waals bond length $R_{Ar\cdots I_2}$ of 0.035 Å upon ionisation from the $[^2\Pi_{3/2}]_c$ 7s; 1_g Rydberg state. The Franck-Condon calculation carried out in section 6.2.2 for the $[^2\Pi_{3/2}]_c$ 7s; 1_g Rydberg state, indicated a reduction in the van der Waals bond length, $R_{Ar\cdots I_2}$, of 0.38 Å. An overall reduction in the van der Waals bond length for ionisation into the $\tilde{X}\ ^2\Pi_{g,3/2}$ ionic state from the ground state of the neutral can therefore be calculated to be 0.415 Å. The lack of any other intermolecular vibrational structure other than that arising from the

van der Waals stretch, strongly supports the conclusion that the potential which describes the motion of the argon atom parallel to the I···I co-ordinate (i.e. the van der Waals bend) undergoes almost no change upon ionisation and consequently we can say that the complex retains a T-shaped geometry in the ion.

6.7 The $\tilde{X}\ ^2\Pi_{g,1/2}$ ionic state of I_2–Ar

6.7.1 The (2+1) REMPI Spectrum of I_2-Ar in the Range 67600-68875 cm^{-1}

The mass resolved (2+1) REMPI excitation spectrum of I_2-Ar in the range 67600-68875 cm^{-1} two photon energy is presented in Figure 6.12. For the sake of clarity, the spectrum was recorded with circularly polarised light which excludes the 1_g states. Although two states appear in the spectrum (the $[^2\Pi_{1/2}]_c$ 7s; 0_g^+ and $[^2\Pi_{3/2}]_c$ 8s; 2_g Rydberg states), it is the $[^2\Pi_{1/2}]_c$ 7s; 0_g^+ state which should provide us with the best means to access the $\tilde{X}\ ^2\Pi_{g,1/2}$ spin-orbit ionic state, if we assume a preference for core preservation upon ionisation.

6.7.2 The (2+1') ZEKE-PFI Spectrum of I_2-Ar Ionised *via* the $[^2\Pi_{1/2}]_c$ 7s; 0_g^+ State

The ZEKE-PFI signal for the $\tilde{X}\ ^2\Pi_{g,1/2}$ state was of considerably lower intensity than those recorded for the $\tilde{X}\ ^2\Pi_{g,3/2}$ state and consequently the only ZEKE-PFI spectrum which was recordable, was that via the strongest transition in the $[^2\Pi_{1/2}]_c$ 7s; 0_g^+ Rydberg state. The two colour (2+1') ZEKE-PFI spectrum of I_2-Ar ionised *via* the 3_0^2 band of the $[^2\Pi_{1/2}]_c$ 7s; 0_g^+ Rydberg state at 67778 ± 2 cm^{-1} (i.e. two quanta excited in the van der Waals stretch, ν_3) is presented in Figure 6.13. The spectrum reveals, as expected, a propensity for the $\Delta v=0$ transition but now with considerable intensity (~40%) in the $\Delta v= \pm 1$ transitions. Although no observed intensity appears in the band origin we can extrapolate back to the origin to obtain a

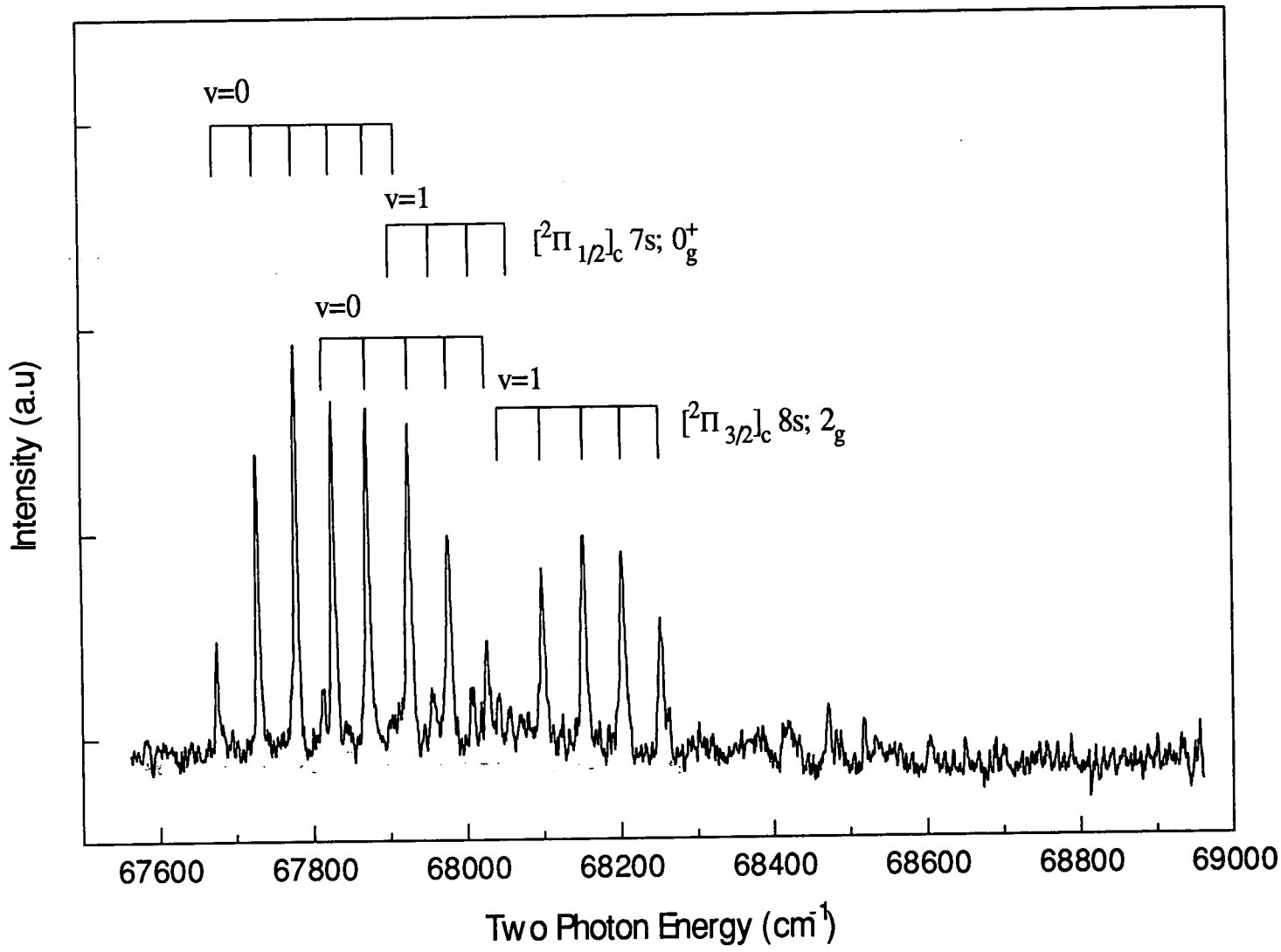

Figure 6.12 The (2+1) mass resolved REMPI excitation spectrum of jet-cooled I_2–Ar recorded in the range 67600-68875 cm^{-1} recorded using circularly polarised light and monitoring the I_2^+–Ar mass channel.

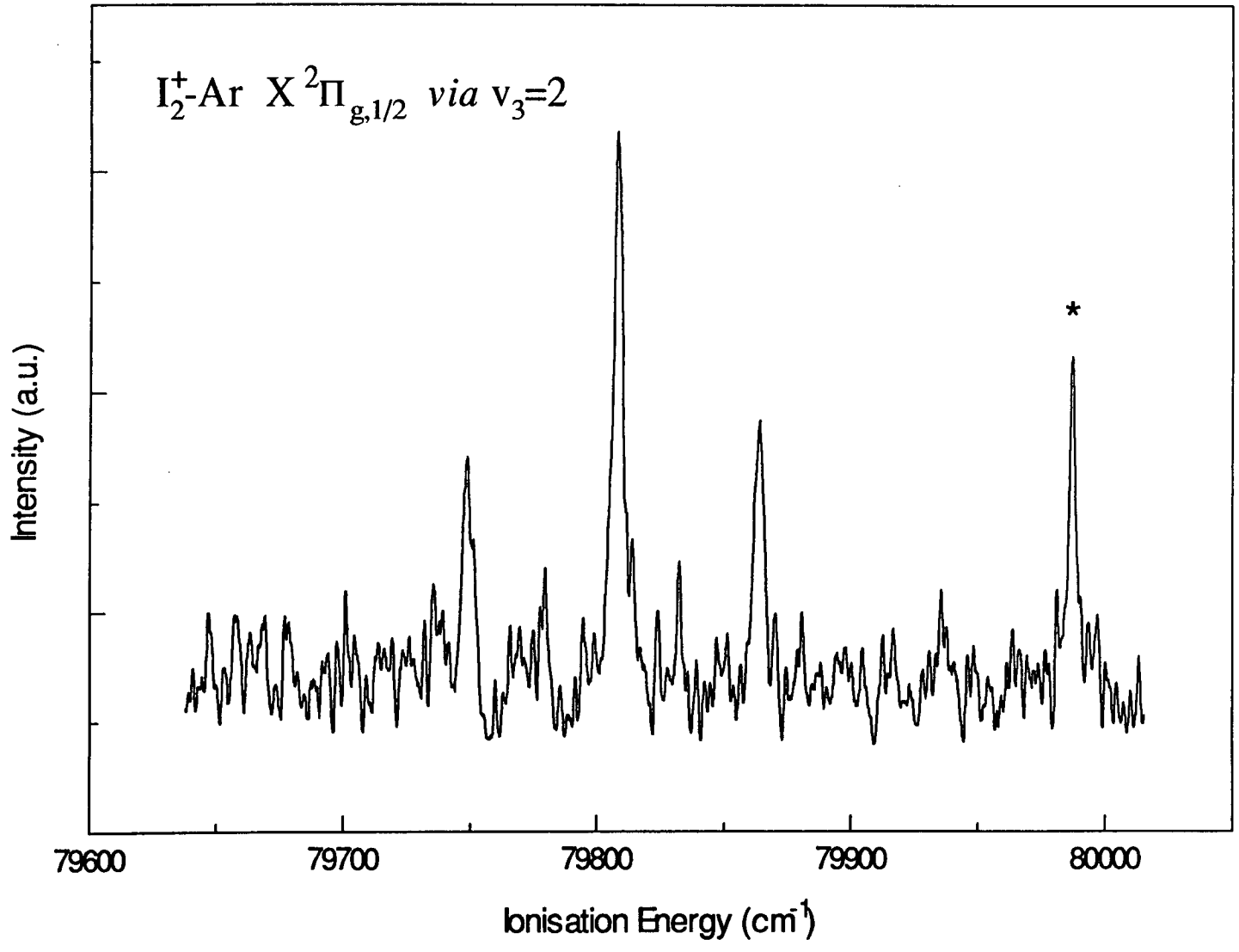

Figure 6.13 The (2+1') ZEKE-PFI spectra of the $\tilde{X}\ ^2\Pi_{g,1/2}$ state of I_2^+–Ar ionised *via* the 3_0^2 band of the $[^2\Pi_{1/2}]_c$ 7s; 0_g^+ Rydberg state at 67778 cm^{-1} (i.e two quanta excited in the van der Waals stretch, ν_3. * denotes an accidental A←X neutral state resonance in I_2.

value for the adiabatic ionisation energy of 79692 ± 3 cm^{-1} for the $\tilde{X}\ ^2\Pi_{g,1/2}$ state. This represents an ionisation energy red shift of 574 ± 5 cm^{-1} with respect to the adiabatic ionisation energy of the X $^2\Pi_{g,1/2}$ spin-orbit state (80266 ± 2 cm^{-1}) of molecular iodine. Given a value for D_0 in the ground state of I_2-Ar of 237 ± 3 cm^{-1}, we can calculate a lower limit to D_0 in the $\tilde{X}\ ^2\Pi_{g,1/2}$ ionic state of 811 ± 6 cm^{-1}. A plot of $\Delta G_{v+1/2}$ against v yields values for ω_e and $\omega_e x_e$ of 62 ± 2 cm^{-1} and 1.7 ± 0.1 cm^{-1} respectively.

Having determined the adiabatic ionisation energies for the two spin-orbit components of the $\tilde{X}\ ^2\Pi_{g,i}$ state, a value for the spin-orbit splitting can be calculated to be 5169 ± 5 cm^{-1}. This can be compared with a spin-orbit splitting in I_2 of 5197 ± 5 cm^{-1}.

Table 6.9 Spectroscopic data obtained for the $\tilde{X}\ ^2\Pi_{g,3/2}$ and $\tilde{X}\ ^2\Pi_{g,1/2}$ ionic states of I_2^+–Ar

Ionic state	I.E. / cm^{-1}	ΔI.E. [a] / cm^{-1}	D_0 [b] / cm^{-1}	ω_e [c] / cm^{-1}	$\omega_e x_e$ [c] / cm^{-1}	D_e / cm^{-1}
$\tilde{X}\ ^2\Pi_{g,3/2}$	74523±2	546±4	783±5	62±2	1.2±0.1	814±9
$\tilde{X}\ ^2\Pi_{g,1/2}$	79692±3	574±5	811±6	62±2	1.7±0.1	842±10

[a] Ionisation energy red shift.

[b] Zero-point dissociation energy calculated from observed spectral red-shift.

[c] Calculated from a plot of $\Delta G_{v+1/2}$ versus v for the I_2···Ar stretching mode progression.

6.8 Discussion

One of the main motivations for carrying out a ZEKE-PFI investigation of the I_2–Ar complex was to obtain a limit to which the van der Waals binding energy converges as the Rydberg electron is excited into progressively higher orbits, leading eventually to ionisation. A comparison of the binding energies for the two spin-orbit components of the $\tilde{X}\ ^2\Pi_{g,i}$ state of I_2^+-Ar, with those previously obtained from the REMPI spectra of the *n*s Rydberg states of I_2-Ar (n=6 to 8), provides us with an indication of the extent to which the penetration of the Rydberg electron modifies the contribution of charge-induced dipole forces to the overall van der Waals interaction. The picture we have of the Rydberg excited complex, is one in which the Rydberg electron lies in an orbit substantially larger than the size of the complex. In this model the polarisable argon atom effectively sees a proportion of the positive charge of the ionic core. However, the exact proportion depends on the level of penetration of the Rydberg electron into the core. As the Rydberg electron is excited into progressively higher orbits, so the binding energy of the van der Waals complex will increase as the level of shielding of the positive charge is decreased. To compare the Rydberg spectral red-shifts with the averaged ionisation energy red-shifts for the two ionic spin-orbit components, requires the quoted spectral red-shifts for a particular *n*s Rydberg orbital to be averaged over all core states and Ω quantum numbers such that only the principal quantum number of the Rydberg state is referred to. As a further aid the approximate radii of the Rydberg orbitals (the outer turning point of the classical motion of the Rydberg electron) have been calculated by assuming a classical picture of the Rydberg electron in a Coulomb potential (see Table 6.10).

The observed increase in spectral red-shift resulting from the promotion of a Rydberg electron from the 6s to the 7s Rydberg orbital is approximately 164 cm^{-1}. This increases by a further 210 cm^{-1} when the Rydberg electron is promoted from the 7s to the 8s Rydberg orbital. However, these substantial increases contrast quite dramatically with the ~30 cm^{-1} increase, observed on promoting the Rydberg electron from the 8s Rydberg orbital to infinity (i.e. the ionic state). Clearly, the binding

energy of the complex cannot be said to be smoothly converging to the ionic limit asymptote for the lower *n* Rydberg states described here.

In order to illustrate the interaction between the argon atom and the iodine ionic core, a simple model has been used in which all interactions between the ion and the argon atom are ignored except the charge-induced dipole interaction. In the ionic state we assume that the argon atom is polarised by the full positive charge of I_2^+ located at the mid-point of the I-I bond. This yields a polarisation energy of 575 cm^{-1}, for an assumed vdW bond length of 3.6 Å, which we can equate directly with the experimentally averaged ionisation energy red shift, over both spin-orbit components, of 560 cm^{-1}. In order to extend this model to describe the changes in spectral red-shifts observed for the Rydberg states, the polarisation energy has been calculated by varying the percentage of the effective ionic core charge seen by the argon atom in order to mimic the depth of penetration of the Rydberg electron. In spite of the simplicity of the model, it should allow a qualitative picture to be obtained of the changes in the interaction that occur as the principal quantum number of the Rydberg complex increases. From the averaged experimental spectral red-shifts determined for the Rydberg states shown in Table 6.10 and assuming that the polarisation energy can be equated to the spectral red-shift, the approximate percentage effective ionic core charge seen by the argon atom for each *n*s Rydberg state can be deduced. Assuming a vdW bond length of 3.6 Å allows us to establish that the spectral red-shift of 152 cm^{-1} determined for the 6s Rydberg state corresponds to the argon atom feeling the effect of ~50% of the ionic core charge. This is consistent with the calculated Rydberg radius for this state of about 5.5 Å which implies a fairly high level of Rydberg electron penetration given a van der Waals bond length of 3.6 Å. The average spectral red-shift of ~310 cm^{-1} obtained for the 7s Rydberg states, which should have a Rydberg orbital radius of about 9.7 Å, corresponds to an effective ionic charge of approximately 75% of the full ionic state value which again seems reasonable in view of the large increase in the size of the Rydberg orbital. Continuing to the 8s Rydberg state where the average experimental spectral red-shift is around 525 cm^{-1}, the Rydberg orbital radius is calculated to be approximately 17.9 Å, almost

double that of the 7s state. This corresponds to the core exerting around 95% of its attractive force on the argon atom which accounts for the large increase in spectral red shift over that observed for the 7s state. The Rydberg electron in Rydberg states with a principal quantum number greater than 8 is therefore at least 18 Å away from the core and has very little influence on the effective ionic core charge seen by the argon atom.

Table 6.10 Spectral red shifts, binding energies and calculated Rydberg orbital radii

Principal quantum number of *n*s Rydberg	6	7	8	9	∞ (ion)
Averaged spectral red shift / cm^{-1} [a] $(G_0(I_2^{*(n)})\text{-}G_0(I_2\text{–}Ar^{*(n)}))$	152	316	526	–	560
Binding energy (D_0) /cm^{-1} [a]	389	553	763	–	797
Radius of *n*s orbital [b]	5.5 Å	9.7 Å	17.9 Å	29.0 Å	–

[a] Averaged over both spin-orbit and Ω quantum numbers.

[b] The outer turning point of the classical motion of the Rydberg electron in a coulomb potential.

The term values of a Rydberg series, whether of the complexed or uncomplexed I_2, vary as $1/(n\text{-}\delta)^2$ (see chapter 5). A plot of I.E.-T_e(Rydberg) *vs* $1/(n\text{-}\delta)^2$ for I_2-Ar shows near-perfect linearity where the quantum defect in the complex is taken to be the same as that found in I_2 [43]. However, the quantum defects calculated for I_2 [43] and those determined in this investigation of I_2–Ar differ by a small amount (~ 0.02-0.04). To account for the slightly different quantum defect in the complex means that we must describe the binding energy of the complex (D_e(n)) by

$$D_e(n) = \frac{Ry}{(n-\delta_{vdW})^2} - \frac{Ry}{(n-\delta_{i_2})^2} + D_e(I_2^+ - Ar) \qquad 6.2$$

Based on the complex quantum defect calculations above, the quantum defect of the complex can be described by $\delta_{vdW} = \delta_{I_2} + x$ such that Equation 6.2, in first order, can be reduced to

$$D_e(n) = \frac{2Ryx}{(n-\delta_{I_2})^3} + D_e(I_2^+ - Ar). \qquad 6.3$$

A plot of the binding energy of the van der Waals complex against $1/(n\text{-}\delta)^3$ (where n is the principal quantum number and δ is the van der Waals quantum defect) should therefore result in a straight line. Plots of D_e(ion) - D_e(Rydberg) *vs* $1/(n\text{-}\delta)^3$ for both spin-orbit states is shown in Figure 6.14. Clearly, neither plot shows a satisfactory linear dependence which would suggest that local perturbations, induced perhaps by the presence of 5d Rydberg states, may be affecting the shape of the potential along the I_2···Ar co-ordinate. It should be noted, however, that it is perhaps unreasonable to expect perfect linearity given the small number of data points in each plot and the effect that comparatively small errors in the total transition energy will have on the appearance of the plot. For example, an error of 60 cm^{-1}, which might arise from an incorrectly assigned REMPI spectrum, will have a much greater effect on the linearity of the De(ion) - D_e(Rydberg) *vs* $1/(n\text{-}\delta)^3$ plot than on that of the I.E.-T_e(Rydberg) *vs* $1/(n\text{-}\delta)^2$ plot.

The measured spin-orbit splitting of 5169 ± 5 cm^{-1} between the $\tilde{X}\ ^2\Pi_{g,3/2}$ ionic state and the $\tilde{X}\ ^2\Pi_{g,1/2}$ ionic state of the complex, is slightly smaller than the corresponding splitting of 5197 ± 4 cm^{-1} in uncomplexed I_2^+. An important difference between the $\tilde{X}\ ^2\Pi_{g,3/2}$ and $\tilde{X}\ ^2\Pi_{g,1/2}$ ionic states is that the latter is coupled by spin-orbit interaction to the $B\ ^2\Sigma^+_{1/2,g}$ excited state which lies about 3 eV to higher energy. The electron configuration of the B state is $\sigma_g^1\pi_u^4\pi_g^4$ and consequently there will be a

(a)

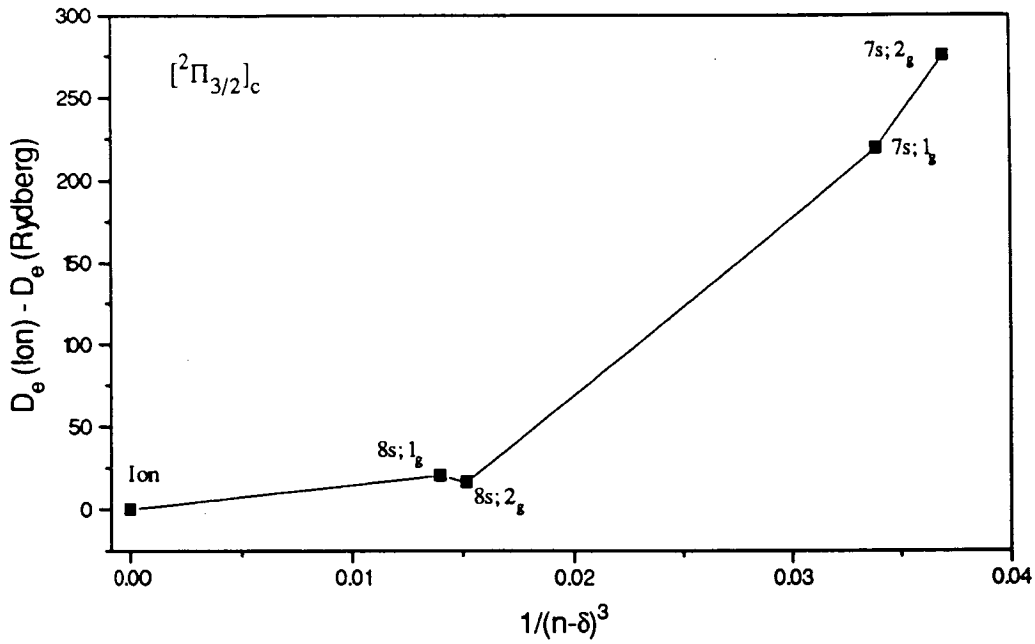

(b)

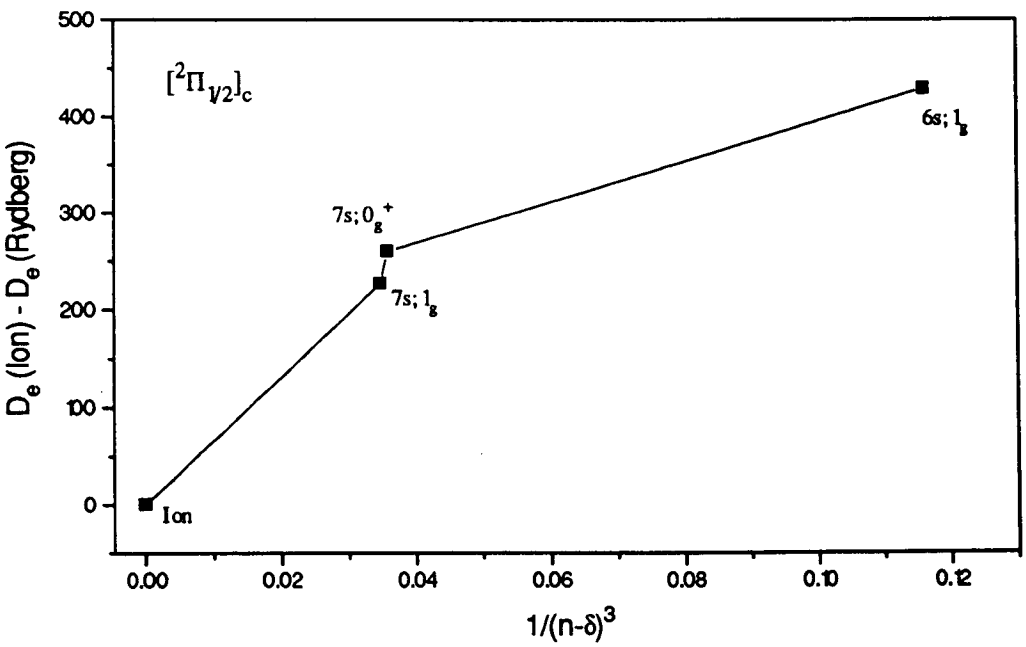

Figure 6.14

A plot of D_e(ion)-D_e(Rydberg) *vs* $1/(n-\delta)^3$ for both spin-orbit components of I_2–Ar

considerable rearrangement of the electron density compared to the ground state of the ion. In particular the greater concentration of net positive charge at the centre of the I-I bond in the $^2\Sigma^+_{1/2,g}$ state will tend to increase the polarisation energy in the complex for this state compared to that in the $^2\Pi_{g,i}$ ground state which will have most of the net positive charge located in the lobes of the π_g orbital. If the interaction energy with the argon atom in the $^2\Sigma^+_{1/2,g}$ state is assumed to be stronger by an amount ΔE, compared to the ground state, then an amount $c^2\Delta E$ (where c is the coefficient of the $^2\Sigma^+_{1/2,g}$ component in the description of the upper spin-orbit state) will be transferred in second order to the $^2\Pi_{g,1/2}$ state through the spin-orbit interaction, leading to an overall reduction in spin-orbit splitting in the complex as observed experimentally.

One final point which deserves some comment is the poor quality of the ZEKE-PFI spectrum recorded for the $\tilde{X}\ ^2\Pi_{g,1/2}$ state compared with the $\tilde{X}\ ^2\Pi_{g,3/2}$ state. It seems unlikely that the dramatic difference in signal to noise is simply due to differences in the relative 2-photon transition probabilities into the $[^2\Pi_{1/2}]_c$ 7s; 0_g^+ and $[^2\Pi_{3/2}]_c$ 7s; 1_g Rydberg states since the REMPI spectra of the two states show comparable signal-to noise ratios. An alternative explanation is that spin-orbit autoionisation of high *n* Rydberg states converging on the $^2\Pi_{g,1/2}$ ionic state results in a loss in intensity to the upper spin-orbit component. Such effects have previously been observed in the ZEKE-PFI spectra of both HCl [49] and HF [50] in which transitions into the lower spin-orbit states were found to be strongly favoured over transitions into the upper spin-orbit state of the ion.

6.9 References

[1] See for example Chem. Rev (1988) No. 6

[2] D.H. Levy, Photoselective Chemistry, edited by J. Jortner, R.D. Levine and S.A. Rice, Adv. Chem. Phys. **XLVII** (1981) 323

[3] G.E. Ewing, Acc. Chem. Res. **8** (1975) 185

[4] B.L. Blaney and G.E. Ewing, Ann. Rev. Phys. Chem. **27** (1976) 553

[5] D.H. Levy, Annu. Rev. Phys. Chem. **31** (1980) 197

[6] M. Rigby, E.B. Smith, W.A. Wakeham and G.C. Maitland, The Forces Between Molecules, Oxford Science Publications (1986)

[7] R.E. Smalley, D.H. Levy and L. Wharton, J. Chem. Phys. 64 (1976) 3266

[8] M.S. Kim, R.E. Smalley, L. Wharton and D.H. Levy, J. Chem. Phys. **65** (1976) 1216

[9] R.E. Smalley, L. Wharton and D.H. Levy, Chem. Phys. Lett. **51** (1977) 392

[10] R.E. Smalley, L. Wharton and D.H. Levy, J. Chem. Phys. **68** (1978) 671

[11] G. Kubiak, P.S.H. Fitch, L. Wharton and D.H. Levy, J. Chem. Phys. **68** (1978) 4477

[12] J.A. Blazy, B.J. DeKoven, T.D. Russell and D.H. Levy, J. Chem. Phys. **72** (1980) 2439

[13] E.J. Bieske, M.W. Rainbird, I.M. Atkinson and A.E.W. Knight, J. Chem. Phys. **91** (1989) 752

[14] T. Troxler and S. Leutwyler, J. Chem. Phys. **95** (1991) 4010

[15] E. Shalev, N. Ben-Horin, U. Even and J. Jortner, J. Chem. Phys. **95** (1991) 3147

[16] J.I. Cline, D.D. Evard, F. Thommen and K.C. Janda, J. Chem. Phys. **84** (1986) 1165

[17] D.D. Evard, J.I. Cline and K.C. Janda, J. Chem. Phys. **88** (1988) 5433

[18] D.E. Brinza, C.M. Western, D.D. Evard, F. Thommen, B.A. Swartz and K.C. Janda, J. Phys. Chem. **88** (1984) 2004

[19] J.C. Drobits and M.I. Lester, J. Chem. Phys. **86** (1987) 1662

[20] T.A. Stephenson, Y. Hong and M.I. Lester, J. Chem. Phys. **94** (1991) 4171

[21] P.R.R. Langridge-Smith, E. Carrasquillo and D.H. Levy, J. Chem. Phys. **74** (1981) 6513

[22] J.C. Miller and W. Cheng, J. Phys. Chem. **89** (1985) 1647

[23] K. Tsuji, K. Shibuya and K. Obi, J. Chem. Phys. **100** (1994) 5441

[24] K. Sato, Y. Achiba and K. Kimura, J. Chem. Phys. **81** (1984) 57

[25] K. Onda, K. Yamanouchi, M. Okunishi and S. Tsuchiya, J. Chem. Phys. **101** (1994) 7290

[26] K.E. Johnson, W. Sharfin and D.H. Levy, J. Chem. Phys. **74** (1981) 163

[27] S.K. Gray, Chem. Phys. Lett. **197** (1992) 86

[28] J.J. Breen, D.M. Willberg, M. Gutmann and A.H. Zewail, J. Chem. Phys. **93** (1990) 9180

[29] S.K. Gray and S.A. Rice, Faraday Discussions Chem. Soc. **82** (1986) 307

[30] D.M. Willberg, M. Gutmann, J.J. Breen and A.H. Zewail, J. Chem. Phys. **96** (1992) 198

[31] T. Kokabo and Y. Fujimura, J. Chem. Phys. **85** (1986) 7106

[32] J.A. Beswick and J. Jortner, J. Chem. Phys. **69** (1978) 512

[33] M.L. Burke and W. Klemperer, J. Chem. Phys. **98** (1993) 6642

[34] O. Roncero, N. Halberstadt and J.A. Beswick, Chem. Phys. Lett. **226** (1994) 82

[35] J.C. Miller, J. Phys. Chem. **91** (1987) 2589

[36] D.B. Smith and J.C. Miller, J. Chem. Phys. **90** (1989) 5203

[37] A.J. Stace, Chem. Phys. Lett. **113** (1985) 335

[38] K.P. Huber and G. Herzberg, Molecular Spectra and Molecular Structure, Vol. 4, Constants of Diatomic molecules, Van Nostrand Reinhold Company, New York (1979)

[39] R.G. Bray and R.M. Hochstrasser, Mol. Phys. **31** (1976) 1199

[40] Private communication with T. Ridley

[41] J.C. Miller and R.N. Compton, J. Chem. Phys. **75** (1981) 2020

[42] H. Wang, J. Asgeirsson, A. Kvaran, R.J. Donovan, R.V. Flood, K.P. Lawley, T. Ridley and A.J. Yencha, J. Mol. Struct. **293** (1993) 217

[43] R.J. Donovan, R.V. Flood, K.P. Lawley, A.J. Yencha and T. Ridley, Chem. Phys. 164 (1992) 439

[44] K. Müller-Dethlefs and E.W. Schlag, Annu. Rev. Phys. Chem. **42** (1991) 109

[45] K. Müller-Dethlefs, O. Dopfer and T.G. Wright, Chem. Rev. **94** (1994) 1845

[46] E.J. Bieske and J.P. Maier, Chem. Rev. **93** (1993) 2603

[47] A.W. Castleman Jr and R.G. Keesee, Chem. Rev. **86** (1986) 589

[48] H-Y. Kim and M.W. Cole, J. Chem. Phys. **90** (1989) 6055

[49] E. de Beer, W.J. Buma and C.A. de Lange, J. Chem. Phys. **99** (1993) 3252

[50] A. Mank, D. Rodgers and J.W. Hepburn, Chem. Phys. Lett. **219** (1994) 169

University Regulations

Whilst pursuing postgraduate research in the Department of Chemistry at the University of Edinburgh I have attended the following courses:

(i) Laser Physics, Department of Physics
(ii) Unigraph Course, Department of Chemistry
(iii) Microsoft Word for Windows Course V6, Computing Services

In addition I have attended the following conferences:

(i) R.S.C. Faraday Division, High Resolution Spectroscopy Group Meeting, Heriot-Watt University, U.K., December 1991
(ii) European Meeting on Photons, Beams and Chemical Dynamics, held at the University of Paris XI at Orsay, France, 8-10 July 1992
(iii) European Research Conference 1993 Series - "Very High Resolution Spectroscopy with Photoelectrons - Excited State Spectroscopy and Dynamics", Giens, France, 18-23 September 1993
(iv) Faraday Discussion No. 97 - Structure and Dynamics of van der Waals Complexes, University of Durham, U.K., 6-8 April 1994.
(v) Symposium Between the Ionisation Studies Groups of Edinburgh and Glasgow Universities, held in the Department of Chemistry, University of Edinburgh, U.K., 8 December 1993
(vi) Symposium Between the Participants in the EEC Science Program Project, held at the University of Paris XI at Orsay, France, 18-19 April 1994
(vii) University of Edinburgh, Department of Chemistry Physical Discussion Evenings, 1991-1994
(viii) University of Edinburgh Laser and Molecular Beam Group Weakly Meetings, 1991-1994

List of publications

(1) *The spectroscopy of Rydberg excited iodine-argon van der Waals complexes*, M.C.R. Cockett, J.G. Goode, K.P. Lawley and R.J. Donovan, Chem. Phys. Lett. **214** (1993) 27

(2) *Resonance Enhanced Multiphoton Ionization Spectra of the $E0^+(^3P_2)$ and $f0^+(^3P_0)$ Ion-Pair States of ICl*, R.J. Donovan, J.G. Goode, K.P. Lawley, T. Ridley and A.J. Yencha, J. Phys. Chem. **98** (1994) 2236

(3) *Rydberg excited iodine-argon van der Waals complexes studied by resonance enhanced multiphoton ionization spectroscopy*, M.C.R. Cockett, J. G. Goode, R.R.J. Maier, K.P. Lawley and R.J. Donovan, J. Chem. Phys. **101** (1994) 126

(4) *Threshold photoelectron spectroscopy of I_2*, A.J. Yencha, M.C.R. Cockett, J.G. Goode, R.J. Donovan, A. Hopkirk and G.C. King, Chem. Phys. Lett. **229** (1994) 347

(5) *Threshold photoelectron spectroscopy of CF_4 up to 60.5 eV*, A.J. Yencha, A. Hopkirk, A. Hiraya, G. Dujardin, A. Kvaran, L. Hellner, M.J. Besnard-Ramage, R.J. Donovan, J.G. Goode, R.R.J. Maier, G.C. King and S. Spyrou, J. Electron Spectroscopy and related Phenomena, **70** (1994) 29

(6) *Zero Kinetic Energy (ZEKE) Photoelectron Spectroscopy of the Rydberg Excited Iodine-Argon van der Waals Complex*, J.G. Goode, M.C.R. Cockett, K.P. Lawley and R.J. Donovan, Chem. Phys. Lett. **231** (1994) 521

(7) *Threshold photoelectron spectroscopy of Cl_2 and Br_2 up to 35 eV*, A.J. Yencha, A. Hopkirk, A. Hiraya, R.J. Donovan, J.G. Goode, R.R.J. Maier, G.C. King and A. Kvaran, J. Phys. Chem. *in press*

(8) *Zero Kinetic Energy (ZEKE) Photoelectron Spectroscopy of Rydberg Excited Molecular Iodine*, M.C.R. Cockett, J.G. Goode, K.P. Lawley and R.J. Donovan, J. Chem. Phys. *in press*